# Design and Properties of Novel Host Materials for Blue TADF OLEDs

## DISSERTATION

zur Erlangung des akademischen Grades eines

Doktors der Naturwissenschaften (Dr. rer. nat.)

im Promotionsprogramm „Polymer Science"

der Graduiertenschule für Mathematik und

Naturwissenschaften der Universität Bayreuth

von

### Francesco Rodella

geboren in Mantova, Italien

Bayreuth, 2021

Die vorliegende Arbeit wurde in der Zeit von Oktober 2018 bis Oktober 2021 am Lehrstuhl Makromolekulare Chemie I der Universität Bayreuth unter Betreuung von Herrn Prof. Dr. Peter Strohriegl angefertigt.

Vollständiger Abdruck der von der Bayreuther Graduiertenschule für Mathemathik und Naturwissenschaften (BayNAT) der Universität Bayreuth genehmigten Dissertation zur Erlangung des akademischen Grades eines Doktors der Naturwissenschaften (Dr. rer. nat.).

Dissertation eingereicht am: 14.10.2021

Zulassung durch das Leitungsgremium: 22.11.2021

Wissenschaftliches Kolloquium: 21.04.2022

Amtierender Direktor: Prof. Dr. Hans Keppler

Prüfungsausschuss:

Prof. Dr. Peter Strohriegl (Gutachter)

Prof. Dr. Andreas Greiner (Gutachter)

Prof. Dr. Werner Köhler (Vorsitz)

Prof. Dr. Rainer Schobert

(Weiterer Gutachter: Prof. Dr. Michael Sommer)

*To my Family*

**"Now I make him the spoon"**

**" Mo je faccio er cucchiaio"**

**F. Totti**

**Table of contents**

**Summary**

Organic light-emitting diodes (OLEDs) represent cutting-edge technology that promises to improve significantly display and lighting applications. However, the blue diode still lacks materials with simultaneous efficiency and stability. The latest and most promising solution to solve this problem is based on thermally activated delayed fluorescence (TADF) emitters. In the development of this new class of molecules, a fundamental role is played by the host matrix, which, together with the emitter molecules, is essential to improve the stability and efficiency of the device. The aim of the thesis is to synthesize and characterize new host materials for blue OLEDs, establish a solid strategy for their design, and study the thermal and morphological properties of hosts and emitters.

The first paper establishes a fundamental strategy for synthesizing high triplet energy host materials. Through a toolbox approach, building blocks (acceptor, donor, and linker) were chosen and combined systematically to form an array of six donor-acceptor molecules. All the molecules possess a triazine acceptor, while carbazole and acridine are used as donors. The connection between donor and acceptor is altered systematically from a para-phenyl to a meta-phenyl linker until having no linker at all. By comparing the molecules, we conclude that the highest triplet energies are obtained when the linker between donor and acceptor is avoided. Furthermore, using a less conjugated donor (acridine instead of carbazole), the highest triplet energy of 3.07 eV is reached for the host ATRZ. This host possesses high thermal and morphological stability (thermal decomposition and glass transition at 341°C and 115°C, respectively). Aside from the publication, the most promising host is tested in blue TADF OLEDs, obtaining high external quantum efficiency of 10.0% and low efficiency roll-off. Furthermore, the device has shown a good lifetime with LT50 (lifetime until half luminance) of 40 hours at 100 cd/m$^2$, which is a reasonable value among the few lifetimes reported in the literature for blue TADF emitters.

In the second paper, the knowledge gained from the toolbox approach is expanded to obtain new high triplet energy hosts and validate the design strategy. Donor and acceptor units were chosen and directly coupled to limit the conjugation and provide higher triplet energy. Additionally, the donor's choice goes on the acridine unit for its high triplet state and bulkiness. This time, the donor is kept constant throughout the series, while three different pyrimidine-based acceptors with varying conjugation lengths are adopted. Their conjugated

system is changed from having two phenyl rings to one phenyl ring until having only one methyl group. We conclude that the host adopting the least conjugated methyl-substituted pyrimidine acceptor provides the highest triplet energy of 3.07 eV, along with bipolar properties and high thermal and morphological stability, i.e., glass transition at 138°C and thermal decomposition at 413°C. Again, the most promising host is tested in blue TADF OLEDs, providing high efficiency of 13.6% and a low efficiency roll-off.

The third paper discusses a series of four new pyridylbenzimidazole-based TADF emitters. Due to the importance of thermal and morphological stability, the thermal properties of these emitters are analyzed. The four emitters differ from the functional group on the acceptor moiety, which increases bulkiness within the series: hydrogen (without substitution), methyl, phenyl, and tert-butyl. The molecule with the phenyl group is the most stable (thermal decomposition at 355°C) due to more π conjugation and π-π interactions. Surprisingly, the morphological stability is the highest for the molecule without substitution (glass transition at 97°C), which is attributed to hydrogen bond formation in the solid-state.

In the fourth paper, a model correlating TADF emitters' orientation with the host's glass transition to increase light outcoupling and hence OLED efficiency is described. The results show that the orientation of TADF emitters doped in a host film depends mostly on three parameters. i) When the molecule is highly elongated, the emitter's intrinsic property (shape) determines the orientation. ii) When emitters are less elongated, the host governs their orientation. iii) within the same glass transition range, certain hosts can rearrange more than others, boosting the horizontal orientation of the emitter. Therefore, also the alignment of the host itself influences the emitter's orientation.

To summarize, the work of this thesis tackles the deficiency of strategies on how to design high triplet energy host materials by reporting a widely applicable approach for their design. Additionally, two novel hosts with triplet energy as high as 3.07 eV were obtained, possessing good thermal and morphological properties and bipolar character. The materials were tested in OLED devices delivering good efficiency and stability. Furthermore, the thermal and morphological properties of new TADF emitters were determined, providing insights into the processability and durability of this category of emitters. Finally, the morphological properties of benchmark hosts were obtained and correlated with TADF emitters' orientation to provide a model helpful to increasing efficiency in OLEDs.

## Zusammenfassung

Organische Leuchtdioden (OLEDs) stellen eine neue Technologie dar, die deutliche Verbesserungen bei Display- und Beleuchtungsanwendungen verspricht. Allerdings fehlt es bei blauen OLEDs noch immer an Materialien, die gleichzeitig effizient und langzeitstabil sind. Eine neue und vielversprechende Lösung für dieses Problem basiert auf thermisch aktivierten verzögerten Fluoreszenz-Emittern (TADF). Bei der Entwicklung dieser neuen Molekülklasse spielen Matrixmaterialien eine wesentliche Rolle, die zusammen mit den Emittermolekülen die Stabilität und Effizienz der OLEDs maßgeblich bestimmen. Ziel dieser Arbeit ist es, neue Matrixmaterialien für blaue OLEDs zu synthetisieren und zu charakterisieren, eine Strategie für ihr Design zu entwickeln und die thermischen und morphologischen Eigenschaften von Wirten und Emittern zu untersuchen.

In der ersten Arbeit wird eine grundlegende Strategie für die Synthese von Matrixmaterialien mit hoher Triplett-Energie entwickelt. Mit Hilfe eines Tool-Box Prinzips wurden Bausteine (Akzeptor, Donor und Linker) ausgewählt und systematisch kombiniert, um eine Reihe von sechs Donor-Akzeptor-Molekülen zu synthetisieren. Alle Moleküle besitzen einen Triazin-Akzeptor, während Carbazol und Acridin als Donoren verwendet werden. Die Verbindung zwischen Donor und Akzeptor wird systematisch von einem para- zu einem meta-Phenyl-Linker verändert, oder der Linker ganz weggelassen. Der Vergleich der Moleküle zeigt, dass die höchsten Triplett-Energien erzielt werden, wenn kein Linker zwischen Donor und Akzeptor vorhanden ist. Darüber hinaus wird bei Verwendung eines weniger konjugierten Donors (Acridin anstelle von Carbazol) die höchste Triplett-Energie von 3,07 eV für den Wirt ATRZ erreicht. Dieser Wirt weist eine hohe thermische und morphologische Stabilität auf (Glasübergang bei 115°C und thermische Zersetzung bei 341°C). Im Anschluss an die Veröffentlichung wurde der vielversprechende Wirt ATRZ in blauen TADF-OLEDs getestet, wobei eine hohe externe Quanteneffizienz von 10,0 % und ein geringer Effizienz-Roll-Off erzielt wurden. Darüber hinaus hat das Bauelement im Vergleich mit den wenigen in der Literatur für blaue TADF-OLEDs bisher berichteten Werten eine gute Lebensdauer mit LT50 (Abfall bis zur halben Leuchtdichte) von 40 Stunden bei 100 cd/m2 gezeigt.

In der zweiten Arbeit werden die Erkenntnisse aus dem Toolbox-Ansatz erweitert, um neue Matrixmaterialien mit hoher Triplett-Energie zu erhalten und die Designstrategie zu validieren. Donor- und Akzeptoreinheiten wurden ausgewählt und direkt gekoppelt, um die

Konjugation zu begrenzen und eine höhere Triplett-Energie zu erzielen. Die Wahl des Donors fiel wegen des hohen Tripletts und des sterischen Anspruchs auf die Acridin-Einheit. In dieser Serie wird der Donor konstant gehalten, während drei verschiedene Akzeptoren auf Pyrimidinbasis mit unterschiedlichen Konjugationslängen verwendet werden. Das konjugierte System wird von zwei Phenylringen über einen Phenylring bis hin zu einer Methylgruppe verändert. Es zeigt sich, dass das Matrixmaterial 1MPA mit dem am wenigsten konjugierten methylsubstituierten Pyrimidin-Akzeptor die höchste Triplett-Energie von 3,07 eV aufweist. Es zeigt bipolaren Transport und hohe thermische und morphologische Stabilität, d. h. einen Glasübergang bei 138 °C und thermische Zersetzung bei 413 °C. Auch hier wurde die vielversprechendste Matrix in blauen TADF-OLEDs getestet, die eine hohe Effizienz von 13,6 % und einen geringen Effizienzabfall aufweisen.

Der dritte Beitrag befasst sich mit einer Reihe von vier neuen TADF-Emittern auf Pyridylbenzimidazol-Basis. Aufgrund der Bedeutung der thermischen und morphologischen Stabilität werden die thermischen Eigenschaften dieser Emitter eingehend untersucht. Die vier Emitter unterscheiden sich durch die funktionelle Gruppe auf der Akzeptoreinheit, die den sterischen Anspruch innerhalb der Serie erhöht: Wasserstoff (ohne Substitution), Methyl, Phenyl und tert-Butyl. Das Molekül mit der Phenylgruppe ist das stabilste (thermische Zersetzung bei 355 °C), da es die höchste π-Konjugation und starke π-π-Wechselwirkungen aufweist. Überraschenderweise ist die morphologische Stabilität bei dem Molekül ohne Substitution am höchsten (Glasübergang bei 97 °C), was auf die Bildung von Wasserstoffbrückenbindungen im festen Zustand zurückzuführen ist.

In der vierten Arbeit wird ein Modell beschrieben, das die Orientierung der TADF-Emitter mit dem Glasübergang der Matrix korreliert, um die Lichtauskopplung und damit die OLED-Effizienz zu erhöhen. Die Ergebnisse zeigen, dass die Ausrichtung von TADF-Emittern, die in einer Matrix dotiert sind, hauptsächlich von drei Parametern abhängt. i) Wenn das Molekül sehr langgestreckt ist, bestimmt die intrinsische Form des Emitters die Ausrichtung. ii) Wenn die Emitter weniger langgestreckt sind, bestimmt die Matrix ihre Ausrichtung. iii) Innerhalb desselben Glasübergang-Bereichs können sich bestimmte Matrixmaterialien stärker umlagern als andere, wodurch die horizontale Ausrichtung des Emitters verstärkt wird. Daher beeinflusst auch die Ausrichtung der Matrix selbst die Ausrichtung des Emitters.

# Zusammenfassung

Zusammenfassend lässt sich sagen, dass in dieser Arbeit mit dem Tool-Box Prinzip ein allgemein anwendbarer Ansatz für die Entwicklung von Matrixmaterialien mit hoher Triplett-Energie für blaue Emitter vorgestellt wird. Darüber hinaus wurden zwei neue Matrixmaterialien mit einer Triplett-Energie von 3,07 eV entwickelt, die gute thermische und morphologische Eigenschaften und bipolaren Transport zeigen. Die Materialien wurden in OLED-Bauelementen getestet und zeigten eine gute Effizienz und Stabilität. Darüber hinaus wurden die thermischen und morphologischen Eigenschaften neuer TADF-Emitter bestimmt, was Einblicke in die Verarbeitbarkeit und Stabilität dieser Kategorie von Emittern ermöglicht. Schließlich wurden die morphologischen Eigenschaften von Benchmark-Matrixmaterialien ermittelt und mit der Ausrichtung der TADF-Emitter korreliert, um ein Modell zu erstellen, das zur Steigerung der Effizienz von OLEDs beitragen kann.

## 1. Introduction

Organic light-emitting diodes (OLEDs) represent one of the most promising technologies concerning light emission. Since their discovery in 1987 at Eastman Kodak,[1] where Tang et al. reported the first efficient low-voltage OLED, they have been widely subjected to research and development due to their potential in display and lighting technologies. In 2007, Sony released the world's first OLED TV,[2] while Nokia commercialized the first OLED smartphone in 2008.[3] The first commercial OLED panels for lighting applications were instead developed by Lumiotec in 2011.[4]



Figure 1: Applications of OLED technology. (1) Foldable smartphone display, Samsung, reproduced from ref. [5] under the license CC BY-SA. (2) Rollable TV, LG, reproduced from ref. [6] under the license CC BY-NC-ND. (3) OLED rear light, Audi, reproduced from ref. [7] under the license CC BY-NC. (4) Virtual reality mask, reproduced from ref. [8] under the license CC BY. (5) White OLED design, reproduced from ref. [9] under the license CC BY.

OLEDs present several advantages if compared with classic liquid crystal displays (LCDs), such as enhanced image quality, faster refresh rates, wider viewing angles, thinner and lighter.[10] Furthermore, since the materials in OLEDs are primarily organic, slack van der Waals bonds between the molecules endow OLEDs with intrinsic flexibility, making them ideal candidates for flexible displays and transparent panels.[11] Nowadays, this technology can be found in many electronic devices such as smartphones, televisions, head-up displays for cars, and wearable devices. For instance, LG has been developing and commercializing ultra-high

definition (UHD) large panel displays, transparent panels, and the world's first rollable TV based on OLED technology.[12–14] Samsung, instead, commercialized foldable smartphones that could be realized due to OLED technology.[15] If utilized for lighting, OLEDs have several advantages such as high efficiency, design flexibility, and no UV emission, together with potential flexibility and transparency. Planar lighting panels present low thickness, light weight, and keep the surface cool, avoiding heat sink technologies.[16] White OLEDs are also mercury-free illumination light sources and meet the requirements of the EU WEEE & RoHS directives.[17] AUDI AG is adopting OLED lighting technologies for rear lights due to improved safety, communication, and design.[18]

The global OLED Display market is valued at 42 billion US$ in 2020 and is expected to reach 185 billion US$ by 2026, with a compound annual growth rate (CAGR) of 23.2% (Figure 2, left).[19] In the same way, the global OLED Lighting Panels market is valued at 45 million US$ in 2020 and is predicted to reach 65 million US$ by 2026 with a CAGR of 5.5% (Figure 2, center).[20] Nowadays, OLEDs for cellphones dominate the OLED sector, comprising 78% of the OLED market revenue in 2020. The second-largest sector is OLED TVs which are 17% of the total market by revenue in 2020. The third-largest OLED application is wearables, which is 2% (Figure 2, right).
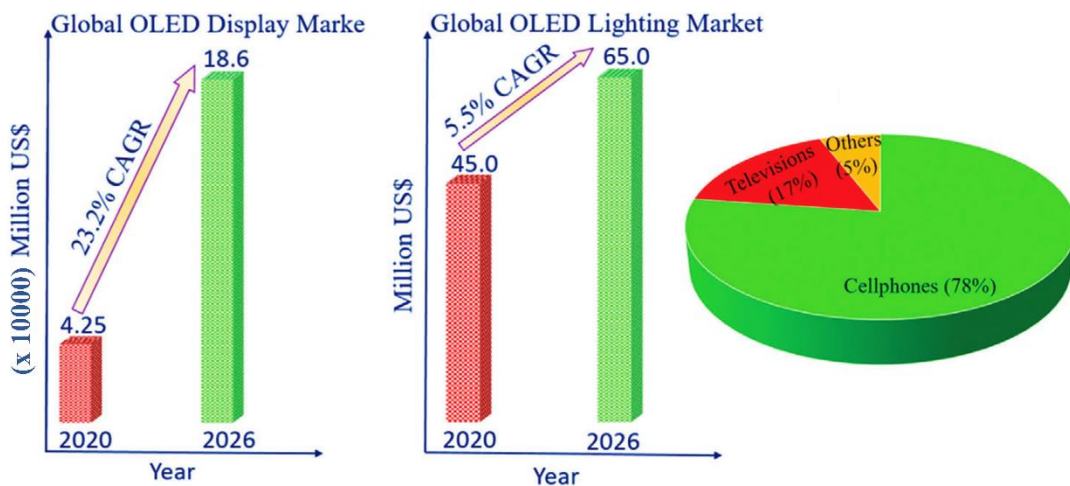


Figure 2: OLED global market revenue overview by the display (left) and lighting application (center). Contribution of OLED technology by application in next-generation electronic devices (right). Adapted from ref.[21]

## 1.1. Luminescence in organic semiconductors

Organic semiconductors are made of unsaturated organic molecules, where $sp^2$-hybridized carbon atoms form a conjugated $\pi$-electron system through their $p_z$-orbitals. As compared to the $\sigma$-bonds, which form the backbone of the molecules, the $\pi$-bonding is significantly weaker. As a result, the lowest energetic electron excitation of conjugated organic molecules occurs through $\pi$-$\pi^*$ type transitions from the HOMO to the LUMO energy levels, which leads to an excited state of the molecule. The energy gap between the LUMO and HOMO is identified as the energy bandgap in organic semiconductors, which is usually between 1.5 and 3 eV, and directly affects optical and charge transport properties.[22] The energy gap may be controlled through molecular design, which unlocks various possibilities for the fine-tuning of optoelectronic properties of organic semiconductors. The excited state of a molecule can have singlet and triplet nature, depending on the relative spin between the electron in the $\pi^*$-orbital and the one left in the $\pi$-orbital. Parallel spin refers to the triplet state, while antiparallel to the singlet state. Coulomb and exchange interactions between the electrons in the molecular orbitals are significant (due to the low dielectric constant of organic semiconductors). The former lowers the energy of singlet and triplet states by the same amount, while the latter increases the singlet state energy and lowers the triplet state energy (see Figure 3).[23]
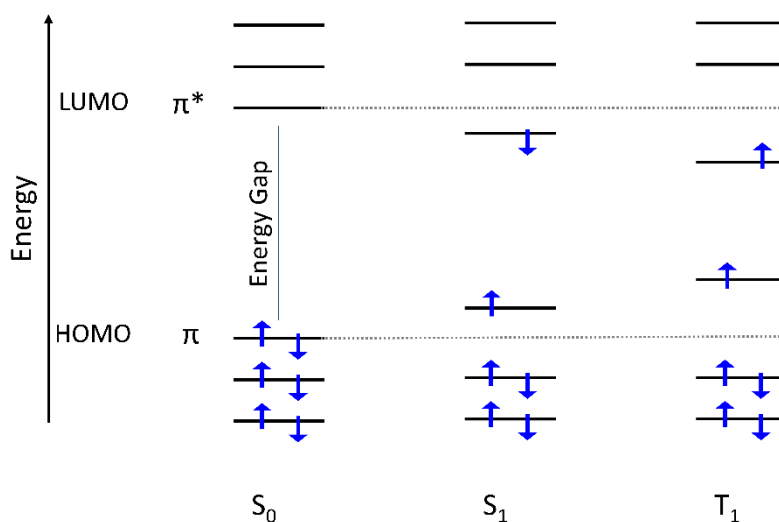


Figure 3: Left: Representation of the ground state ($S_0$), singlet state ($S_1$), and triplet state ($T_1$) of an organic semiconductor. Only one spin configuration is shown for the triplet state. The arrows indicate the electron spin. Coulomb and exchange energies are included in the positions of the frontier orbitals.

This energy difference between singlet and triplet states is twice the value of the exchange integral J, further discussed in section 1.4. Excitation might occur through the absorption of light. However, it can also arise via charge recombination in a molecular film sandwiched between two electrodes, like in OLEDs. In contrast to optical excitation, which preserves spin and thus only creates singlet excitons, electrical excitation leads to the formation of both singlet and triplet states.[24] In particular, the statistical ratio for the triplet and singlet excitons is 3:1.[25] These excited states can undergo radiative decay to the ground state of the molecule, thus emitting light (fluorescence from singlet state and phosphorescence from triplet state). Depending on the kind of excitation, the light emitted will be named photoluminescence or electroluminescence. The latter represents the emission in OLEDs.

## 1.2. Working principles of OLEDs

Due to van der Waals forces, and thus weak electronic coupling between molecules, charge carrier transport in amorphous organic semiconductors is limited by incoherent hopping,[26–28] which leads to low mobility.[29] Therefore, the charge conduction in OLEDs relies on injected charges from the electrodes and the bulk transport characteristics of the organic layers. Figure 4 represents the design and operation principles of a simple monochromic OLED stack for the generation of electroluminescence.
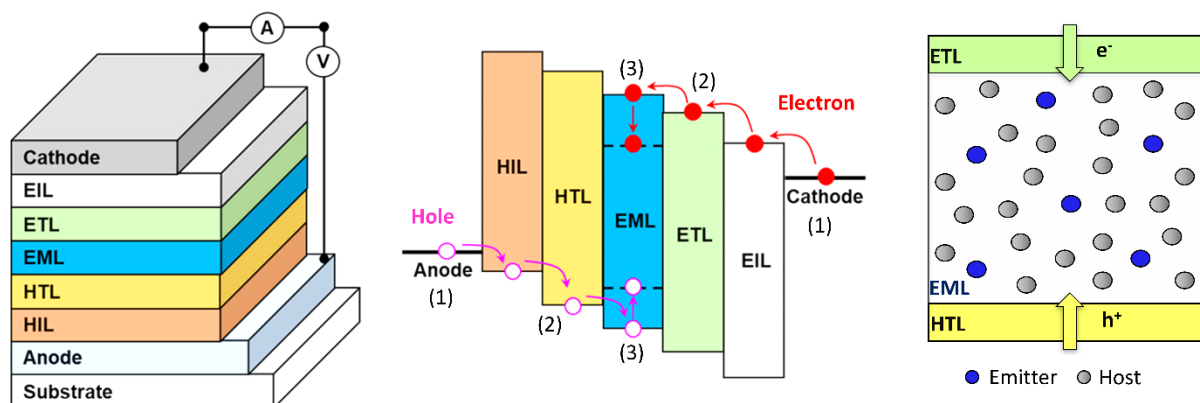


Figure 4: Illustration of OLED stack design (left, reproduced from ref. [30]), operation principle of OLEDs (center, adapted from ref. [30] ), and emitting layer configuration (right). HIL = hole injection layer. EIL = electron injection layer. HTL = hole transporting layer. ETL = electron transporting layer. EML = emitting layer. LUMO and HOMO levels denote the lowest unoccupied molecular orbital and the highest occupied molecular orbital of the organic materials. (1) Charge injection from anode and cathode into the organic layers. (2) Charge transport through HTL and ETL. (3) Charge recombination in the EML.

# 1. Introduction

(1) Under an applied bias voltage between the two electrodes, charge carrier injection into the organic semiconductor occurs. At the anode, electrons are extracted from the HOMO level of the organic material, thus generating holes. On the other side, electrons are injected from the cathode into the LUMO of the organic molecules. This leads to radical cations and radical anions, also called polarons. The anode is generally made of a transparent conducting oxide, such as tin-doped indium oxide (ITO), which allows light extraction. The cathode, instead, is made of reflective metals such as aluminum. The metal/organic semiconductor junction should be ohmic, i.e., with a low injection barrier. This is necessary to facilitate the electron and hole flow so that the current is not limited by the injection. However, the interfacial energy barriers between the electrode materials and common organic semiconductors tend to be large.[31] To mitigate the problems, the electrode surface can be engineered with a buffer layer (HIL and EIL), which is very thin (ca. 1–10 nm) and is used to control the energy level alignment across the electrode-organic interface.[32–34] For the anode can be used a polymer blend such as poly(3,4-ethylene-dioxythiophene):poly(4-styrenesulfonate) (PEDOT:PSS), while for the cathode, an alkali-metal halide like lithium fluoride (LiF).[35,36]

(2) The injected holes and electrons, driven by the applied external electric field, will then migrate through the HTL and the ETL. These transporting materials, which have a thickness of 10-100 nm, must have high thermal stability and high charge mobility. Furthermore, they should possess high triplet energy to isolate the excitons into the EML. They should also block the opposite charge so that recombination is limited to the EML. If these two prerequisites are not satisfied, thin blocking layers of 1-10 nm (HBL and EBL) might be employed between transport layers and EML, which are organic materials with high triplet energy and monopolar properties.[37–39] Generally, aromatic amine-based molecules are used for HTL, as the π-conjugation through the lone-pair electrons on the nitrogen in the HOMO level leads to low ionization potentials and a small energy barrier for hole creation. Furthermore, this is coupled with typically low reorganization energy for the electron transfer between adjacent molecules, reducing the energy barrier for charge hopping.[31] Triarylamine and carbazole building blocks are the most used.[40] On the other side, electron-deficient aromatic molecules such as imidazoles, pyridines, and pyrimidines are used as ETL.[41]

(3) Finally, electrons and holes recombine into the EML due to Coulomb interaction to form tightly bound pairs called excitons. [25] The EML, which is 10-100 nm thick, consists of a host–

dopant combination where the host is combined in higher fractions (typically 80-99 % in weight). The host's role is to dilute the emitter molecules and avoid emitters' concentration quenching. The singlet and triplet energy levels of the host are higher than that of the dopant. Hence, the excitons formed in the hosts will then be transferred to the dopant leading to light emission. The materials and principles of hosts and emitters will be illustrated in detail in sections 1.4 and 1.5.

As mentioned, during OLED operation, electrons and holes are injected from the electrodes and transported through multiple organic layers. Along their path, electrons cross numerous interfaces. At each interface, there is the possibility of an energy barrier that the charges must overcome to enter the following material. Energy barriers increase the driving voltages of OLEDs and, when close to the EML, result in charge-accumulation regions that increase the probability of nonradiative recombination.[32,41,42] Consequently, interfacial energy barriers give rise to high OLED driving voltages and low device efficiencies.

## 1.3. Fabrication and performance of OLEDs

Generally, there are two different fabrication methods for OLED devices, depending on the nature of the organic materials employed. Low molecular weight materials (<1000 g/mol) are usually deposited by vacuum thermal evaporation (VTE). One advantage of VTE is the ability to deposit complex device structures with almost unlimited combinations of different materials**.** It is also one of the cleanest methods and allows to achieve high performance and a long lifetime. On the other hand, only materials with suitable thermal stability must be employed. Furthermore, there is a high waste of material during the deposition process.

Polymeric and high molecular weight materials (>1000 g/mol) are instead processed from solution. A solution-based technique for large panel applications is the printing technique, which promises low production costs. However, the production of multilayer devices with solution-based processes faces the major problem of redissolving previously deposited layers. Therefore, the vapor-deposition technique is the prevailing process for OLED fabrication at the moment.[31]

The most pragmatic approach to construct OLED for display and lighting applications consists of combining monochrome red, green, and blue systems (RGB), allowing the generation of diverse colors. The chromaticity of the light source represents a fundamental feature. It is quantified using the Commission Internationale de l'Eclairage (CIE) 1931 (*x*, *y*) chromaticity diagram (Figure 5), which describes each color with respect to the human's eye perception.
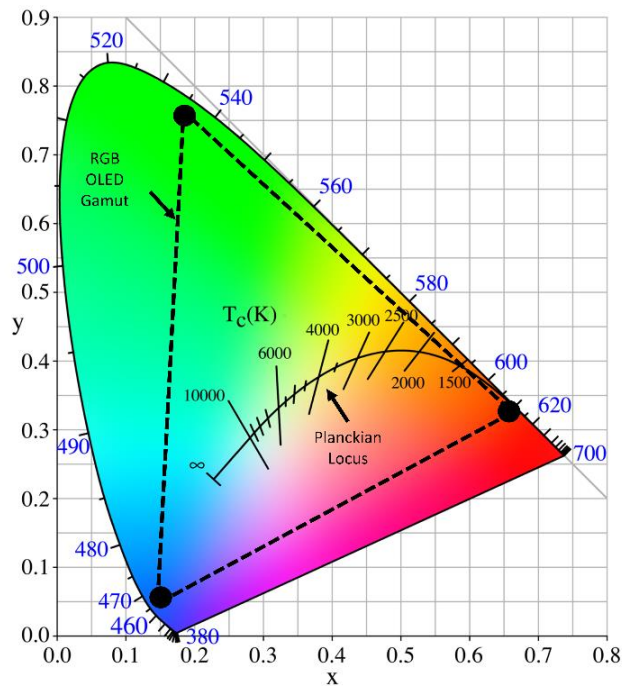


Figure 5: CIE 1931 color space diagram adapted from ref. [43] under the license CC BY-SA.

The curved borderline represents monochromatic light, while the straight boundary is denoted as the line of purples. If three light sources with different chromaticity (represented by the triangle's corners) are mixed at a certain ratio, any chromaticity within the triangular gamut formed by their (*x*, *y*) coordinates can be produced. Therefore, deep RGB emitting materials are necessary to improve the color gamut of a display. For lighting, it is essential the inclusion of the white point (x = 0.33, y = 0.33). The curved line in the middle represents the emission color of the temperature-dependent irradiation of a black body (Planckian Locus), which correlates the color with the temperature and is important for lighting application. Temperatures below 5000 K are regarded as "warm" white, while above 5000 K are denoted as "cold" white.

Another feature for the description of white light is the color rendering index (CRI), which measures (from 0 to 100) the ability of a light source to resemble the color appearance of test objects in comparison to a standard incandescent light bulb.

A crucial metric to evaluate the performance of an OLED is the external quantum efficiency (EQE). The EQE is defined as the ratio of the number of extracted photons out of the device towards the viewer to the total number of injected electrons, and it is defined as follows:[44]

$$\eta_{EQE} = \eta_{OC} * \eta_{IQE} \tag{1}$$

$$= \eta_{OC}(\gamma * \chi * \Phi_{PL}) \tag{2}$$

Here, $\eta_{OC}$ is the outcoupling efficiency, namely the ratio of the extracted vs. generated photons. In general, the majority of generated photons within the EML are lost via optical coupling to the waveguide, substrate, and surface plasmon modes. For this reason, $\eta_{OC}$ is typically limited to 0.2 (or 20%) without any light extraction techniques.[45] The second parameter is $\eta_{IQE}$, which denotes the internal quantum efficiency (IQE), i.e., the ratio between the total number of generated photons into the EML vs. the injected electrons. $\eta_{IQE}$ is determined by the three factors: *the* charge balance factor, $\gamma$, the fraction of the radiative excitons, $\chi$, and the photoluminescence quantum yield, $\Phi_{PL}$. In the modern OLED, $\gamma$ is close to unity because most injected charges are confined within the EML through an optimized device stack (such as using blocking layers). Therefore, almost all the charges participate in the exciton formation. $\Phi_{PL}$ represents the intrinsic quantum yield for the radiative decay of the formed excitons. It depends on the emitter itself and the environment and can also reach unity. $\chi$ is the fraction of excitons resulting in radiative transitions. This is up to 25% for fluorescent emitters and up to 100% for phosphorescent and thermally activated delayed fluorescence (TADF) emitters, as will be discussed in section 1.4. Therefore, considering optimal charge balance and photoluminescence quantum yield ($\gamma = 1$, $\Phi_{PL} = 1$) and a standard outcoupling efficiency ($\eta_{OC} = 0.2$), the maximum EQE of fluorescent-based OLEDs would be only 5%, while for phosphorescence and TADF devices would be 20%.

As mentioned, several interfaces arise from the difference in optical properties between adjacent layers, and these interfaces are responsible for the light trapping. However, several methods to improve efficiency are in progress, also from the molecular point of view.[46] In general, vacuum-deposited organic films are amorphous. However, recent findings indicate

that some organic films do possess a preferred orientation.[47] It is also known that the orientation of the transition dipole moment vectors (TDMVs) of the emitting molecules with respect to the plane of the OLED substrate has a large effect on light extraction.[48,49] In fact,

the light is emitted mainly in the direction normal to the transition dipole moment, which for elongated molecules follows the main axes. Therefore, a possible solution is to design a rod-shaped emitter that would lay flat upon deposition, creating a preferred horizontal orientation due to geometrical constraints of the emitting molecule.[46] In doped films, the emitter orientation is also found to be influenced by the host properties, such as its glass transition ($T_g$). Namely, the molecular surface mobility is reduced on a host with high $T_g$, which suppresses the randomization of the molecular orientation during vacuum thermal evaporation, leading to the more favorable flat orientation.[50] Other important photometric quantities used in displays include luminance (L) and current efficiency ($\eta_C$). The luminance measures the luminous intensity per unit area of multipoint or area light sources with the unit of candela per square meter (cd/m2). The current efficiency is the luminous intensity per injected current to the device with the unit of cd/A. For lighting, the power efficiency, as well as the luminance, are generally used. The power efficiency corresponds to the ratio of the luminous flux to the consumed electrical power with units of lumens per Watt (lm/W). Finally, for commercial applications, it is essential to know the durability of the device. For this reason, another important metric is the lifetime, usually reported as LT. Lifetime is usually measured by applying a constant current to the OLED device and monitoring the decreasing of luminance over time. For instance, LT95 represents when the OLED loses 5% of its luminance under a constant current. LT97 (3% lost in luminance) is typically quoted as the lifetime for display applications.[31]

## 1.4. Emitter generations

The organic emitters should fulfill several parameters to be suitable for OLEDs. Firstly, they must have high photoluminescence quantum yields (PLQYs), which directly impact the device efficiency, as well as they must demonstrate sufficient thermal and morphological stability. Aside from these requirements, a crucial issue to address is the management of hole and electron recombination within the device.[10] In fact, unlike photoexcitation, the formation of excitons through hole and electron recombination results in 25% singlets and 75% triplets,

according to spin statistics.[51] Throughout the development of OLEDs, three main classes of emitters can be distinguished, which lead to three diverse OLED generations (Figure 6).
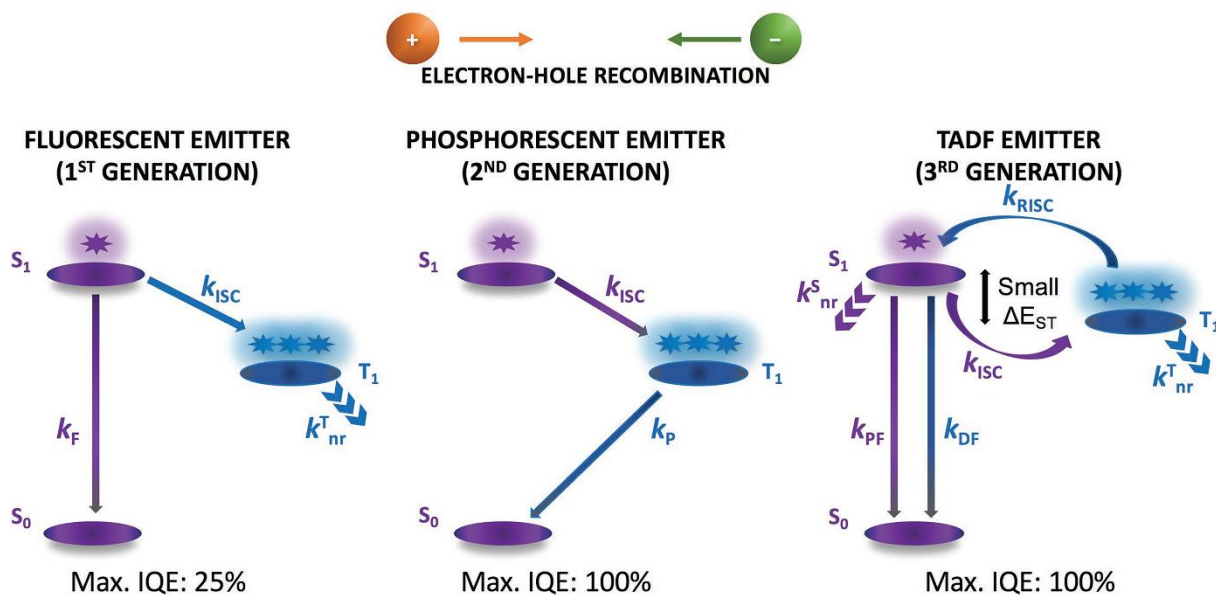


Figure 6: Comparison of emission mechanism in first-generation (fluorescent), second-generation (phosphorescent), and third-generation (thermally activated delayed fluorescent, TADF) emitters. $S_0$ = ground state; $S_1$ = lowest singlet state; $T_1$ = lowest triplet state; $k_F$ = rate constant of fluorescence; $k_P$ = rate constant of phosphorescence; $k_{PF}$ = rate constant of prompt fluorescence; $k_{DF}$ = rate constant of delayed fluorescence; $k_{ISC}$ = rate constant of intersystem crossing; $k_{RISC}$ = rate constant of reverse intersystem crossing; $\Delta E_{ST}$ = the energy difference between the first excited singlet and triplet states; $k^S_{nr}$ = rate constant of nonradiative decay of the $S_1$ state; $k^T_{nr}$ = rate constant of nonradiative decay of the $T_1$ state; IQE = internal quantum efficiency. Reproduced from ref. [10]

The first-generation of OLEDs is known as fluorescent OLEDs and typically employs organic dyes (Figure 7). Its discovery parallelled the first efficient OLED by Tang et al. in 1987. In these kinds of emitters, the singlet state contributes to light emission by fluorescence ($k_F$) with a short emission lifetime (nanosecond regime). On the other side, emission from the triplet state ($T_1$) via phosphorescence does not occur due to the long emission lifetime (millisecond regime), which is given by its spin-forbidden nature (slow spin-flip from singlet to triplet state). In fact, the long emission lifetime makes the triplet excitons vulnerable to nonradiative deactivation as heat loss. Therefore, a maximum of only 25% of the excitons can be harvested for luminescence. However, for blue emission, the advantages of long lifetime and low cost of fluorescent organic materials make them still widely used in OLED products at present.[52]
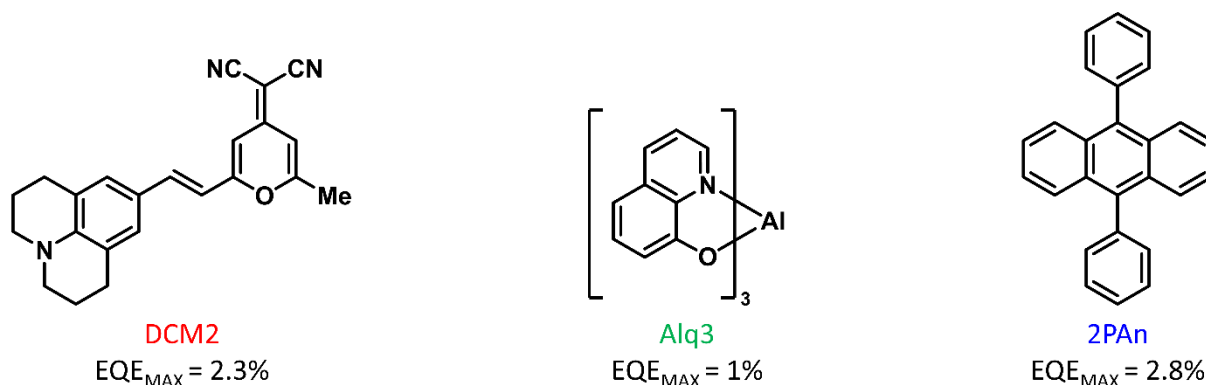
Figure 7: Molecular structures of some classic fluorescent emitters (first generation). The name denotes the RGB (red, green, and blue) color of the emitter. The maximum external quantum efficiency (EQE_MAX, which is the maximum value of EQE) of the OLED device based on the relative emitter is also reported.[1,53,54]

To get access to the remaining 75% of excitons in the triplet state, heavy-metal complexes have been investigated and developed as emitters for the second generation of OLEDs. Baldo et al., in 1998, reported the first example of a platinum complex that delivered an IQE of 23%.[55] Successively, in 2001, the first heavy metal-based emitters (iridium and platinum complexes) with an IQE of nearly 100% were reported by Adachi et al.,[56] which were far above the 25% limit of the first generation. Basically, the enhanced spin-orbit coupling induced by heavy metal atoms (such as iridium or platinum) facilitates the intersystem crossing ($k_{ISC}$) from the $S_1$ state to the $T_1$ state,[25,51,55,57] and the emission of phosphorescence within a useful millisecond regime. Some examples of second-generation emitters are reported in Figure 8.
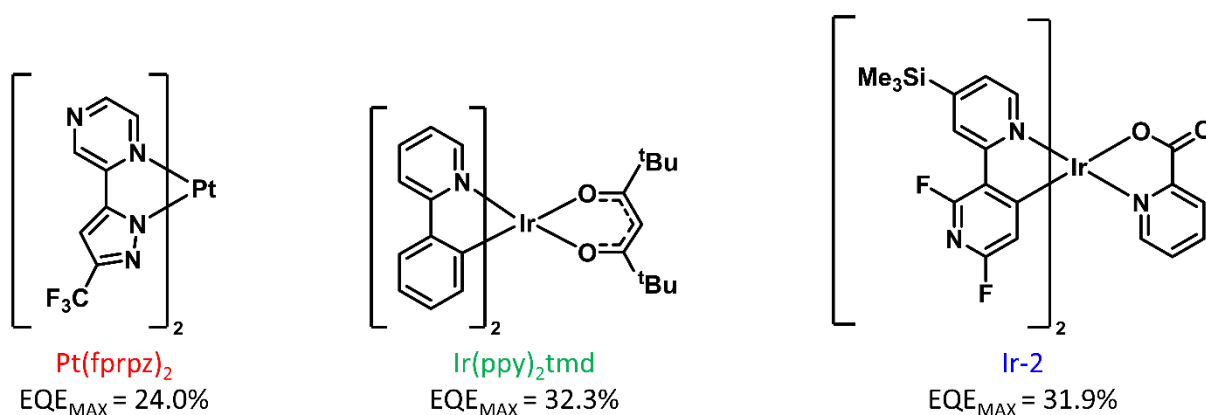


Figure 8: Molecular structures of state-of-the-art phosphorescence emitters (second generation). The name denotes the RGB (red, green, and blue) color of the emitter. The maximum external quantum efficiency (EQE_MAX, which is the maximum value of EQE) of the OLED device based on the relative emitter is also reported.[49,58,59]

The second generation of emitters allows to reach high efficiency and, in some cases, stable devices. In fact, due to the high performance and stability of these molecules, commercial OLED displays currently rely on green- and red-emitting iridium complexes.[60] However, also this technology presents some drawbacks. Generally, rare heavy metals contribute to increasing the device cost and present environmental concerns.[61] Additionally, unlike green and red emitters, the blue metal complexes suffer from poor stability, color purity, and low luminance during device operation. Likely explanations comprise triplet-polaron annihilation (TPA), which results in highly energetic polarons that cause device degradation,[62] and unstable radical cations on the complex, which cause ligand dissociation or complex isomerization.[63,64] Hence, the inefficient first generation of emitters is presently used in commercial blue OLEDs. Table 1 shows the Universal Display Corporation (UDC) OLED material performance compared with classic fluorescent OLEDs, presented by Prof. S. R. Forrest at the American Physical Society (APS) March meeting 2018, illustrating the lifetime issue for blue phosphorescence OLEDs.

| Color | Phosphorescent OLEDs (2$^{nd}$ gen.) | | Fluorescent OLEDs (1$^{st}$ gen) | |
|---|---|---|---|---|
| | 1931 CIE coordinates | LT$_{50}$ (hours) | 1931 CIE coordinates | LT$_{50}$ (hours) |
| Red | (0.64, 0.36) | 900 000 | (0.67, 0.33) | 160 000 |
| Green | (0.31, 0.63) | 400 000 | (0.31, 0.63) | 200 000 |
| Blue | - | <100 | (0.14, 0.12) | 11 000 |

Table 1: Universal Display Corporation (UDC) phosphorescence OLED material performance compared with fluorescent OLEDs as of 2016.[65,66]

Therefore, the development of blue OLEDs that are simultaneously stable and efficient and can avoid the usage of high-cost and environmentally precarious elements is essential. In response to this necessity, thermally activated delayed fluorescence (TADF) is the most promising exciton harvesting mechanism used in OLED devices and represents the third generation of OLEDs. Since the first reported TADF OLED by Endo et al. in 2011,[67] incredible attention in recent years has been dedicated to developing this technology.[68] An important advantage of TADF emitters is that they can be purely organic, thus avoiding the problems associated with the use of heavy-metal-based organometallic complexes.[69] Analogous to the phosphorescence emitters, purely organic TADF emitters can recruit both singlet and triplet excitons for light emission and hence achieve 100% IQE.[70] Figure 9 shows state-of-the-art red,

green and blueTADF emitters, which through molecular engineering and device optimization reached among the best efficiencies so far know in OLEDs.



TPA-PZCN
EQE$_{MAX}$ = 27.4%

CzDBA
EQE$_{MAX}$ = 37.8%
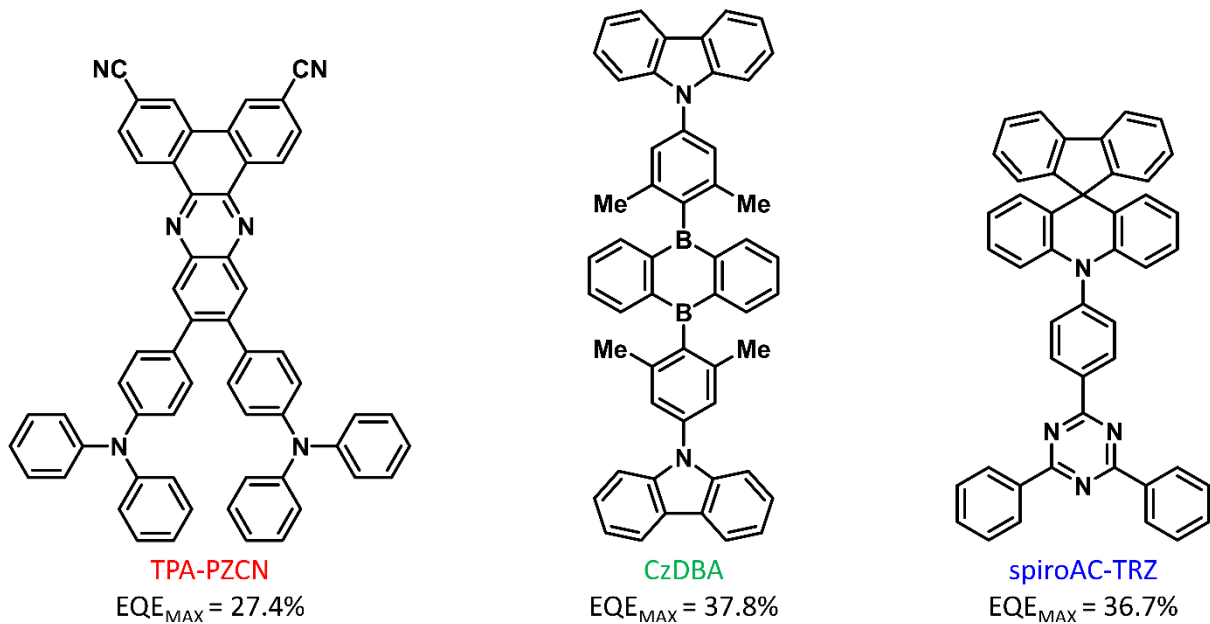
spiroAC-TRZ
EQE$_{MAX}$ = 36.7%

Figure 9: Molecular structures of state-of-the-art thermally activated delayed fluorescence emitters (third generation). The name denotes the RGB (red, green, and blue) color of the emitter. The maximum external quantum efficiency (EQE$_{MAX}$, which is the maximum value of) of the OLED device based on the relative emitter is also reported.[71–73]

The peculiarity of these molecules is that they rely on a small singlet-triplet energy gap ($\Delta E_{ST}$) between S$_1$ and T$_1$ states (usually <0.1 eV). Therefore, thermal upconversion from the triplet state to the singlet state by reverse intersystem-crossing (k$_{RISC}$) becomes possible, allowing the triplet excitons to be harvested. TADF emitters characteristically show two types of photoluminescence: the prompt fluorescence (k$_{PF}$), which comes from excitons that were exclusively singlet states, and delayed fluorescence (k$_{DF}$), which is the result of an initial (k$_{isc}$) to the triplet state followed by repopulation of the singlet state via k$_{RISC}$.[74]

As mentioned, TADF relies on a small $\Delta E_{ST}$, which governs the exciton harvesting via reverse intersystem crossing, according to the following Boltzmann distribution:[75]

$$K_{RISC} \propto \exp\left(-\frac{\Delta E_{ST}}{k_b T}\right) \tag{3}$$

where $k_b$ is Boltzmann's constant and $T$ is the temperature.

Therefore, a small $\Delta E_{ST}$ will provide a greater $k_{RISC}$, namely, more efficient harvesting of excitons from the triplet to the single state. It is important to mention that the $\Delta E_{ST}$ increases exponentially with the HOMO-LUMO overlap,[76] expressed by the integral J:[77]

$$\Delta E_{ST} = 2J \tag{4}$$

Consequently, engineering the molecular structure of a molecule to reduce its HOMO-LUMO overlap plays a fundamental role in obtaining efficient TADF emitters. A common way to achieve this is to use donor and acceptor structure, often linked by a C-N bond. The LUMO will stay mainly on the acceptor, while the HOMO on the donor (Figure 10). The C-N bond usually provides perpendicular steric conformation between donor and acceptor orbitals, thus decreasing their overlap. The normally spin-forbidden ISC and RISC processes in purely organic TADF emitters can become efficient thanks to a small $\Delta E_{ST}$ and can be explained by the following equation:[74]

$$\lambda \propto \frac{H_{SO}}{\Delta E_{ST}} \tag{5}$$

where $\lambda$ and $H_{SO}$ are the first-order mixing coefficient between singlet and triplet states and the spin-orbital interaction, respectively. The mixing of singlet and triplet states is essential to obtain efficient exciton harvesting. $H_{SO}$, which is crucial for the metal complexes (second generation of emitters), is small for purely organic molecules. However, with a sufficiently small $\Delta E_{ST}$, the ISC and RISC processes can occur.
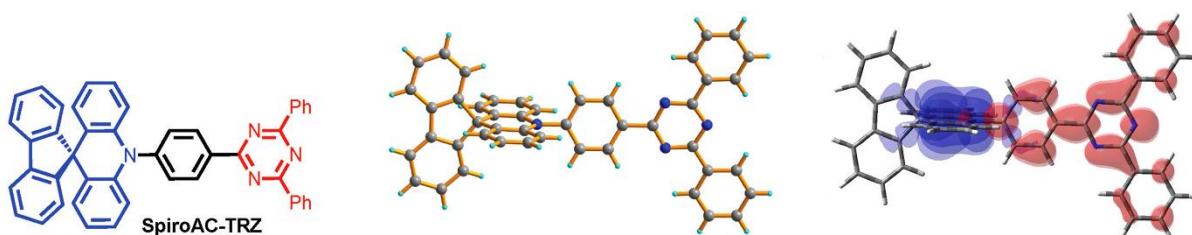


Figure 10: Chemical structure (left). X-ray structure (center) and calculated HOMO (blue)/LUMO (red) (right) for the blue TADF emitter SpiroAC-TRZ. Adapted from ref.[73]

## 1.5. Host materials

Even though TADF emitting materials exhibit good efficiencies, concentration quenching and exciton annihilations represent significant issues, which lead to efficiency roll-off.[51,78] Additionally, in the case of blue TADF emitters, high emission energy (>2.7 eV) and long triplet

exciton lifetime easily create hot excitons or hot polarons (≈6 eV) by exciton annihilation processes, which accelerates the material degradation due to higher energy than bond dissociation energies.[79,80] A general solution to suppress these problems is the dispersion of emitting materials in a high triplet (and singlet) energy host to diminish exciton concentration and annihilation. Generally, the primary roles of the hosts are to transport charges, generate excitons, and transfer the exciton energy to the emitters. Holes and electrons are injected from transport layers and then transported into the emitting layer. Typically, the transport occurs through the hosts, although the dopants can trap some carriers.[81] Therefore, most holes and electrons recombine and form excitons in the host. These excitons are then transferred to the dopants via Förster[82] and Dexter[83] energy transfer mechanisms (Figure 11).
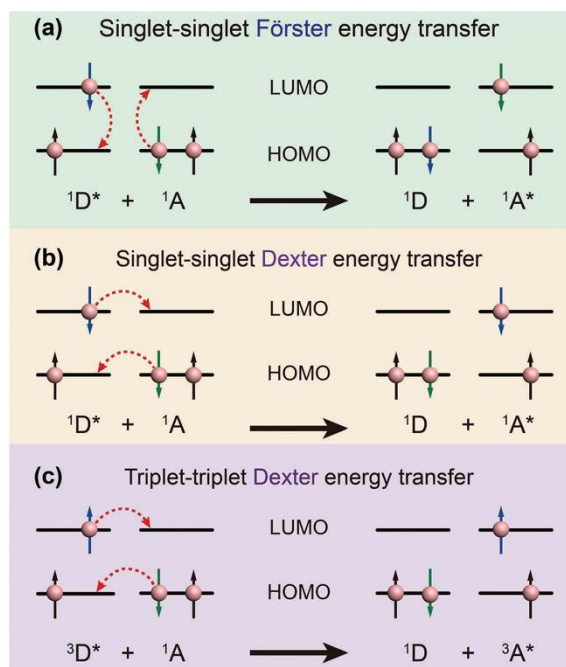


Figure 11: Schematic diagrams of (a) Förster energy transfer and (b, c) Dexter energy transfer. D and A denote donor and acceptor, respectively. Reproduced from ref.[60]

For the Förster energy transfer to occur, three primary conditions need to be met. Firstly, the donor and acceptor molecules must be in close proximity to one another (typically in the range of 1 to 10 nm). Then the absorption spectrum of the acceptor (such as the emitter) must overlap the emission spectrum of the donor (such as the host). Lastly, the orientations of donor and acceptor transition dipoles must be approximately parallel.[84] In contrast, Dexter energy transfer can only take place at short distances (<1 nm) for both singlet and triplet excited states, as there must be wavefunction overlap of electron clouds between donor and

acceptor.[83] Finally, the excited states of the dopant decay radiatively (emitting light) or nonradiatively (through heat dissipation). Host materials need to fulfill several criteria: (i) possess higher triplet energy than dopant emitters (> 3 eV for blue TADF emitters) to limit reverse energy transfer from the dopant to the host and to ensure the confinement of triplet excitons on the dopant (see Figure 12); (ii) exhibit matching of the HOMO and LUMO energy levels with those of adjacent layers to reduce the charge injection barrier, thereby dropping the device operation voltages; (iii) they are expected to have well-balanced charge carrier transport properties for achieving the hole-electron recombination process and display the exciton confinement in the emissive layer; (iv) possess high thermal stability; (v) exhibit high morphological stabilities.[85]
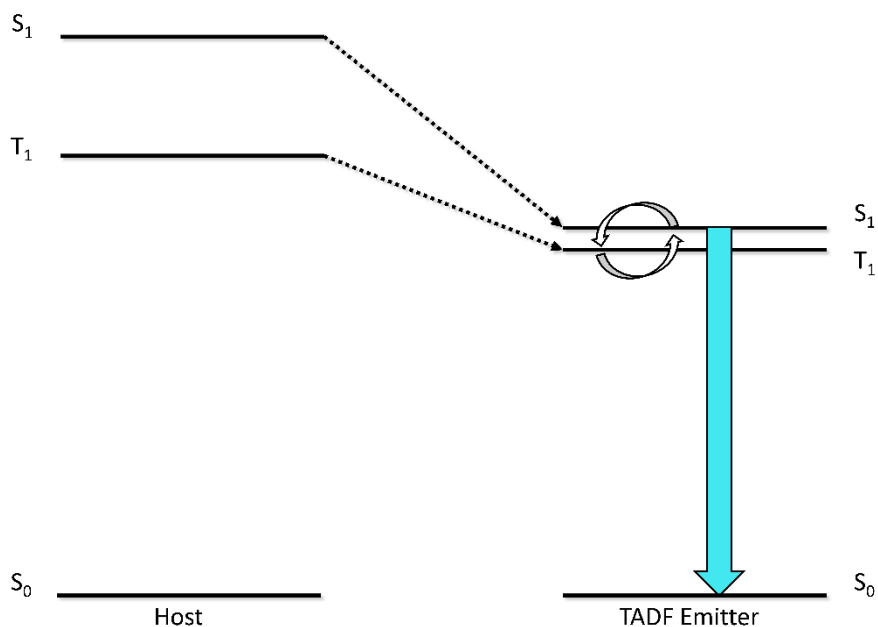


Figure 12: Example of a suitable host for TADF emitters, where the excited states are higher in energy than the emitter. The dotted arrows represent the exciton transfer, the white arrows the intersystem crossing between singlet and triplet states of the emitter, and the light blue arrow shows the emitter's emission.

Despite the developments made for green and red materials, blue materials still face complications that obstruct their practical applications. The host material should possess a higher $T_1$ than its dopant. Therefore, the design of host materials for blue emitters is much more complicated than for green and red ones, making this one of the biggest challenges for OLEDs. Many hosts have been developed to satisfy the required criteria, improving the external quantum efficiency and device lifetime. However, the device lifetime of these high-efficiency blue OLEDs is not long enough, and further exploration of the design strategy and

new chemical structures is strongly needed[79]. The majority of the blue TADF OLEDs are based on conventional host materials, which come from the first and second generations, such as those depicted in Figure 13.



Figure 13: Molecular structures of the most common host materials employed in TADF OLEDs.

Due to the high triplet energy required, the choice of functional groups is restricted, and the majority of host materials are based either on phosphine oxide or carbazole groups. These materials can be produced in bulk quantities at a relatively low cost. Moreover, their physical and chemical properties have been well documented.[86] One of the most commonly used ho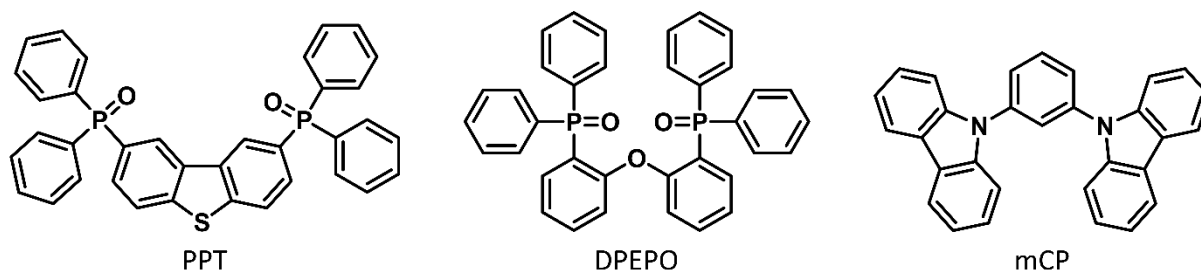st materials is DPEPO,[87–89] which benefits from a high triplet level of 3.0 eV[90] and prevents undesirable energy transfer from the dopant to the host. However, due to its phosphine oxide nature, it suffers from limited stability,[86,91,92] which limits its use to research purposes. Furthermore, the strong electron-withdrawing oxide groups confer DPEPO a monopolar nature, which leads to unbalanced carrier transport. Another widely employed phosphine oxide-based host is PPT, with a triplet of 3.0 eV.[85,93–95] Aside from this category, the majority of the hosts are based on carbazole moiety. Carbazole is the most widely used electron-donating building block in OLED materials, owing to its high triplet energy (3.02 eV), excellent hole-transporting ability, and good thermal stability. It features an sp3-hybridized nitrogen atom at the 9-position, and hence, its derivatives exhibit more rigid structures, resulting in thermally stable molecules that provide a better film morphology.[96] Among these, mCP has been widely employed for blue TADF OLEDs due to its high triplet energy of 2.9 eV.[97] However, it presents monopolar properties (hole conducting material) and low morphological stability ($T_g$ = 65°C).[98] Another approach is to use two monopolar hosts to provide charge balance.[99] Several molecular strategies have been adopted in recent years to cope with the scarce availability of host materials for blue TADF emitters. The most successful strategy is to combine donor and acceptor groups with high triplet energy to provide bipolar properties (see Figure 14). In this way, hosts can transport holes and electrons evenly. Therefore, the device

performances of the bipolar transport hosts are often better than those of the p-type and n-type hosts due to balanced charge density and broad recombination zone in the emitting layer.[79]
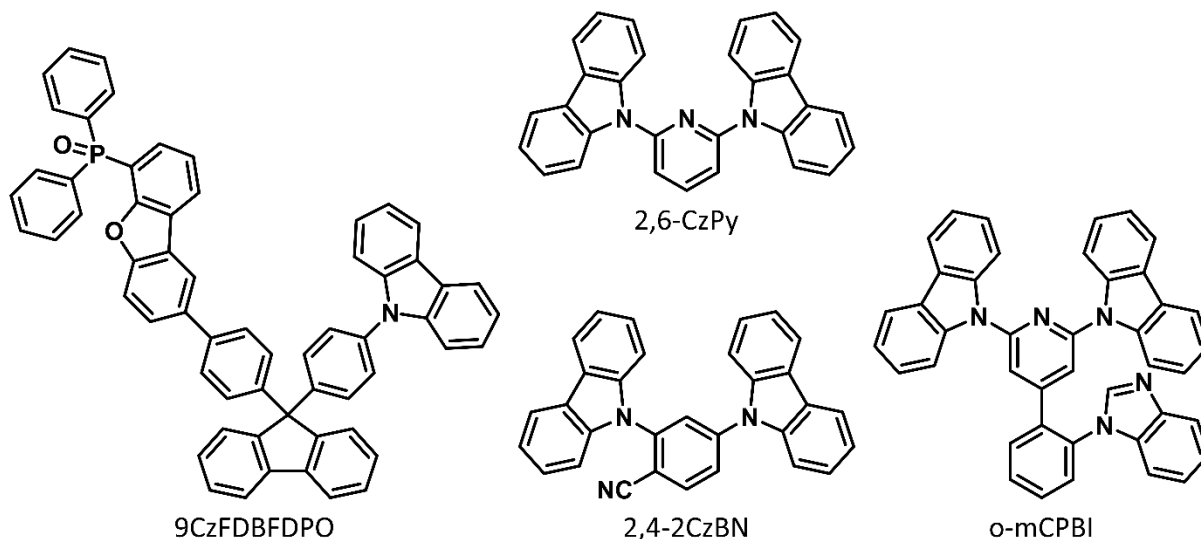


Figure 14: Molecular structures of bipolar host materials employed in TADF OLEDs.

Zhang et al. produced bipolar hosts based on carbazole and phosphine oxide groups. Blue TADF OLEDs were produced, and the host 9CzFDBFDPO, having a triplet energy of 3.01 eV, gave the best results with an EQE of 20.2 %.[100] However, while carbazole remains the most frequent choice as the donor, the phosphine oxide groups are usually replaced with more stable groups because of the aforementioned problems. The cyano group is an alternative electron-accepting unit that can be used to induce electron deficiency in organic molecules, thus enhancing electron transport character. Moreover, it has large bond dissociation energy values (due to the sp-hybridized carbon), which is beneficial to improve the stability of host materials with a little decrease of the triplet energy by extended conjugation. Duan and co-workers[101] designed a series of hosts where they substituted the central phenyl ring of the classic host mCP with cyano groups. Blue TADF OLEDs were fabricated, and the device based on the host 2,4-2CzBN realized EQE of 21.5% and ultralow onset voltage of 2.8 V. The introduction of a small-sized CN unit has no negative impact on the triplet energy (2.95 eV), which is even slightly higher than mCP. Higher electron mobilities are also achieved. Moreover, the twisted structures between the carbazole unit and the benzene ring induced the spatially separated frontier orbital distributions, resulting in relatively low $\Delta E_{ST}$, which is the cause of the low voltage turn-on.

Pyridine is also a common electron-transporting moiety with good electron affinity and is used in electron-transporting materials. Consequently, the pyridine unit was incorporated with donor moieties to provide bipolar hosts. The pair carbazole-pyridine has often been used since it can readily balance carriers for high efficiency.[79] Huang and co-workers synthesized a series of pyridine-carbazole hybrid hosts based on a one-step simple aromatic nucleophilic substitution reaction.[102] The host 2,6-CzPy ($T_1$ = 3.0 eV), which is essentially similar to mCP except for the central pyridine ring, was then utilized in a blue TADF OLED which delivered an EQE of 10.4%.[103]

Imidazole is an aromatic unit possessing two distinct nitrogen atoms (one electron-rich and one electron-poor), which endows bipolar electronic characters (although the acceptor strength prevails). Thus, this unique electronic structure pushed imidazole derivatives to be widely applied in OLEDs as emitters, hosts, and electron transporting layers. Due to the higher triplet energy, benzimidazole has been employed in blue TADF hosts. Zhao et al. integrated a benzimidazole moiety on mCP (o-mCPBI, $T_1$ = 3.0 eV), which was used in a blue TADF OLED delivering and $EQE_{MAX}$ of 10.2%.[104] Aside from these acceptors, also carboline, triazine, boron, and sulfone-based units have been utilized.[81]

## 1.6. Thermal and morphological properties

Significant attention is paid to the stability of organic semiconducting materials, as their stability governs the overall durability of OLED displays.[105–107] Through evaporation and solution processing, the materials are deposited as amorphous films. A crucial factor for the durability of an OLED is the morphological stability of its organic materials. Precisely, the glass transition temperature ($T_g$) of these materials plays a central role as the current flows through the organic layers and leads to Joule heating.[108,109] This phenomenon causes local temperature increases inside OLEDs, and organic materials with a low $T_g$ inevitably experience molecular vibrations and may move from their initial positions within the device layers. This might cause thermal expansion and recrystallization. The vicinal layers (see section 1.2 for multilayer structure) are also directly affected, eventually destroying the display.[110] Typically, each layer should be thermally stable to improve the overall lifetime of the OLED. However, exceptionally high $T_g$ is necessary for the organic layers in contact with the electrodes and for the materials within the emitting layer. The organic-inorganic interface is particularly

vulnerable to the destruction caused by the difference in thermal expansion, which occurs via Joule heating generated by high energy barriers (Figure 15). At the same time, the emitting layer is exposed to heat generated as a byproduct of nonradiative exciton decay (see Figure 6).[30]
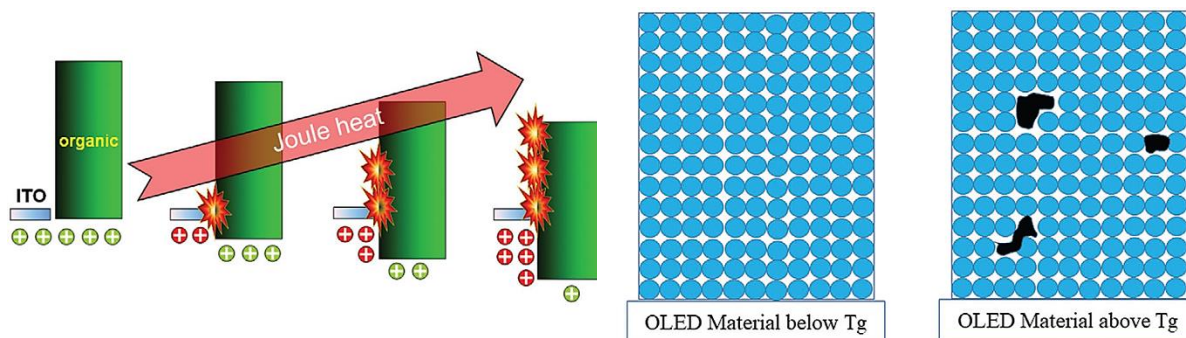


Figure 15: High injection barrier generating high joule heat (left). General schematic illustration of the influence of glass transition temperature ($T_g$) in the thermal degradation of OLED materials (right). Adapted from ref.[21]

Aside from the operational stability of OLEDs, another important thermal feature of semiconducting materials is the thermal decomposition ($T_d$), which represents the maximum temperature at which the compound does not degrade. This is relevant for practical applications while fabricating an OLED through the vacuum thermal evaporation process, as it determines the process temperature range. This is not generally an issue in low deposition rate research systems where the substrates are small and the rates are low, but for production systems, thermal degradation is usually the limiting factor in scaling both size and throughput.[31]

Differential scanning calorimetry (DSC) and thermogravimetric analysis (TGA) are two of the most widely used thermal analysis techniques in the characterization of OLED materials. DSC measures various thermal transitions associated with a material when it is heated or cooled in a controlled manner. The thermal transition could be due to a physical transformation or a chemical reaction. Physical transformations, such as melting, crystallization, and glassy state, are always associated with a change in enthalpy. This enthalpy change is detected over a particular temperature range using a predetermined heating rate under a controlled atmosphere. TGA is used to measure changes in the mass of a material as a function of temperature using a predetermined heating rate under a controlled atmosphere.[111] Usually,

favorable thermal and morphological properties are obtained through nonplanar molecular spatial configuration, bulky and rigid substituents, and large molecular size.[112]

In this chapter, the basics of OLEDs relevant to the thesis are introduced. The device principles and properties are illustrated together with the generations of emitters. Particular emphasis is given to host materials for blue OLEDs, which are at the center of this work. Furthermore, the importance of thermal properties is mentioned. The following chapter focuses on the objective and overview of the thesis.

(1) Tang, C. W.; VanSlyke, S. A. Organic electroluminescent diodes. *Appl. Phys. Lett.* **1987**, *51* (12), 913–915. DOI: 10.1063/1.98799.

(2) *Sony Launches World's First *1 OLED TV*. https://www.sony.com/en/SonyInfo/News/Press/200710/07-1001E/ (accessed September 2021).

(3) Florin T. *Did you know? Nokia made smartphones with AMOLED screens before Samsung*. https://www.phonearena.com/news/Did-you-know-Nokia-made-smartphones-with-AMOLED-screens-before-Samsung_id72704 #:~:text=Announced%20in%20August%202008%2C%20and%20released%20in%20early,camera%20with%20auto%20focus%20and%20Carl%20Zeiss%20lens. (accessed October 2021).

(4) *Lumiotec to Market Two OLED Luminaires -- World First in Mass-produced Models --*. http://www.lumiotec.com/en/news/pdf/20110727_lumiotecnewsrelease_eng.pdf (accessed September 2021).

(5) *Samsung cancella il Galaxy Fold*. https://www.htnovo.net/2019/05/samsung-cancella-il-galaxy-fold.html (accessed September 2021).

(6) *Lg presenterà la tv oled arrotolabile che scende dal soffitto*. https://www.wired.it/gadget/audio-e-tv/2020/01/02/tv-oled-arrotolabile-lg-soffitto/ (accessed September 2021).

(7) *AUDI y lo último en tecnología de iluminación*. https://www.racing5.cl/audi-y-lo-ultimo-en-tecnologia-de-iluminacion/ (accessed September 2021).

(8) Ingrid Fadelli. *How Virtual and Augmented Reality Could Aid Science Communication*. https://www.scientia.global/scicomm-corner-how-virtual-and-augmented-reality-could-aid-science-communication/ (accessed September 2021).

(9) *LG Display exhibits new OLED products*. https://grendz.com/pin/1276/ (accessed September 2021).

(10) Wong, M. Y.; Zysman-Colman, E. Purely Organic Thermally Activated Delayed Fluorescence Materials for Organic Light-Emitting Diodes. *Advanced materials (Deerfield Beach, Fla.)* **2017**, *29* (22). DOI: 10.1002/adma.201605444. Published Online: Mar. 3, 2017.

(11) Zhang, D.; Huang, T.; Duan, L. Emerging Self-Emissive Technologies for Flexible Displays. *Advanced materials (Deerfield Beach, Fla.)* **2020**, *32* (15), e1902391. DOI: 10.1002/adma.201902391. Published Online: Oct. 9, 2019.

(12) Young Kwan Jung, Hong Seok Choi, So Yeon Ahn, Seunghyun Kim, Heedong Choi, Chang Wook Han, Binn Kim, Se June Kim, Jongmoo Kim, Jeong Hyeon Choi, SooYoung Yoon, Yoon Heung Tak, Hyun Chul Choi, Byung Chul Ahn, In Byeong Kang. 52-3: Distinguished Paper: 3 Stacked Top Emitting White OLED for High Resolution OLED TV.

(13) LG Electronics. *OLED R*. https://www.lg.com/global/lg-signature/rollable-oled-tv-r (accessed September 2021).

(14) Hong-Jae Shin, Shinji Takasugi, Kwang-Mo Park, Soo-Hong Choi, Yun-Sik Jeong, Byung-Chan Song, Han-Seop Kim, Chang-Ho Oh, Byung-Chul Ahn. 7.1: Invited Paper: Novel OLED Display Technologies for Large-Size UHD OLED TVs.

(15) Samsung. *Galaxy Z Fold3 5G*. https://www.samsung.com/de/smartphones/galaxy-z-fold3-5g/buy/ (accessed September 2021).

(16) Koden, M. *OLED displays and lighting*; Wiley series in display technology; Wiley/IEEE Press, 2017.

(17) Sasabe, H.; Kido, J. Development of high performance OLEDs for general lighting. *J. Mater. Chem. C* **2013**, *1* (9), 1699. DOI: 10.1039/c2tc00584k.

(18) AUDI AG. *OLED Lighting technology*. www.audi-technology-portal.com.

(19) The Market Publicist. *New Report 2026: OLED Display Market will grow at CAGR of 23.2 % to cross revenue of 185830 million USD*. https://themarketpublicist.com/2020/08/14/new-report-2026-oled-display-market-will-grow-at-cagr-of-23-2-to-cross-revenue-of-185830-million-usd/ (accessed September 2021).

(20) The Express Wire. *OLED Lighting Panels Market : Rising Trends with Top Countries Data, Technology and Business Outlook 2020 to 2026*. https://www.theexpresswire.com/pressrelease/OLED-Lighting-Panels-Market-Rising-Trends-with-Top-Countries-Data-Technology-and-Business-Outlook-2020-to-2026_11639725 (accessed Seprember 2021).

(21) Sudheendran Swayamprabha, S.; Dubey, D. K.; Shahnawaz; Yadav, R. A. K.; Nagar, M. R.; Sharma, A.; Tung, F.-C.; Jou, J.-H. Approaches for Long Lifetime Organic Light Emitting Diodes. *Advanced science (Weinheim, Baden-Wurttemberg, Germany)* **2020**, *8* (1), 2002254. DOI: 10.1002/advs.202002254. Published Online: Nov. 12, 2020.

(22) Brütting, W., Ed. *Physics of organic semiconductors*; Wiley-VCH, 2005.

(23) Turro, N. J. *Modern Molecular Photochemistry*, 1991.

(24) Köhler, A.; Bässler, H. Triplet states in organic semiconductors. *Materials Science and Engineering: R: Reports* **2009**, *66* (4-6), 71–109. DOI: 10.1016/j.mser.2009.09.001.

(25) Minaev, B.; Baryshnikov, G.; Agren, H. Principles of phosphorescent organic light emitting devices. *Physical chemistry chemical physics : PCCP* **2014**, *16* (5), 1719–1758. DOI: 10.1039/c3cp53806k.

(26) Bässler, H. Localized States and Electronic Transport in Single Component Organic Solids with Diagonal Disorder. *Phys. Stat. Sol. (B)* **1981**, *107*, 9. DOI: 10.1046/j.0013-0427.2003.00027.x.

(27) Bässler, H. Charge Transport in Disordered Organic Photoconductors:A Monte Carlo Simulation Study. *Phys. Stat. Sol. (B)* **1993**, *175*, 15. DOI: 10.1046/j.0013-0427.2003.00027.x.

(28) Chang, Y.-L. *Efficient Organic Light Emitting-Diodes (OLEDs)*; Pan Stanford, 2015.

(29) Coropceanu, V.; Cornil, J.; Da Silva Filho, D. A.; Olivier, Y.; Silbey, R.; Brédas, J.-L. Charge transport in organic semiconductors. *Chemical reviews* **2007**, *107* (4), 926–952. DOI: 10.1021/cr050140x. Published Online: Mar. 23, 2007.

(30) Lee, S.; Kim, H.; Kim, Y. Progress in organic semiconducting materials with high thermal stability for organic light-emitting devices. *InfoMat* **2021**, *3* (1), 61–81. DOI: 10.1002/inf2.12123.

(31) Gaspar, D. J.; Polikarpov, E. *OLED fundamentals:Materials, devices, and processing of organic light-emitting diodes*; CRC Press, 2015.

(32) Kampen, T. U. Electronic structure of organic interfaces – a case study on perylene derivatives. *Appl. Phys. A* **2006**, *82* (3), 457–470. DOI: 10.1007/s00339-005-3368-0.

(33) Koch, N. Organic electronic devices and their functional interfaces. *Chemphyschem : a European journal of chemical physics and physical chemistry* **2007**, *8* (10), 1438–1455. DOI: 10.1002/cphc.200700177.

(34) Koch, N. Energy levels at interfaces between metals and conjugated organic molecules. *J. Phys.: Condens. Matter* **2008**, *20* (18), 184008. DOI: 10.1088/0953-8984/20/18/184008.

(35) Brown, T. M.; Kim, J. S.; Friend, R. H.; Cacialli, F.; Daik, R.; Feast, W. J. Built-in field electroabsorption spectroscopy of polymer light-emitting diodes incorporating a doped poly(3,4-ethylene dioxythiophene) hole injection layer. *Appl. Phys. Lett.* **1999**, *75* (12), 1679–1681. DOI: 10.1063/1.124789.

(36) Hung, L. S.; Tang, C. W.; Mason, M. G. Enhanced electron injection in organic electroluminescence devices using an Al/LiF electrode. *Appl. Phys. Lett.* **1997**, *70* (2), 152–154. DOI: 10.1063/1.118344.

(37) Zamani Siboni, H.; Aziz, H. The influence of the hole blocking layers on the electroluminescence stability of phosphorescent organic light emitting devices. *Organic Electronics* **2011**, *12* (12), 2056–2060. DOI: 10.1016/j.orgel.2011.08.023.

(38) Weichsel, C.; Reineke, S.; Lüssem, B.; Leo, K. Influence of the Electron Blocking Layer on the Performance of Multilayer White Organic Light-Emitting Diodes. *MRS Proc.* **2012**, *1402.* DOI: 10.1557/opl.2012.452.

(39) Jeon, S. K.; Lee, J. Y. Four times lifetime improvement of blue phosphorescent organic light-emitting diodes by managing recombination zone. *Organic Electronics* **2015**, *27*, 202–206. DOI: 10.1016/j.orgel.2015.09.016.

(40) Shahnawaz, S.; Sudheendran Swayamprabha, S.; Nagar, M. R.; Yadav, R. A. K.; Gull, S.; Dubey, D. K.; Jou, J.-H. Hole-transporting materials for organic light-emitting diodes: an overview. *J. Mater. Chem. C* **2019**, *7* (24), 7144–7158. DOI: 10.1039/C9TC01712G.

(41) Hughes, G.; Bryce, M. R. Electron-transporting materials for organic electroluminescent and electrophosphorescent devices. *J. Mater. Chem.* **2005**, *15* (1), 94. DOI: 10.1039/b413249c.

(42) Scott, J. C. Metal–organic interface and charge injection in organic electronic devices. *Journal of Vacuum Science & Technology A: Vacuum, Surfaces, and Films* **2003**, *21* (3), 521–531. DOI: 10.1116/1.1559919.

(43) en:User:PAR. *PlanckianLocus*. https://commons.wikimedia.org/wiki/File: PlanckianLocus.png (accessed September 2021).

(44) Chang, Y.-L.; Lu, Z.-H. White Organic Light-Emitting Diodes for Solid-State Lighting. *J. Display Technol.* **2013**, *9* (6), 459–468. DOI: 10.1109/JDT.2013.2248698.

(45) Brütting, W.; Frischeisen, J.; Schmidt, T. D.; Scholz, B. J.; Mayr, C. Device efficiency of organic light-emitting diodes: Progress by improved light outcoupling. *Phys. Status Solidi A* **2013**, *210* (1), 44–65. DOI: 10.1002/pssa.201228320.

(46) Salehi, A.; Fu, X.; Shin, D.-H.; So, F. Recent Advances in OLED Optical Design. *Adv. Funct. Mater.* **2019**, *29* (15), 1808803. DOI: 10.1002/adfm.201808803.

(47) Osada, K.; Goushi, K.; Kaji, H.; Adachi, C.; Ishii, H.; Noguchi, Y. Observation of spontaneous orientation polarization in evaporated films of organic light-emitting diode materials. *Organic Electronics* **2018**, *58*, 313–317. DOI: 10.1016/j.orgel.2018.04.026.

(48) Frischeisen, J.; Yokoyama, D.; Endo, A.; Adachi, C.; Brütting, W. Increased light outcoupling efficiency in dye-doped small molecule organic light-emitting diodes with horizontally oriented emitters. *Organic Electronics* **2011**, *12* (5), 809–817. DOI: 10.1016/j.orgel.2011.02.005.

(49) Kim, K.-H.; Moon, C.-K.; Lee, J.-H.; Kim, S.-Y.; Kim, J.-J. Highly efficient organic light-emitting diodes with phosphorescent emitters having high quantum yield and horizontal orientation of transition dipole moments. *Advanced materials (Deerfield Beach, Fla.)* **2014**, *26* (23), 3844–3847. DOI: 10.1002/adma.201305733. Published Online: Apr. 8, 2014.

(50) Kim, K.-H.; Kim, J.-J. Origin and Control of Orientation of Phosphorescent and TADF Dyes for High-Efficiency OLEDs. *Advanced materials (Deerfield Beach, Fla.)* **2018**, *30* (42), e1705600. DOI: 10.1002/adma.201705600. Published Online: Apr. 30, 2018.

(51) Baldo, M. A.; Adachi, C.; Forrest, S. R. Transient analysis of organic electrophosphorescence. II. Transient analysis of triplet-triplet annihilation. *Phys. Rev. B* **2000**, *62* (16), 10967–10977. DOI: 10.1103/PhysRevB.62.10967.

(52) Xu, Z.; Tang, B. Z.; Wang, Y.; Ma, D. Recent advances in high performance blue organic light-emitting diodes based on fluorescence emitters. *J. Mater. Chem. C* **2020**, *8* (8), 2614–2642. DOI: 10.1039/C9TC06441A.

(53) Tang, C. W.; VanSlyke, S. A.; Chen, C. H. Electroluminescence of doped organic thin films. *Journal of Applied Physics* **1989**, *65* (9), 3610–3616. DOI: 10.1063/1.343409.

(54) Adachi, C.; Tsutsui, T.; Saito, S. Blue light-emitting organic electroluminescent devices. *Appl. Phys. Lett.* **1990**, *56* (9), 799–801. DOI: 10.1063/1.103177.

(55) Baldo, M. A.; O'Brien, D. F.; You, Y.; Shoustikov, A.; Sibley, S.; Thompson, M. E.; Forrest, S. R. Highly efficient phosphorescent emission from organic electroluminescent devices. *Nature* **1998**, *395* (6698), 151–154. DOI: 10.1038/25954.

(56) Adachi, C.; Baldo, M. A.; Forrest, S. R.; Lamansky, S.; Thompson, M. E.; Kwong, R. C. High-efficiency red electrophosphorescence devices. *Appl. Phys. Lett.* **2001**, *78* (11), 1622–1624. DOI: 10.1063/1.1355007.

(57) Sasabe, H.; Kido, J. Recent Progress in Phosphorescent Organic Light-Emitting Devices. *Eur. J. Org. Chem.* **2013**, *2013* (34), 7653–7663. DOI: 10.1002/ejoc.201300544.

(58) Tuong Ly, K.; Chen-Cheng, R.-W.; Lin, H.-W.; Shiau, Y.-J.; Liu, S.-H.; Chou, P.-T.; Tsao, C.-S.; Huang, Y.-C.; Chi, Y. Near-infrared organic light-emitting diodes with very high external quantum efficiency and radiance. *Nature Photon* **2017**, *11* (1), 63–68. DOI: 10.1038/nphoton.2016.230.

(59) Shin, H.; Ha, Y. H.; Kim, H.-G.; Kim, R.; Kwon, S.-K.; Kim, Y.-H.; Kim, J.-J. Controlling Horizontal Dipole Orientation and Emission Spectrum of Ir Complexes by Chemical Design of Ancillary Ligands for Efficient Deep-Blue Organic Light-Emitting Diodes. *Advanced materials (Deerfield Beach, Fla.)* **2019**, *31* (21), e1808102. DOI: 10.1002/adma.201808102. Published Online: Apr. 10, 2019.

(60) Xu, H.; Chen, R.; Sun, Q.; Lai, W.; Su, Q.; Huang, W.; Liu, X. Recent progress in metal-organic complexes for optoelectronic applications. *Chemical Society reviews* **2014**, *43* (10), 3259–3302. DOI: 10.1039/c3cs60449g. Published Online: Feb. 17, 2014.

(61) Volz, D.; Wallesch, M.; Fléchon, C.; Danz, M.; Verma, A.; Navarro, J. M.; Zink, D. M.; Bräse, S.; Baumann, T. From iridium and platinum to copper and carbon: new avenues for more sustainability in organic light-emitting diodes. *Green Chem.* **2015**, *17* (4), 1988–2011. DOI: 10.1039/C4GC02195A.

(62) Zhang, Y.; Lee, J.; Forrest, S. R. Tenfold increase in the lifetime of blue phosphorescent organic light-emitting diodes. *Nature communications* **2014**, *5*, 5008. DOI: 10.1038/ncomms6008. Published Online: Sep. 25, 2014.

(63) Moraes, I. R. de; Scholz, S.; Lüssem, B.; Leo, K. Analysis of chemical degradation mechanism within sky blue phosphorescent organic light emitting diodes by laser-desorption/ionization time-of-flight mass spectrometry. *Organic Electronics* **2011**, *12* (2), 341–347. DOI: 10.1016/j.orgel.2010.11.004.

(64) Klubek, K. P.; Dong, S.-C.; Liao, L.-S.; Tang, C. W.; Rothberg, L. J. Investigating blue phosphorescent iridium cyclometalated dopant with phenyl-imidazole ligands. *Organic Electronics* **2014**, *15* (11), 3127–3136. DOI: 10.1016/j.orgel.2014.08.038.

(65) Forrest, S. How Organic Light Emitting Diodes Revolutionized Displays (and maybe lighting). *Bulletin of the American Physical Society*. http://meetings.aps.org/link/BAPS.2018.MAR.L32.3.

(66) APS Physics. *How Organic Light Emitting Diodes Revolutionized Displays: Stephen Forrest*. https://www.youtube.com/watch?v=PeEwueVaHVY.

(67) Endo, A.; Sato, K.; Yoshimura, K.; Kai, T.; Kawada, A.; Miyazaki, H.; Adachi, C. Efficient up-conversion of triplet excitons into a singlet state and its application for organic light emitting diodes. *Appl. Phys. Lett.* **2011**, *98* (8), 83302. DOI: 10.1063/1.3558906.

(68) Tao, Y.; Yuan, K.; Chen, T.; Xu, P.; Li, H.; Chen, R.; Zheng, C.; Zhang, L.; Huang, W. Thermally activated delayed fluorescence materials towards the breakthrough of organoelectronics. *Advanced materials (Deerfield Beach, Fla.)* **2014**, *26* (47), 7931–7958. DOI: 10.1002/adma.201402532. Published Online: Sep. 17, 2014.

(69) Zhang, Q.; Li, B.; Huang, S.; Nomura, H.; Tanaka, H.; Adachi, C. Efficient blue organic light-emitting diodes employing thermally activated delayed fluorescence. *Nature Photon* **2014**, *8* (4), 326–332. DOI: 10.1038/nphoton.2014.12.

(70) Adachi, C. Third-generation organic electroluminescence materials. *Jpn. J. Appl. Phys.* **2014**, *53* (6), 60101. DOI: 10.7567/JJAP.53.060101.

(71) Zhang, Y.-L.; Ran, Q.; Wang, Q.; Liu, Y.; Hänisch, C.; Reineke, S.; Fan, J.; Liao, L.-S. High-Efficiency Red Organic Light-Emitting Diodes with External Quantum Efficiency Close to 30%

Based on a Novel Thermally Activated Delayed Fluorescence Emitter. *Advanced materials (Deerfield Beach, Fla.)* **2019**, *31* (42), e1902368. DOI: 10.1002/adma.201902368. Published Online: Sep. 6, 2019.

(72) Wu, T.-L.; Huang, M.-J.; Lin, C.-C.; Huang, P.-Y.; Chou, T.-Y.; Chen-Cheng, R.-W.; Lin, H.-W.; Liu, R.-S.; Cheng, C.-H. Diboron compound-based organic light-emitting diodes with high efficiency and reduced efficiency roll-off. *Nature Photon* **2018**, *12* (4), 235–240. DOI: 10.1038/s41566-018-0112-9.

(73) Lin, T.-A.; Chatterjee, T.; Tsai, W.-L.; Lee, W.-K.; Wu, M.-J.; Jiao, M.; Pan, K.-C.; Yi, C.-L.; Chung, C.-L.; Wong, K.-T.; Wu, C.-C. Sky-Blue Organic Light Emitting Diode with 37% External Quantum Efficiency Using Thermally Activated Delayed Fluorescence from Spiroacridine-Triazine Hybrid. *Advanced materials (Deerfield Beach, Fla.)* **2016**, *28* (32), 6976–6983. DOI: 10.1002/adma.201601675. Published Online: Jun. 6, 2016.

(74) Uoyama, H.; Goushi, K.; Shizu, K.; Nomura, H.; Adachi, C. Highly efficient organic light-emitting diodes from delayed fluorescence. *Nature* **2012**, *492* (7428), 234–238. DOI: 10.1038/nature11687.

(75) Palmeira, T.; Berberan-Santos, M. N. Kinetic Criteria for Optimal Thermally Activated Delayed Fluorescence in Photoluminescence and in Electroluminescence. *J. Phys. Chem. C* **2017**, *121* (1), 701–708. DOI: 10.1021/acs.jpcc.6b10554.

(76) Yersin, H. *Highly efficient OLEDs with phosphorescent materials*; Wiley-VCH, 2007. DOI: 10.1002/9783527621309.

(77) Shizu, K.; Sakai, Y.; Tanaka, H.; Hirata, S.; Adachi, C.; Kaji, H. [Paper] Meta-linking Strategy for Thermally Activated Delayed Fluorescence Emitters with a Small Singlet-Triplet Energy Gap. *MTA* **2015**, *3* (2), 108–113. DOI: 10.3169/mta.3.108.

(78) Reineke, S.; Walzer, K.; Leo, K. Triplet-exciton quenching in organic phosphorescent light-emitting diodes with Ir-based emitters. *Phys. Rev. B* **2007**, *75* (12). DOI: 10.1103/PhysRevB.75.125328.

(79) Wang, Y.; Yun, J. H.; Wang, L.; Lee, J. Y. High Triplet Energy Hosts for Blue Organic Light-Emitting Diodes. *Adv. Funct. Mater.* **2021**, *31* (12), 2008332. DOI: 10.1002/adfm.202008332.

(80) Chen, H.-W.; Lee, J.-H.; Lin, B.-Y.; Chen, S.; Wu, S.-T. Liquid crystal display and organic light-emitting diode display: present status and future perspectives. *Light, science & applications* **2018**, *7*, 17168. DOI: 10.1038/lsa.2017.168. Published Online: Mar. 23, 2018.

(81) Wang, Y.; Yun, J. H.; Wang, L.; Lee, J. Y. High Triplet Energy Hosts for Blue Organic Light-Emitting Diodes. *Adv. Funct. Mater.* **2021**, *31* (12), 2008332. DOI: 10.1002/adfm.202008332.

(82) Scholes, G. D. Long-range resonance energy transfer in molecular systems. *Annual review of physical chemistry* **2003**, *54*, 57–87. DOI: 10.1146/annurev.physchem.54.011002.103746. Published Online: Mar. 21, 2002.

(83) Dexter, D. L. A Theory of Sensitized Luminescence in Solids. *The Journal of Chemical Physics* **1953**, *21* (5), 836–850. DOI: 10.1063/1.1699044.

(84) Förster, T. Intermolecular Energy Migration and Fluorescence. *Ann. Phys.* **1948** (437), 55–75.

(85) Nishimoto, T.; Yasuda, T.; Lee, S. Y.; Kondo, R.; Adachi, C. A six-carbazole-decorated cyclophosphazene as a host with high triplet energy to realize efficient delayed-fluorescence OLEDs. *Mater. Horiz.* **2014**, *1* (2), 264–269. DOI: 10.1039/C3MH00079F.

(86) Chatterjee, T.; Wong, K.-T. Perspective on Host Materials for Thermally Activated Delayed Fluorescence Organic Light Emitting Diodes. *Advanced Optical Materials* **2019**, *7* (1), 1800565. DOI: 10.1002/adom.201800565.

(87) Zhang, Q.; Li, J.; Shizu, K.; Huang, S.; Hirata, S.; Miyazaki, H.; Adachi, C. Design of efficient thermally activated delayed fluorescence materials for pure blue organic light emitting diodes. *Journal of the American Chemical Society* **2012**, *134* (36), 14706–14709. DOI: 10.1021/ja306538w. Published Online: Aug. 29, 2012.

(88) Liu, M.; Seino, Y.; Chen, D.; Inomata, S.; Su, S.-J.; Sasabe, H.; Kido, J. Blue thermally activated delayed fluorescence materials based on bis(phenylsulfonyl)benzene derivatives. *Chemical communications (Cambridge, England)* **2015**, *51* (91), 16353–16356. DOI: 10.1039/c5cc05435d.

(89) Lee, S. Y.; Yasuda, T.; Yang, Y. S.; Zhang, Q.; Adachi, C. Luminous butterflies: efficient exciton harvesting by benzophenone derivatives for full-color delayed fluorescence OLEDs.

*Angewandte Chemie (International ed. in English)* **2014**, *53* (25), 6402–6406. DOI: 10.1002/anie.201402992. Published Online: May. 18, 2014.

(90) Han, C.; Zhao, Y.; Xu, H.; Chen, J.; Deng, Z.; Ma, D.; Li, Q.; Yan, P. A simple phosphine-oxide host with a multi-insulating structure: high triplet energy level for efficient blue electrophosphorescence. *Chemistry (Weinheim an der Bergstrasse, Germany)* **2011**, *17* (21), 5800–5803. DOI: 10.1002/chem.201100254. Published Online: Apr. 18, 2011.

(91) Hirata, S.; Sakai, Y.; Masui, K.; Tanaka, H.; Lee, S. Y.; Nomura, H.; Nakamura, N.; Yasumatsu, M.; Nakanotani, H.; Zhang, Q.; Shizu, K.; Miyazaki, H.; Adachi, C. Highly efficient blue electroluminescence based on thermally activated delayed fluorescence. *Nature materials* **2015**, *14* (3), 330–336. DOI: 10.1038/nmat4154. Published Online: Dec. 8, 2014.

(92) Kim, M.; Jeon, S. K.; Hwang, S.-H.; Lee, J. Y. Stable blue thermally activated delayed fluorescent organic light-emitting diodes with three times longer lifetime than phosphorescent organic light-emitting diodes. *Advanced materials (Deerfield Beach, Fla.)* **2015**, *27* (15), 2515–2520. DOI: 10.1002/adma.201500267. Published Online: Mar. 10, 2015.

(93) Tsai, Y.-S.; Hong, L.-A.; Juang, F.-S.; Chen, C.-Y. Blue and white phosphorescent organic light emitting diode performance improvement by confining electrons and holes inside double emitting layers. *Journal of Luminescence* **2014**, *153*, 312–316. DOI: 10.1016/j.jlumin.2014.03.040.

(94) Cai, X.; Padmaperuma, A. B.; Sapochak, L. S.; Vecchi, P. A.; Burrows, P. E. Electron and hole transport in a wide bandgap organic phosphine oxide for blue electrophosphorescence. *Appl. Phys. Lett.* **2008**, *92* (8), 83308. DOI: 10.1063/1.2885117.

(95) Park, W. J.; Lee, Y.; Kim, J. Y.; Yoon, D. W.; Kim, J.; Chae, S. H.; Kim, H.; Lee, G.; Shim, S.; Yang, J. H.; Lee, S. J. Effective thermally activated delayed fluorescence emitter and its performance in OLED device. *Synthetic Metals* **2015**, *209*, 99–104. DOI: 10.1016/j.synthmet.2015.07.008.

(96) Godumala, M.; Choi, S.; Cho, M. J.; Choi, D. H. Thermally activated delayed fluorescence blue dopants and hosts: from the design strategy to organic light-emitting diode applications. *J. Mater. Chem. C* **2016**, *4* (48), 11355–11381. DOI: 10.1039/C6TC04377A.

(97) Dong, S.-C.; Zhang, L.; Liang, J.; Cui, L.-S.; Li, Q.; Jiang, Z.-Q.; Liao, L.-S. Rational Design of Dibenzothiophene-Based Host Materials for PHOLEDs. *J. Phys. Chem. C* **2014**, *118* (5), 2375–2384. DOI: 10.1021/jp412107g.

(98) Naqvi, B. A.; Schmid, M.; Crovini, E.; Sahay, P.; Naujoks, T.; Rodella, F.; Zhang, Z.; Strohriegl, P.; Bräse, S.; Zysman-Colman, E.; Brütting, W. What Controls the Orientation of TADF Emitters? *Frontiers in chemistry* **2020**, *8*, 750. DOI: 10.3389/fchem.2020.00750. Published Online: Sep. 4, 2020.

(99) Wang, Q.; Tian, Q.-S.; Zhang, Y.-L.; Tang, X.; Liao, L.-S. High-efficiency organic light-emitting diodes with exciplex hosts. *J. Mater. Chem. C* **2019**, *7* (37), 11329–11360. DOI: 10.1039/C9TC03092A.

(100) Zhang, Z.; Ding, D.; Wei, Y.; Zhang, J.; Han, C.; Xu, H. Excited-state engineering of universal ambipolar hosts for highly efficient blue phosphorescence and thermally activated delayed fluorescence organic light-emitting diodes. *Chemical Engineering Journal* **2020**, *382*, 122485. DOI: 10.1016/j.cej.2019.122485.

(101) Zhang, D.; Cai, M.; Bin, Z.; Zhang, Y.; Zhang, D.; Duan, L. Highly efficient blue thermally activated delayed fluorescent OLEDs with record-low driving voltages utilizing high triplet energy hosts with small singlet-triplet splittings. *Chemical science* **2016**, *7* (5), 3355–3363. DOI: 10.1039/c5sc04755b. Published Online: Feb. 12, 2016.

(102) Tang, C.; Bi, R.; Tao, Y.; Wang, F.; Cao, X.; Wang, S.; Jiang, T.; Zhong, C.; Zhang, H.; Huang, W. A versatile efficient one-step approach for carbazole-pyridine hybrid molecules: highly efficient host materials for blue phosphorescent OLEDs. *Chemical communications (Cambridge, England)* **2015**, *51* (9), 1650–1653. DOI: 10.1039/c4cc08335k.

(103) Zhao, X.-H.; Han, C.-M.; Li, Y.; Bai, M.-G.; Yang, J.-C.; Xu, H.; Yuan, S.-D.; Xie, L.-H.; Xu, Z.-J. Bulky 9-phenylfluorene fuctionalized 2,6-bis(N-carbazolyl)- pyridine with high triplet energy level as host for blue thermally activated delayed fluorescence devices. *Dyes and Pigments* **2020**, *175*, 108127. DOI: 10.1016/j.dyepig.2019.108127.

(104) Zhao, Y.; Wu, C.; Qiu, P.; Li, X.; Wang, Q.; Chen, J.; Ma, D. New Benzimidazole-Based Bipolar Hosts: Highly Efficient Phosphorescent and Thermally Activated Delayed Fluorescent Organic Light-Emitting Diodes Employing the Same Device Structure. *ACS applied materials &*

*interfaces* **2016**, *8* (4), 2635–2643. DOI: 10.1021/acsami.5b10464. Published Online: Jan. 21, 2016.

(105) Lee, J.-H.; Chen, C.-H.; Lee, P.-H.; Lin, H.-Y.; Leung, M.; Chiu, T.-L.; Lin, C.-F. Blue organic light-emitting diodes: current status, challenges, and future outlook. *J. Mater. Chem. C* **2019**, *7* (20), 5874–5888. DOI: 10.1039/C9TC00204A.

(106) Kotadiya, N. B.; Blom, P. W. M.; Wetzelaer, G.-J. A. H. Efficient and stable single-layer organic light-emitting diodes based on thermally activated delayed fluorescence. *Nat. Photonics* **2019**, *13* (11), 765–769. DOI: 10.1038/s41566-019-0488-1.

(107) Liu, C.-F.; Liu, X.; Lai, W.-Y.; Huang, W. Design and Synthesis of Conjugated Starburst Molecules for Optoelectronic Applications. *Chemical record (New York, N.Y.)* **2019**, *19* (8), 1571–1595. DOI: 10.1002/tcr.201800146. Published Online: Dec. 4, 2018.

(108) Thaengthong, A.-M.; Saengsuwan, S.; Jungsuttiwong, S.; Keawin, T.; Sudyoadsuk, T.; Promarak, V. Synthesis and characterization of high Tg carbazole-based amorphous hole-transporting materials for organic light-emitting devices. *Tetrahedron Letters* **2011**, *52* (37), 4749–4752. DOI: 10.1016/j.tetlet.2011.07.002.

(109) Loy, D. E.; Koene, B. E.; Thompson, M. E. Thermally Stable Hole-Transporting Materials Based upon a Fluorene Core. *Adv. Funct. Mater.* **2002**, *12* (4), 245. DOI: 10.1002/1616-3028(20020418)12:4<245:AID-ADFM245>3.0.CO;2-5.

(110) Zhou, X.; He, J.; Liao, L. S.; Lu, M.; Ding, X. M.; Hou, X. Y.; Zhang, X. M.; He, X. Q.; Lee, S. T. Real-Time Observation of Temperature Rise and Thermal Breakdown Processes in Organic LEDs Using an IR Imaging and Analysis System. *Adv. Mater.* **2000**, *12* (4), 265–269. DOI: 10.1002/(SICI)1521-4095(200002)12:4<265:AID-ADMA265>3.0.CO;2-L.

(111) STEPHEN R. BYRN, GEORGE ZOGRAFI and XIAOMING (SEAN) CHEN. Differential Scanning Calorimetry and Thermogravimetric Analysis.

(112) Dechun, Z. Chemical and photophysical properties of materials for OLEDs. In *Organic Light-Emitting Diodes (OLEDs)*; Elsevier, 2013; pp 114–142. DOI: 10.1533/9780857098948.1.114.

## 2. Objective of the thesis

At present, organic light-emitting diodes represent cutting-edge technology for light emission, especially for display applications. Both industry and academia are continuously developing new materials and technologies for the further improvement of this field. However, the blue light embodies the bottleneck of this technology. Materials exhibiting both high efficiency and stability for blue OLEDs still need to be achieved. This would lead to a decreased power consumption compared to the fluorescent emitters currently used. Material chemistry plays a fundamental role in the development of new solutions to this problem. Several classes of materials have been studied in the last years. The latest and most promising technology, called the 3$^{rd}$ generation, is based on TADF emitters allowing high efficiency and promising higher stability due to their pure organic structure. All the materials involved in the device need to be advanced and optimized to keep up with the new technology. A fundamental role is played by the host matrix, which dilutes the emitter molecules, and is essential to improve the stability and efficiency of the device. Host molecules require the simultaneous presence of several properties, making their design challenging. Firstly, they must possess high triplet energy to ensure efficient energy transfer and localization of the excited states on the emitter molecule. This is particularly problematic for blue TADF OLEDs, where high energies are involved. Secondly, they must own high thermal stability to be optimally vacuum-processed and be morphologically stable under device operation to retain their amorphous state and avoid recrystallization. Thermal properties are critical not just for the proper working of the device but also for the enhancement of the OLED's efficiency. This extends to emitters and all the materials used for OLEDs. Thirdly, the hosts should also have good charge carrier mobility (for both electrons and holes).

The simultaneous presence of requirements and the lack of systematic strategies make the design of new host molecules for blue TADF OLEDs an arduous task. Furthermore, particular attention should be brought to the thermal properties of materials due to their vital importance. The aim of the thesis is to synthesize and characterize new host materials for blue OLEDs and establish a solid strategy for their design, as well as study the thermal and morphological properties of hosts and emitters. Here, the objectives of the thesis are summarized and briefly presented:

The first part of the thesis aims to establish a fundamental approach for synthesizing high triplet energy host materials. Their design is of prime importance for the development of blue OLEDs. The task of simultaneously fulfilling different requirements combined with high triplet energies makes their realization an arduous task. So far, the majority of hosts come from previous generations of OLED emitters and are often monopolar and with unstable groups. Well-defined strategies for the design of hosts are also rare. A series of triazine-based materials with similar structures and systematic variation in functional groups was selected for the study. The structure-property relationship of these molecules will be analyzed and compared throughout the series. This approach, called "Tool box", will allow us to build new high triplet energy hosts and a widely applicable strategy for their design. Triplet energy is of prime importance to address this scope and will be the leading parameter for the creation of new hosts. Bulky and stable groups will be used to improve thermal properties, while donor and acceptor groups will provide both electron and hole transport. Thermal analysis of the most promising hosts will be performed to determine their suitability for device application, together with the determination of molecular orbital values. Finally, the materials will be tested in blue OLEDs.

The second part follows the fundamental "toolbox" approach, aiming to further develop the concept and expand its application. Here, we will apply the information learned in the first part and some new insights to design a series of new pyrimidine-based molecules. The new molecules will be fully characterized, and the structure-property relationship will be determined, like in the first case. The thermal analysis will be performed, and the molecules compared. The values of the molecular orbitals will be determined to build up a tailored device stack around the emitting layer. Finally, the most promising candidate in terms of triplet energy and thermal analysis will be employed in blue OLEDs.

The third part deals with the thermal analysis of a series of new TADF emitters. The emitters usually are doped 1-20 % w/w in the host material to avoid self-quenching. Though the more significant percentage of the host, the emitter is not negligible to the overall morphology of the emitting layer, and it must be considered. For new molecules, it is also essential to make complete thermal analyses to understand their morphology in the solid-state and their thermal behavior during the evaporation process for OLEDs fabrication. The thermal properties of the new TADF emitters will be evaluated and compared.

The fourth part relates to the glass transition of host materials as a critical parameter for TADF emitters' orientation. One of the most effective approaches to increase the light outcoupling and the efficiency of devices is to induce the emitter to be horizontally oriented with respect to the substrate. This can be achieved via the horizontal orientation of the host matrix, which is correlated to its glass transition. In fact, the higher the glass transition, the less the host rearranges on the substrate's surface during the deposition. This leads to a more flat orientation of the host and, as a consequence, of the emitter. For this, the glass transition of benchmark host materials will be evaluated under the same conditions, which will help to establish a model that describes the orientation of TADF emitters into doped films.

## 3. Synopsis

The thesis focuses on the design and characterization of new host materials for blue TADF OLEDs and their application, as well as characterizing the essential thermal properties of hosts and emitters. A graphical overview of the topics is given in Figure 1.
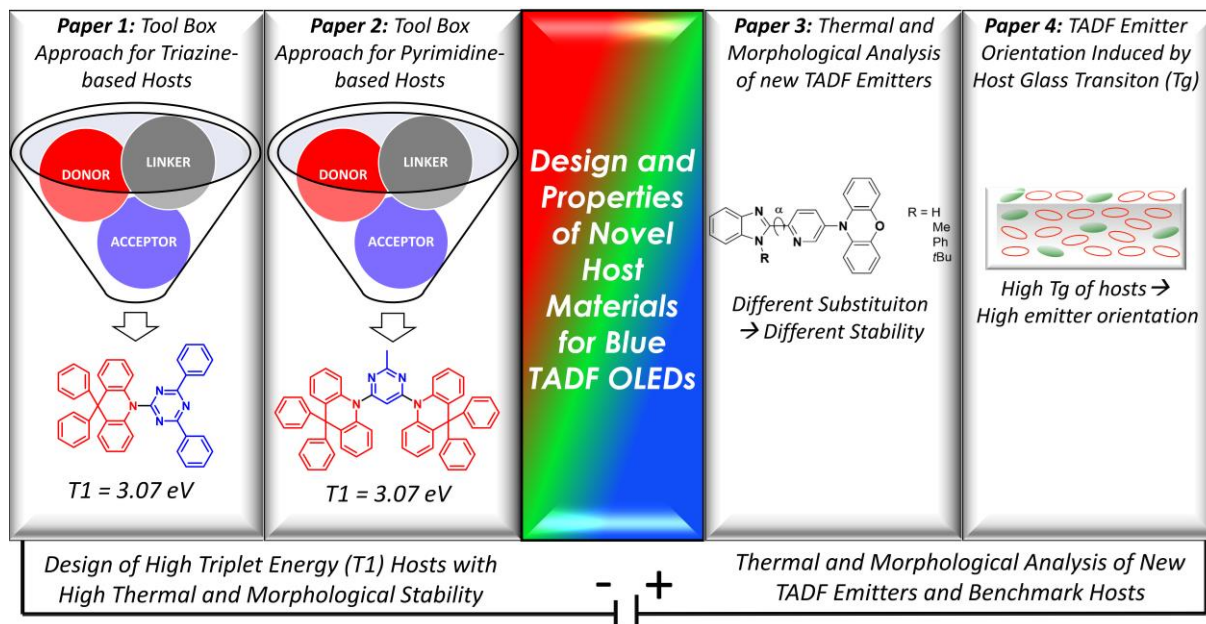


Figure 1: Overview of the four papers of this cumulative thesis. Paper 1: High Triplet Energy Host Materials for Blue TADF OLEDs-A Tool Box Approach. Paper 2: Low efficiency roll-off blue TADF OLEDs employing a novel acridine-pyrimidine-based high triplet energy host. Paper 3: Substitution Effects on a New Pyridylbenzimidazole Acceptor for Thermally Activated Delayed Fluorescence and Their Use in Organic Light-Emitting Diodes. Paper 4: What Controls the Orientation of TADF Emitters?

As mentioned in the objective, the development of blue TADF OLEDs requires an advance in host materials that can provide high triplet energy and, at the same time, good thermal and morphological stability and charge transport. To tackle this problem, we decided to make a systematic study for understanding critical insights into molecular design, with the purpose of generating a fundamental and widely applicable strategy for the creation of host materials. For this, we present six bipolar host materials based on triazine as an acceptor and two types of donors, i.e., carbazole and acridine. Using a toolbox approach, the chemical structure of the materials is systematically changed. Both donors are connected to the triazine acceptor via a para- or a meta-phenyl ring or are linked directly to each other. In this way, we can methodically compare the properties using spectroscopic analysis supported by DFT calculations and get valuable conclusions. From the study, we conclude that the highest triplet

energy is obtained when donor and acceptor are directly connected. Furthermore, via utilizing a less conjugated donor (acridine instead of carbazole), the triplet energy is further improved up to 3.07 eV. The most promising host ATRZ was found to have high thermal and morphological stability (due to the bulky acridine group), and the HOMO and LUMO values were estimated. Finally, a blue TADF OLED was fabricated to prove its potential (Paper 1). Subsequently, we apply this strategy with a different acceptor, pyrimidine, to create new high triplet energy host materials and to develop the approach. Learning from the first work, we opted for the same high triplet energy acridine-based donor, and we connect it directly to three different pyrimidine units, avoiding linkers. Three new host materials were synthesized. Through the series, the acceptor pyrimidine is decreased in size and thus conjugation, and the properties are studied. Spectroscopic and DFT studies are performed to characterize the molecules and asses the excited states. We find that the highest triplet energy host is the one with the least conjugated acceptor (1MPA). The thermal and morphological properties of the newly synthesized hosts are determined, along with the HOMO and LUMO values. Finally, the most promising host, 1MPA, was used to fabricate blue OLEDs (Paper 2). The thermal and morphological properties of materials are essential not just for hosts but also for emitter molecules. These materials must be thermally stable during the evaporation process and morphologically stable, especially when they are present in high doping concentrations in the emitting layer. A complete thermal characterization was carried out on a series of new TADF emitters to determine their suitability for OLED devices (Paper 3). Thermal properties affect not just the processing of materials and the stability of devices. An essential parameter for OLEDs is the external quantum efficiency. Usually, 70-80% of the light produced is lost before it exits the device. Many efforts have been made trying to increase the light outcoupling of OLEDs. One interesting approach is to orient the emitter horizontally within the emitting layer. This is found to be dependent on several factors, of which the glass transition of host materials is important. For this scope, the $T_g$ of benchmark host materials was determined and correlated with other parameters to build up a model that describes the orientation of emitters in the host matrix (Paper 4).

## 3.1. High Triplet Energy Host Materials for Blue TADF OLEDs-A Tool Box Approach

Here, a systematic approach for the design of high triplet energy hosts is reported. The study aims to create new bipolar host materials with high triplet energy and to consolidate a molecular strategy for their creation. Basically, several building blocks (acceptor, donor, and linker) with good stability and high triplet energy were chosen and combined systematically to form an array of six molecules. The choice of donors and acceptors lies in the bipolar charge carrier transport of the final material. All the molecules possess a biphenyl triazine acceptor, while two different donors are used (carbazole and acridine). In this way, two classes of molecules based on different donors can be distinguished (carbazole series and acridine series). Within each series, the connection is altered systematically from a para-phenyl linker to a meta-phenyl linker until having no linker (Figure 2). By comparing the molecules, it is possible to obtain useful structure-property information.



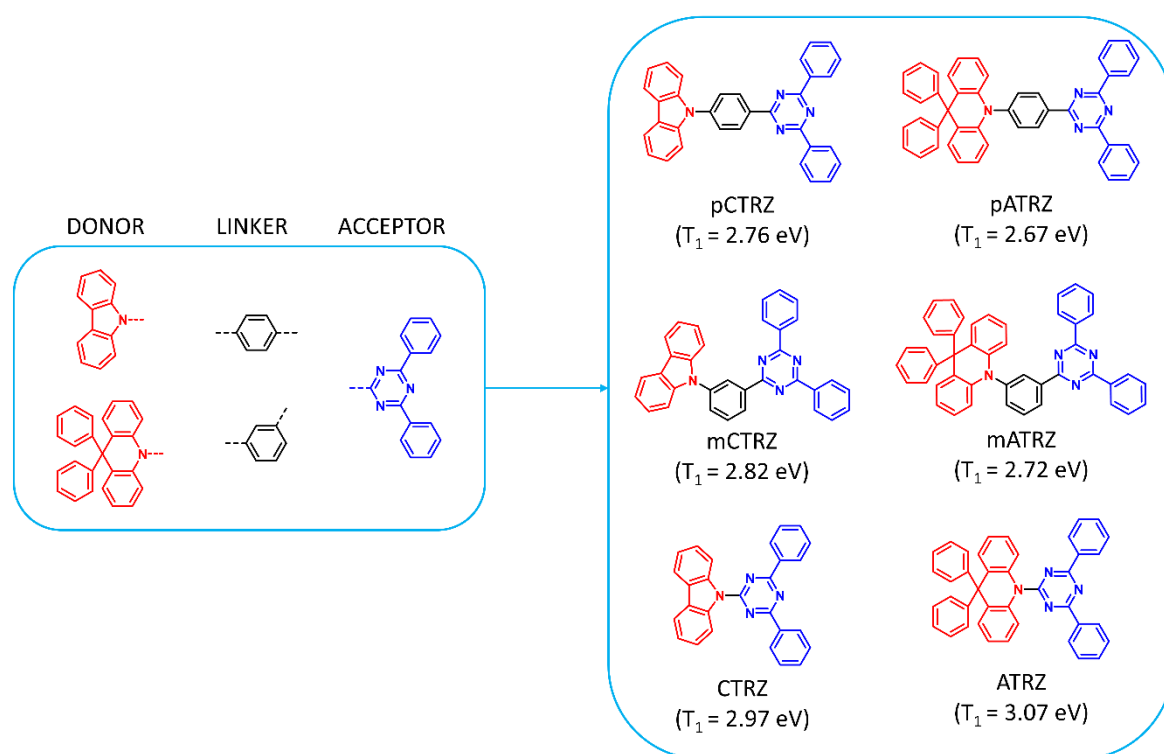Figure 2: Tool box approach for the design of triazine-based hosts. Chemical structures of the molecular constituents used and the resulting target compounds, along with their names and triplet energies. Adapted from Rodella et al.[1]

Four of the molecules were synthesized using a Buchwald-Hartwig cross-coupling reaction (mCTRZ, mATRZ and ATRZ) and a nucleophilic substitution (CTRZ). The compounds were

obtained highly pure through train sublimation with yields from 30 to 70%. The molecules mATRZ and ATRZ are entirely new, while the others are only partially studied under different conditions. The compounds were spectroscopically evaluated in order to obtain information about the excited states, with a particular focus on the triplet energy. From these results, we can conclude that for both the series, the replacement of the para-phenyl linker with a meta-phenyl linker is translated into an increase in the triplet energy, which becomes even higher when the linker is omitted (see Figure 2). Furthermore, we are interested in knowing the origin of the $T_1$ states. We, therefore, compared the phosphorescence spectra of the molecules with the ones of the functional groups. We find that for the compounds with the phenyl bridge, phosphorescence spread from the center of the molecules into adjacent moieties. In contrast, for the compounds without the bridge, the triplet state is localized strictly on the donor (CTRZ) or acceptor (ATRZ). All the energy values and the transition of the triplet states are in good agreement with the theoretical calculations. This gives a hint on the design of hosts with high triplet energy. In fact, via connecting donor and acceptor directly and possibly limiting their conjugation, we can reach high triplet energies. In fact, by replacing the carbazole with a less conjugated unit (acridine) we obtain a high triplet energy host with 3.07 eV (ATRZ).

Aside from the results which have been published in Frontiers in Chemistry, the most promising host of the series in terms of triplet energy (ATRZ) was further studied. The molecule possesses a high glass transition of 115°C and thermal stability (Figure 3 a and b), making it a good candidate for device fabrication. Cyclic voltammetry was also performed (Figure 3 c) to estimate the molecular orbital values. A blue TADF OLED using a commercial blue emitter was produced to verify the potential of the host material, obtaining high efficiency and low efficiency roll-off, even at high brightness (Figure 3 d and e). The device shows a good stability of 40 hours (LT50) at a luminance of 100 cd/m$^2$. A summary of the essential thermal properties and device data is shown in Table 1.
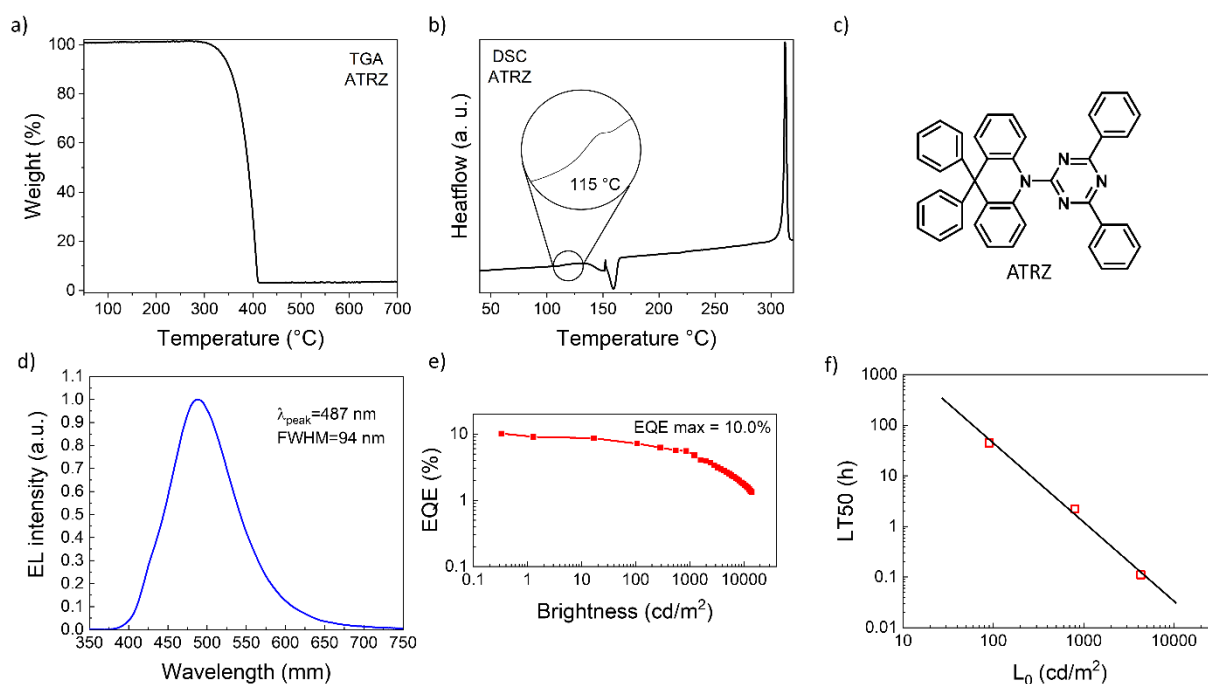
Figure 3: Thermal analysis of the host ATRZ and device data of a blue TADF OLED employing ATRZ as host. a) Thermogravimetric analysis (TGA) of ATRZ at 10 K/min under $N_2$ atmosphere. b) Second scan of differential scanning calorimetry (DSC) of ATRZ at 10 K/min after cooling with liquid $N_2$. c) Molecular structure of ATRZ. For experimental details, see Rodella et al.[1] d) Electroluminescence peak, along with the maximum peak emission ($\lambda_{peak}$) and full width at half maximum (FWHM) of the ATRZ-based OLED. e) External quantum efficiency (EQE) versus brightness, along with the maximum external quantum efficiency ($EQE_{max}$) of the ATRZ-based OLED. f) Lifetime until half luminance is reached (LT50) versus initial luminance ($L_0$) of the ATRZ-based OLED.

| | $T_1$ (eV) | $T_d$ (°C) | $T_g$ (°C) | $T_m$ (°C) | $T_r$ (°C) | HOMO/ LUMO* (eV) | $\lambda_{peak}$ (nm)/ $EQE_{max}$ (%) ** | LT50 at 100 cd/m$^2$ (hours) ** |
|---|---|---|---|---|---|---|---|---|
| ATRZ | 3.07 | 341 | 115 | 312 | 150 | -5.3/-2.2 | 487/10.0 | 40 |

Table 1: Main thermal and device properties of the most promising host ATRZ. $T_1$ = triplet energy. $T_d$ = decomposition temperature at 5% weight loss. $T_g$ = glass transition temperature. $T_m$ = melting temperature. $T_r$ = recrystallization temperature. * LUMO = (HOMO − absorption energy gap). ** device data.

## 3.2. Low efficiency roll-off blue TADF OLEDs employing a novel acridine-pyrimidine based high triplet energy host

In this work, the synthesis, characterization and application of three new pyrimidine-based hosts are described. The knowledge gained from the toolbox approach is used and expanded to other functional groups, aiming to obtain high triplet energy hosts. Initially, donor and acceptor units were chosen and directly coupled, without linkers, to limit the conjugation. The choice of the donor goes on the acridine unit for its high triplet energy and bulkiness. The three acceptors all contain a pyrimidine core, but their conjugated system is varied from having two additional phenyl rings, to one phenyl ring, until having only one methyl group. In this way, a series of three host materials with different acceptor's conjugation is obtained. The first molecule has a pyrimidine core linked to two phenyl rings and one acridine (2PPA). In the second molecule (1PPA), one phenyl ring is replaced by a second acridine, and the acceptor's conjugation is decreased. In the third molecule (1MPA), the last phenyl ring is replaced with a methyl group, leading to even less conjugation of the central pyrimidine core.
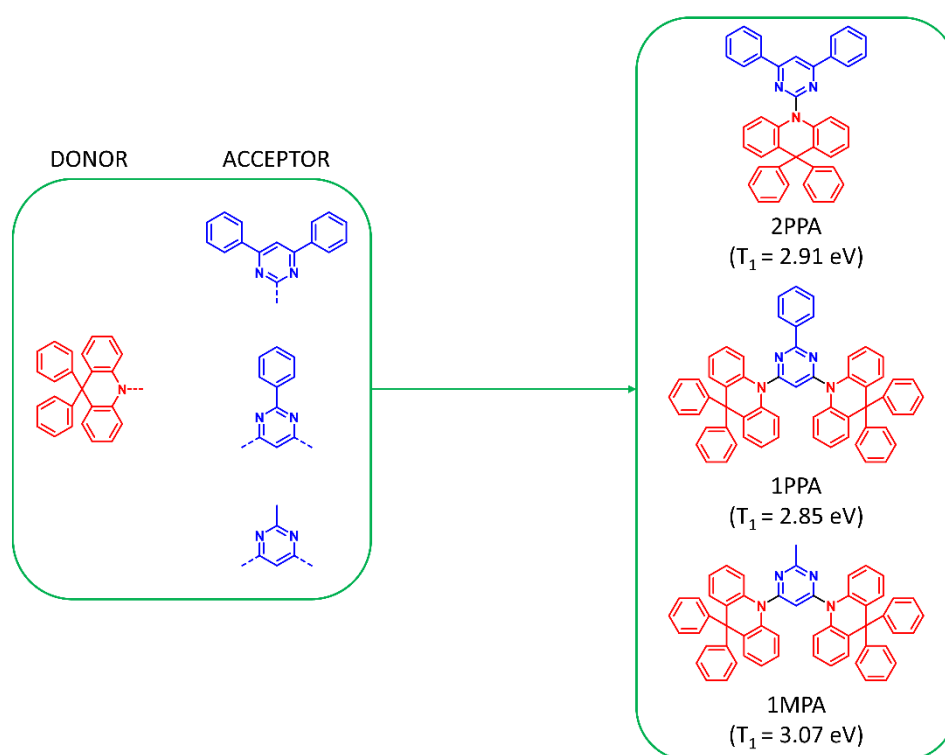


Figure 4: Tool box approach applied to pyrimidine-based hosts. Chemical structures of the molecular constituents used and the resulting target compounds, along with their names and triplet energies.

# 3. Synopsis

The synthesis was performed following a Buchwald-Hartwig protocol with the same conditions used for the triazine-based series, and the compounds were sublimed to reach high purity with overall yields between 25-58%.

Spectroscopic analysis and computational calculations were carried out to determine the value and origin of the triplet energies. The results show that for 2PPA and 1PPA, the lowest triplet state is similar (2.91 eV and 2.85 eV, respectively) and is extended on the pyrimidine core with one phenyl ring. When the last phenyl ring is replaced with a methyl group (1MPA), the triplet energy increases to 3.07 eV. Here, the acceptor and donors are very high in energy, leaving a partial CT state as the lowest triplet energy of the molecule.

The thermal properties were then analyzed. The DSC results clearly show that the introduction of the second acridine (present in 1PPA and 1MPA) delivers superior morphological properties, with clearly higher glass transition and recrystallization temperatures. The melting temperatures of the materials are instead similar, with a slight decrease in 1MPA. TGA data indicate, once again, higher decomposition temperatures of the compounds with two acridine units. TGA also indicates that all the materials leave none or only minor residues, which means that all three hosts completely evaporate already at normal pressure and are ideal candidates for OLED fabrication via evaporation. Additionally, cyclic voltammetry of the three hosts was carried out to explore the electrochemical properties and to estimate the HOMO values. All the compounds show two quasi-reversible oxidation peaks. The first oxidation peak always appears slightly above 0.2 V vs. Ag/AgCl, and it corresponds to the oxidation of the donor acridine. The LUMO is then obtained by subtracting the absorption's energy gap from the HOMO. Among the series, the most promising molecule in terms of high glass transition and triplet energy (1MPA) was chosen for device application. The host is used in blue TADF OLED devices with a commercial blue emitter, which shows good efficiencies up to 13.6%, low-efficiency roll-off even at high brightness and electroluminescent emissions of 493 nm. The host is also employed with a deeper blue OLED, delivering 461 nm as an emission peak and confirming its potential. The results are summarized in Table 2.
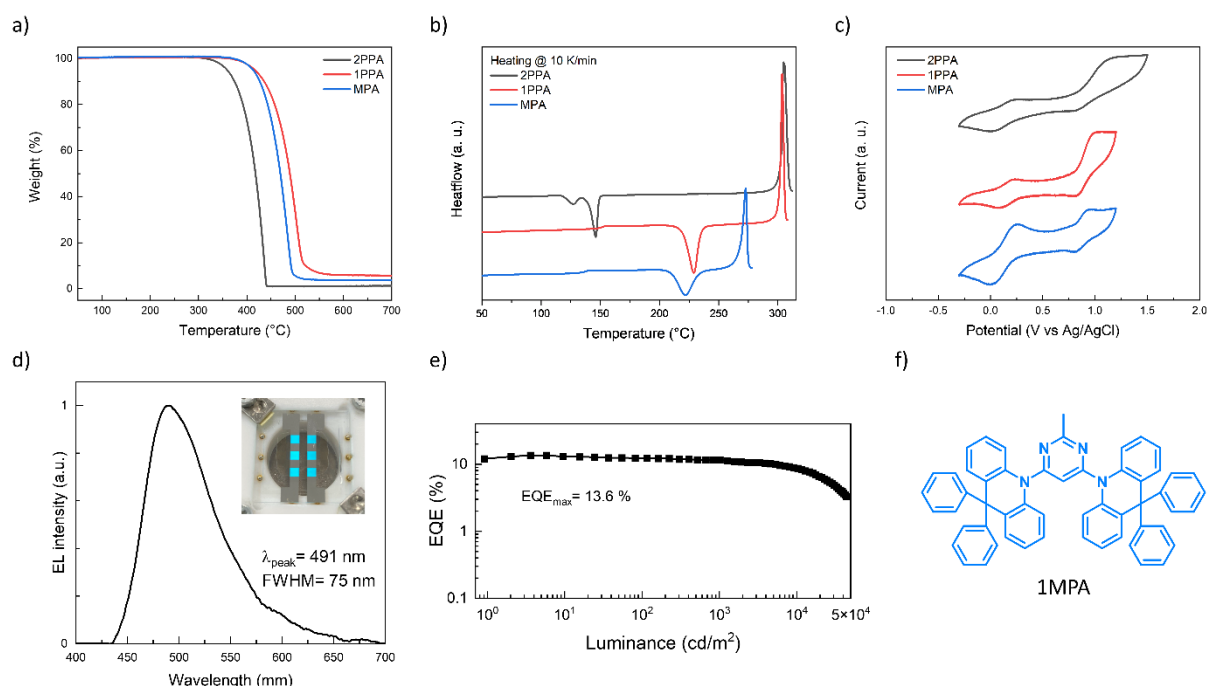
Figure 5: Thermal analysis of the hosts 2PPA, 1PPA, and 1MPA; and device data of a blue TADF OLED employing 1MPA as host. a) Thermogravimetric analysis (TGA) of 2PPA, 1PPA, and 1MPA. b) Differential scanning calorimetry (DSC) 2PPA, 1PPA, and 1MPA. c) Cyclic voltammetry (CV) of 2PPA, 1PPA, and 1MPA. d) Electroluminescence peak, along with the peak maximum ($\lambda_{peak}$) and full width at half maximum (FWHM) of the 1MPA-based OLED. e) Maximal external quantum efficiency, along with the maximum external quantum efficiency (EQE$_{max}$) of the 1MPA-based OLED. f) Molecular structure of 1MPA. For experimental details, see Paper 2.

| | $T_1$ (eV) | $T_d$ (°C) | $T_g$ (°C) | $T_m$ (°C) | $T_r$ (°C) | HOMO/LUMO* (eV) | $\lambda_{peak}$ (nm)/ EQE$_{max}$ (%) ** |
|---|---|---|---|---|---|---|---|
| 2PPA | 2.91 | 359 | 108 | 305 | 127, 147 | -5.12/-2.00 | - |
| 1PPA | 2.85 | 417 | 150 | 304 | 229 | -5.11/-1.71 | - |
| 1MPA | 3.07 | 413 | 138 | 273 | 222 | -5.10/-1.55 | 491/13.6 |

Table 2: Main thermal and device properties of the hosts 2PPA, 1PPA, and 1MPA. $T_1$ = triplet energy. $T_d$ = decomposition temperature at 5% weight loss. $T_g$ = glass transition temperature. $T_m$ = melting temperature. $T_r$ = recrystallization temperature. * LUMO = (HOMO – absorption energy gap). ** device data.

**3.3. Substitution Effects on a New Pyridylbenzimidazole Acceptor for Thermally Activated Delayed Fluorescence and Their Use in Organic Light-Emitting Diodes**

Thermal and morphological stabilities are crucial for the manufacturing and durability of OLEDs. In this chapter, the thermal analysis is applied to a series of new TADF emitters based on a pyridylbenzimidazole acceptor. When creating new materials, parameters that describe their behavior with temperature need to be determined before proceeding with device fabrication. This means knowing the material's processability and how it behaves during the device's operation. Thus, thermal analysis is an essential investigation for materials employed in OLEDs. Thermal stability helps determine whether an emitter can be processed through vacuum thermal evaporation to form an OLED and at what temperature it decomposes. Morphological stability is particularly vital in the emitting layer, where joule heat is generated. Precisely, this is very important for hosts and emitters due to their key role in the recombination processes and relative thermal stress caused through device operation. The morphology steadiness is described by the Tg, namely, the point where the molecules become mobile and above which crystallization may occur. This is an essential parameter and has to be relatively high to avoid recrystallization within the device and its degradation. $T_g$ is a bulk property and, therefore, the host material contributes the most to the stability of the emitting layer. Nonetheless, the influence of the emitter is considerable. The thermal analysis is completed with the determination of the melting and recrystallization points, significant for a complete understanding of the materials. Figure 6 shows the molecular structure of the new pyridylbenzimidazole-based TADF emitters H, Me, Ph and tBu (named after the functional group), prepared in the group of E. Zysman-Colman in St. Andrews.[2]
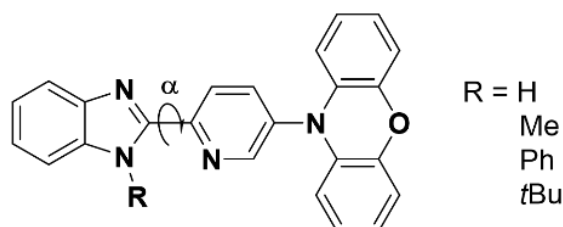


Figure 6: Molecular structure of the four TADF emitters H, Me, Ph, and tBu. Adapted from Hall et al.[2]

Characterization of the molecules and device fabrication have been carried out. However, the focus of this chapter will be on the thermal analysis of the materials, a crucial factor to determine their potential as emitters for OLEDs. The molecules are similar but present

different substitutions, i.e., an H, Me, Ph, and tBu group on the benzimidazole moiety. TGA and DSC analyses were performed to assess the thermal and morphological properties, as shown in Figures 7 a and b, respectively. The results are then summarized in Table 4.
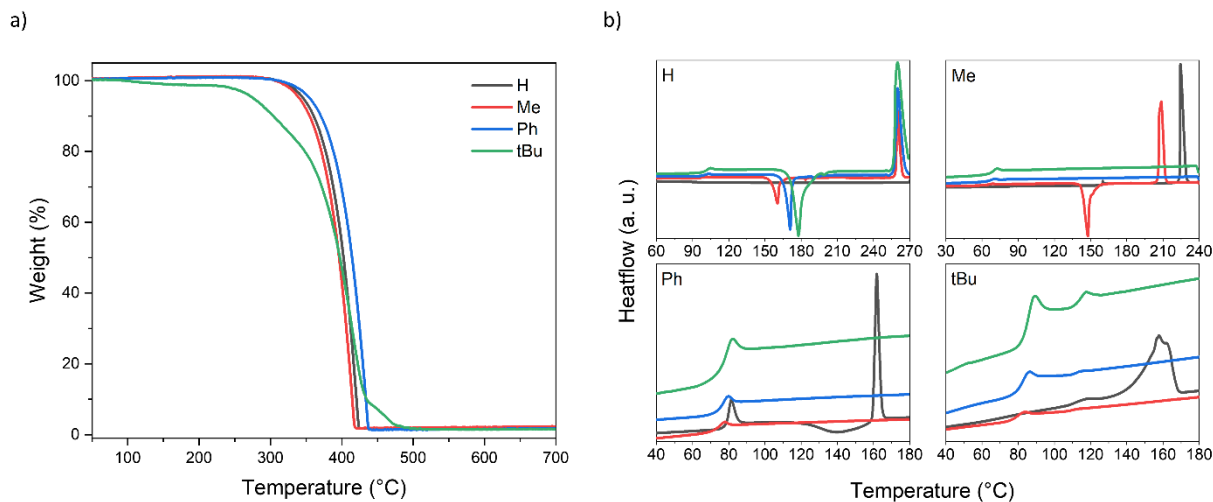


Figure 7: a) Thermogravimetric analysis of the four emitters, used to determine the decomposition temperatures. b) Differential scanning calorimetry of the four emitters showing the four heating scans (1st heating at 10 K/min in black, 2nd heating at 10 K/min in red, 3rd heating at 20 K/min in blue, 4th heating at 40 K/min in green), utilized to obtain glass transition, recrystallization, and melting temperatures.

Throughout the series, we found that the molecules present a $T_d$ that ranges from 276°C to 355 °C. The molecule with Ph group is the most stable (355°C) due to more π conjugation and π-π interactions. Then there are the H group (346°C) and the Me group (341°C) that are similar. Since the H group is linked to nitrogen, hydrogen bonds in the solid-state take place, slightly improving the stability. Finally, we found tBu having substantially less stability (276°C), due the high steric repulsion of the tert-butyl group and less aromaticity. Furthermore, the complete decrease of the weight down to zero suggests that the materials do not leave carbon residues, thus a signal of complete evaporation. The $T_g$ is the highest for the molecule H (97°C), due to the presence of increased hydrogen bonds given by the NH group. Among the substituted molecules, we find that the bulkier the group, the higher is the $T_g$: 80°C for tBu, 73°C for Ph and 60°C for Me. The $T_m$ is again the highest for H (260°C) due to the presence of hydrogen bonds, followed by the molecule with the Me group, for which we can attribute two different melting temperatures given by two polymorphs (210°C and 225°C). The molecule with the Ph group has a lower melting at 162°C, due to a less densely packed structure. Finally, we couldn't attribute a melting point for the molecule with the tBu group due to a broad exothermic zone, probably due to the start of decomposition. At around 140-160 °C, we see

recrystallization of the molecules with H and Me groups, due to the absence of a sterically demanding functional group on the acceptor moiety.

| Compound | $T_d$ (°C) | $T_g$ (°C) | $T_m$ (°C) | $T_r$ (°C) |
|----------|------------|------------|------------|------------|
| H | 346 | 97 | 260 | 160 |
| Me | 341 | 64 | 210, 225 | 140, 150 |
| Ph | 355 | 73 | 162 | - |
| tBu | 276 | 80 | - | - |

Table 4: Thermal and morphological properties of the four TADF emitters. $T_d$ = decomposition temperature at 5% weight loss. $T_g$ = glass transition temperature. $T_m$ = melting temperature. $T_r$ = recrystallization temperature.

We conclude that morphological stability is the highest when the acceptor has a small H group. This might be counter-intuitive, but it is necessary to consider the presence of hydrogen bonds. Instead, the more extended conjugation given by the Ph group delivers the highest thermal stability.

## 3.4. What Controls the Orientation of TADF Emitters?

The external quantum efficiency, i.e., the ratio between extracted photons from a device divided by the number of injected charges, represents one of the most important parameters in characterizing OLEDs performance. About 75% of the photons generated are normally lost before they leave the device. Therefore, effective methods for light extraction are essential. One of these methods is to induce emitter molecules to be horizontally oriented within the emitting layer. In this work, we determine under identical conditions the glass transition temperature ($T_g$) of benchmark hosts, which is a crucial factor for the orientation of TADF emitters. In order to build a model that describes the orientation of TADF emitter within the emitting layer, two TADF emitters were co-evaporated with different host materials, maintaining at constant temperature the substrate. One of the emitters has a donor-acceptor-donor (DAD) assembly and is highly elongated (ICzTRZ). The other emitter (DMAC-TRZ) has a less extended donor-acceptor (DA) construction, typical for TADF molecules. The structures are reported in Figure 8.
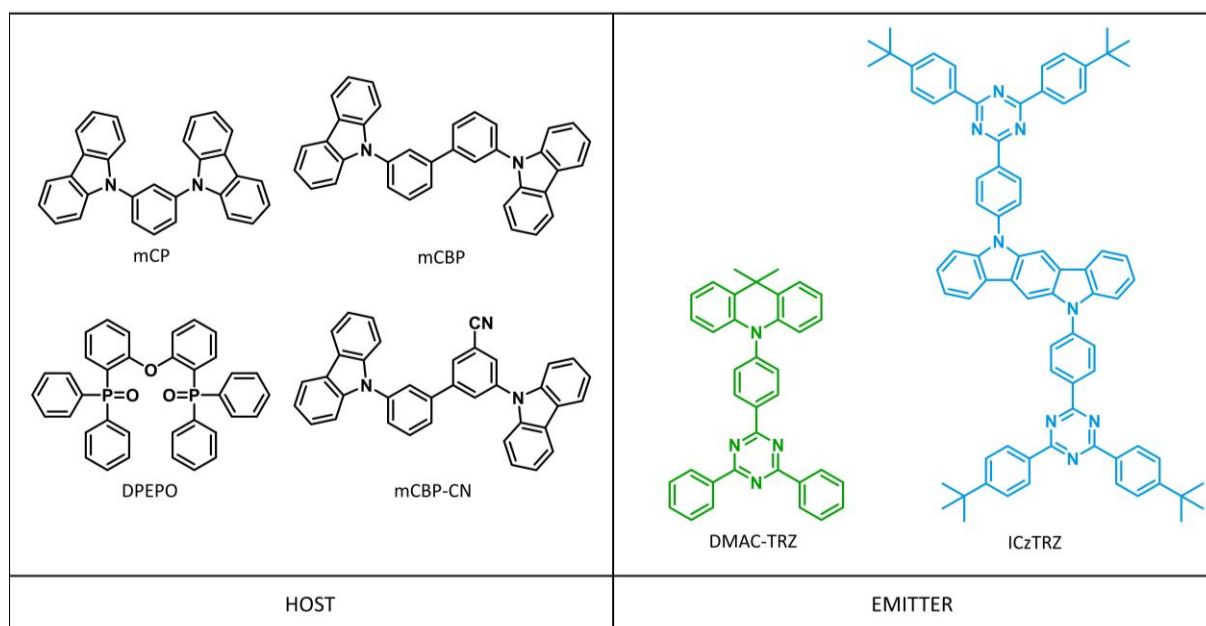


Figure 8: Molecular structure of the host materials and emitters analyzed by differential scanning calorimetry.

The host materials were chosen because they cover a wide range of glass transition temperatures, which is expected to have an effect on orientation, based on previous studies.

Since the morphological data are not known for all hosts, the $T_g$ of the host materials was determined. The results show a clear trend for carbazole-based molecules. mCP comprises

two carbazole moieties meta-linked through a phenyl ring. Although the meta position provides a twisted structure, the $T_g$ of the material is as low as 65°C, due to the low molecular weight. When a phenyl ring is added (mCBP), the molecular weight increases and the $T_g$ is 92°C. Finally, for mCBP-CN, only a cyano group is added. Although the functional group is relatively small, the host material has the highest $T_g$ of 113°C. The highly polar CN group provides more interactions, increasing the temperature at which the glassy state persists. In the case of DPEPO, the highly polar phosphine oxide groups together with the high conformational motion given by the ether bridge provide a $T_g$ of 93°C. The $T_g$ of the emitters was also determined. As expected, the long and heavy molecule ICzTRZ provides a $T_g$ with the value of 253°C and the shorter and lighter emitter DMAC-TRZ provides 93°C.
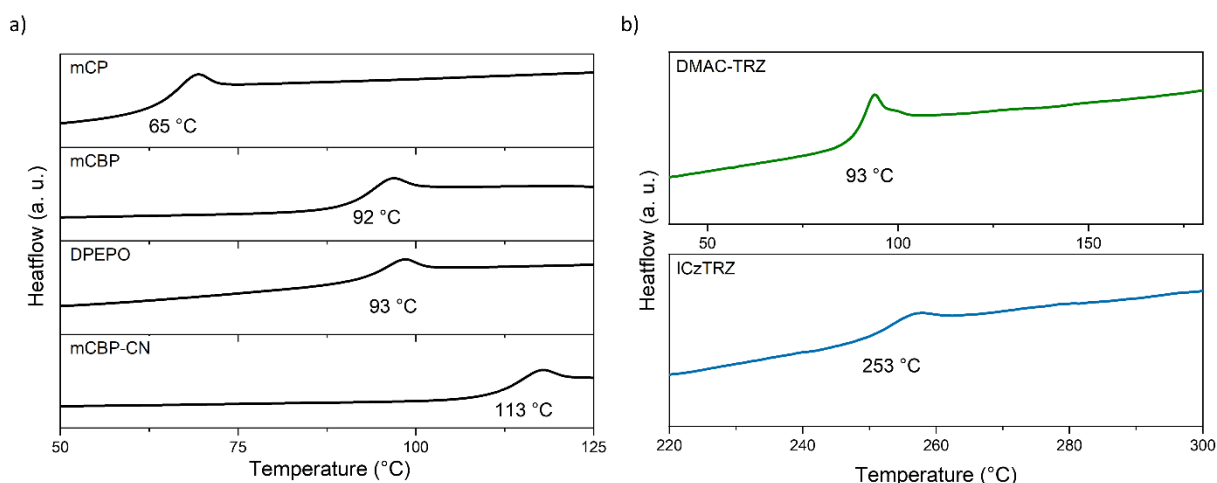


Figure 9: Differential scanning calorimetry showing the second heating scan of: the hosts mCBP-CN, DPEPO, mCBP and mCP. b) the emitters DMAC-TRZ and ICzTRZ. The values of the glass transition temperatures are included. Adapted from Naqvi et al.[3]

The emitter orientation factor Θ for each host-guest film was obtained through angular dependent photoluminescence spectroscopy in the group of W. Brütting in Augsburg. Then, Θ was correlated with the $T_g$ of the hosts (Figure 10 a). The results show two different regimes. Firstly, for less elongated emitters (DMAC-TRZ), a higher $T_g$ of the host delivers better emitter orientation (low Θ values). This proves the crucial role of the host in governing the spatial disposition of the emitter. In fact, low $T_g$ values (similar to the substrate temperature $T_s$) allow the rearrangement of the molecules, thus preferring a vertical orientation (Figure 10 b). Instead, when the $T_g$ is high, rearrangement of the molecules is limited, leading to a more

favorable horizontal disposition (Figure 10 c). However, when the molecule is relatively long (ICzTRZ), the effect is less pronounced. This occurs because the elongated molecule rearranges mainly horizontally, almost independently from the surrounding host molecules (Figure 10 d). In this last case, the emitter's intrinsic property (shape) determines the orientation.
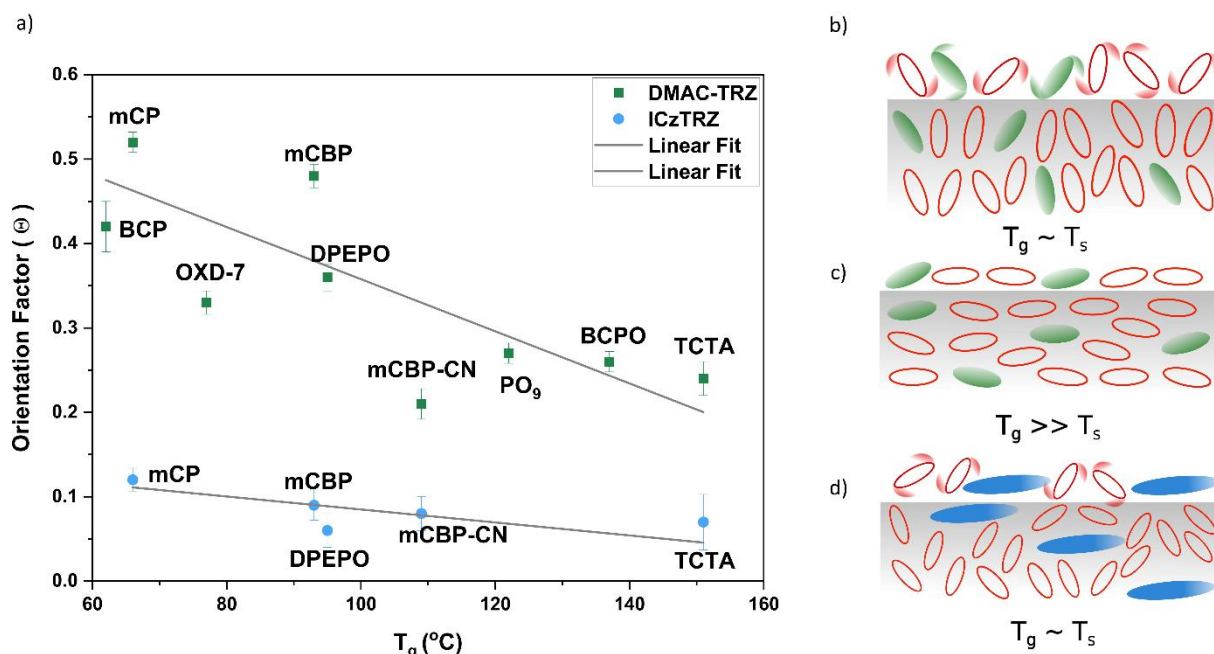


Figure 10: a) Dependency of the emitter's transition dipole moment (TDM) orientation factor ($\Theta$) vs. $T_g$ of the hosts. b–d) Schematic illustration of the effect of $T_g$ (mobility of host molecules) on the orientation of emitter molecules. Host molecules are shown in red, DMAC-TRZ in green, and ICzTRZ in blue. b) Enhanced molecular mobility and adoption of vertical orientation of host and DMAC-TRZ molecules for $T_g \sim T_s$, while in C) pronounced horizontal orientation is observed when $T_g \gg T_s$. D) The long ICzTRZ is relatively unaffected by the mobile host molecules regardless of their $T_g$'s. Adapted from Naqvi et al.[3]

Although the data have well fit, in the case of DMAC-TRZ another observation is necessary. In fact, different orientation factors can occur within the same $T_g$ range (see DPEPO and mCBP, Figure 10 a, green squares). This concludes that $T_g$ is the dominant factor, but not the only one. For this reason, through impedance spectroscopy, the fraction of oriented permanent dipole moments of the host materials was determined and correlated with the emitter's orientation factor $\Theta$. The results reveal a higher horizontal alignment of the host DPEPO than for mCBP. Thus, within the same $T_g$ range, certain hosts (such as DPEPO) can rearrange better, boosting the horizontal orientation of the emitter.

To conclude, the orientation of emitters depends mostly on three parameters (see Figure 11 for a summary). Firstly, on the intrinsic properties of the emitter, i.e., the shape of the emitting

molecules. The longer and more rodlike it is, the stronger will be its tendency to lie down when evaporated on a surface. Therefore, it will be less affected by the surrounding host. Secondly, if the emitter is relatively short, like in most TADF emitters, the host matrix takes over the role of determining emitters' orientation. In particular, the glass transition temperature of the host is of primary importance. A high $T_g$ reduces the surface diffusivity of molecules so that they do not have enough time to equilibrate and, thus, adopt the favored lying flat orientation. Thirdly, alignment of the host material itself promotes TADF emitter orientation.
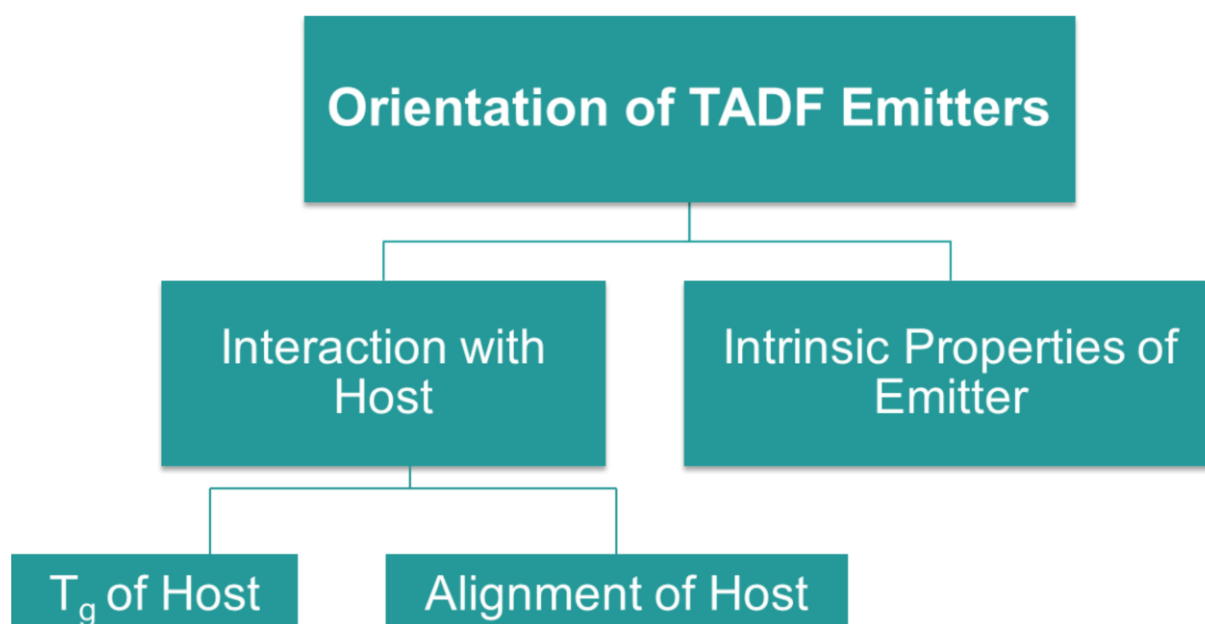
Figure 11: Proposed model for the dominant factors affecting TADF emitter orientation. Reproduced from Naqvi et al.[3]

To summarize, the first paper establishes a fundamental strategy for synthesizing bipolar high triplet energy host materials through a toolbox approach. The results show that a high triplet energy host is obtained by using donor-acceptor structures, avoiding linkers, and decreasing the conjugation of the donor. The host also has good thermal and morphological stability. Furthermore, the material is used in blue OLED devices delivering good efficiency and stability. The second paper follows the toolbox approach. In fact, donor and acceptor units were directly coupled, and the less conjugated donor was used, like in the first strategy. Here, another acceptor is introduced, and through decreasing its conjugation, a new high triplet energy host is obtained. This host also possesses good thermal and morphological properties and delivers blue OLEDs with good efficiencies. The third paper discusses the thermal and morphological properties of new TADF emitters, providing insights into the processability and

the durability of this new category of molecules. Finally, the fourth paper reports the morphological properties of benchmark hosts, which are correlated with the orientation of TADF emitters to provide a model helpful to increase efficiency in OLEDs.

(1) Rodella, F.; Bagnich, S.; Duda, E.; Meier, T.; Kahle, J.; Athanasopoulos, S.; Köhler, A.; Strohriegl, P. High Triplet Energy Host Materials for Blue TADF OLEDs-A Tool Box Approach. *Frontiers in chemistry* **2020**, *8*, 657. DOI: 10.3389/fchem.2020.00657. Published Online: Jul. 29, 2020.

(2) Hall, D.; Rajamalli, P.; Duda, E.; Suresh, S. M.; Rodella, F.; Bagnich, S.; Carpenter-Warren, C. L.; Cordes, D. B.; Slawin, A. M. Z.; Strohriegl, P.; Beljonne, D.; Köhler, A.; Olivier, Y.; Zysman-Colman, E. Substitution Effects on a New Pyridylbenzimidazole Acceptor for Thermally Activated Delayed Fluorescence and Their Use in Organic Light-Emitting Diodes. *Adv. Optical Mater.* **2021**, 2100846. DOI: 10.1002/adom.202100846.

(3) Naqvi, B. A.; Schmid, M.; Crovini, E.; Sahay, P.; Naujoks, T.; Rodella, F.; Zhang, Z.; Strohriegl, P.; Bräse, S.; Zysman-Colman, E.; Brütting, W. What Controls the Orientation of TADF Emitters? *Frontiers in chemistry* **2020**, *8*, 750. DOI: 10.3389/fchem.2020.00750. Published Online: Sep. 4, 2020.

## 3.6. Individual contribution to joint publications

The publications presented in this thesis arose from joint collaborations. The following section specifies the individual contributions of the authors:

**Paper 1**

"High Triplet Energy Host Materials for Blue TADF OLEDs—A Tool Box Approach"

By F. Rodella, S. Bagnich, E. Duda, T. Meier, J. Kahle, S. Athanasopoulos, A. Köhler an P. Strohriegl.

Published as Frontiers in Chemistry **2020**, 8, 657.

I conceived the toolbox approach and conducted the synthesis and characterization of host materials. S. Bagnich and E. Duda performed and interpreted the photophysical measurements. T. Meier, J. Kahle, and S. Athanasopoulos were responsible for DFT calculations. A. Köhler and P. Strohriegl supervised the project and corrected the manuscript.

**Paper 2**

"Low efficiency roll-off blue TADF OLEDs employing a novel acridine-pyrimidine based high triplet energy host"

By F. Rodella, R. Saxena, S. Bagnich, D. Banevičius, G. Kreiza, S. Athanasopoulos, S. Juršėnas, K. Kazlauskas, A. Köhler and P. Strohriegl.

Submitted to Journal of Materials Chemistry C.

I performed the synthesis and characterization of the host materials, as well as the thermal and electrochemical analysis. R. Saxena and S. Bagnich performed photophysical studies. D. Banevičius and G. Kreiza fabricated OLED devices. S. Athanasopoulos was responsible for DFT calculations. S. Juršėnas, K. Kazlauskas, A. Köhler and P. Strohriegl supervised the experiments and corrected the manuscript.

**Paper 3**

"Substitution Effects on a New Pyridylbenzimidazole Acceptor for Thermally Activated Delayed Fluorescence and Their Use in Organic Light-Emitting Diodes"

By D. Hall, P. Rajamalli, E. Duda, S. M. Suresh, F. Rodella, S. Bagnich, C. L. Carpenter-Warren, D. B. Cordes, A. M. Z. Slawin, P. Strohriegl, D. Beljonne, A. Köhler, Y. Olivier, E. Zysman-Colman.

Published as Adv. Optical Mater. **2021**, 2100846.

I performed the thermal analysis of the TADF emitters. D. Hall conducted synthesis and characterization of materials, computational calculations, electrochemistry and solution photophysics. P. Rajamalli fabricated OLED devices. E. Duda and S. Bagnich performed solid-state photophysics and transient lifetime measurements. S. M. Suresh assisted the purification of compounds. C. L. Carpenter-Warren, D. B. Cordes, and A. M. Z. Slawin characterized and interpreted single crystals. P. Strohriegl, D. Beljonne, A. Köhler, Y. Olivier, and E. Zysman-Colman supervised the experiments and corrected the manuscript.

**Paper 4**

"What Controls the Orientation of TADF Emitters?"

By B. A. Naqvi, M. Schmid, E. Crovini, P. Sahay, T. Naujoks, F. Rodella, Z. Zhang, P. Strohriegl, S. Bräse, E. Zysman-Colman, W. Brütting.

Published as Frontiers in Chemistry **2020**, 8, 750.

I measured the glass transition temperatures of emitters and host materials. B. A. Naqvi prepared samples and performed angular dependent PL measurements and their analysis to obtain TDM orientation. M. Schmid and E. Crovini performed TD-DFT on the emitter molecules. M. Schmid further calculated PDMs of host materials and analyzed their alignment by impedance spectroscopy. P. Sahay and T. Naujoks prepared OLED devices and performed simulations. Z. Zhang synthesized the emitter ICzTRZ. P. Strohriegl, S. Bräse, E. Zysman-Colman, and W. Brütting supervised the project and corrected the manuscript. B. A. Naqvi, M. Schmid, E. Crovini, E. Zysman-Colman, and W. Brütting conceived the project.

## 4. Publications

### 4.1. Paper 1: High Triplet Energy Host Materials for Blue TADF OLEDs—A Tool Box Approach

**frontiers** in Chemistry

# High Triplet Energy Host Materials for Blue TADF OLEDs—A Tool Box Approach

Francesco Rodella[1†], Sergey Bagnich[2†], Eimantas Duda[2], Tobias Meier[2], Julian Kahle[2], Stavros Athanasopoulos[3], Anna Köhler[2,4] and Peter Strohriegl[1,4*]

[1] Macromolecular Chemistry I, University of Bayreuth, Bayreuth, Germany, [2] Soft Matter Optoelectronics, University of Bayreuth, Bayreuth, Germany, [3] Departamento de Física, Universidad Carlos III de Madrid, Madrid, Spain, [4] Bayreuth Institute of Macromolecular Research (BIMF), University of Bayreuth, Bayreuth, Germany

The synthesis of stable blue TADF emitters and the corresponding matrix materials is one of the biggest challenges in the development of novel OLED materials. We present six bipolar host materials based on triazine as an acceptor and two types of donors, namely, carbazole, and acridine. Using a tool box approach, the chemical structure of the materials is changed in a systematic way. Both the carbazole and acridine donor are connected to the triazine acceptor via a para- or a meta-linked phenyl ring or are linked directly to each other. The photophysics of the materials has been investigated in detail by absorption-, fluorescence-, and phosphorescence spectroscopy in solution. In addition, a number of DFT calculations have been made which result in a deeper understanding of the photophysics. The presence of a phenyl bridge between donor and acceptor cores leads to a considerable decrease of the triplet energy due to extension of the overlap electron and hole orbitals over the triazine-phenyl core of the molecule. This decrease is more pronounced for the para-phenylene than for the meta-phenylene linker. Only direct connection of the donor group to the triazine core provides a high energy of the triplet state of 2.97 eV for the carbazole derivative CTRZ and 3.07 eV for the acridine ATRZ. This is a major requirement for the use of the materials as a host for blue TADF emitters.

Keywords: thermally activated delayed fluorescence, TADF, host, organic light emitting diode, tool box approach, high triplet energy

## INTRODUCTION

Organic light emitting diodes (OLEDs) are overtaking the field of display applications due to several favorable characteristics in comparison with classic liquid crystal devices (LCDs) such as lower energy consumption and simpler technology (Endo et al., 2011; Sasabe and Kido, 2013). For these reasons, in the past years, much effort was dedicated to develop new materials and technologies for OLEDs. The current focus is, in particular, to improve their efficiency and long-time stability. Starting from classic fluorescent emitters (1st generation) with an internal quantum efficiency (IQE) limited to 25%, research moved to phosphorescence emitters (2nd generation) with an increased IQE of 100% and then to thermally activated delayed fluorescence (TADF), which represents the last and very promising generation of OLED materials (Endo et al., 2011; Uoyama et al., 2012). In comparison with phosphorescence emitters that use less available and more expensive noble metals, TADF emitters often rely on pure organic molecules with donor

and acceptor groups. This donor-acceptor structure often leads to a small singlet ($S_1$)-triplet ($T_1$) energy gap ($\Delta E_{ST}$) that allows reverse intersystem crossing (RISC) from the triplet into the singlet state, permitting a theoretical 100% IQE by emission of prompt and delayed fluorescence. Lin et al. reported a state of the art TADF OLED with an IQE of 100%, and, more surprisingly, an external quantum efficiency (EQE) of 37%. So far this is one of the highest efficiency ever reported for TADF emitters (Lin et al., 2016). Another promising way to obtain TADF molecules with pure emission is based on multiple resonance effect (Hatakeyama et al., 2016). Most of the work on TADF focuses on new emitters. Pure emitter layers usually show self quenching, thus it is necessary to dilute the emitters in suitable host materials. These hosts have to fulfill several requirements such as having a high triplet energy level, chemical and thermal robustness, and balanced charge carrier mobilities (Wong and Zysman-Colman, 2017). One of the recent challenges is to develop efficient and stable blue OLED host/emitter systems that can replace the less efficient fluorescent ones of the 1st generation, currently used in display applications (Cai and Su, 2018). While designing a host, the triplet energy level is the first key point to look at, especially if the aim is to use it for blue emitters since they require hosts with a triplet energy of about 3 eV. So far, the reported hosts with a triplet energy suitable for blue emitters are mostly monopolar and made with groups such as phosphine oxide, which are known to have limited stability (Hirata et al., 2014; Chen et al., 2015; Kim et al., 2015; Yook and Lee, 2015; Zhang et al., 2015; Chatterjee and Wong, 2018). Among them, DPEPO is one of the most used hosts for TADF blue emitters since it has a high energy triplet level of 3 eV (Han et al., 2011). Several carbazole-based hosts have been developed, with the advantage to have higher stability. Some of them, still monopolar, come from

the 2nd generation such as mCP and mCBP (Wong and Zysman-Colman, 2017). Successively, in order to have a balanced charge carrier transport, bipolar carbazole-based hosts were developed by adding acceptor units such as cyano, triazine, and phosphine oxide groups (An et al., 2011; Ding et al., 2015; Kukhta et al., 2017; Shin et al., 2018) or formation of dimers and trimers (Tomkeviciene et al., 2011). Most of these carbazole-based hosts are limited to the use of blue greenish emitters since their triplet energies are below 3 eV. Hosts with less common functional groups such as cyclophosphazene (Nishimoto et al., 2014), silicon (Ren et al., 2004), and benzimidazobenzothiazole (Cui et al., 2016a) were also developed in order to increase the triplet energy. Furthermore, trying to avoid the problem of suitable hosts, non-doped emitting layers are also under investigation by using sterically demanding molecules such as dendrimers, but they still suffer from lower efficiencies in comparison with doped emitting layers (Wong and Zysman-Colman, 2017; Cai and Su, 2018; Wei et al., 2018). Overall, host materials remain less developed in comparison with emitters, therefore some standard approaches and guidelines could be helpful to progress this field.

In this paper we present a systematic study called "tool box approach" illustrated in **Figure 1** in order to understand how to increase the triplet energy of triazine-based bipolar molecules. Namely, one acceptor (triazine), two linkers (meta and ortho phenyl rings), and two donors (carbazole and acridine) were chosen as building blocks because of their stability and common use, then combined to obtain six molecules (**pCTRZ**, **mCTRZ**, **CTRZ**, **pATRZ**, **mATRZ**, **ATRZ**), of which two are new (**mATRZ** and **ATRZ**). All the target compounds were compared through spectroscopic characterization and theoretical calculations. This allows to understand the contribution of the single building blocks on the triplet energy of the final molecules and so to give



FIGURE 1 | Tool box approach. Chemical structures of the molecular constituents used and the resulting target compounds, along with their names.

57
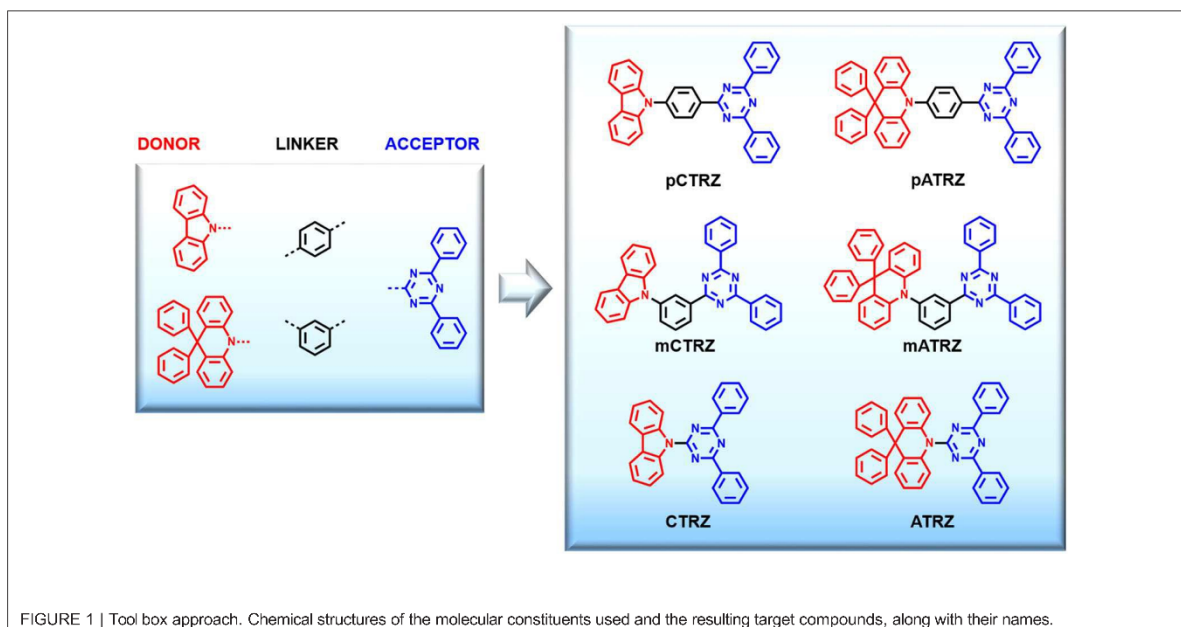
a structure-property relationship. We note that spectroscopic and computational data on **pCTRZ**, **mCTRZ**, **CTRZ**, **pATRZ** are already available, yet sometimes not complete across the series, and sometimes contradictory. Here we study the entire set of 6 compounds under identical conditions which facilitates comparison. We show that by using a direct linkage between donor and acceptor it is possible to reach triplet $T_1$ energy values above 3 eV. The strategy here proposed can be helpful to design new bipolar molecules with high triplet energies and stable functional groups, permitting to obtain potential hosts for blue TADF OLEDs.

## METHODS

### Materials
All the starting materials needed for the synthesis were purchased from abcr and Acros Organics. The two reference compounds **pATRZ** and **pCTRZ** were purchased from Lumtec. The reference compounds CBP and spiro-2CBP were purchased from Sigma Aldrich. mCBP was synthesized as described in literature (Schroegel et al., 2011). Their chemical structures can be found in the **Supplementary Information**.

### Purification
The synthesized compounds **mCTRZ**, **mATRZ**, **CTRZ**, and **ATRZ** were purified by train sublimation in a Carbolite split tube furnace HZS 12/450.

### Characterization
$^1$H NMR and $^{13}$C NMR spectra were recorded on a Bruker Avance III HD (500 MHz) and the chemical shifts were referred to chloroform-d3 (7.26 ppm). MS spectra were obtained on a Finningan MAT 8500 using electron impact ionization.

### Photophysical Measurements
For the absorption and emission measurements, we prepared solutions of 0.05 mg/ml of the compounds in toluene. Absorption spectra were recorded at room temperature on a Cary 5000 double beam spectrophotometer. Steady-state and time resolved photoluminescence spectra in solution and films were recorded at 298 and 77 K using a Jasco FP-8600 spectrofluorometer. For **pCTRZ** and **pATRZ**, fluorescence could be taken at 77 K in steady state operation without superimposed phosphorescence signal. For **mCTRZ** and **mATRZ**, the stronger intensity of the phosphorescence required us to use the chopped excitation from the Jasco spectrofluorometer and gated detection (delay time of 50 µs, integration time of 50 µs) in order to obtain only fluorescence without contribution of the phosphorescence. To exclude the even stronger phosphorescence signal in the fluorescence measurements of **CTRZ** and **ATRZ**, we used a 355 nm pulsed laser excitation with iCCD camera, a delay time of 10 ns and an integration time of 30 ns.

Values for the photoluminescence quantum yield (PL QY) of the molecules in solution were obtained using the Jasco FP-8600 spectrofluorometer equipped with an integrating sphere. The intensity decay of the fluorescence was measured using a Q-switched QS laser MPL15100-DP at $\lambda = 355$ nm as the excitation

source and an Andor iCCD camera (iStar A-DH334T-18F-03) as the detector. Rate constants for the decay of singlet state were calculated using following relation: $\Phi = \kappa_r / (\kappa_r + \kappa_{nr})$, $\tau = 1 / (\kappa_r + \kappa_{nr})$, where $\Phi$ is fluorescence quantum yield and $\tau$ is the decay time. $\kappa_r$ is the rate of radiative decay of the singlet state, $\kappa_{nr}$ is the rate of the non-radiative deactivation of the singlet state.

## Computational Calculations
*Density functional theory (*DFT) and linear response time-dependent density functional theory (TD-DFT) calculations have been performed using the Gaussian 16 package (Frisch et al., 2016). For the calculation of ground and excited state configurations the hybrid exchange-correlation functional M06-2X has been used, unless stated otherwise (Zhao and Truhlar, 2008). This functional is considered suitable for predicting singlet-triplet gaps (Uoyama et al., 2012; Sun et al., 2015). It also offers the possibility to calculate excited state geometries. The 6-31+G(d) atomic basis set has been chosen as it provides a good balance between accuracy and computational cost (Sun et al., 2015). Furthermore, the Tamm-Dancoff approximation (TDA) has been used for more accurate triplet energies (Hirata and Head-Gordon, 1999; Peach et al., 2011).
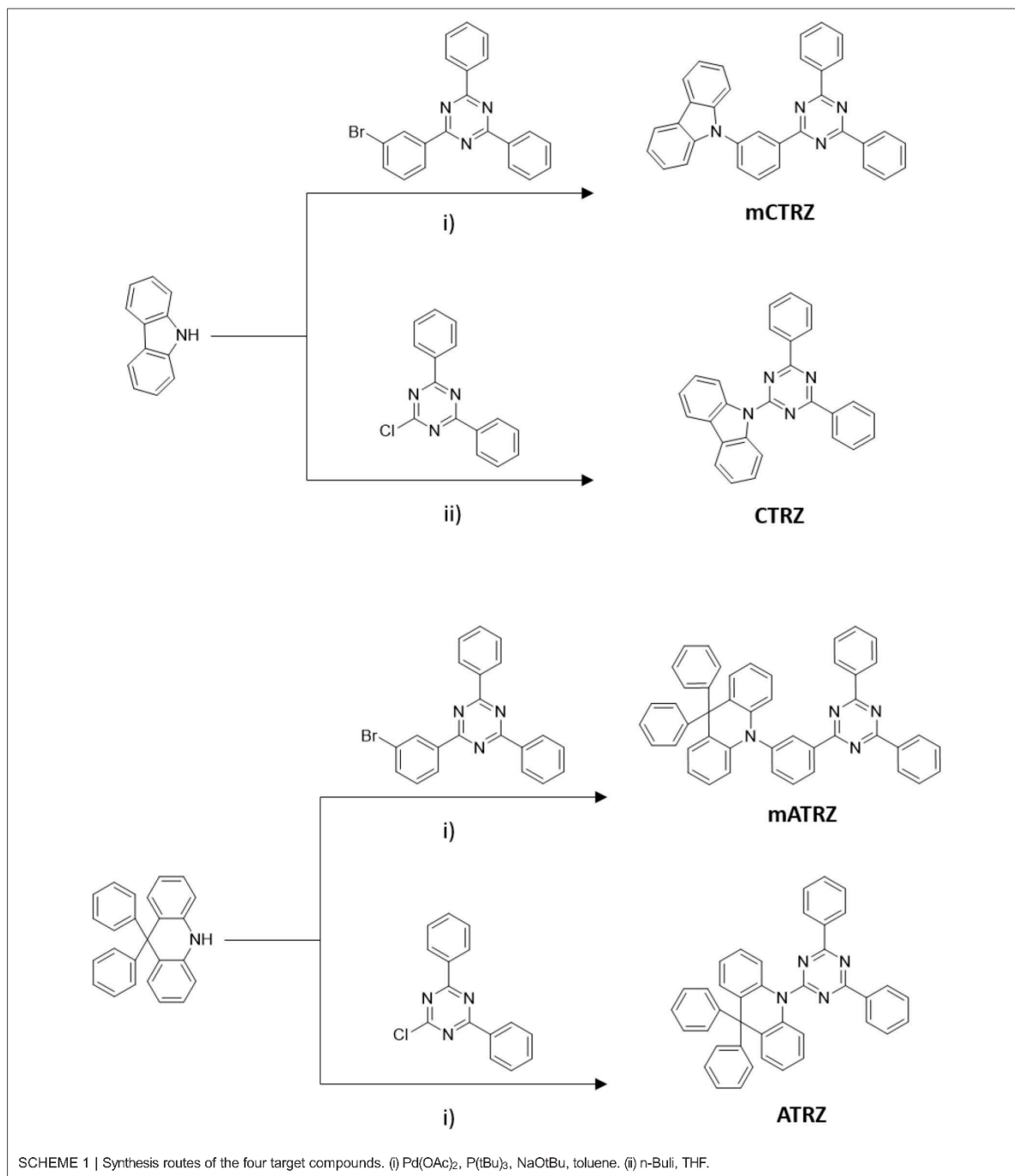
## SYNTHESIS

### The Tool Box Approach
The aim of this work is to obtain new bipolar and high energy triplet host materials suitable for blue TADF emitters and to consolidate a new molecular strategy that allows to increase the triplet energy of bipolar molecules. For this purpose we introduce a systematic study called tool box approach (**Figure 1**). Basically, we choose building blocks (donor, acceptor, and linker) that are known to be stable and to have high triplet energies. Practically, triazine was chosen as acceptor group and carbazole and acridine as donor moieties. These groups were combined both with or without linkers obtaining essentially two classes of donor-acceptor molecules (carbazole-triazine and acridine-triazine). For each class we can distinguish between para-phenyl linker, meta-phenyl linker, and without linker. This approach allows us to understand how varying the linker between donor and acceptor affects the final molecule, and so to understand the structure-property relationship. Furthermore, by studying in parallel two classes of molecules, we can demonstrate that via direct linkage between donor and acceptor it is possible to increase the triplet energy above 3 eV and so to create potential bipolar host materials for TADF blue emitters. The reference molecules **pCTRZ** and **pATRZ** were commercially available. The other four molecules (**mCTRZ**, **mATRZ**, **CTRZ**, and **ATRZ**) were synthesized.

The compounds **mCTRZ**, **mATRZ**, and **ATRZ** were synthesized following a general Buchwald-Hartwig protocol, where the NH group comes from carbazole and acridine derivatives, while the halogenated part is contained in the triazine acceptor (or in the meta-linker-acceptor moiety). The compound **CTRZ** can be obtained via simple nucleophilic aromatic substitution of the carbazole with

SCHEME 1 | Synthesis routes of the four target compounds. (i) Pd(OAc)₂, P(tBu)₃, NaOtBu, toluene. (ii) n-Buli, THF.

the electron poor triazine ring using nBuLi (**Scheme 1**). The compounds were obtained with yields from 30 to 57%. **CTRZ** and **mCTRZ** were purified, respectively, via precipitation and column chromatography in a first step. All the compounds were finally purified through vacuum train sublimation.

59

## 9-(3-(4,6-diphenyl-1,3,5-triazin-2-yl)phenyl)-9H-carbazole
### (mCTRZ)

9H-carbazole (259 mg, 1.55 mmol), 2-(3-bromophenyl)-4,6-diphenyl-1,3,5-triazine (500 mg, 1.29 mmol), sodium tert-butoxide (207 mg, 2.15 mmol), palladium acetate (12 mg, 0.05 mmol) and toluene (10 ml) were added to a three necked flask equipped with a stirring bar. The solution was degassed by three freeze-pump-thaw cycles and the flask backfilled with argon. Tri(tert-butyl)phosphine in toluene (1 mol/l, 0.1 mmol) was subsequently added to the flask and the mixture refluxed 12 h. After cooling to room temperature, ethyl acetate was added and the solution washed with water. The organic phase was dried over sodium sulfate, filtered and the solvent evaporated under reduced pressure. The pure white product was obtained after purification by column chromatography on silica gel (hexane:dichloromethane = 9:1) and by train sublimation (yield 38%). 1H NMR (CDCl$_3$, 500 MHz): $\delta$[ppm] 8.98 (s, 1H), 8.90 (d, J = 7.0 Hz, 2H), 8.76 (d, J = 7.0 Hz, 4H), 8.21 (d, J = 7.5 Hz, 2H), 7.82 (m, 2H), 7.59 (m, 6H), 7.47 (m, 4H), 7.34 (t, J = 7.0 Hz, 2H). 13C NMR (CDCl$_3$, 500 MHz): $\delta$[ppm] 171.9, 171.0, 141.0, 138.5, 138.3, 136.0, 132.7, 131.2, 130.3, 129.0, 128.7, 128.1, 127.7, 126.2, 123.5, 120.4, 120.1, 109.8. EI-MS $m/z$ [M]$^+$: 474.

## 10-(3-(4,6-diphenyl-1,3,5-triazin-2-yl)phenyl)-9,9-diphenyl-9,10-dihydroacridine
### (mATRZ)

The synthesis of **mATRZ** was adapted from Lin et al.[4] A reaction set up similar to that of **mCTRZ** is performed by using 9,9-diphenyl-9,10-dihydroacridine (200 mg, 0.6 mmol), 2-(3-bromophenyl)-4,6-diphenyl-1,3,5-triazine (210 mg, 0.54 mmol), sodium tert-butoxide (68 mg, 0.7 mmol), palladium acetate (5 mg, 0.022 mmol), tri(tert-butyl)phosphine in toluene (1 mol/l, 0.044 mmol) and toluene (20 ml). After refluxing 12 h, the mixture was filtered through a pad of celite while still hot. Then the filtrate was washed with water and brine, then dried over MgSO$_4$ and the solvent evaporated under reduced pressure. The brownish yellow crude product was washed with hexane and dichloromethane and finally purified by train sublimation, obtaining a light yellow solid (yield 30%). 1H NMR (CDCl$_3$, 500 MHz): $\delta$[ppm] 8.90 (d, J = 8.0 Hz 1H), 8.73 (d, J = 7.0 Hz, 4H), 8.50 (s, 1H), 7.76 (t, J = 8 Hz, 1H), 7.60 (m, 6H), 7.31 (m, 7H), 7.07 (m, 6H), 6.92 (m, 4H), 6.52 (d, J = 8.0 Hz, 2H). 13C NMR (CDCl$_3$, 500 MHz): $\delta$ [ppm] 171.8, 170.8, 146.4, 142.1, 141.1, 139.1, 136.0, 135.7, 132.7, 131.9, 130.9, 130.5, 130.0, 129.8, 129.1, 128.8, 128.7, 127.7, 127.0, 126.3, 120.3, 114.1, 56.9. EI-MS $m/z$ [M]$^+$: 640.

## 9-(4,6-diphenyl-1,3,5-triazin-2-yl)-9H-carbazole
### (CTRZ)

**CTRZ** was synthesized according to the procedure reported by An et al. (2011) without using a catalyst. 9H-carbazole (150 mg, 0.9 mmol) and dry tetrahydrofuran (15 ml) were added to a pre-dried three-necked flask under argon atmosphere. The solution was cooled in an ice bath and stirred for 10 min. Then n-butyllithium in hexane (2.5 mol/l, 0.9 mmol) was slowly added and the solution was stirred for 30 min at room temperature.

Subsequently, a solution of 2-chloro-4,6-diphenyl-1,3,5-triazine (200 mg, 0.75 mmol) in tetrahydrofuran (5 ml) was added and the mixture was then refluxed for 12 h. The precipitate was filtered and washed with water, acetone and chlorobenzene. The pure white product was obtained after purification by train sublimation (yield 57%). 1H NMR (CDCl$_3$, 500 MHz): $\delta$[ppm] 9.17 (d, J = 8.5 Hz, 2H), 8.78 (d, J = 6.5 Hz, 4H), 8.10 (d, J = 8.0 Hz, 2H), 7.64 (m, 8H), 7.45 (t, J = 7.0 Hz, 2H). 13C NMR (CDCl$_3$, 500 MHz): $\delta$[ppm] 172.49, 165.26, 139.2, 136.3, 132.8, 129.2, 128.9, 127.0, 126.7, 123.3, 119.7, 117.7. EI-MS $m/z$ [M]$^+$: 398.

## 10-(4,6-diphenyl-1,3,5-triazin-2-yl)-9,9-diphenyl-9,10-dihydroacridine
### (ATRZ)

The synthesis of **ATRZ** was adapted from Lin et al. (2016) 9,9-diphenyl-9,10-dihydroacridine (273 mg, 0.82 mmol), 2-chloro-4,6-diphenyl-1,3,5-triazine (200 mg, 0.75 mmol), sodium tert-butoxide (93 mg, 0.97 mmol), palladium acetate (7 mg, 0.03 mmol) and toluene (20 ml) were added to a three necked flask equipped with a stirring bar. The solution was degassed by three freeze-pump-thaw cycles and the flask backfilled with argon. Tri(tert-butyl)phosphine in hexane (10% wt, 0.018 ml, 0.06 mmol) was subsequently added to the flask and the mixture refluxed 12 h. After cooling to room temperature an extraction with water was performed. The organic phase was dried over sodium sulfate, filtered and the solvent evaporated under reduced pressure. The pure light yellow product was obtained after purification by train sublimation (yield 30%). 1H NMR (CDCl$_3$, 500 MHz): $\delta$[ppm] 8.36 (d, J = 8.0 Hz 4H), 7.98 (d, J = 8.0 Hz, 2H), 7.51 (7, J = 7.0 Hz 2H), 7.45 (t, J = 7.5 Hz, 6H), 7.24 (t, J = 7.5 Hz 2H), 7.03 (m, 8H), 6.88 (m, 4H). 13C NMR (CDCl$_3$, 500 MHz): $\delta$[ppm] 168.5, 162.3, 141.4, 140.8, 137,4, 134.4, 129.6, 129.6, 126.5, 126.1, 126.0, 125.3, 125.2, 124.5, 123.6, 122.8, 56.6. EI-MS $m/z$ [M]$^+$: 564.

Except for **mATRZ** and **ATRZ**, all compounds have already been investigated in some part, either experimentally, or by calculations, or both (An et al., 2011, 2015; Lin et al., 2016; Duan et al., 2018; Arjona-Esteban et al., 2019; Fan et al., 2019; Liu et al., 2019; Sharma et al., 2019). These previous investigations do not form a complete and consistent data set, and sometimes are even contradictory. We therefore decided to perform a systematic spectroscopic and theoretical study that is conducted for all compounds under identical conditions.

## TD-DFT-ANALYSIS
### Choice of Functional

The calculation of excitation energies for donor-acceptor type molecules with charge-transfer characteristic can be a challenge for density functional theory calculations (Sun et al., 2015). In order to obtain results with good accuracy, we therefore first performed a study on the suitable choice of the functional. For this, we employed six popular exchange-correlation functionals on the molecule **CTRZ** which has been well-characterized experimentally in previous works (An et al., 2011; Duan

60

TABLE 1 | Emission energies as well as their difference (in eV) in optimized $S_1$ and $T_1$ geometries for the molecule CTRZ calculated with different exchange-correlation DFT functionals and a 6-31+G(d) basis set.

|            | $S_1$ | $T_1$ | $\Delta(S_1 - T_1)$ |
|------------|-------|-------|---------------------|
| Experiment | 3.21  | 2.97  | 0.24                |
| M06-2X     | 3.18  | 3.00  | 0.18                |
| CAM-B3LYP  | 3.26  | 2.77  | 0.49                |
| M06-HF     | 3.57  | 3.28  | 0.29                |
| PBE0       | 2.29  | 2.31  | −0.02               |
| PW6B95D3   | 2.36  | 2.38  | −0.02               |
| ωB97XD     | 3.51  | 2.85  | 0.66                |

*The experimental value is taken from the spectroscopic analysis in this paper.*

TABLE 2 | Emission energies (in eV) in optimized $S_1$ and $T_1$ geometries calculated at the M06-2X/6-31+G(d) level.

|        | $S_1^a$ exp. (eV) | $T_1^b$ exp. (eV) | $\Delta E_{ST}$, exp. (eV) | $S_1$ (M06-2X) | $T_1$ (M06-2X) | $\Delta E_{ST}$ (eV) |
|--------|-------------------|-------------------|----------------------------|----------------|----------------|----------------------|
| pCTRZ  | 3.22 | 2.76 | 0.46 | 3.48 | 2.69 | 0.79 |
| mCTRZ  | 3.21 | 2.82 | 0.39 | 3.44 | 2.82 | 0.62 |
| CTRZ   | 3.21 | 2.97 | 0.24 | 3.18 | 3.00 | 0.18 |
| pATRZ  | 2.92 | 2.67 | 0.25 | 3.06 | 2.60 | 0.46 |
| mATRZ  | 2.94 | 2.72 | 0.22 | 3.02 | 2.92 | 0.10 |
| ATRZ   | 3.25 | 3.07 | 0.18 | 3.33 | 3.03 | 0.30 |

*For comparison, the experimental values are also given for molecules in toluene at 77 K, as derived below.*
*[a] The energy of the singlet state was determined by fitting the spectral lineshape of the CT absorption and fluorescence, Figure 4 [b] The energy of the triplet state was taken from the 0-0 the position of the phosphorescence at 77 K.*

et al., 2018) as well as in this work. We used two range-separated hybrid functionals, CAM-B3LYP (Yanai et al., 2004) and ωB97XD (Chai and Head-Gordon, 2008), three hybrid meta-GGA functionals, M06-2X (56% exact exchange), M06-HF (100 % exact exchange) (Zhao and Truhlar, 2008) and PW6B95D3(28% exact exchange) (Zhao and Truhlar, 2005) and a meta-GGA functional, PBE0(25% exact exchange) (Adamo and Barone, 1999). **Table 1** compares the calculated $S_1$ and $T_1$ emission energies, in the relaxed excited state geometry, obtained for **CTRZ** with these 6 functionals with the experimentally measured value (see next section). The best match between experiment and calculation for the $S_1$ energy is found for the functional CAM-B3LYP, closely followed by M06-2X. However, for the $T_1$ energy, which is most important to us, M06-2X is closest to the experimental value. We therefore decided to calculate the $S_1$ and $T_1$ excitation energies for all 6 molecules with M06-2X, and, for reference, also with the widely employed functional CAM-B3LYP. **Table 2** compares the resulting energies with the experimental values all taken from the subsequent section "spectroscopic analysis." While all calculated values are in good agreement with the experiment, the excellent match obtained for the triplet energies using M06-2X is noteworthy. Even though this functional is considered suitable for predicting singlet-triplet gaps (Uoyama et al., 2012; Sun et al., 2015), the agreement between calculated values and experimental ones is lessened for the singlet-triplet gap. Results for the functional CAM-B3LYP can be found in the supporting information (**Table S1**).

We next considered how the natural transition orbitals (NTO) obtained with M06-2X for our reference molecule **CTRZ** compare to those obtained by other functionals. The NTOs obtained for the ground state $S_0$ geometry of **CTRZ** for M06-2X are shown in the supporting information (**Figure S2**). The orbitals are in excellent agreement with the ones from Duan et al. (2018) who used the range-separated functional LC-ωPBE. Finally, we calculated and compared the NTOs in the excited state $S_1$ geometry for all 6 functionals (**Figure S3**). Five out of six functionals show a strong charge transfer character for the $S_1$ state and a localized excitation for the $T_1$ state, among them M06-2X, suggesting that this is likely to be the prevailing scenario (as will be confirmed on the basis of the spectroscopic data further below).

## Ground State Geometries and Excited State NTOs

**Figure 2** shows the molecules in the relaxed $S_0$ ground state geometry, alongside the dominant NTOs for the $S_1$ and $T_1$ in the relaxed excited state geometry. It is well-known that the electronic coupling between the donor and acceptor depends strongly on the dihedral angle between them. This angle is indicated in **Figure 2** in green color and detailed in **Table 3**. We find that **pCTRZ** and **mCTRZ** are strongly twisted with practically the same value of about 52°, while **CTRZ** is more planar. Similarly, for the acridine based molecules **pATRZ** and **mATRZ** we observe an almost orthogonal configuration between donor and acceptor moiety while **ATRZ** shows essentially no twist between donor and acceptor though it has a bended shape of acridine core. When going from the ground to the excited states, we find an overall more planar geometry for the $T_1$ state, while the $S_1$ state becomes even slightly more twisted for the carbazole-derivatives. For the **pATRZ** and **mATRZ**, the $S_1$ geometry remains more or less unaltered, and it planarizes for the **ATRZ**.

The NTOs of the molecules in the optimized lowest singlet $S_1$ and triplet $T_1$ excited state geometry deserve some consideration. For all molecules, the calculations predict that the $S_1 \rightarrow S_0$ transition is accompanied by an electron transfer from the acceptor part of molecule to the donor unit, though there is also some overlap of differing degree on the phenyl bridge or triazine ring. This implies a mixed nature of the transition, with a dominant charge transfer (CT) character, in agreement with conclusions published earlier for some of the compounds (An et al., 2011; Lin et al., 2016; Duan et al., 2018; Fan et al., 2019; Liu et al., 2019). The oscillator strengths for this transition is given in **Table 3**. From the para to the meta-connection, the oscillator strength reduces significantly, while there is no further significant reduction when going from **mCTRZ** to **CTRZ** and even a small increase from **mATRZ** to **ATRZ**.

Regarding the triplet $T_1$ state, we find a pronounced difference between the molecules with a p-phenyl or m-phenyl bridge and
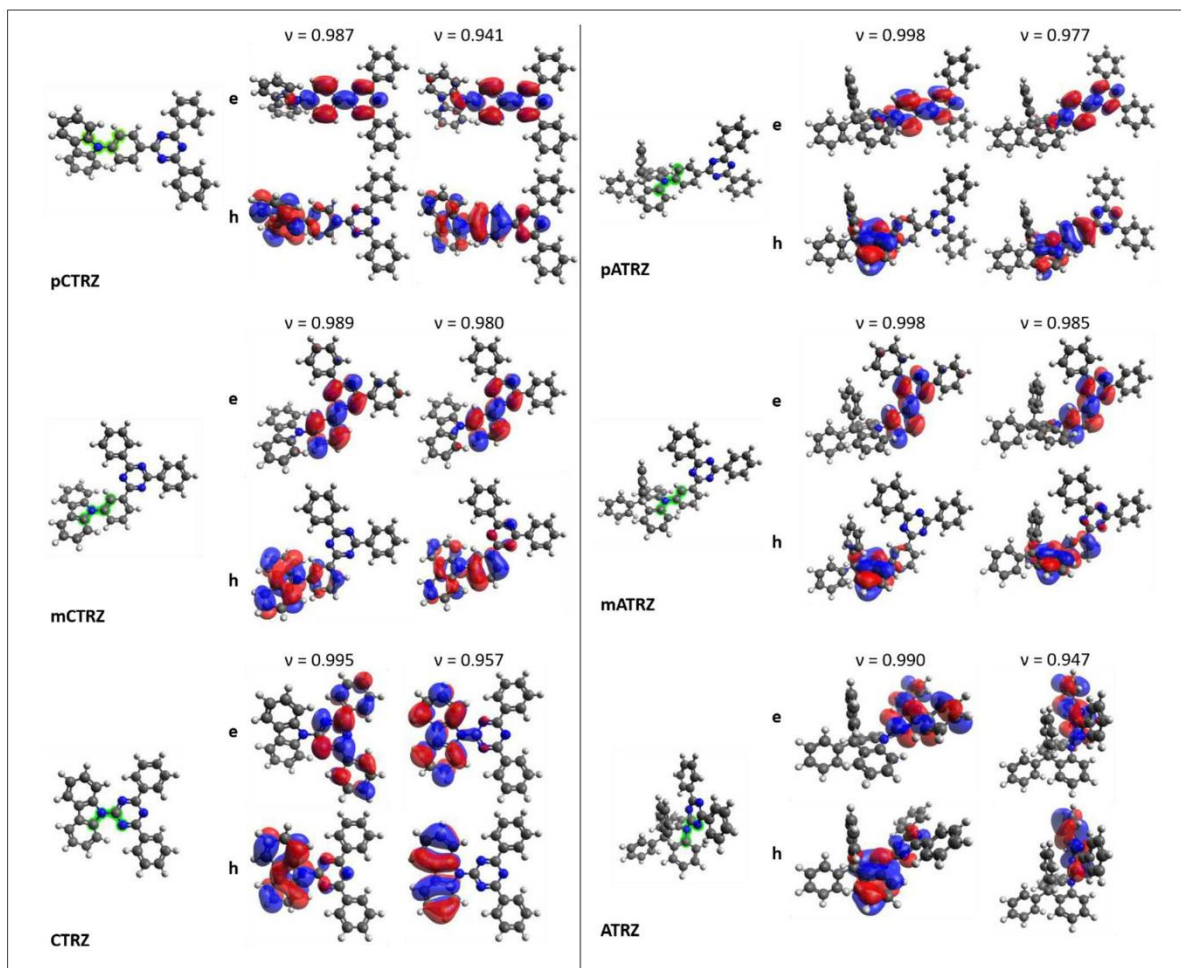
61

FIGURE 2 | Electronic and structural properties of the investigated molecules derived from DFT/TD-DFT calculations at the M06-2X/6-31+G(d) level. Optimized ground state $S_0$ structures of the molecules with the investigated dihedral from Table 1 highlighted in green are shown next to the dominant NTOs of the molecules in relaxed singlet $S_1$ and triplet $T_1$ state structure. Top images represent the electron density e and bottom images the hole density h. The corresponding weight $v$ of the NTO is also given.

the molecules without a linker between donor and acceptor. With the phenyl bridge, and in particular for the $p$-phenyl, the electron and hole orbitals of $T_1$ demonstrate a somewhat stronger overlap than for the $S_1$ state, even though some charge transfer still takes place. In previous works, the character of the $T_1$ state was therefore interpreted either as a CT state with strong overlap of electron and hole orbitals at the triazine, phenyl bridge, and the amino part of the carbazole unit, (Fan et al., 2019) or as a localized excitation (LE) spread over the triazine, phenyl bridge, and carbazole unit (Sun et al., 2015). It was also described as a superposition of the CT state with an LE state in the acceptor (Duan et al., 2018). Our calculations confirm the general

mixed CT-LE character of the $p$-phenyl and $m$-phenyl bridge donor-acceptor compounds, with a stronger LE contribution for T1 than for S1.

In contrast to this, we find a strongly LE character for the $T_1$ state of the molecules without bridge, i.c., **ATRZ** and **CTRZ**, with the excitation fully on the donor for **CTRZ** and fully on the acceptor for **ATRZ**. For **CTRZ**, this differs from the prediction of Duan et al. who predicts a strong contribution from orbitals delocalized over the entire molecule (Duan et al., 2018). We attribute this difference to the fact that Duan et al. based their calculations on the ground state geometry, while we were considering the relaxed $T_1$ excited state geometry. The calculations predict the triplet from this confined LE state to be at

higher energy than the triplet from the molecules with the phenyl ring bridge.

## SPECTROSCOPIC ANALYSIS

## Absorption and Fluorescence in Toluene Solution at Room Temperature

The absorption spectra of our 6 molecules under investigation in toluene at low concentration are shown in **Figure 3**. The spectra are consistent with those published previously (An et al., 2015;

TABLE 3 | Dihedral angles (in degree) between the donor and acceptor unit in the ground and excited state geometry calculated at the M06-2X/6-31+G(d) level.

|  | $S_0$ (°) | $S_1$ (°) | $T_1$ (°) | $f$ | $S_1$ (eV) |
|---|---|---|---|---|---|
| pCTRZ | 52 | 66 | 43 | 0.5872 | 3.91 |
| mCTRZ | 53 | 56 | 40 | 0.0170 | 3.93 |
| CTRZ | 19 | 40 | 13 | 0.0071 | 4.21 |
| pATRZ | 97 | 93 | 55 | 0.0005 | 3.66 |
| mATRZ | 100 | 86 | 62 | 0.0002 | 3.73 |
| ATRZ | 14 | 2 | 10 | 0.0129 | 4.47 |

*In case of asymmetry of the molecule only the smaller dihedral is shown. The oscillator strength f for the $S_0 \rightarrow S_1$ transition is also given, along with the energy for the vertical transition from the relaxed ground state geometry.*

Lin et al., 2016; Fan et al., 2019; Liu et al., 2019). For reference, the spectra of the constituent units, carbazole, diphenyltriazine, and diphenylacridine, are displayed in the supporting information (**Figure S1**).

The absorption of **pCTRZ** is characterized by presence of strong broad band in the range 3.1–4.1 eV with maximum at 3.41 eV, followed by structured features at 3.63 and 3.80 eV. Comparison with the absorption spectrum of carbazole (**Figure S1**) readily identifies the features at 3.63 and 3.80 eV as resulting from a $\pi - \pi$ *transition (and its vibrational replica) localized on the carbazole moiety. When the para-connection is replaced by a meta-linkage, as in **mCTRZ**, the features remain at the same energy yet the extinction of the broad band at 3.41 eV reduces by about one order of magnitude, as is evident from the display on the logarithmic scale (bottom panel of **Figure 3**). This band at 3.41 eV is commonly interpreted as corresponding to CT transition, (Cui et al., 2016b; Fan et al., 2019) though the high absorption for **pCTRZ**, consistent with the high calculated oscillator strength of about 0.6 (see **Table 3**, and of 0.3 by Fan et al., 2019) suggests a strong influence of the $\pi - \pi$ * transitions from the carbazole. This is further supported by the drastic reduction in the extinction coefficient and calculated oscillator strength when reducing the conjugation through the meta-linkage in **mCTRZ**. It is remarkable that the influence of the para- and meta-connection on the CT-dominated absorption
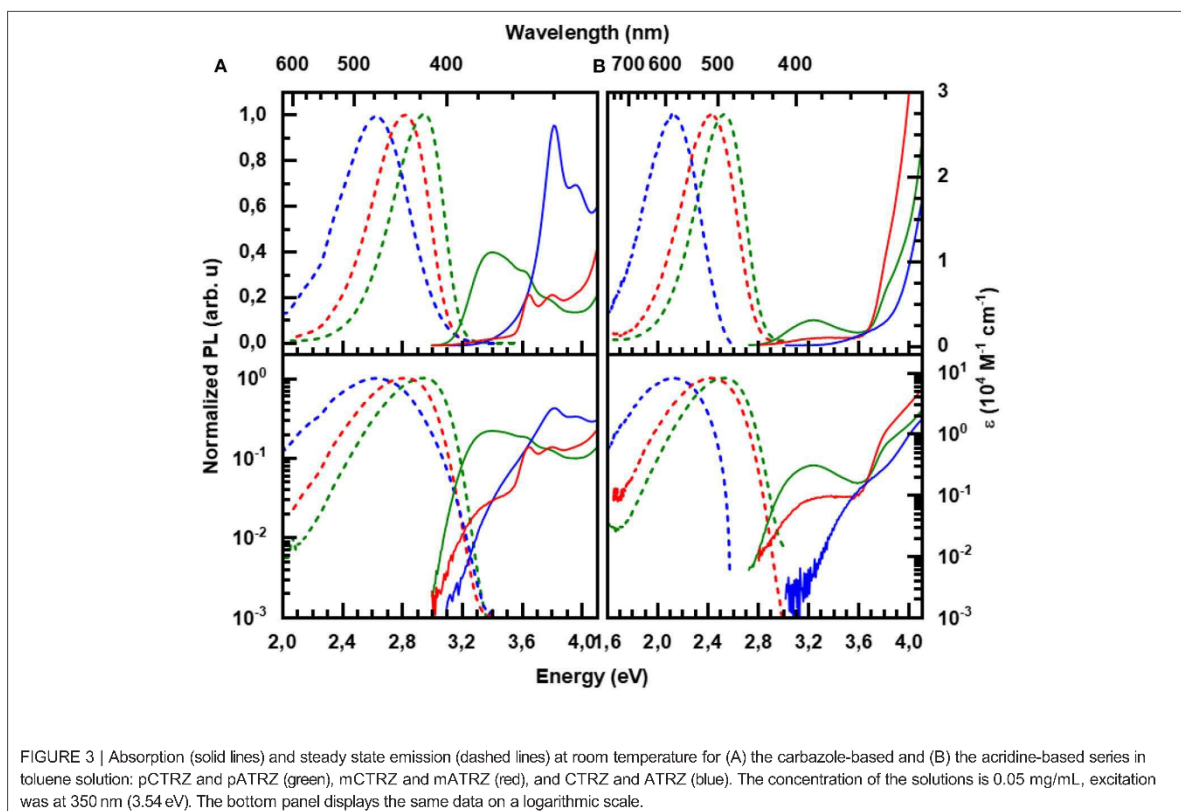


FIGURE 3 | Absorption (solid lines) and steady state emission (dashed lines) at room temperature for (A) the carbazole-based and (B) the acridine-based series in toluene solution: pCTRZ and pATRZ (green), mCTRZ and mATRZ (red), and CTRZ and ATRZ (blue). The concentration of the solutions is 0.05 mg/mL, excitation was at 350 nm (3.54 eV). The bottom panel displays the same data on a logarithmic scale.

band is only reflected in the band's intensity, yet not in the energetic positions of either the CT-dominated band or the $\pi - \pi^*$ transitions from the carbazole. In **CTRZ**, where the phenyl linker is entirely omitted this is different. The direct connection of carbazole to diphenyltriazine shifts the carbazole $\pi - \pi^*$ band to higher energy by about 0.15 eV, and increases its oscillator strength. Compared to carbazole (**Figure S1**), the low energy edge has a pronounced tail. On the logarithmic scale, a superimposed broad transition centered at about 3.5 eV with similar extinction than the CT band in mCTRZ becomes evident, suggesting that the 3.5 eV feature is the CT band in CTRZ. Thus, it is evident that the extinction coefficient of the CT band decreases from **pCTRZ** to **mCTRZ** and **CTRZ**, roughly consistent with the calculated oscillator strengths of 0.587, 0.017, and 0.007, and suggestive of a reduced wavefunction overlap between donor and acceptor in **mCTRZ** and **CTRZ** compared to **pCTRZ**.

The acridine-based series (**Figure 3B**) shows some similarities in their general spectroscopic properties to the carbazole-based series. Like **pCTRZ** and **mCTRZ**, **pATRZ** and **mATRZ** show a broad, weak transition centered at 3.24 eV for both compounds, that reduces in intensity when the para-connection is replaced by a meta-linkage. Based on the broad structureless shape and its low extinction coefficient, we attribute this band to a CT-transition, consistent with the NTOs obtained in the $S_0$ geometry (**Figure S4**). Analogous to **CTRZ**, for **ATRZ**, this CT band is blue shifted by about 0.15 eV and similar in intensity to the CT band in **mATRZ**. The transitions between 3.6 and 4.0 eV can be attributed to the $n - \pi^*$ transitions of the acridine chromophore that dominate over the $n - \pi^*$ transition of triazine by comparison with the absorption of the constituent units (**Figure S1**). Above 4 eV, transitions of the solvent toluene take over. A pronounced difference to the carbazole-based series is the lower extinction of the CT bands. This can be credited to the different geometry of the phenyl-linked molecules in the ground state. As detailed in **Table 3**, for **pCTRZ** and **mCTRZ**, the angle between donor and acceptor is 52 and 53°, while for **pATRZ** and **mATRZ**, it is 97 and 100°, respectively. As a result, the donor and acceptor in these acridine compounds are more decoupled, consistent with the $S_0$ NTOs (**Figure S4**). Conversely, the more planar structure in **ATRZ** thus leads to still sizable oscillator strength and some wavefunction overlap despite the general donor-acceptor nature of this compound (c.f. **Figure S4**).

**Figure 3** presents also the room temperature emission spectra of the compounds in the toluene solution. As detailed in **Table 4**, the emission decays within a few ns for the carbazole-series and within a few tens of ns for the acridine-series, thus identifying it as fluorescence. For both series, the PL QY reduces along the series. When calculating the decay rates the higher radiative rate for the para-connected compounds becomes evident as cause for the relatively high PLQYs, which are more typical for $\pi - \pi^*$ emission than CT emission. This is in agreement with the trends in wavefunction overlap for the relaxed $S_1$ state (c.f. **Figure 2**). The meta-linked compounds and compounds without phenyl connection have similarly low radiative decay rates. However, when the phenyl ring is omitted, the non-radiative decay rate increases. We suggest that in **CTRZ** and **ATRZ** the torsional

TABLE 4 | PL Quantum yield and lifetime for the compounds in x mg/ml toluene at 300 K.

| Compound | QY | τ (ns) | $k_r$, ($10^8$ $s^{-1}$) | $k_{nr}$ ($10^8$ $s^{-1}$) |
| --- | --- | --- | --- | --- |
| pCTRZ | 0.85 | 3.8[a] | 2.40 | 0.40 |
| mCTRZ | 0.15 | 18.6[a] | 0.08 | 0.46 |
| CTRZ | 0.04 | 6.2[a] | 0.06 | 1.56 |
| pATRZ | 0.19 | 13 (99%), 52 (1%)[b] | 0.15 | 0.64 |
| mATRZ | 0.05 | 25 (97%), 90 (3%)[b] | 0.02 | 0.38 |
| ATRZ | 0.03 | 12 (80%), 35 (20%)[b] | 0.02 | 0.81 |

*The radiative and non-radiative decay rates, $k_r$, and $k_{nr}$, are derived as detailed in the experimental section. To avoid any contribution from delayed fluorescence or phosphorescence, the solution was saturated with air.*
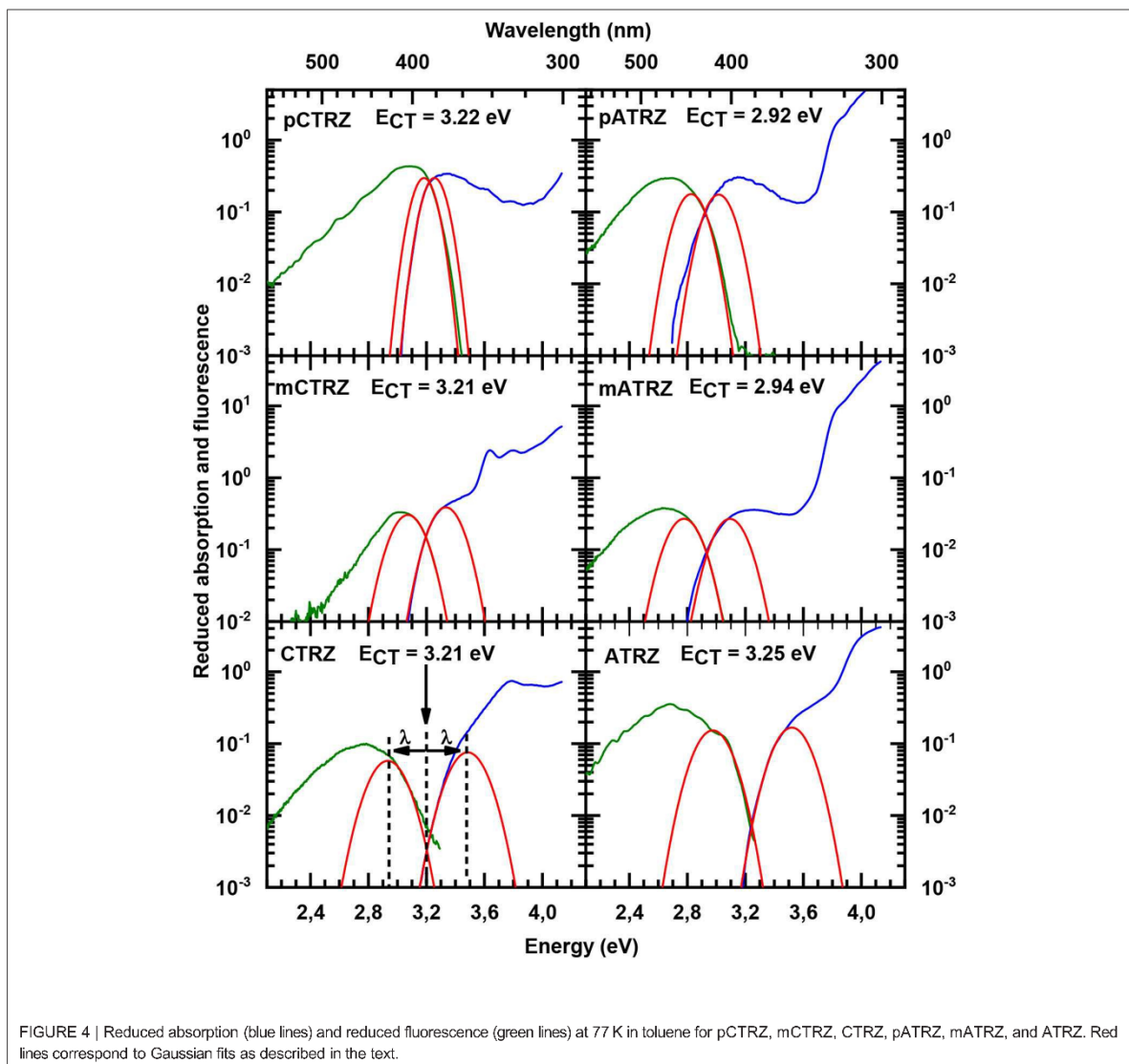[a] *Taken from an exponential fit to the decay curve (Figure S8).*
[b] *Taken from a biexponential fit to the decay curve (Figure S8). The values in bracket give the weight of the two exponential decay.*

modes enhance non-radiative decay routes, notably intersystem crossing (ISC) (Beljonne et al., 2001).

For both series, we find that the peak of the CT absorptions coincides for the compounds with a para or meta-connected phenyl ring, and it is 0.15 eV more blue if the phenyl ring is omitted. In contrast, the fluorescence peaks are distinct for within a series, and the peak energies decrease from para-linked to meta-linked followed by no link. Clearly, for such structureless spectra the determination of excited state energy is a challenge. Using the onset of the fluorescence or absorption spectra is a frequently used approach, but it carries a large uncertainty. A more precise value can be obtained by employing an approach that is common to determine the CT state energy in compounds used for organic solar cell applications, first introduced to the field by Vandewaal and co-workers (Gould et al., 1993; Vandewal, 2016; Kahle et al., 2018; Vandewal et al., 2010, 2017). For this, absorption and emission are plotted as reduced absorption and reduced emission spectra, i.e., the absorption (already displayed in energy intervals) is multiplied by the photon energy, and the emission (also already displayed in energy intervals) is divided by photon energy. The high energy edge of the emission and the low energy edge of the absorption are then fitted with the same gaussian lineshape. The intersection of the two curves indicates the position of the CT state 0-0 transition energy. The energy difference between the intersection and the maxima of the gaussian lineshape gives the reorganization energy associated with the CT state. The presentation of the spectra in this form is shown in **Figure 4**. The values obtained this way are presented in **Table 2**. One can see that such an analysis gives essentially the same CT state energy for all three carbazole-based molecules. They only differ in the value of the associated reorganization energy that increases along the series. Regarding the acridine-based series, the same CT state energy is obtained for **pATRZ** and **mATRZ**. while the **ATRZ** compound has its CT band blue-shifted to them and also shows a significantly larger reorganization energy.

This larger reorganization energy for **CTRZ** and **ATRZ** can be due to intra-molecular reorganization, e.g., associated with the change in torsion angle between the $S_0$ and $S_1$ geometry (**Table 3**) that prevails for CTRZ and ATRZ, and

FIGURE 4 | Reduced absorption (blue lines) and reduced fluorescence (green lines) at 77 K in toluene for pCTRZ, mCTRZ, CTRZ, pATRZ, mATRZ, and ATRZ. Red lines correspond to Gaussian fits as described in the text.

that does not occur to a similar extent in the compounds linked by a phenyl ring. The reorganization energy usually includes both, contributions from changes in the molecular geometry as well as contributions from solvent reorganization. At 77 K, the solvent is frozen, implying that solvent reorganization is very limited. At room temperature it will, however, also include strong contributions from the solvent reorganization that reflect different strength in the CT character of the excited state. The larger reorganization energy for **ATRZ** is therefore likely to involve intra-molecular rearrangements. This can be assessed by considering the fluorescence taken in solvents of different polarity, such as toluene, tetrahydrofurane (THF), and dichloromethane (DCM), which have relative polarities of 0.099, 0.207, and 0.309, respectively (Reichardt, 2002) (**Figure 5**).

We observe a weaker solvent dependence of the fluorescence peaks in **CTRZ** and **ATRZ** compared to the phenyl-bridged compounds. This seems counter-intuitive, as it would suggest a weaker CT-character. At closer inspection, one notices that in the most polar solvent, DCM, where the CT-state can be expected to be most stabilized, the fluorescence of all compounds within a series roughly coincide in their peak position. For less polar solvents, the emission from the meta-linked and even more from the para-linked compounds is blueshifted, implying a reduced stabilization from a lesser CT-character of the excited state. The fact that **CTRZ** and **ATRZ** have a large reorganization energy even in less polar solvent therefore suggests that the dominant contribution to its reorganization is due to the change in molecular geometry such as the
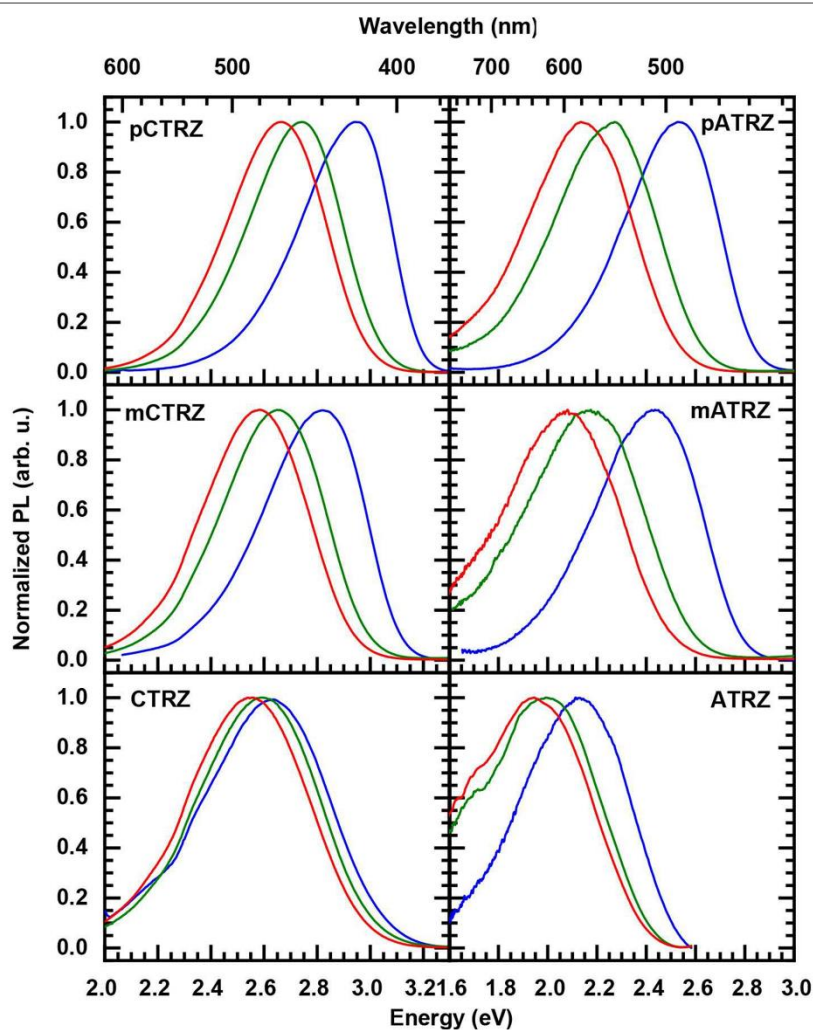
65

FIGURE 5 | Solvent-dependent 300 K steady state emission spectra of pCTRZ and pATRZ, mCTRZ and mATRZ, CTRZ and ATRZ in toluene (blue lines), THF (green lines), and DCM (red lines). Concentration of the solutions is 0.05 mg/mL. Excitation is at 350 (3.54 eV) nm.
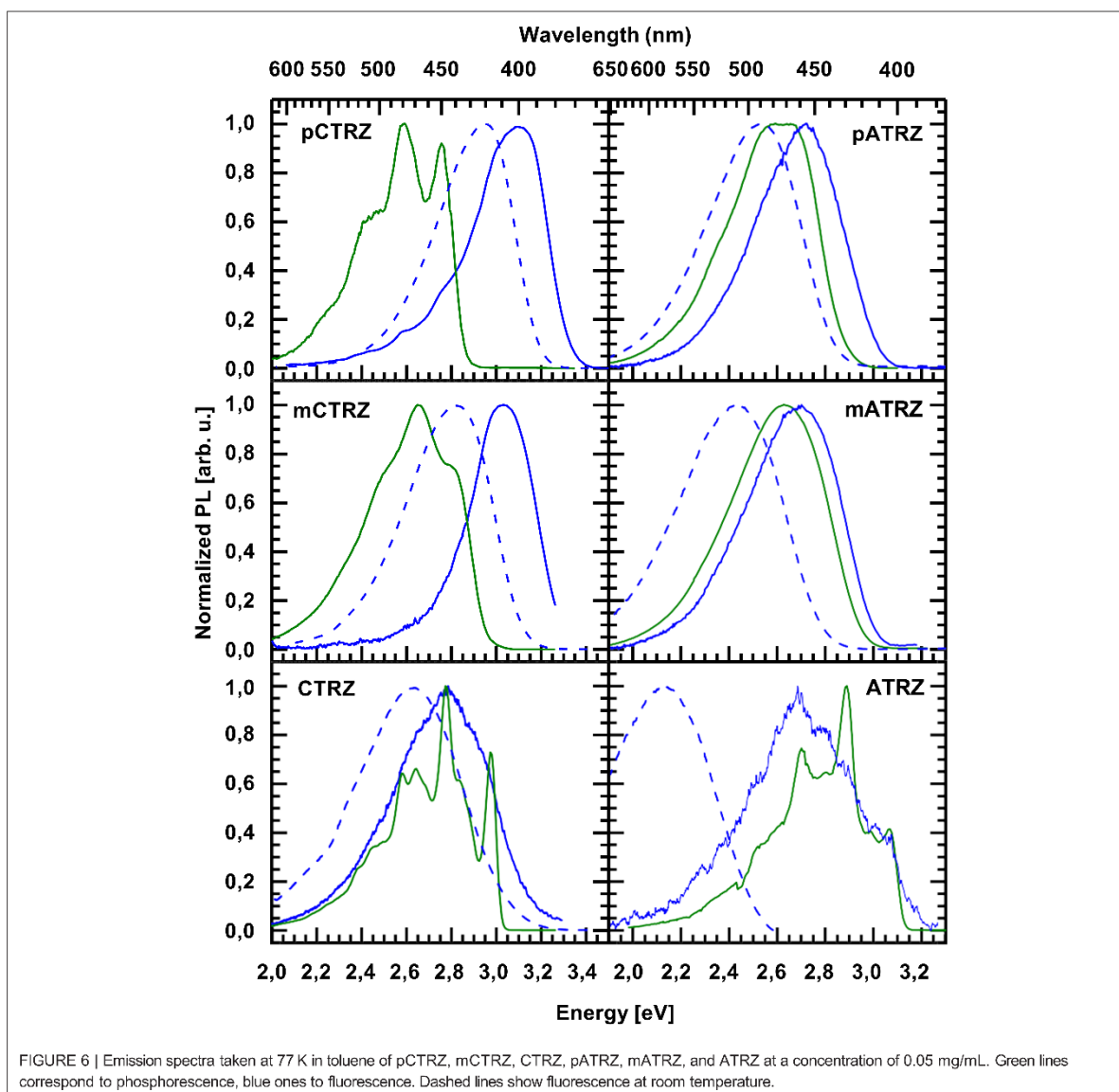
increased dihedral angle predicted by the TD-DFT calculation (**Table 3**). We recall that the TD-DFT calculations are carried out for the gas phase, and that more sophisticated calculations (beyond the scope of this paper) including the effect of solvent polarizability would be required to address this issue in a quantitative manner.

## Fluorescence and Phosphorescence at 77 K

We turn to measurements taken at 77 K, displayed in **Figure 6**. Upon cooling, the fluorescence spectra shift to the blue spectral range. The shifts are 0.15, 0.20, and 0.15 eV along the carbazole-based series, and 0.20, 0.30, and 0.60 eV for

the acridine-based series. We attribute the hypsochromic shift to the freezing out of molecular motion. The solvent shell molecules can no longer reorient after the transition of the molecule to the excited state, thus precluding the stabilization of the CT state. Based on the (gas phase) TD-DFT calculations (**Table 3**) and the polarity dependence observed in **Figure 5** it seems that for **CTRZ** and **ATRZ**, there is also a contribution from the impediment of structural changes of the emitter molecules after excitation, such as changes in the dihedral angle, at 77 K.
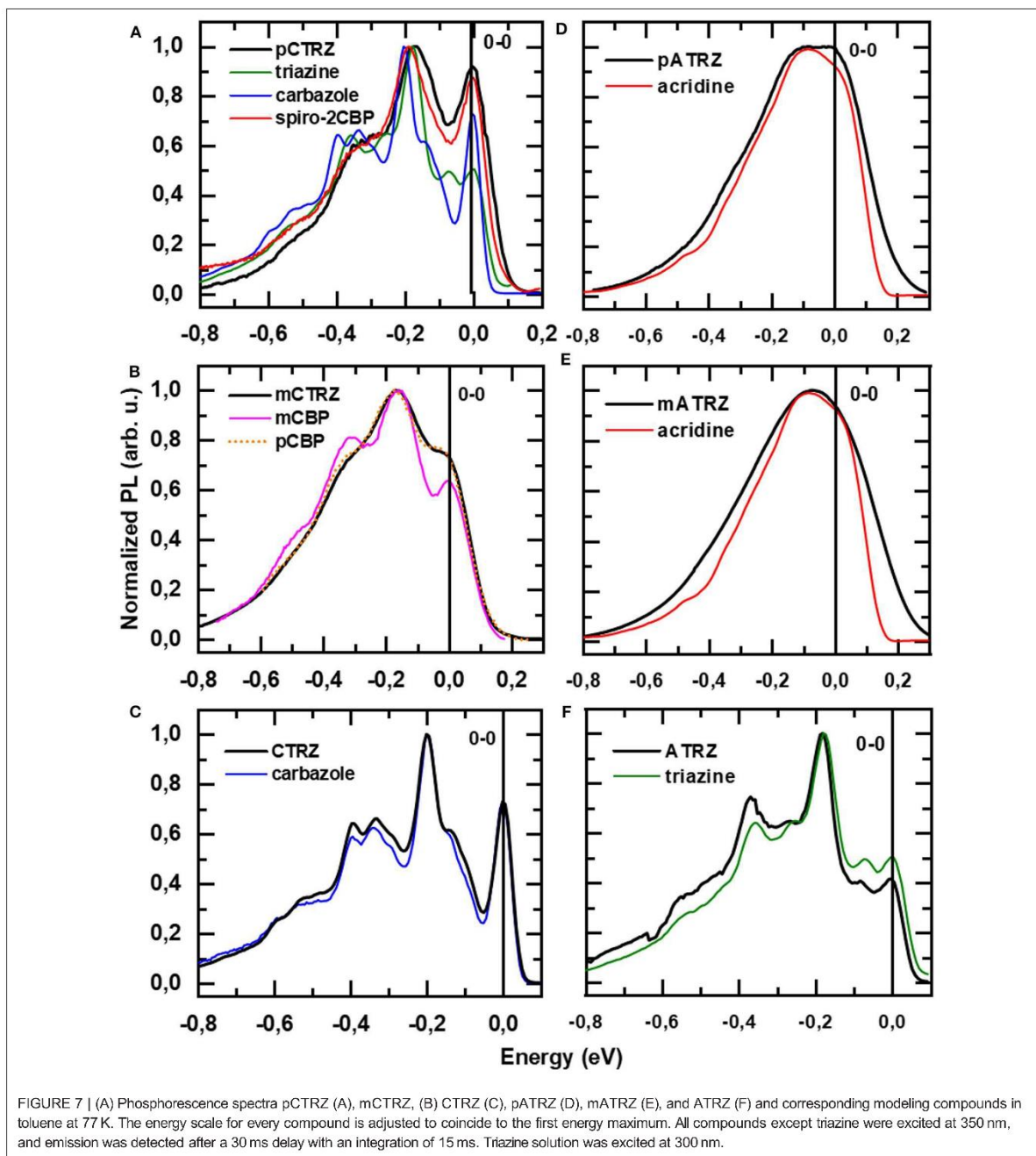
Regarding the phosphorescence, we are interested to experimentally identify not only the $S_1$-$T_1$ gap, but also the part of the molecule from which the transition originates.

FIGURE 6 | Emission spectra taken at 77 K in toluene of pCTRZ, mCTRZ, CTRZ, pATRZ, mATRZ, and ATRZ at a concentration of 0.05 mg/mL. Green lines correspond to phosphorescence, blue ones to fluorescence. Dashed lines show fluorescence at room temperature.

We associate the $T_1$ energy with the position of the 0-0 phosphorescence peak. For the carbazole-based series and for **ATRZ**, these can be clearly identified as 2.76, 2.82, 2.97, and 3.07 eV. For **pATRZ**, the 0-0 peak is just resolvable at 2.67 eV. The spectral resolution is poorer for **mATRZ**. Comparing the spectra of **pATRZ** and **mATRZ** (see **Figure S5**), we find that **mATRZ** is overall shifted to the blue by 0.05 eV, so we estimate the 0-0 position to be at about 2.72 eV. All triplet energies are summarized in **Table 2**.

In order to identify the origin of the $T_1$ state, we compare the vibrational structure of the phosphorescence spectra of our two series with that from their molecular constituents (**Figure 7**).

To ease comparison, all spectra are shifted in energy so that the 0-0 positions coincide at 0 eV. The original spectra are given in the supporting information (**Figure S6**). It is immediately evident that the spectra of **CTRZ** and of **ATRZ** coincide with the spectral form obtained from only a carbazole or triazine. The observation that the vibrational sidebands coincide implies that the transition is localized on the carbazole moiety in the case of **CTRZ** and on the triazine moiety in the case of **ATRZ**. In fact, even the energies of the transitions agree well (**Figure S6**). This spectroscopic result is in excellent agreement with the TD-DFT calculations and, for **CTRZ**, at variance with earlier suggestions that involve transitions delocalized over the entire

67

FIGURE 7 | (A) Phosphorescence spectra pCTRZ (A), mCTRZ, (B) CTRZ (C), pATRZ (D), mATRZ (E), and ATRZ (F) and corresponding modeling compounds in toluene at 77 K. The energy scale for every compound is adjusted to coincide to the first energy maximum. All compounds except triazine were excited at 350 nm, and emission was detected after a 30 ms delay with an integration of 15 ms. Triazine solution was excited at 300 nm.

**CTRZ** molecule (Duan et al., 2018). A different picture results for the compounds that are bridged by a phenyl ring. The vibrational structure in the phosphorescence of **pCTRZ** and **mCTRZ** resembles neither that observed in carbazole nor that of triazine. Rather, it closely resembles the structure obtained for

carbazole-biphenyl derivatives, where the triplet state was found to be localized on the central two phenyl rings (Brinen et al., 1966; Bagnich et al., 2015a,b). Thus, we conclude that the triplet state is dominated by the transition localized on the phenyl bridge and the triazine core, again in very good agreement with the

theoretical predictions. For **pATRZ** and **mATRZ**, the spectra are broad and differ drastically from the phosphorescence spectra of **pCTRZ** and **mCTRZ**. Rather, they are close in shape to spectrum of the donor, 9,9-diphenyl-9,10-di-hydroacridine. Spectra with practically the same shape were observed for other donor-acceptor materials containing acridine (Liu et al., 2015, 2016a,b). It allows to infer that triplet state localization includes also donor molecule, as also implied by the DFT calculations. Overall, we can summarize that for the compounds without bridge, the triplet state is localized strictly on the donor or acceptor moiety, while for the compounds with the phenyl bridge, the orbitals involved in phosphorescence spread from the center of the molecules into adjacent moieties.

We note that within a series the relative intensity of the phosphorescence differs. In the case of **pCTRZ** and **pATRZ**, phosphorescence is so weak that it does not contribute in the low temperature steady-state luminescence (**Figure S7**). For meta-derivatives the steady-state luminescence consists mostly from the phosphorescence, though some fluorescence is still observed as blue shoulder. Finally, only phosphorescence is observed in the steady-state luminescence of **CTRZ** and **ATRZ**. The data presented in **Table 4** allow to understand the different contribution of the phosphorescence. In the case of **pCTRZ** the main channel of the singlet state deactivation is radiative decay with a rate that is 6 times larger than rate of non-radiative decay, that includes internal conversion and ISC. In this case ISC cannot compete with radiative decay of the singlet state that responsible for intensity of fluorescence. Change of carbazole position in the molecule from para to meta or removing of the phenyl bridge lead to a strong (about 30–40 times) decrease of value for radiative decay rate, so that the non-radiative processes, in particular the ISC, dominate. This is particularly strong for **CTRZ**, where the non-radiative rate increases compared to **mCTRZ**. The same trend takes place for acridine based compounds.

## DISCUSSION AND SUMMARY

The aim of our "toolbox approach" was to understand how to maximize the triplet energy in donor-acceptor type bipolar compounds through the choice of connection. We find that the use of a para-phenyl bridge or a meta-phenyl bridge both moves the lowest energy triplet state onto the center of the molecule so that its orbitals expand over more than two rings. This lowers the triplet state energy. This finding is consistent with earlier observations by us made on carbazole-biphenyl type molecules that do not contain any donor-acceptor type interactions, as well as with studies by Brunner and coworkers on carbazole derivatives, who emphasized the strong dependence of the triplet state energy on the number of aromatic rings over which the triplet wavefunction can spread (Brunner et al., 2004; Bagnich et al., 2015a,b). Thus, the lower triplet energy relates predominantly to the structure of the connection that allows for the triplet to spread over more than two rings. Similarly, when the phenyl bridge is omitted, as in **CTRZ** and **ATRZ**, the triplet is strongly localized on the smaller donor or

acceptor unit, and thus has a high triplet energy, characteristic for small molecular units. The highest triplet energy in our series, 3.07 eV for **ATRZ**, is consequently also found for the molecule where the triplet is confined onto the phenyl triazine moiety, as confirmed by the vibrational structure and the TD-DFT calculations (**Figure 2**), see also **Figure S10** for a different projection of **ATRZ**). We note that this is one of the highest triplet energies reported so far for potential OLED bipolar host materials. Our results further suggest that obtaining higher triplet energies would imply localizing the triplet on an even smaller unit.

There are two further points emerging from our study that are worth commenting on. First, we recall the stronger dependence of the fluorescence maximum on solvent polarity that we observed for the phenyl-bridged compounds, even though they have ππ* admixtures in their excited state wavefunction, compared to the non-bridged compounds **CTRZ** and **ATRZ** that have a dominant CT character. Evidently, this implies a caveat that the lack of a strong shift with solvent polarity is not an unambiguous proof for a weak CT character, as it can be masked by effects due to conformational changes.

Second, our study illustrates the difficulty in defining a measure for the excited state energies. When the fluorescence and phosphorescence spectra are well-structured, so that the 0-0 emission peak can be clearly identified, quoting the energy of that peak is a very good approach, if not even the best practice. Difficulties arise if one of the spectra is poorly structured. We determined the S1 energy by spectral fitting as is common for CT states in organic solar cells (Gould et al., 1993; Vandewal et al., 2010, 2017; Vandewal, 2016; Kahle et al., 2018). One alternative is to consider the onset of fluorescence and phosphorescence, identified by extrapolating the slope of the high energy tail. Tacitly, this adds the sum of the linewidth to the transition energy and it bears the danger of misjudging singlet-triplet gaps if the linewidth differs between fluorescence and phosphorescence. If the high-energy edges of the fluorescence and phosphorescence have comparable slopes, implying comparable linewidth, taking the difference between the high-energy edges, e.g., at half maximum, can be an approximation to obtain the energy splitting between the two transitions without too much error (see also, **Table S2**).

In summary, using a tool box approach we synthesized and investigated six bipolar host materials that vary in the way how donor and acceptor are connected. Our detailed photophysical characterization supported by quantum chemical calculations show how this connection controls the excited states and their energies. Only direct connection of the donor group to the triazine core provides a high energy of the triplet state (2.97 eV for **CTRZ** and 3.07 eV for **ATRZ** in toluene), which is of prime importance for the use of the materials as a host for blue TADF emitters.

## DATA AVAILABILITY STATEMENT

The datasets generated for this study are available on request to the corresponding author.

# 4. Publications

## AUTHOR CONTRIBUTIONS

FR conducted the synthesis and characterization of the materials. ED and SB carried out and interpreted the photophysical measurements. TM, SA, and JK were responsible for the DFT calculations. AK and PS supervised the experiments and corrected the manuscript. All authors contributed to the article and approved the submitted version.

## FUNDING

## SUPPLEMENTARY MATERIAL

The Supplementary Material for this article can be found online at: https://www.frontiersin.org/articles/10.3389/fchem.2020.00657/full#supplementary-material

## REFERENCES

Adamo, C., and Barone, V. (1999). Toward reliable density functional methods without adjustable parameters: the PBE0 model. *J. Chem. Phys.* 110, 6158–6170. doi: 10.1063/1.478522

An, Z., Zheng, C., Tao, Y., Chen, R., Shi, H., Chen, T., et al. (2015). Stabilizing triplet excited states for ultralong organic phosphorescence. *Nat. Mater.* 14, 685–690. doi: 10.1038/nmat4259

An, Z.-F., Chen, R.-F., Yin, J., Xie, G.-H., Shi, H.-F., Tsuboi, T., et al. (2011). Conjugated asymmetric donor-substituted 1,3,5-triazines: new host materials for blue phosphorescent organic light-emitting diodes. *Chem. A Eur. J.* 17, 10871–10878. doi: 10.1002/chem.201101118

Arjona-Esteban, A., Szafranowska, B., and Ochsmann, J. (2019). "TADF technology for efficient blue OLEDs: status and challenges from an industrial point of view," in *Luminescence - OLED Technology and Applications*, ed S. Pyshkin (London: IntechOpen), 1–18. doi: 10.5772/intechopen.86534

Bagnich, S. A., Athanasopoulos, S., Rudnick, A., Schroegel, P., Bauer, I., Greenham, N. C., et al. (2015a). Excimer formation by steric twisting in carbazole and triphenylamine-based host materials. *J. Phys. Chem. C* 119, 2380–2387. doi: 10.1021/jp512772j

Bagnich, S. A., Rudnick, A., Schroegel, P., Strohriegl, P., and Köhler, A. (2015b). Triplet energies and excimer formation in meta- and para-linked carbazolebiphenyl matrix materials. *Philos. Trans. R. Soc.* 373, 20140446. doi: 10.1098/rsta.2014.0446

Beljonne, D., Shuai, Z., Pourtois, G., and Bredas, J. L. (2001). Spin–orbit coupling and intersystem crossing in conjugated polymers: a configuration interaction description. *J. Phys. Chem. A* 105, 3899–3907. doi: 10.1021/jp010187w

Brinen, J. S., Koren, J. G., and Hodgson, W. G. (1966). ESR and phosphorescence spectra of the triplet states of phenyls-triazines and phenyl benzenes. *J. Chem. Phys.* 44, 3095–3099. doi: 10.1063/1.1727185

Brunner, K., Dijken, A. V., Börner, H., Bastiaansen, J. J. A. M., Kiggen, N. M. M., and Langeveld, B. M. W. (2004). Carbazole compounds as host materials for triplet emitters in organic light-emitting diodes: tuning the HOMO level without influencing the triplet energy in small molecules. *J. Am. Chem. Soc.* 126, 6035–6042. doi: 10.1021/ja049883a

Cai, X., and Su, S.-J. (2018). Marching toward highly efficient, pure-blue, and stable thermally activated delayed fluorescent organic light-emitting diodes. *Adv. Funct. Mater.* 28:1802558. doi: 10.1002/adfm.201802558

Chai, J.-D., and Head-Gordon, M. (2008). Long-range corrected hybrid density functionals with damped atom–atom dispersion corrections. *Phys. Chem. Chem. Phys.* 10:6615. doi: 10.1039/b810189b

Chatterjee, T., and Wong, K.-T. (2018). Perspective on host materials for thermally activated delayed fluorescence organic light emitting diodes. *Adv. Optical Mater.* 7:1800565. doi: 10.1002/adom.201800565

Chen, W.-C., Lee, C.-S., and Tong, Q.-X. (2015). Blue-emitting organic electrofluorescence materials: progress and prospective. *J. Mater. Chem. C* 3, 10957–10963. doi: 10.1039/C5TC02420J

Cui, L.-S., Kim, J. U., Nomura, H., Nakanotani, H., and Adachi, C. (2016a). Benzimidazobenzothiazole-based bipolar hosts to harvest nearly all of the excitons from blue delayed fluorescence and phosphorescent organic light-emitting diodes. *Angew. Chem.* 128, 6978–6982. doi: 10.1002/ange.201601136

Cui, L.-S., Nomura, H., Geng, Y., Kim, J. U., Nakanotani, H., and Adachi, C. (2016b). Controlling singlet-triplet energy splitting for deep-blue thermally activated delayed fluorescence emitters. *Angew. Chem. Int. Ed.* 56, 1571–1575. doi: 10.1002/anie.201609459

Ding, D., Zhang, Z., Wei, Y., Yan, P., and Xu, H. (2015). Spatially optimized quaternary phosphine oxide host materials for high-efficiency blue phosphorescence and thermally activated delayed fluorescence organic light-emitting diodes. *J. Mater. Chem. C* 3, 11385–11396. doi: 10.1039/C5TC02726H

Duan, Y.-C., Wen, L.-L., Gao, Y., Wu, Y., Zhao, L., Geng, Y., et al. (2018). Fluorescence, phosphorescence, or delayed fluorescence?—A theoretical exploration on the reason why a series of similar organic molecules exhibit different luminescence types. *J. Phys. Chem. C* 122, 23091–23101. doi: 10.1021/acs.jpcc.8b06533

Endo, A., Sato, K., Yoshimura, K., Kai, T., Kawada, A., Miyazaki, H., et al. (2011). Efficient up-conversion of triplet excitons into a singlet state and its application for organic light emitting diodes. *Appl. Phy. Lett.* 98:083302–083302-3. doi: 10.1063/1.3558906

Fan, X., Li, C., Wang, Z., Wei, Y., Duan, C., Han, C., et al. (2019). Enhancing reverse intersystem crossing via secondary acceptors: toward sky-blue fluorescent diodes with 10-fold improved external quantum efficiency. *ACS Appl. Mater. Interfaces* 11, 4185–4192. doi: 10.1021/acsami.8b18041

Frisch, M. J., Trucks, G. W., Schlegel, H. B., Scuseria, G. E., Robb, M. A., Cheeseman, J. R., et al. (2016). *Gaussian 16 Rev. C.01*. Wallingford, CT: Gaussian Inc.

Gould, I. R., Noukakis, D., Gomez-Jahn, L., Young, R. H., Goodman, J. L., and Farid, S. (1993). Radiative and nonradiative electron transfer in contact radical-ion pairs. *Chem. Phys.* 176, 439–456. doi: 10.1016/0301-0104(93)80253-6

Han, C., Zhao, Y., Xu, H., Chen, J., Deng, Z., Ma, D., et al. (2011). A simple phosphine-oxide host with a multi-insulating structure: high triplet energy level for efficient blue electrophosphorescence. *Chem. A Eur.J.* 17, 5800–5803. doi: 10.1002/chem.201100254

Hatakeyama, T., Shiren, K., Nakajima, K., Nomura, S., Nakatsuka, S., Kinoshita, K., et al. (2016). Ultrapure blue thermally activated delayed fluorescence molecules: efficient HOMO-LUMO separation by the multiple resonance effect. *Adv. Mater.* 28, 2777–2781. doi: 10.1002/adma.201505491

Hirata, S., and Head-Gordon, M. (1999). Time-dependent density functional theory within the Tamm–Dancoff approximation. *Chem. Phys. Lett.* 314, 291–299. doi: 10.1016/S0009-2614(99)01149-5

Hirata, S., Sakai, Y., Masui, K., Tanaka, H., Lee, S. Y., Nomura, H., et al. (2014). Highly efficient blue electroluminescence based on thermally activated delayed fluorescence. *Nat. Mater.* 14, 330–336. doi: 10.1038/nmat4154

Kahle, F.-J., Rudnick, A., Bässler, H., and Köhler, A. (2018). How to interpret absorption and fluorescence spectra of charge transfer states in an organic solar cell. *Mater. Horiz.* 5, 837–848. doi: 10.1039/C8MH00564H

Kim, M., Jeon, S. K., Hwang, S.-H., and Lee, J. Y. (2015). Stable blue thermally activated delayed fluorescent organic light-emitting diodes with three times longer lifetime than phosphorescent organic light-emitting diodes. *Adv. Mater.* 27, 2515–2520. doi: 10.1002/adma.201500267

Kukhta, N. A., Matulaitis, T., Volyniuk, D., Ivaniuk, K., Turyk, P., Stakhira, P., et al. (2017). Deep-blue high-efficiency TTA OLED using para- and meta-conjugated cyanotriphenylbenzene and carbazole derivatives as emitter and host. *J. Phys. Chem. Lett.* 8, 6199–6205. doi: 10.1021/acs.jpclett.7b02867

Lin, T.-A., Chatterjee, T., Tsai, W.-L., Lee, W.-K., Wu, M.-J., Jiao, M., et al. (2016). Sky-blue organic light emitting diode with 37% external quantum efficiency using thermally activated delayed fluorescence from spiroacridine-triazine hybrid. *Adv. Mater.* 28, 6976–6983. doi: 10.1002/adma.201601675

Liu, D., Li, D., Meng, H., Wang, Y., and Wu, L. (2019). Multifunctional applications of triazine/carbazole hybrid thermally activated delayed fluorescence emitters in organic light emitting diodes. *J. Mater. Chem. C* 7, 12470–12481. doi: 10.1039/C9TC03808F

Liu, X.-Y., Liang, F., Cui, L.-S., Yuan, X.-D., Jiang, Z.-Q., and Liao, L.-S. (2015). Effective host materials for blue/white organic light-emitting diodes by utilizing the twisted conjugation structure in 10-Phenyl-9,10-dihydroacridine block. *Chem. Asian J.* 10, 1402–1409. doi: 10.1002/asia.201500235

Liu, X.-Y., Liang, F., Ding, L., Li, Q., Jiang, Z.-Q., and Liao, L.-S. (2016b). A new synthesis strategy for acridine derivatives to constructing novel host for phosphorescent organic light-emitting diodes. *Dyes Pigments* 126, 131–137. doi: 10.1016/j.dyepig.2015.11.016

Liu, X.-Y., Liang, F., Yuan, Y., Jiang, Z.-Q., and Liao, L.-S. (2016a). Utilizing 9,10-dihydroacridine and pyrazine-containing donor–acceptor host materials for highly efficient red phosphorescent organic light-emitting diodes. *J. Mater. Chem. C* 4, 7869–7874. doi: 10.1039/C6TC02180H

Nishimoto, T., Yasuda, T., Lee, S. Y., Kondo, R., and Adachi, C. (2014). A six-carbazole-decorated cyclophosphazene as a host with high triplet energy to realize efficient delayed-fluorescence OLEDs. *Mater. Horiz.* 1, 264–269. doi: 10.1039/C3MH00079F

Peach, M. J. G., Williamson, M. J., and Tozer, D. J. (2011). Influence of triplet instabilities in TDDFT. *J. Chem. Theory Comput.* 7, 3578–3585. doi: 10.1021/ct200651r

Reichardt, C. (2002). *Solvents and Solvent Effects in Organic Chemistry.* Weinheim: WILEY-VCH Verlag GmbH & Co. KGaA. doi: 10.1002/3527601791

Ren, X., Li, J., Holmes, R. J., Djurovich, P. I., Forrest, S. R., and Thompson, M. E. (2004). Ultrahigh energy gap hosts in deep blue organic electrophosphorescent devices. *Chem. Mater.* 16, 4743–4747. doi: 10.1021/cm049402m

Sasabe, H., and Kido, J. (2013). Recent progress in phosphorescent organic light-emitting devices. *Eur. J. Organic Chem.* 2013, 7653–7663. doi: 10.1002/ejoc.201300544

Schroegel, P., Langer, N., Schildknecht, C., Wagenblast, G., Lennartz, C., and Strohriegl, P. (2011). Meta-linked CBP-derivatives as host materials for a blue iridium carbene complex. *Organic Electron.* 12, 2047–2055. doi: 10.1016/j.orgel.2011.08.012

Sharma, N., Spuling, E., Mattern, C. M., Li, W., Fuhr, O., Tsuchiya, Y., et al. (2019). Turn on of sky-blue thermally activated delayed fluorescence and circularly polarized luminescence (CPL) via increased torsion by a bulky carbazolophane donor. *Chem. Sci.* 10, 6689–6696. doi: 10.1039/C9SC01821B

Shin, S. K., Han, S. H., and Lee, J. Y. (2018). High triplet energy exciplex host derived from a CN modified carbazole based n-type host for improved efficiency and lifetime in blue phosphorescent organic light-emitting diodes. *J. Mater. Chem. C* 6, 10308–10314. doi: 10.1039/C8TC02918K

Sun, H., Zhong, C., and Brédas, J.-L. (2015). Reliable prediction with tuned range-separated functionals of the singlet–triplet gap in organic emitters for thermally activated delayed fluorescence. *J. Chem. Theory Comput.* 11, 3851–3858. doi: 10.1021/acs.jctc.5b00431

Tomkeviciene, A., Grazulevicius, J. V., Kazlauskas, K., Gruodis, A., Jursenas, S., Ke, T.-H., et al. (2011). Impact of linking topology on the properties of carbazole trimers and dimers. *J. Phys. Chem. C* 115, 4887–4897. doi: 10.1021/jp111333v

Uoyama, H., Goushi, K., Shizu, K., Nomura, H., and Adachi, C. (2012). Highly efficient organic light-emitting diodes from delayed fluorescence. *Nature* 492, 234–238. doi: 10.1038/nature11687

Vandewal, K. (2016). Interfacial charge transfer states in condensed phase systems. *Ann. Rev. Phys. Chem.* 67, 113–133. doi: 10.1146/annurev-physchem-040215-112144

Vandewal, K., Benduhn, J., Schellhammer, K. S., Vangerven, T., Rückert, J. E., Piersimoni, F., et al. (2017). Absorption tails of donor:C60 blends provide insight into thermally activated charge-transfer processes and polaron relaxation. *J. Am. Chem. Soc.* 139, 1699–1704. doi: 10.1021/jacs.6b12857

Vandewal, K., Tvingstedt, K., Gadisa, A., Inganäs, O., and Manca, J. V. (2010). Relating the open-circuit voltage to interface molecular properties of donor:acceptor bulk heterojunction solar cells. *Phys. Rev. B .* 81, 125204-1–125204-8. doi: 10.1103/PhysRevB.81.125204

Wei, Q., Ge, Z., and Voit, B. (2018). Thermally activated delayed fluorescent polymers: structures, properties, and applications in OLED devices. *Macromol. Rapid Commun.* 40:1800570. doi: 10.1002/marc.201800570

Wong, M. Y., and Zysman-Colman, E. (2017). Purely organic thermally activated delayed fluorescence materials for organic light-emitting diodes. *Adv. Mater.* 29:1605444. doi: 10.1002/adma.201605444

Yanai, T., Tew, D. P., and Handy, N. C. (2004). A new hybrid exchange–correlation functional using the Coulomb-attenuating method (CAM-B3LYP). *Chem. Phys. Lett.* 393, 51–57. doi: 10.1016/j.cplett.2004.06.011

Yook, K. S., and Lee, J. Y. (2015). Bipolar host materials for organic light-emitting diodes. *Chem. Rec.* 16, 159–172. doi: 10.1002/tcr.20150 0221

Zhang, J., Ding, D., Wei, Y., Han, F., Xu, H., and Huang, W. (2015). Multiphosphine-oxide hosts for ultralow-voltage-driven true-blue thermally activated delayed fluorescence diodes with external quantum efficiency beyond 20%. *Adv. Mater.* 28, 479–485. doi: 10.1002/adma.201502772

Zhao, Y., and Truhlar, D. G. (2005). Design of density functionals that are broadly accurate for thermochemistry, thermochemical kinetics, and nonbonded interactions. *J. Phys. Chem. A* 109, 5656–5667. doi: 10.1021/jp0 50536c

Zhao, Y., and Truhlar, D. G. (2008). The M06 suite of density functionals for main group thermochemistry, thermochemical kinetics, noncovalent interactions, excited states, and transition elements: two new functionals and systematic testing of four M06-class functionals and 12 other functionals. *Theoret. Chem. Acc.* 120, 215–241. doi: 10.1007/s00214-007-0310-x

Supporting information available (DOI: 10.3389/fchem.2020.00657):
https://www.frontiersin.org/articles/10.3389/fchem.2020.00657/full#supplementary-material

**4.2. Paper 2: Low efficiency roll-off blue TADF OLEDs employing a novel acridine-pyrimidine based high triplet energy host**

Francesco Rodella,[a] Rishabh Saxena,[b] Sergey Bagnich,[b] Dovydas Banevičius,[c] Gediminas Kreiza,[c] Stavros Athanasopoulos,[d] Saulius Juršėnas,[c] Karolis Kazlauskas,[c] Anna Köhler[b,e] and Peter Strohriegl[a,e].

[a] Macromolecular Chemistry I, University of Bayreuth, Bayreuth 95440, Germany.

[b] Soft Matter Optoelectronics, University of Bayreuth, Bayreuth 95440, Germany.

[c] Institute of Photonics and Nanotechnology, Vilnius University, Saulėtekio av. 3, LT-10257 Vilnius, Lithuania.

[d] Departamento de Física, Universidad Carlos III de Madrid, Avenida Universidad 30, 28911 Leganés, Madrid, Spain.

[e] Bayreuth Institute of Macromolecular Research (BIMF), University of Bayreuth, Bayreuth 95440, Germany.

**Abstract**

The development of efficient blue emitter-host combinations is one of the biggest challenges in organic light-emitting diode (OLED) research. Host materials play a crucial role when it comes to enhance efficiency, improve the lifetime and decrease the efficiency roll-off of the device. The need for new hosts is of prime importance, especially for blue phosphorescence and thermally activated delayed fluorescence (TADF) emitters, due to their high exciton energies. The hosts are less investigated than the emitters and require further progress. This work provides a new molecular strategy that combines an acridine derivative (donor) and pyrimidine moieties (acceptors) to obtain three novel host materials. This approach

demonstrates that via careful selection of donor and acceptor units, it is possible to manage the properties of the host materials, obtaining at the same time superior thermal and morphological properties and high triplet energies up to 3.07 eV. The decrease of the conjugation in the acceptor unit was found to play a crucial role in increasing the triplet energy. The most promising host **1MPA** was used to fabricate blue TADF OLEDs. Using a sky-blue emitter, we achieved electroluminescence at 491 nm and maximum external quantum efficiency (EQE) of 13.6%, combined with a low efficiency roll-off, even beyond the practical brightness of 1000 cd/m. The host **1MPA** was also combined with a deep blue emitter to deliver a blue OLED with color coordinates of x=0.16 and y=0.18.

**Introduction**

Presently, organic light-emitting diodes (OLEDs) are expanding their boundaries and applications, such as in flat panel displays and smartphones, due to their significant advantages like facile preparation, cost-effectiveness, and energy efficiency.(*1, 2*) For these reasons, much effort is put into developing this technology, both in academia and industry. Especially for display applications, commercial OLEDs contain stable and efficient green and red emitters based on iridium complexes (*3*). In contrast, blue emitters suffer from lacking simultaneous efficiency and stability.(*4, 5*) In the last years, thermally activated delayed fluorescence (TADF) emitters seem to be among the most promising candidates to solve this problem. Their capacity of harvesting triplet excited states can allow for an internal quantum efficiency of up to 100% through prompt and delayed fluorescence emission. Rapid thermally activated transfer of the excitation from the triplet to the singlet state, followed by efficient delayed fluorescence, avoids degradation processes that could otherwise occur when the excitation prevails for a long time in the triplet state. TADF OLEDs contain purely organic molecules, which avoid rare and costly noble metals and allow a broad range of molecular engineering. Aside from emitters, host materials play an essential role in obtaining the desired performance of the OLED. Emitters are frequently doped in a host matrix to decrease detrimental bimolecular effects caused by longer-lived triplet states.(*6*) The dilution into the host is thus essential to enhance lifetime, increase efficiency, and reduce efficiency roll-off of the device.(*7*) The hosts, in general, must have high and balanced charge carrier mobility, good thermal and morphological stability, and chemical stability. They also must have high triplet

energy to confine the excitons on the emitter, which is particularly challenging for blue-emitting OLEDs.(*8*)

The majority of host materials adopt carbazole or less stable phosphine oxide groups.(*9*) In this work, we present host molecules based on acridine and pyrimidine groups instead. Acridine is often used as a donor (D) in emitter molecules because of its rigidity and strong donating feature.(*10–13*) Few cases report its use in hosts for red phosphorescence OLEDs.(*14, 15*) Furthermore, what brought our attention to the acridine group, is that it has higher triplet energy than carbazole (due to less conjugation).(*16*) The pyrimidine unit is also a building block for TADF emitters due to its acceptor (A) properties.(*17–20*) It is also used as a building block for hosts in phosphorescence OLEDs, with triplet energies of these hosts laying below 3 eV.(*21–23*) Another use of pyrimidine is as an electron transport material (ETM).(*24*)

In this work, we report a strategy to obtain high triplet energy donor-acceptor host materials based on acridine and pyrimidine moieties. In particular, via careful molecular modification, it is possible to limit the conjugation of the acceptor pyrimidine, leading to high triplet energy of more than 3 eV. To prove the strategy's applicability, we fabricated blue TADF OLEDs using the most promising host of the series (**1MPA**), expressing blue emission (from 461 nm to 493 nm) with low efficiency roll-off even beyond a practical brightness of 1000 cd/m$^2$.

**Experimental**

*Materials*

9,9-Diphenyl-9,10-dihydroacridine; 2-chloro-4,6-diphenylpyrimidine; 4,6-Dichloro-2-phenylpyrimidine; 4,6-Dichloro-2-methylpyrimidine; palladium(II) acetate and tri(tert-butyl)phosphine(10 wt.% in hexane) were purchased from abcr. Sodium tert-butoxide was purchased from TCI.

*Synthesis*

10-(4,6-diphenylpyrimidin-2-yl)-9,9-diphenyl-9,10-dihydroacridine (**2PPA**). 9,9-Diphenyl-9,10-dihydroacridine (1 g, 3 mmol, 1.1 eq), 2-chloro-4,6-diphenylpyrimidine (727 mg, 2.73 mmol, 1 eq), sodium tert-butoxide (340 mg, 3.54 mmol, 1.3 eq), palladium(II) acetate (25 mg, 0.11 mmol, 0.04 eq) and toluene (25 ml) were placed with a stirring bar in a Schlenk tube. The

mixture was then degassed three times through freeze-pump thaw cycles and the tube backfilled with argon. Subsequently, tri(tert-butyl)phosphine(10 wt.% in hexane) (0.07 ml, 0.22 mmol, 0.08 eq) was added and the mixture was then refluxed for 12 h. The reaction mixture was extracted with water and the organic phase was dried over anhydrous sodium sulphate before to evaporate the solvent with reduced pressure. Finally, the compound was purified by column chromatography on silica gel (20% ethyl acetate / hexane) and by train sublimation, obtaining 25% yield of pure product. 1H NMR (CDCl$_3$, 500 MHz, Me$_4$Si): δ [ppm] 8.01 (d, J = 7.5 Hz, 2H), 7.92 (d, J = 7.5 Hz, 4H), 7.45-7.42 (m, 7H), 7.39 (t, J = 7.5 Hz, 2H), 7.17 (t, J = 7.5 Hz, 2H), 7.05-6.99 (m, 6H), 6.96 (d, J = 7.0 Hz, 2H), 6.90 (d, J = 6.5 Hz, 4H). 13C NMR (CDCl$_3$, 500 MHz, Me$_4$Si): δ [ppm] 164.21, 160.05, 144.35, 142.55, 140.91, 137.73, 130.63, 130.27, 128.60, 128.04, 127.45, 127.28, 127.04, 126.32, 125.55, 124.07, 104.45, 58.62. EI-MS *m/z* [M]$^+$: 564.

10,10'-(2-phenylpyrimidine-4,6-diyl)bis(9,9-diphenyl-9,10-dihydroacridine) (**1PPA**). **1PPA** was synthesized following a similar procedure as described for **2PPA**; using 9,9-Diphenyl-9,10-dihydroacridine (977 mg, 2.93 mmol, 2.2 eq), 4,6-Dichloro-2-phenylpyrimidine (300 mg, 1.33 mmol, 1 eq), sodium tert-butoxide (320 mg, 3.33 mmol, 2.5 eq), palladium(II) acetate (25 mg, 0.11 mmol, 0.08 eq), tri(tert-butyl)phosphine(10 wt.% in hexane) (0.07 ml, 0.22 mmol, 0.16 eq) and toluene (25 ml). Yield = 28%. 1H NMR (CDCl$_3$, 500 MHz, Me$_4$Si): δ [ppm] 8.27 (m, 2H), 7.44-7.37 (m, 7H), 7.22 (t, J = 7.5 Hz, 4H), 7.16-7.10 (m, 12H), 7.07 (t, J = 7.5 Hz, 4H), 6.89 (d, J = 7.5 Hz, 4H), 6.82 (d, J = 7.5 Hz, 8H), 5.65 (s, 1H). 13C NMR (CDCl$_3$, 500 MHz, Me$_4$Si): δ [ppm] 162.68, 161.44, 144.60, 140.17, 140.15, 138.37, 130.40, 130.15, 128.93, 128.30, 128.17, 127.56, 126.63, 126.09, 123.74, 123.69, 91.1, 58.12. EI-MS *m/z* [M]$^+$: 818.

10,10'-(2-methylpyrimidine-4,6-diyl)bis(9,9-diphenyl-9,10-dihydroacridine) (**1MPA**). **1MPA** was synthesized following a similar procedure as described for **2PPA**; using 9,9-Diphenyl-9,10-dihydroacridine (2.35 g, 7.05 mmol, 2.3 eq), 4,6-Dichloro-2-methylpyrimidine (0.50 g, 3.07 mmol, 1 eq), sodium tert-butoxide (0.77 g, 8.01 mmol, 2.6 eq), palladium(II) acetate (55 mg, 0.25 mmol, 0.08 eq), tri(tert-butyl)phosphine(10 wt.% in hexane) (0.15 ml, 0.49 mmol, 0.16 eq) and toluene (25 ml). Yield = 58%. 1H NMR (CDCl$_3$, 500 MHz, Me$_4$Si): δ [ppm] 7.23 (d, J = 7.5 Hz, 4H), 7.18 (t, J = 7.5 Hz, 4H), 7.14-7-10 (m, 12H), 7.04 (t, J = 7.5 Hz, 4H), 6.87 (d, J = 7.5 Hz, 4H), 6.80 (d, J = 7.5 Hz, 8H), 5.60 (s, 1H), 2.43 (s, 3H). 13C NMR (CDCl$_3$, 500 MHz, Me$_4$Si): δ

[ppm] 144.76, 140.07, 138.81, 130.34, 130.06, 129.01, 127.88, 127.55, 126.60, 126.28, 123.36, 122.31, 94.77, 57.92, 26.17. EI-MS *m/z* [M]$^+$: 756.

*Purification*

The synthesized compounds 2PPA, 1PPA, and 1MPA were purified by train sublimation in a Carbolite split tube furnace HZS 12/450.

*Characterization*

$^1$H NMR and $^{13}$C NMR spectra were recorded on a Bruker Avance III HD (500 MHz), the chemical shifts were referred to chloroform-d3 (7.26 ppm), and the J values are given in Hz. MS spectra were obtained on a Finningan MAT 8500 using electron impact ionization.

*Thermal measurements*

Thermogravimetric analysis (TGA) was conducted on a Mettler TGA/DSC3 with a heating rate of 10 K/min under nitrogen flow. Differential scanning calorimetry was performed with a Mettler DSC3+ in pierced Al pans at 10 K/min under nitrogen flow. The glass transition $T_g$ was determined as the midpoint temperature of the step. $T_m$ and $T_r$ were determined as the peak temperature of the melting peak and recrystallization peak, respectively. These calculations were performed by Mettler STARe 15.00a software.

*Electrochemical measurements*

Cyclic voltammetry measurements were carried out using a standard three electrode electrochemical micro-cell kit from Ametek Scientific Instruments, consisting of a Platinum wire counter electrode, a Platinum disk working electrode, and a Silver/Silver chloride reference electrode. A Gamry Interface 1010T served as the potentiostat. Electrochemistry grade solvent was used, and 100 mM tetrabutylammonium hexafluorophosphate was the supporting electrolyte. The solutions were thoroughly purged with dry nitrogen for 10 minutes before each measurement.

*Computational details*

We have used density functional theory to obtain the ground state geometries of the compounds employing the M06-2X exchange-correlation functional in combination with a 6-31+G(d,p) atomic basis set. Geometry optimizations were successfully converged, and no

imaginary frequencies were observed following a vibrational frequency analysis. Singlet and triplet emission energies were further obtained by optimizing the structures with linear response time-dependent density functional theory at the M06-2X/6-31+G(d,p) level(*25*) and within the Tamm-Dancoff approximation.(*26*) Electron-hole natural transition orbitals (NTOs) were calculated to characterize the excited state transitions.(*27*) All calculations were performed using the Gaussian 16 software package,(*28*) and orbitals were visualized using the Avogadro molecular editor software.(*29*) Charge transfer numbers $\omega_{CT}$ with values in the range between 0 (for a Frenkel exciton) and 1 (for a complete charge transfer exciton) were computed by a transition density matrix analysis,(*30, 31*) based on defragmentation of the molecules in acridine and pyrimidine groups (D-A-D for 1PPA and 1MPA and D-A for 2PPA). Electron-hole correlation plots of the $\Omega$ matrix for the excitations were also constructed based on the fragments. The average electron-hole distance $\Delta r$, based on the charge centroids of the orbitals involved in the transition,(*32*) was also computed as a complementary indicator to the nature of the states using the Multiwfn software.(*33*)

*Photophysical measurements.*

For measurements in solution, all the compounds were dissolved in toluene or mTHF at a concentration of 6-9 x $10^{-5}$M. Solutions were sonicated for 15 minutes after preparation. Absorption spectra were recorded using a Varian Cary 5000 spectrophotometer. Fluorescence spectra, phosphorescence spectra, and room temperature (RT) photoluminescence quantum yield (PLQY) were measured using a Jasco FP-8600 spectrofluorometer. For phosphorescence measurements, the detector unit was opened at a delay of 150 ms after excitation, and the signal was acquired for 50 ms. The excitation wavelength for both fluorescence and phosphorescence was 300 nm (unless specified in the text or figure). For the 77 K measurements, the sample or cuvette was immersed in liquid nitrogen. Values for the photoluminescence quantum yield of the molecules in solution were obtained using the Jasco FP- 8600 spectrofluorometer equipped with an integrating sphere.

*OLED fabrication and characterization.*

OLEDs were fabricated on pre-patterned indium tin oxide (ITO)-coated glass substrates (Kintec) with ITO layer thickness of 100 nm and a sheet resistance of 15-20 $\Omega/\square$. Prior to device fabrication, the substrates were cleaned by sonicating consecutively in detergent (Hellmanex II), distilled water, acetone, isopropyl alcohol, boiling distilled water, and finally treated with

O$_2$-plasma for 10 min. The substrates were then transferred into a vacuum evaporation chamber (Vacuum Systems and Technologies Ltd) integrated inside the nitrogen-filled glove box, where the stack of organic layers was deposited at a rate of 0.5-1 Å/s and pressure <10$^{-6}$ Torr. The doping of the emissive layer was accomplished by co-evaporating the host and guest materials from different evaporation sources at distinct rates for the desired doping concentration. Afterward, the samples were transported by the robotic arm to a metal deposition chamber without breaking the vacuum, which was followed by deposition of lithium fluoride (LiF) and aluminum (Al) layers at a rate of 0.2 and 2 Å /s, respectively. The active area of the devices was 4 mm$^2$ as defined by the ITO pattern and the shadow mask used for cathode deposition. The completed devices were removed from the vacuum chamber to the N$_2$-filled glove box without exposure to air and encapsulated by using a glass cover and UV-curable epoxy KATIOBOND LP655 (DELO). A system consisting of a calibrated integrating sphere (ORB Optronix), a spectrometer PMA-11 (Hamamatsu), and a source-meter unit 2601A (Keithley) was utilized for evaluation of the electrical-optical properties of OLEDs such as current–voltage-luminance (I-V-L) characteristics, EQE and efficiency roll-off.

**Results and Discussion**

*Design and synthesis*

In this work, a strategy to increase the triplet energy of donor-acceptor molecules is shown. For this purpose, three novel host molecules were designed. As presented in previous work,(*34*) by direct connection of donors (acridine and carbazole) and acceptors (triazine), it is possible to increase the triplet energy of donor-acceptor molecules compared to the case where the connection occurs via a conjugated bridge. In this work, acridine (donor) and three different pyrimidines (acceptors) with a different size of the conjugated system of the pyrimidine were chosen to obtain a sequence of three materials. Throughout the series, from **2PPA** to **1PPA,** to **1MPA**, it is possible to see a decrease in the conjugation of the acceptor moiety, a key strategy to reach a high-energy triplet (Figure 1). **2PPA** presents a donor-acceptor structure where the pyrimidine core is linked in positions 4 and 6 to two phenyl rings and position 2 to one acridine. **1PPA** has a donor-acceptor-donor (DAD) structure; i.e., the pyrimidine moiety is linked to just one phenyl ring (in position 2) while two acridines occupy positions 4 and 6. The last molecule of the series, **1MPA**, still has the same DAD configuration,

but the pyrimidine is substituted with a methyl group (in position 2) and two acridines (in positions 4 and 6). By replacing the phenyl ring with a methyl group, the conjugation of the acceptor is limited to the central pyrimidine ring. The products were synthesized using a general Buchwald-Hartwig protocol between the donor acridine and the chlorinated pyrimidine acceptor, which provides an efficient way for the formation of C-N bonds (Figure 1). Furthermore, all products were purified via train sublimation to obtain highly pure compounds.
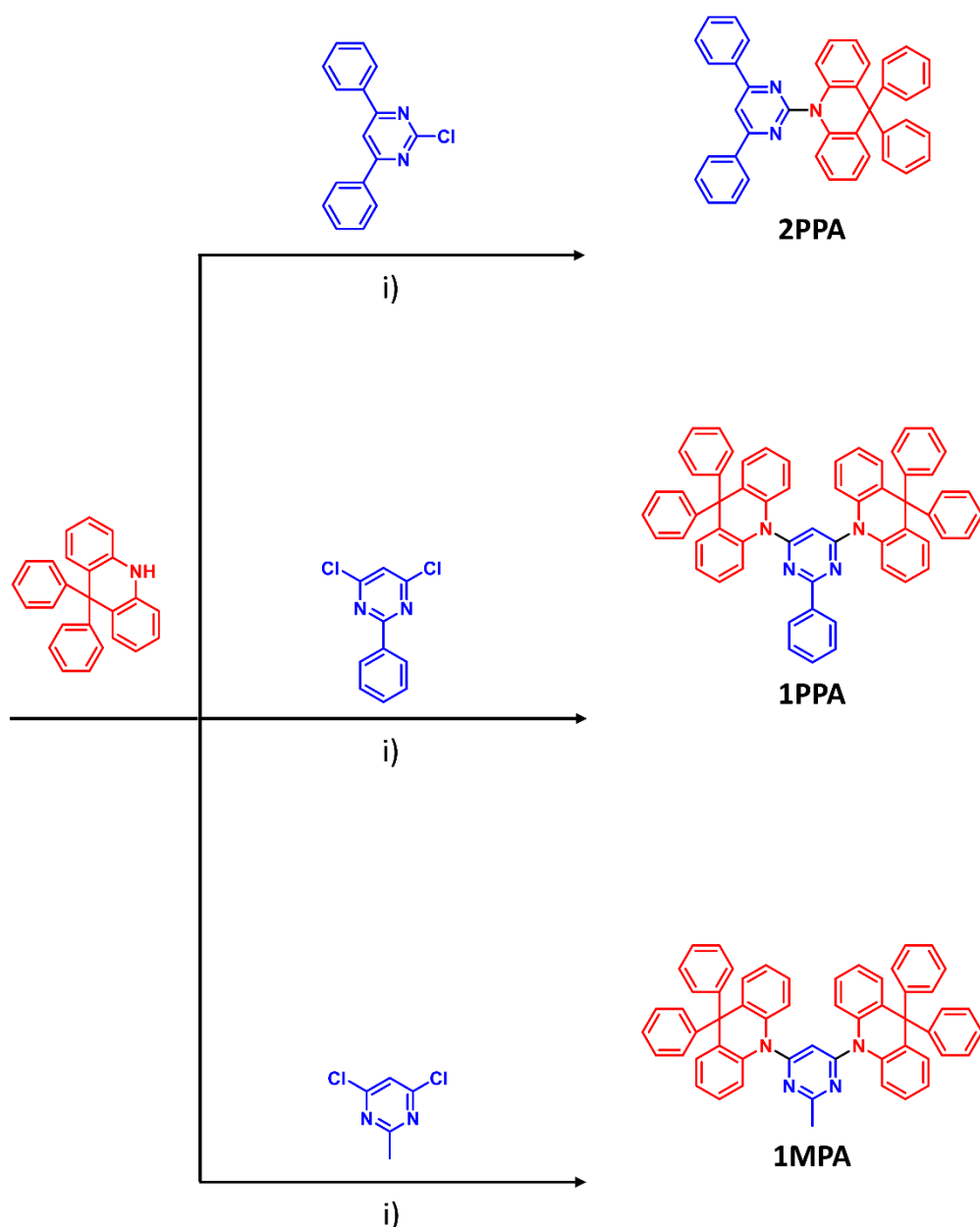


Figure 1: Synthesis route to the three host materials **2PPA**, **1PPA** and **1MPA**. i)  Pd(Oac)$_2$, P(tBu)$_3$, NaOtBu, toluene, reflux, 12 h.

*Thermal and electrochemical analysis*

The thermal properties of the compounds were investigated by differential scanning calorimetry (DSC) and thermogravimetric analysis (TGA), as shown in Figures 2 a and b. DSC shows that all the compounds are morphologically stable beyond 100°C with glass transitions ($T_g$) of 108 °C (**2PPA**), 150 °C (**1PPA**), and 138 °C (**1MPA**) and that recrystallization ($T_r$) upon heating occurs above 100°C for **2PPA** and above 200°C for **1PPA** and **1MPA**, due to the addition of a second bulky acridine. The heating scan of **2PPA** was obtained after the sample was melted and directly cooled with liquid nitrogen. This was necessary to obtain the amorphous material during the cooling process. The melting temperatures ($T_m$) are around 300°C for **2PPA** and **1PPA** and 273°C for **1MPA**.

TGA data show high decomposition temperatures ($T_d$) above 300°C for **2PPA** and above 400°C for **1PPA** and **1MPA**. TGA also indicates that all the materials leave none or only minor residues what means that all three hosts completely evaporate already at normal pressure what makes them ideal candidates for OLED fabrication via evaporation. Furthermore, throughout the series, it is possible to see that by adding a second acridine, the $T_g$, $T_r$, and $T_d$ of the materials are improved. The melting points are instead similar, with a small decrease in **1MPA**. These data confirm the high thermal stability of the materials and their potential applicability as hosts in OLEDs.

Furthermore, cyclic voltammetry of the three hosts was carried out to explore the electrochemical properties and to estimate the HOMO values (Figure 2 c). All the compounds show two quasi-reversible oxidation peaks. The first oxidation peak always appears slightly above 0.2 V vs. Ag/AgCl, and it corresponds to the oxidation of the acridine donor moiety. The HOMO values for the three compounds were estimated by the half-wave potential of the first oxidation potential, considering the solvent correction according to Gräf et al.(*35*) The LUMO values were then calculated by adding the optical band gap to the HOMO values (Table 1).
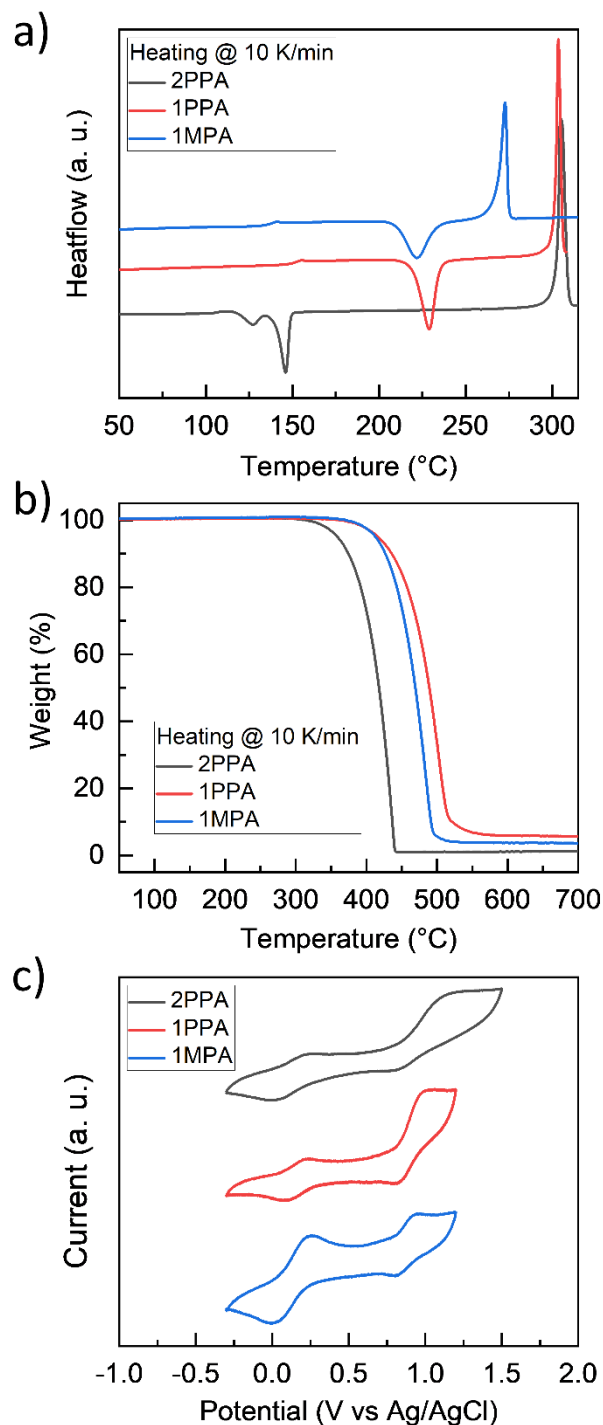
Figure 2: Thermal and electrochemical properties of **2PPA**, **1PPA** and **1MPA.** a) Differential scanning calorimetry showing the second heating scan. b) Thermogravimetric analysis. c) Cyclic voltammograms (cathodic scan) measured in $CH_2Cl_2$ at room temperature with tetra-n-butylammonium hexafluorophosphate (0.1 M) as supporting electrolyte and a scan rate of 100 mV s$^{-1}$.

| | $T_g$ (°C) | $T_r$ (°C) | $T_m$ (°C) | $T_d$ (°C) | HOMO (eV) | LUMO (eV) |
|---|---|---|---|---|---|---|
| **2PPA** | 108 | 127, 147 | 305 | 359 | -5.12 | -2.00 |

| | | | | | | |
|---|---|---|---|---|---|---|
| **1PPA** | 150 | 229 | 304 | 417 | -5.11 | -1.71 |
| **1MPA** | 138 | 222 | 273 | 413 | -5.10 | -1.55 |

Table 1: Glass transition ($T_g$), recrystallization ($T_r$), melting ($T_m$), and decomposition at 5 wt% loss ($T_d$) temperatures determined from differential scanning calorimetry and thermogravimetric analysis. HOMO and LUMO values of **2PPA**, **1PPA**, and **1MPA**, calculated from cyclic voltammetry and the optical bandgap, respectively. Absorption and photoluminescence in solution.

Absorption and photoluminescence studies of **2PPA**, **1PPA**, and **1MPA** were performed in dilute toluene solutions to analyze their intrinsic photophysical properties, with a focus on determining their triplet state energies. Figure 3 a shows the room temperature absorption spectrum of **2PPA**, **1PPA**, and **1MPA**. **2PPA** exhibits a band attributed to CT absorption from around 3.2 - 3.9 eV. This assignment is based on the structureless absorption profile and comparatively low extinction of this particular band. **1PPA** and **1MPA** do not show any pronounced signatures of a CT state absorption. The absorption of **2PPA**, **1PPA**, and **1MPA** differ significantly from the absorption of either donor or acceptor (Figure S1 a, b, and c). This indicates the existence of strong electronic interactions between the donor and acceptor units in these compounds.

In order to estimate the triplet and singlet energies of the host materials, phosphorescence (Ph) and steady-state (SS) measurements were carried out at liquid nitrogen temperature (77 K). For **2PPA** (Figure 3 b), the phosphorescence is structured with a 0-0 vibrational peak at 2.81 eV (442 nm). The steady-state spectrum is a combination of fluorescence and phosphorescence as the spectrum below 2.9 eV matches completely with the phosphorescence spectrum. Thus, the lowest singlet in **2PPA** is a state exhibiting a structureless emission centered around 3 eV, with an onset at 3.15 eV (394 nm), with the lack of vibrational structure probably indicating a CT-character. In **1PPA,** the lowest singlet and triplet states are both structured and have 0-0 peaks at 3.36 eV (369 nm) and 2.76 eV (449 nm), respectively, as shown in Figure 3 c. The phosphorescence of **2PPA** and **1PPA** are similar to the ones of their respective pyrimidine acceptors (Figure S2), indicating that the triplet is localized on the pyrimidine acceptor moieties. Due to the strong emission from the pyrimidine-based singlet state in **1PPA**, we cannot discern whether there is also a CT singlet state at about 3 eV with lower oscillator strength buried under it. When we measured the spectra with different excitation wavelengths between 300 nm and 350 nm, we found them to be independent of excitation wavelength (Figure S3).

The emission of **1MPA**, in contrast, depends on the excitation wavelength, and the corresponding spectra are shown in Figure 3 d. As before, Ph and SS measurements were carried out at 77 K. For excitation at 300nm and 320 nm  (4.13 eV and 3.88 eV, respectively), we obtain a structured phosphorescence band with a 0-0 peak at 3.18 eV. However, when exciting at 335 nm and at 350 nm (3.70 eV and 3.54 eV), the emission band has a similar shape, yet it is shifted to lower energy, and it is broadened with a shoulder at 2.88 eV and an onset at 3.07 eV. To clarify the origin of these two bands, we performed photoluminescence excitation (PLE) spectra, and we also measured the phosphorescence of the acridine donor as well as the methylpyrimidine acceptor. These data are available in the ESI (Figure S4 and S5). For the higher energy phosphorescence, two assignments are principally possible, that is, to a locally excited (LE) state localized either on the acridine donor or on the pyrimidine acceptor. Based on the data in Figure S4 and S5 and the arguments detailed in the ESI, we tentatively assign the higher energy phosphorescence band to a $^3$LE state localized on the acridine donor, and we attribute the lower energy phosphorescence band to a triplet state with mixed CT-LE character, where the LE contribution would be again from the acridine.

The fluorescence in **1MPA** shows the same excitation dependence. For excitation at 300 nm and 320 nm, we observe a broad band centered at about 3.6 eV (Figure 3 e), while for excitation at 335 nm and 350 nm, the fluorescence is centered at 3.0 eV (Figure 3 f). By comparison to the acridine fluorescence spectrum (Figure S4), the band at 3.6 eV is readily assigned to a $^1$LE state localized mainly on the acridine. The band at 3.0 eV, by virtue of its lower energy, must have some significant CT contribution.
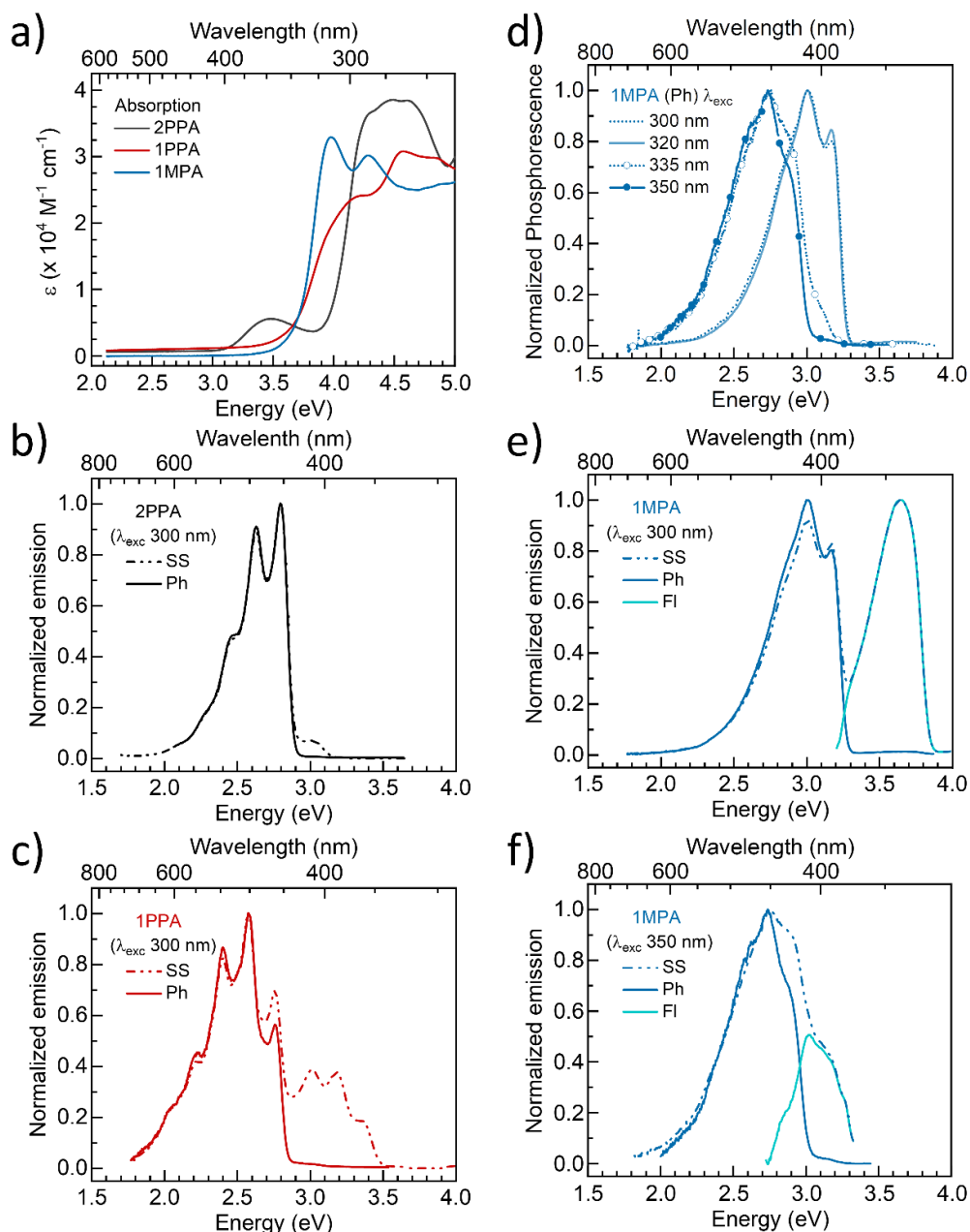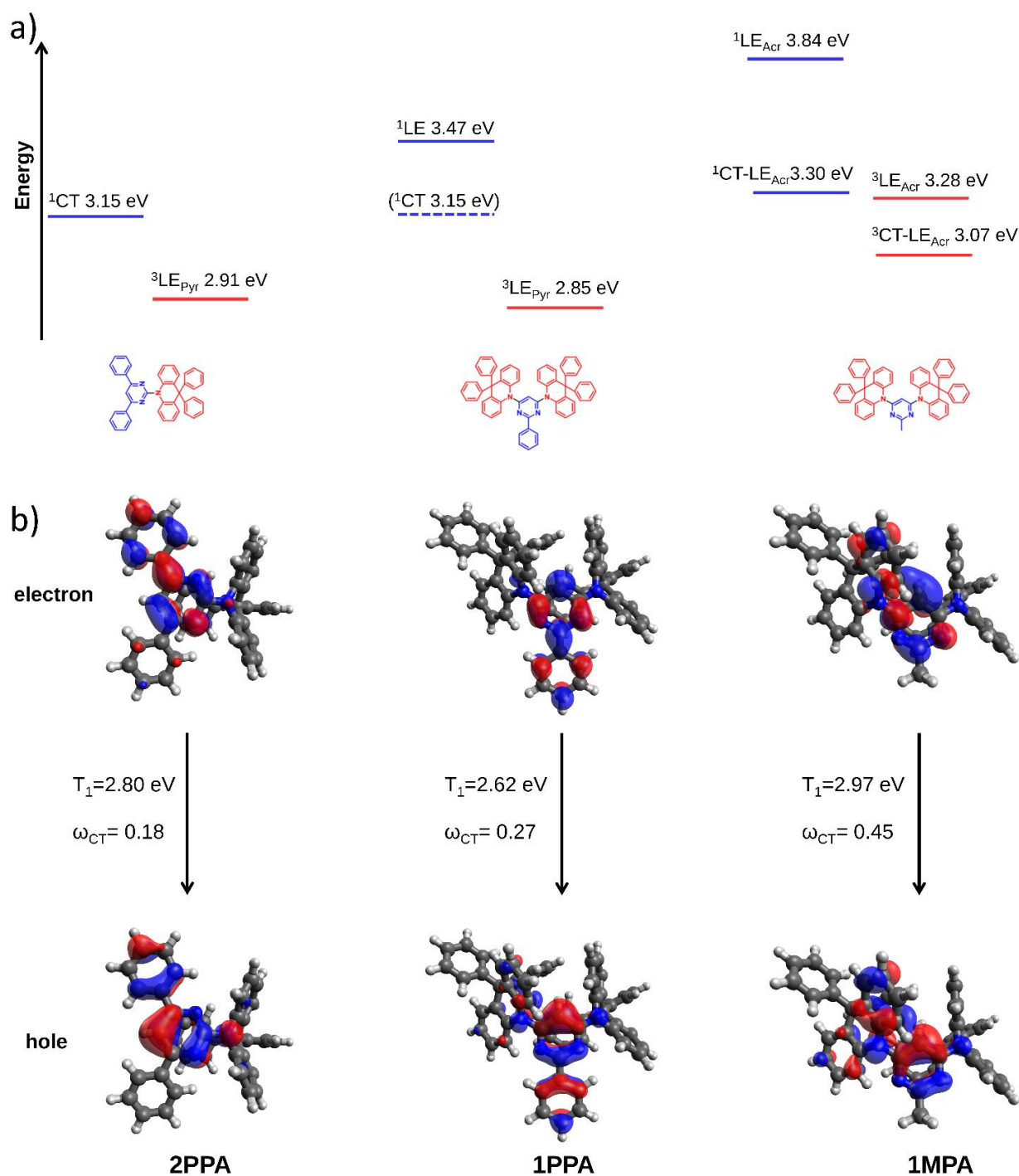
**Figure 3:** a) The absorption spectra of **2PPA**, **1PPA,** and **1MPA** in toluene solution at 300 K. b) The emission spectra of **2PPA** taken at 77 K in a toluene glass under steady-state conditions (SS), so that both fluorescence and phosphorescence show up, and taken with a delay of 150 ms after excitation and a gate width of 50 ms so that only phosphorescence (Ph) is visible. Excitation was at 300 nm. c) The emission spectra were taken under the same conditions for **1PPA.** d) The phosphorescence (Ph) spectra of **1MPA** in toluene glass at 77 K, taken for different excitation wavelengths as indicated. e) Comparison of the Ph and SS spectra for excitation at 300 nm and f) at 350 nm. Also indicated is the fluorescence spectrum obtained from subtracting the Ph from the SS.

Figure 4 a summarizes the insights obtained on the energies and character of the excited states in **2PPA**, **1PPA**, and **1MPA** based on the spectroscopic data. All energy values are taken from the onset of the emission spectra. It exemplifies the impact of reducing the conjugation length of the pyrimidine acceptor. While for 2PPA and 1PPA, the [3]LE state localized on the 2-phenylpyrimidine (2PhPy) and 1-phenylpyrimidine (1PhPy) is the lowest triplet state with an onset at around 2.9 eV, this is no longer the case when the conjugation is reduced in methylpyrimidine (MePy). The triplet state for the units pyrimidine and methylpyrimidine have 0-0 peaks at 3.50 eV and 3.42 eV, respectively (see Nishi et al.(*36*) and Figure S5 b), i.e., well above the onset of phosphorescence for the acridine moiety (Figure S4 and S5 b). As a result, in **1MPA**, the lowest triplet state becomes one with a mixed CT-LE character, where the LE contribution is from the acridine unit. We also comment on the unusual observation of an excitation wavelength-dependent phosphorescence. It implies that when exciting into the acridine-based singlet LE state, the rates of intersystem crossing to its triplet state and phosphorescence can compete with the charge transfer required to form the CT-based singlet or triplet state. Evidently, the twists between the units slow down the charge transfer, which needs to take place through a bond.

a)

Energy

$^{1}LE_{Acr}$ 3.84 eV

$^{1}LE$ 3.47 eV

$^{1}CT$ 3.15 eV

$(^{1}CT$ 3.15 eV)

$^{1}CT\text{-}LE_{Acr}$ 3.30 eV     $^{3}LE_{Acr}$ 3.28 eV

$^{3}CT\text{-}LE_{Acr}$ 3.07 eV

$^{3}LE_{Pyr}$ 2.91 eV

$^{3}LE_{Pyr}$ 2.85 eV

b)

electron

$T_{1}$=2.80 eV

$\omega_{CT}$= 0.18

$T_{1}$=2.62 eV

$\omega_{CT}$= 0.27

$T_{1}$=2.97 eV

$\omega_{CT}$= 0.45

hole

**2PPA**               **1PPA**               **1MPA**

**Figure 4:** a) Excited state energy level diagram for **2PPA**, **1PPA,** and **1MPA**, based on the spectroscopic data, along with their structure (donor in red and acceptor in blue). The values are taken from the onset of the emission spectra. b) TDA-DFT computed natural transition orbitals, emission energies, and charge transfer numbers for the lowest triplet state for **2PPA**, **1PPA,** and **1MPA** at the M06-2X/6-31+G(d,p) level. Pyr represents pyrimidine acceptors and Acr the acridine donor.

*Theoretical calculations*

For a deeper understanding of the excited states, we turn our attention to the electronic structure calculations. We find that for all molecules, acridine units lose planarity, and their central ring adopts a distorted boat conformation both at the ground and excited state geometries. At the same time, there is an intramolecular pi-stacking arrangement between the phenyl ring of one of the acridine donor units and the pyrimidine acceptor moiety (Figure S7). The obtained conformations suggest a strong electronic mixing between the donor and acceptor units, consistent with the observations made in the absorption spectra. The TDA-DFT calculated lowest excited singlet and triplet energies are in very good agreement with the fluorescence and phosphorescence spectroscopic data, respectively, as summarized in Table 2. Calculations support the above spectroscopic assignment on the nature of the emissive triplet states. Figure 4 b illustrates the spatial extent of the hole-electron NTO pairs for the optimized lowest triplet state of 2PPA, 1PPA, and 1MPA, along with the calculated charge transfer numbers $\omega_{CT}$. These transitions can be described by a single NTO pair. The calculated relaxed $T_1$ state for 2PPA and 1PPA has a LE character and is localized on the pyrimidine unit, whereas the relaxed $T_1$ state for 1MPA has a mixed CT-LE character, with the LE part on the acridine. An energy level diagram based on the spectroscopic data is depicted in Figure 4 a. The NTOs for fluorescence can be found in Figure S7. The emissive singlet for 2PPA is localized on the pyrimidine, which is in contrast to the spectroscopic assignment of a CT state. This comes from the fact that the obtained gas-phase geometry from the TDA-DFT calculations leads to a distorted acridine. However, in the solid state, intermolecular interactions might favor pi-pi stacking configurations between the acridine units of the molecules and result in a twisted intramolecular CT state. For 1PPA, the obtained lowest singlet is at 3.41 eV and has a CT character. The lowest singlet state for 1MPA is at 3.13 eV, which displays a strong charge transfer character as depicted by the hole-electron pair natural transition orbitals and the electron-hole correlation plot of the $\Omega$ matrix (Figure S8) and has a weak oscillator strength f=0.0037. Following optimization of the second lowest singlet state, $S_2$, we find that it is located at 3.50 eV and has an oscillator strength f=0.0134 (Figure S7). Although the charge transfer numbers obtained are similar for the two states, the electron-hole distance index $\Delta r$ is larger for the $S_1$ state ($\Delta r$=3.26 Å) than for the $S_2$ state ($\Delta r$=2.07 Å), indicating a larger CT length for the $S_1$ state. The hole NTO for $S_2$ is delocalized across both acridine units. This could explain the experimentally observed excitation wavelength dependent emission described in the previous

section. Given the relatively large energy difference between the $S_2$ and $S_1$ states and the fact that relaxation from the Franck-Condon state requires large conformational rearrangement, vibrational relaxation and internal conversion to $S_1$ might compete with radiative emission from the $S_2$ state leading to non-Kasha emission.([37])

| Compound | $S_1 \rightarrow S_0$ [eV] | Fl | $T_1 \rightarrow S_0$ [eV] | Ph |
|---|---|---|---|---|
| 2PPA | 3.23 | 3.15 | 2.80 | 2.91 |
| 1PPA | 3.41 | 3.47 | 2.62 | 2.85 |
| 1MPA | 3.50 ($S_2 \rightarrow S_0$) | 3.84 | 2.97 | 3.28 |
| | 3.13 ($S_1 \rightarrow S_0$) | 3.30* | | 3.07* |

Table 2: TDA-DFT computed singlet ($S_1 \rightarrow S_0$) and triplet ($T_1 \rightarrow S_0$) emission energies of **2PPA**, **1PPA,** and **1MPA** at the M06-2X/6-31+G(d,p) level along with the energy values of fluorescence (Fl) and phosphorescence (Ph) taken from the onset of the spectra at 77 K in toluene solution for 300 nm excitation. *excitation at 350 nm.

*OLED properties*

After having established that the acridine-pyrimidine based compound **1MPA** is the one with the highest triplet energy (>3.0 eV) among the studied compounds, we employed it as a host for the fabrication of blue OLED. We combined it with the previously reported blue TADF emitters **mPTC**([38]) and **OBA-O**([39]) as dopants (Figure S9 e). In the case of **mPTC**, a doping concentration of 12 wt% was used based on photoluminescence quantum yield measurements (Table S1). For the emitter **OBA-O** we used several doping concentrations (5, 8, and 13 wt%) with a view to examine the emission wavelength tunability of the device. The choice of **mPTC** and **OBA-O** as TADF emitters was based on i) their shallow HOMO levels (-5.12 and -5.15 eV, respectively), which were similar to that of **1MPA**, ii) their triplet energies being lower than that of the host to allow for triplet exciton confinement and iii) their high photoluminescence quantum yields. OLEDs were fabricated using the following simple device architecture: ITO (100 nm)/ TAPC (30 nm)/ EML (x wt% **mPTC** and **OBA-O** in **1MPA**, 30 nm)/ TmPyPB (40 nm)/ LiF (0.8 nm)/ Al (100 nm). Here, ITO was used as a transparent anode, (1,1-bis[(di-4-tolylamino)phenyl]cyclohexane) TAPC and (1,3,5-tri(m-pyridin-3-ylphenyl)benzene) TmPyPB for hole and electron injection/transport, respectively, LiF/Al as the reflective

cathode, whereas x denotes the doping concentration (in weight percentage) of the particular TADF emitter in the emissive layer (EML).

The configuration and the energy level diagram of the device with the EML (12 wt% **mPTC** in **1MPA**) is displayed in Figure 5 a. The main device characteristics are provided in Figures 5 b, c, d and Table 3. The OLED demonstrated a low turn-on voltage ($V_{on}$) of 3.25 V, greenish-blue electroluminescence at 491 nm with the full width at half maximum (FWHM) of 75 nm resulting in Commission Internationale de L'Eclairage (CIE) coordinates of (0.2, 0.4). The maximum external quantum efficiency (EQE$_{max}$) was determined to be 13.6%, which is in good agreement with PLQY of **mPTC** in mCP host (PLQY $\approx$ 55%) (*38*) if typical device outcoupling efficiency of 20-30% is taken into account.(*40*) The fabricated device exhibited low efficiency roll-off at practically useful brightness, i.e., EQE dropped down to 12.3% at the brightness of 100 cd/m$^2$ and to 11.6% at 1000 cd/m$^2$ (Figure 5 b). Notably, EQE remained above 10% up to the very high brightness of 5000 cd/m$^2$. This behavior could be explained by the optimal device architecture and well-balanced electron and hole currents. Further increase of the bias caused degradation of the device performance, most likely due to exciton-polaron annihilation processes as detailed below. Nonetheless, the maximum luminance achieved by the device was nearly 44000 cd/m$^2$. The properties of analogous devices based on the same host, yet the different TADF emitter **OBA-O** at various doping concentrations in the EML, are presented in Figure S9 and Table 3. The **OBA-O** device with a similar doping concentration (13 wt%) as the previous one based on **mPTC** expressed comparable emission properties. Explicitly, peak emission wavelength, bandwidth, CIE color coordinates, and maximum EQE were found to be alike. On the other hand, the much steeper I-V and L-V curves in the **OBA-O** device indicated a significantly improved charge carrier mobility in the EML. Importantly, the reduced **OBA-O** concentration down to 5 wt% in the EML shifted the emission wavelength from greenish-blue (493 nm) to deep-blue (461 nm), demonstrating the potential of **1MPA** to host deep-blue TADF emitters. The picture of the deep-blue emitting OLED is shown in the inset of Figure S9. The reduced emitter concentration concomitantly caused a broadening of emission bandwidth (up to 94 nm) and an accelerated EQE roll-off. We attribute the roll-off at higher luminance and in particular the accelerated roll-off in the **OBA-O** devices at low emitter concentrations predominantly to exciton-polaron annihilation since it reduces with increasing emitter concentration (see Figure S9 b). If the origin of the roll-off was exciton-exciton annihilation, this should increase with emitter concentration. Further, since there is a barrier

of about 1.15 eV for electron injection onto the host yet not for injection onto the guest, the likely scenario is that electron transport proceeds by hopping between emitter molecules while hole transport occurs via the host, where hole injection is barrier-free. This results in a charge carrier imbalance that increases as the emitter concentration decreases, and thus favors exciton-hole quenching. We note that the lifetime of delayed fluorescence in mPTC (6 s) is more than 30 times shorter than that in OBO-A (190-340 s), consistent with its lower susceptibility to exciton quenching processes (Figure S6 and Table S2). Nevertheless, the obtained results show that high-triplet-energy host **1MPA** is suitable for the fabrication of efficient blue TADF OLEDs, delivering low efficiency roll-off even beyond the practical brightness of 1000 cd/m$^2$.
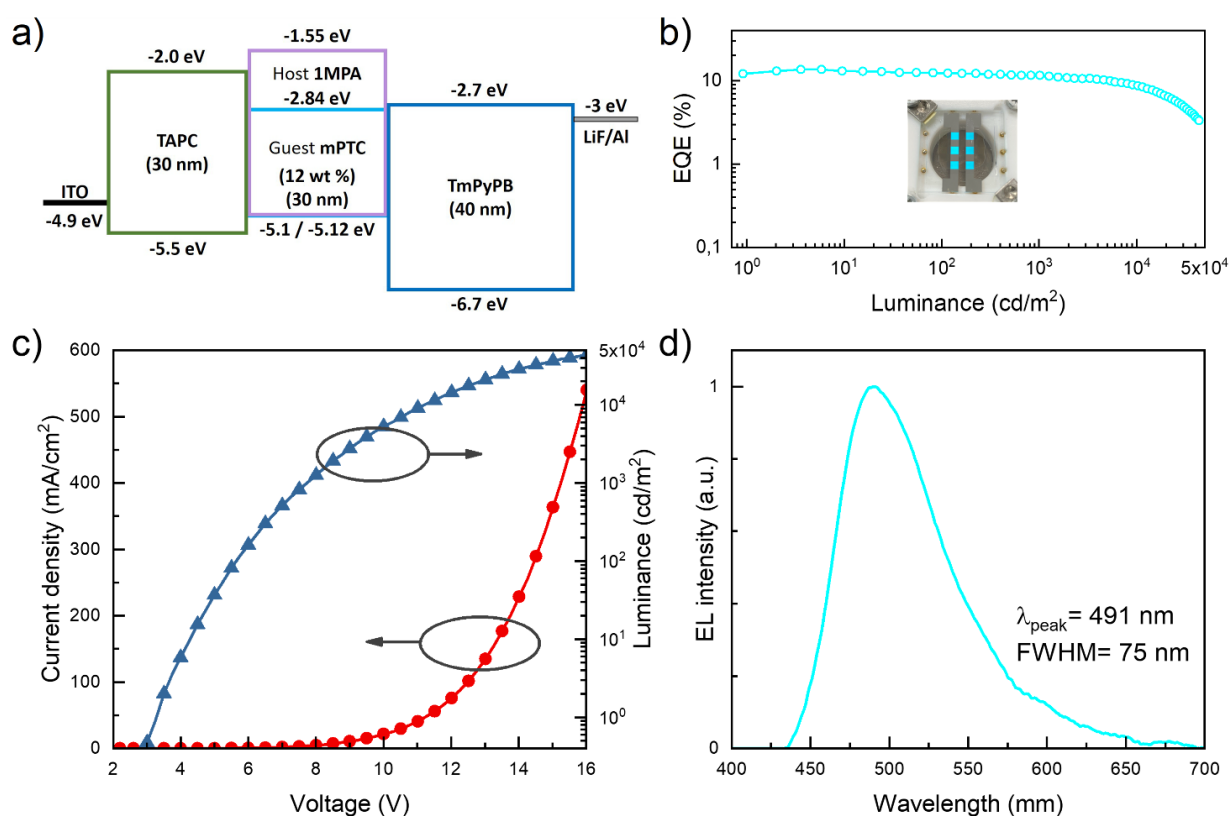
Figure 5. Main properties of the TADF OLED based on **1MPA** host doped with 12 wt% of **mPTC**. a) energy level diagram. b) EQE vs. luminance. c) current density and luminance vs. applied voltage. d) electroluminescence spectrum with working device picture shown in the inset.

| Emitter | $V_{on}$[a] (V) | EQE[b] (%) | $L_{max}$[c] (cd/m$^2$) | $CE_{max}$[d] (cd/A) | $LE_{max}$[e] (lm/W) | $\lambda_{max}$[f] (nm) | FWHM[g] (nm) | CIE 1931[h] (x, y) |
|---|---|---|---|---|---|---|---|---|
| **mPTC** (12 wt%) | 3.25 | 13.6/12.3/11.5 | 43911 | 33.3 | 27.5 | 491 | 75 | (0.2, 0.4) |
| **OBA-O** (13 wt%) | 2.75 | 14.2/11.9/8.9 | 30247 | 36.6 | 36.4 | 493 | 83 | (0.2, 0.38) |
| **OBA-O** (8 wt%) | 3.25 | 14.9/6.8/2.9 | 8449 | 26.2 | 24.5 | 475 | 93 | (0.16, 0.21) |
| **OBA-O** (5 wt%) | 3.5 | 10.6/3.5/1.6 | 5283 | 14.4 | 12.1 | 461 | 94 | (0.16, 0.18) |

Table 3: Main parameters of blue TADF OLEDs based on **1MPA** host doped with **mPTC** and **OBA-O** emitters. [a] Turn-on voltage at 1 cd·m$^{-2}$; [b] maximum EQE/ EQE at 100 cd·m$^{-2}$/ EQE at 1000 cd·m$^{-2}$; [c] maximum brightness; [d] maximum current efficiency; [e] maximum luminous efficiency; [f] peak emission wavelength; [g] full width at half maximum; [h] Commission Internationale de L'Eclairage color coordinates (x, y).

**Conclusions**

In this work, we present three newly synthesized host molecules that adopt acridine and pyrimidine units. The bulky acridine provides superior thermal and morphological properties, further improved when two acridines are used, like in **1PPA** and **1MPA**. The donor and acceptor combination allows transporting both holes and electrons. Throughout the series, it is possible to see a decrease in the conjugation of the acceptor moiety within the hosts. When the acceptor unit is limited to only one pyrimidine ring (**1MPA** host), the triplet energy is the highest, with a value of 3.07 eV. Through theoretical calculations and spectroscopy, we attribute its nature to a mixed CT-LE state. Finally, to demonstrate the potential of these molecules, **1MPA** is employed as the host material to fabricate blue TADF OLEDs. Using the emitter mPTC we achieved a sky-blue OLED with electroluminescence at 491 nm and maximum EQE of 13.6%, combined with a low roll-off. The host **1MPA** is also shown to be suitable for deep-blue emitters like OBA-O, delivering blue OLED with color coordinates of x=0.16 and y=0.18.

References

1.    Wei, Q.; Fei, N.; Islam, A.; Lei, T.; Hong, L.; Peng, R.; Fan, X.; Chen, L.; Gao, P.; Ge, Z. Small-Molecule Emitters with High Quantum Efficiency: Mechanisms, Structures, and Applications in OLED Devices. *Advanced Optical Materials [Online]* **2018,** *6* (20), 1800512.

2.    Wong, M. Y.; Zysman-Colman, E. Purely Organic Thermally Activated Delayed Fluorescence Materials for Organic Light-Emitting Diodes. *Advanced materials (Deerfield Beach, Fla.)* **2017,** *29* (22). DOI: 10.1002/adma.201605444.

3.    Xu, H.; Chen, R.; Sun, Q.; Lai, W.; Su, Q.; Huang, W.; Liu, X. Recent progress in metal-organic complexes for optoelectronic applications. *Chemical Society reviews [Online]* **2014,** *43* (10), 3259–3302.

4.    Zhang, Y.; Lee, J.; Forrest, S. R. Tenfold increase in the lifetime of blue phosphorescent organic light-emitting diodes. *Nature communications [Online]* **2014,** *5*, 5008.

5.    Xu, Z.; Tang, B. Z.; Wang, Y.; Ma, D. Recent advances in high performance blue organic light-emitting diodes based on fluorescence emitters. *J. Mater. Chem. C [Online]* **2020,** *8* (8), 2614–2642.

6.    Yang, Z.; Mao, Z.; Xie, Z.; Zhang, Y.; Liu, S.; Zhao, J.; Xu, J.; Chi, Z.; Aldred, M. P. Recent advances in organic thermally activated delayed fluorescence materials. *Chemical Society reviews [Online]* **2017,** *46* (3), 915–1016.

7.      Wang, Y.; Yun, J. H.; Wang, L.; Lee, J. Y. High Triplet Energy Hosts for Blue Organic Light-Emitting Diodes. *Adv. Funct. Mater. [Online]* **2020**, 2008332.

8.      Godumala, M.; Choi, S.; Cho, M. J.; Choi, D. H. Thermally activated delayed fluorescence blue dopants and hosts: from the design strategy to organic light-emitting diode applications. *J. Mater. Chem. C [Online]* **2016,** *4* (48), 11355–11381.

9.      Chatterjee, T.; Wong, K.-T. Perspective on Host Materials for Thermally Activated Delayed Fluorescence Organic Light Emitting Diodes. *Advanced Optical Materials [Online]* **2019,** *7* (1), 1800565.

10.     Zhang, Q.; Li, B.; Huang, S.; Nomura, H.; Tanaka, H.; Adachi, C. Efficient blue organic light-emitting diodes employing thermally activated delayed fluorescence. *Nature Photon [Online]* **2014,** *8* (4), 326–332.

11.     Lin, T.-A.; Chatterjee, T.; Tsai, W.-L.; Lee, W.-K.; Wu, M.-J.; Jiao, M.; Pan, K.-C.; Yi, C.-L.; Chung, C.-L.; Wong, K.-T.; Wu, C.-C. Sky-Blue Organic Light Emitting Diode with 37% External Quantum Efficiency Using Thermally Activated Delayed Fluorescence from Spiroacridine-Triazine Hybrid. *Advanced materials (Deerfield Beach, Fla.) [Online]* **2016,** *28* (32), 6976–6983.

12.     Serdiuk, I. E.; Ryoo, C. H.; Kozakiewicz, K.; Mońka, M.; Liberek, B.; Park, S. Y. Twisted acceptors in the design of deep-blue TADF emitters: crucial role of excited-state relaxation in the photophysics of methyl-substituted s -triphenyltriazine derivatives. *J. Mater. Chem. C [Online]* **2020,** *8* (18), 6052–6062.

13.     Serevičius, T.; Skaisgiris, R.; Fiodorova, I.; Kreiza, G.; Banevičius, D.; Kazlauskas, K.; Tumkevičius, S.; Juršėnas, S. Single-exponential solid-state delayed fluorescence decay in TADF compounds with minimized conformational disorder. *J. Mater. Chem. C [Online]* **2021,** *9* (3), 836–841.

14.     Liu, X.-Y.; Liang, F.; Yuan, Y.; Cui, L.-S.; Jiang, Z.-Q.; Liao, L.-S. An effective host material with thermally activated delayed fluorescence formed by confined conjugation for red phosphorescent organic light-emitting diodes. *Chemical communications (Cambridge, England) [Online]* **2016,** *52* (52), 8149–8151.

15.     Liu, X.-Y.; Ma, Y.-Y.; Zhang, W.; Song, B.; Ding, L.; Fung, M.-K.; Fan, J. A Novel Linking Strategy of Using 9,10-Dihydroacridine to Construct Efficient Host Materials for Red

Phosphorescent Organic Light-Emitting Diodes. *Chemistry (Weinheim an der Bergstrasse, Germany) [Online]* **2018,** *24* (45), 11755–11762.

16.     Im, Y.; Kim, M.; Cho, Y. J.; Seo, J.-A.; Yook, K. S.; Lee, J. Y. Molecular Design Strategy of Organic Thermally Activated Delayed Fluorescence Emitters. *Chem. Mater. [Online]* **2017,** *29* (5), 1946–1963.

17.     Li, B.; Li, Z.; Hu, T.; Zhang, Y.; Wang, Y.; Yi, Y.; Guo, F.; Zhao, L. Highly efficient blue organic light-emitting diodes from pyrimidine-based thermally activated delayed fluorescence emitters. *J. Mater. Chem. C [Online]* **2018,** *6* (9), 2351–2359.

18.     Wu, K.; Zhang, T.; Zhan, L.; Zhong, C.; Gong, S.; Jiang, N.; Lu, Z.-H.; Yang, C. Optimizing Optoelectronic Properties of Pyrimidine-Based TADF Emitters by Changing the Substituent for Organic Light-Emitting Diodes with External Quantum Efficiency Close to 25 % and Slow Efficiency Roll-Off. *Chemistry (Weinheim an der Bergstrasse, Germany) [Online]* **2016,** *22* (31), 10860–10866.

19.     Park, I. S.; Lee, J.; Yasuda, T. High-performance blue organic light-emitting diodes with 20% external electroluminescence quantum efficiency based on pyrimidine-containing thermally activated delayed fluorescence emitters. *J. Mater. Chem. C [Online]* **2016,** *4* (34), 7911–7916.

20.     Park, H.-J.; Han, S. H.; Lee, J. Y. Molecular Design of Thermally Activated Delayed-Fluorescent Emitters Using 2,2'-Bipyrimidine as the Acceptor in Donor-Acceptor Structures. *Chemistry, an Asian journal [Online]* **2017,** *12* (18), 2494–2500.

21.     Son, K. S.; Yahiro, M.; Imai, T., Yoshizaki, H.; Adachi, C. Blue organic electrophosphorescence diodes using diarylamino-substituted heterocyclic compounds as host material. *J. Photopolym. Sci. Technol. [Online]* **2007,** No. 20, 47–51.

22.     Su, S.-J.; Cai, C.; Kido, J. RGB Phosphorescent Organic Light-Emitting Diodes by Using Host Materials with Heterocyclic Cores: Effect of Nitrogen Atom Orientations. *Chem. Mater. [Online]* **2011,** *23* (2), 274–284.

23.     Su, S.-J.; Cai, C.; Kido, J. Three-carbazole-armed host materials with various cores for RGB phosphorescent organic light-emitting diodes. *J. Mater. Chem. [Online]* **2012,** *22* (8), 3447.

24.     Komatsu, R.; Sasabe, H.; Kido, J. Recent progress of pyrimidine derivatives for high-performance organic light-emitting devices. *J. Photon. Energy [Online]* **2018,** *8* (03), 1.

25.     Zhao, Y.; Truhlar, D. G. The M06 suite of density functionals for main group thermochemistry, thermochemical kinetics, noncovalent interactions, excited states, and transition elements: two new functionals and systematic testing of four M06-class functionals and 12 other functionals. *Theor Chem Account [Online]* **2008,** *120* (1-3), 215–241.

26.     Hirata, S.; Head-Gordon, M. Time-dependent density functional theory within theTamm–Dancoff approximation. *Chemical Physics Letter [Online]* **1999,** No. 314, 291–299.

27.     Martin, R. L. Natural transition orbitals. *The Journal of Chemical Physics [Online]* **2003,** *118* (11), 4775–4777.

28.     Frisch, M. J.; Trucks, G. W.; Schlegel, H. B.; Scuseria, G. E.; Robb, M. A.; Cheeseman, J. R.; Scalmani, G.; Barone, V.; Petersson, G. A.; Nakatsuji, H.; Li, X.; Caricato, M.; Marenich, A. V.; Bloino, J.; Janesko, B. G.; Gomperts, R.; Mennucci, B.; Hratchian, H. P.; Ortiz, J. V.; Izmaylov, A. F.; Sonnenberg, J. L.; Williams-Young, D.; Ding, F.; Lipparini, F.; Egidi, F.; Goings, J.; Peng, B.; Petrone, A.; Henderson, T.; Ranasinghe, D.; Zakrzewski, V. G.; Gao, J.; Rega, N.; Zheng, G.; Liang, W.; Hada, M.; Ehara, M.; Toyota, K.; Fukuda, R.; Hasegawa, J.; Ishida, M.; Nakajima, T.; Honda, Y.; Kitao, O.; Nakai, H.; Vreven, T.; Throssell, K.; Montgomery, J. A., Jr.; Peralta, J. E.; Ogliaro, F.; Bearpark, M. J.; Heyd, J. J.; Brothers, E. N.; Kudin, K. N.; Staroverov, V. N.; Keith, T. A.; Kobayashi, R.; Normand, J.; Raghavachari, K.; Rendell, A. P.; Burant, J. C.; Iyengar, S. S.; Tomasi, J.; Cossi, M.; Millam, J. M.; Klene, M.; Adamo, C.; Cammi, R.; Ochterski, J. W.; Martin, R. L.; Morokuma, K.; Farkas, O.; Foresman, J. B.; Fox, D. J. G. Gaussian 16, Revision C.01. *Gaussian Inc. Wallingford CT*.

29.     Hanwell, M. D.; Curtis, D. E.; Lonie, D. C.; Vandermeersch, T.; Zurek, E.; Hutchison, G. R. Avogadro: an advanced semantic chemical editor, visualization, and analysis platform. *Journal of cheminformatics [Online]* **2012,** *4* (1), 17.

30.     Plasser, F. TheoDORE: A toolbox for a detailed and automated analysis of electronic excited state computations. *The Journal of Chemical Physics [Online]* **2020,** *152* (8), 84108.

31.     Plasser, F.; Lischka, H. Analysis of Excitonic and Charge Transfer Interactions from Quantum Chemical Calculations. *Journal of chemical theory and computation [Online]* **2012,** *8* (8), 2777–2789.

32.    Guido, C. A.; Cortona, P.; Mennucci, B.; Adamo, C. On the Metric of Charge Transfer Molecular Excitations: A Simple Chemical Descriptor. *Journal of chemical theory and computation [Online]* **2013,** *9* (7), 3118–3126.

33.    Lu, T.; Chen, F. Multiwfn: a multifunctional wavefunction analyzer. *Journal of computational chemistry [Online]* **2012,** *33* (5), 580–592.

34.    Rodella, F.; Bagnich, S.; Duda, E.; Meier, T.; Kahle, J.; Athanasopoulos, S.; Köhler, A.; Strohriegl, P. High Triplet Energy Host Materials for Blue TADF OLEDs-A Tool Box Approach. *Frontiers in chemistry [Online]* **2020,** *8*, 657.

35.    Gräf, K.; Rahim, M. A.; Das, S.; Thelakkat, M. Complementary co-sensitization of an aggregating squaraine dye in solid-state dye-sensitized solar cells. *Dyes and Pigments [Online]* **2013,** *99* (3), 1101–1106.

36.    Nishi N, Shimada R, Kanda Y. The Phosphorescence Processes in Pyrimidine and 2-Chloropymidine. *Bulletin of the Chemical Society of Japan [Online]* **1970,** No. 43, 41–46.

37.    Demchenko, A. P.; Tomin, V. I.; Chou, P.-T. Breaking the Kasha Rule for More Efficient Photochemistry. *Chemical reviews [Online]* **2017,** *117* (21), 13353–13381.

38.    Chen, D.-Y.; Liu, W.; Zheng, C.-J.; Wang, K.; Li, F.; Tao, S. L.; Ou, X.-M.; Zhang, X.-H. Isomeric Thermally Activated Delayed Fluorescence Emitters for Color Purity-Improved Emission in Organic Light-Emitting Devices. *ACS applied materials & interfaces [Online]* **2016,** *8*, 16791–16798.

39.    Song, D.; Yu, Y.; Yue, L.; Zhong, D.; Zhang, Y.; Yang, X.; Sun, Y.; Zhou, G.; Wu, Z. Asymmetric thermally activated delayed fluorescence (TADF) emitters with 5,9-dioxa-13 b -boranaphtho[3,2,1- de ]anthracene (OBA) as the acceptor and highly efficient blue-emitting OLEDs. *J. Mater. Chem. C [Online]* **2019,** *7* (38), 11953–11963.

40.    Greenham, N. C.; Friend, R. H.; Bradley, D. D. Angular Dependence of the Emission from a Conjugated Polymer Light-Emitting Diode: Implications for efficiency calculations. *Advanced materials (Deerfield Beach, Fla.) [Online]* **1994,** *6* (6), 491–494.

**Supporting Information**

**Low efficiency roll-off blue TADF OLEDs employing a novel acridine-pyrimidine based high triplet energy host**

Francesco Rodella,[a] Rishabh Saxena,[b] Sergey Bagnich,[b] Dovydas Banevičius,[c] Gediminas Kreiza,[c] Stavros Athanasopoulos,[d] Saulius Juršėnas,[c] Karolis Kazlauskas,[c] Anna Köhler[b,e] and Peter Strohriegl[a,e].

[a] Macromolecular Chemistry I, University of Bayreuth, Bayreuth 95440, Germany.

[b] Soft Matter Optoelectronics, University of Bayreuth, Bayreuth 95440, Germany.

[c] Institute of Photonics and Nanotechnology, Vilnius University, Saulėtekio av. 3, LT-10257 Vilnius, Lithuania.

[d] Departamento de Física, Universidad Carlos III de Madrid, Avenida Universidad 30, 28911 Leganés, Madrid, Spain.

[e] Bayreuth Institute of Macromolecular Research (BIMF), University of Bayreuth, Bayreuth 95440, Germany.

Donors and acceptors used for spectroscopic studies:



2PhPy          1PhPy          MePy          Acridine
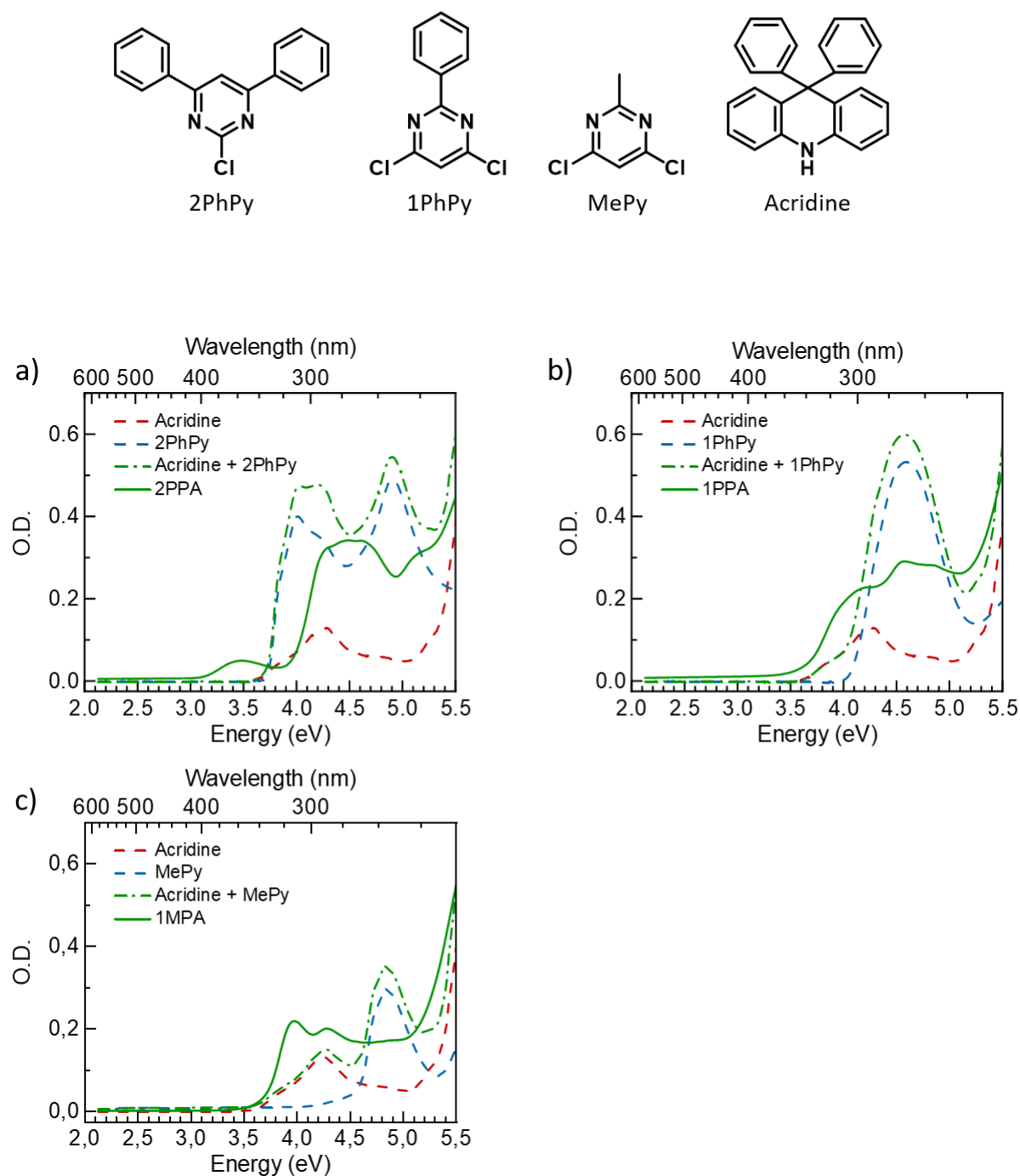


Figure S1: a), b) and c) show the absorption spectra (solid green line) of **2PPA**, **1PPA** and **1MPA** solutions (concentration = 0.05 mg/mL) in toluene along with acridine absorption (dashed red line) and **2PhPy**, **1PhPy** and **MePy** acceptors (dashed blue line) respectively. The sum of donor and acceptor absorption is shown by green dash-dot line. d) Acridine and 2PhPy (red and blue dashed line) absorption spectra in Figure S1 a are shifted in energy to match the sum of acridine + 2PhPy spectrum (green dash-dot line) with the absorption spectrum of **2PPA** (solid green line).
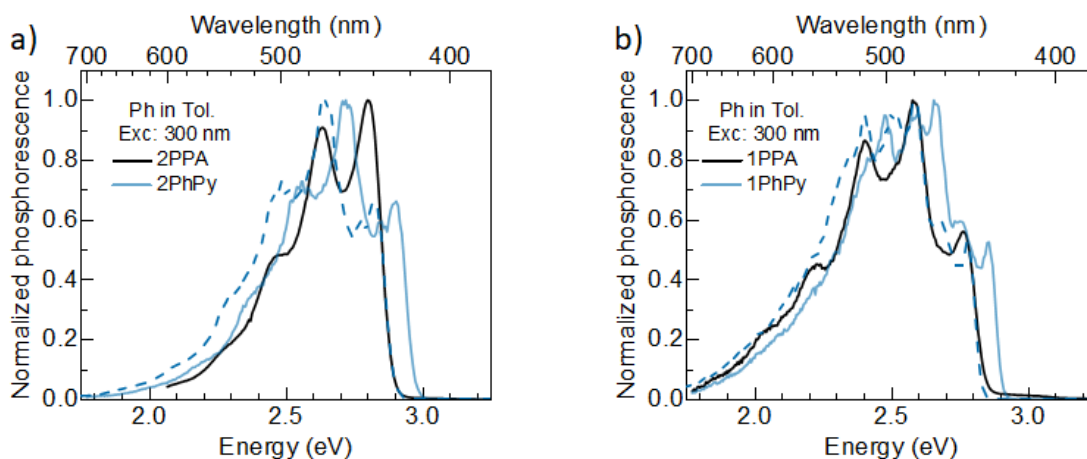
Figure S2: a) and b) show the comparison of **2PPA** and **1PPA** spectra (black line) with the horizontally translated Ph spectra of **2PhPy** and **1PhPy** spectra (blue dashed line) respectively. For reference the original **2PhPy** and **1PhPy** spectra is shown with a semi-transparent blue line.
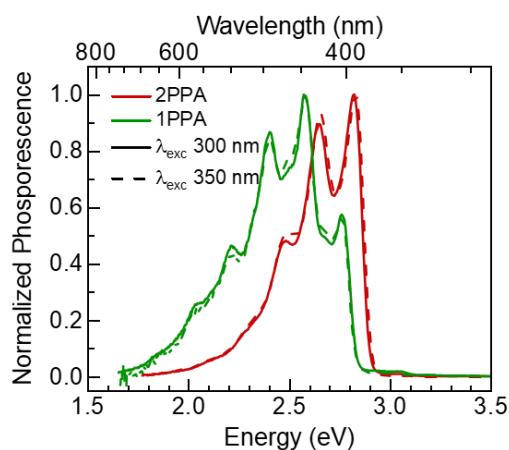


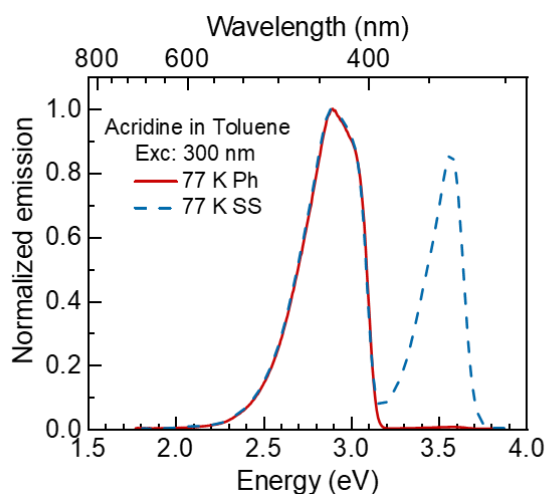Figure S3: Excitation wavelength Ph spectra is shown for **2PPA** and **1PPA** in mTHF.



Figure S4: 77 K phosphorescence (red solid line) and steady-state (blue dashed line) for acridine solution in toluene (concentration = 0.05 mg/mL). Phosphorescence is collected with a delay time of 150 ms and a gate width of 50 ms.
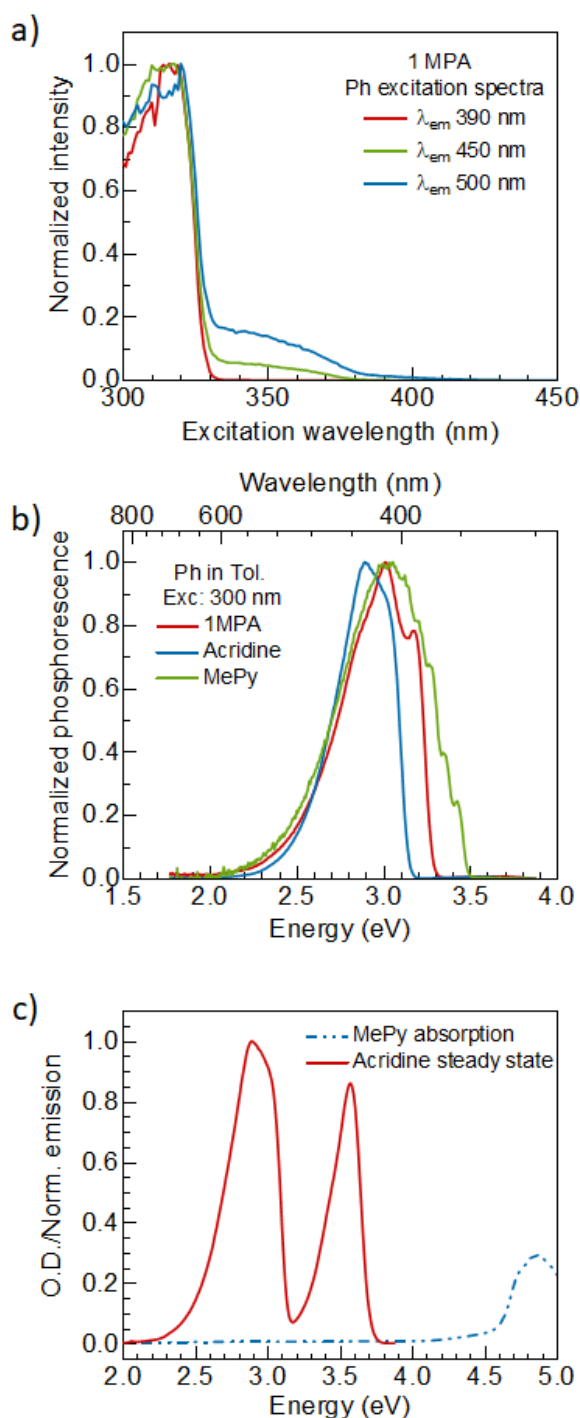
Figure S5: a) Phosphorescence (delay time 50 ms, gating time 50 ms) excitation spectrum for 1MPA solution in toluene glass (77 K). b) 77 K phosphorescence for 1MPA (red), acridine (blue) and methylpyriminine (MePy – green) solution in toluene (concentration = 0.05 mg/mL). Phosphorescence is collected with a delay time of 150 ms and a gate width of 50 ms. c) MePy absorption (blue dash-dot-dot line) and 77 K SS steady state emission of acridine solution (red solid) in toluene.
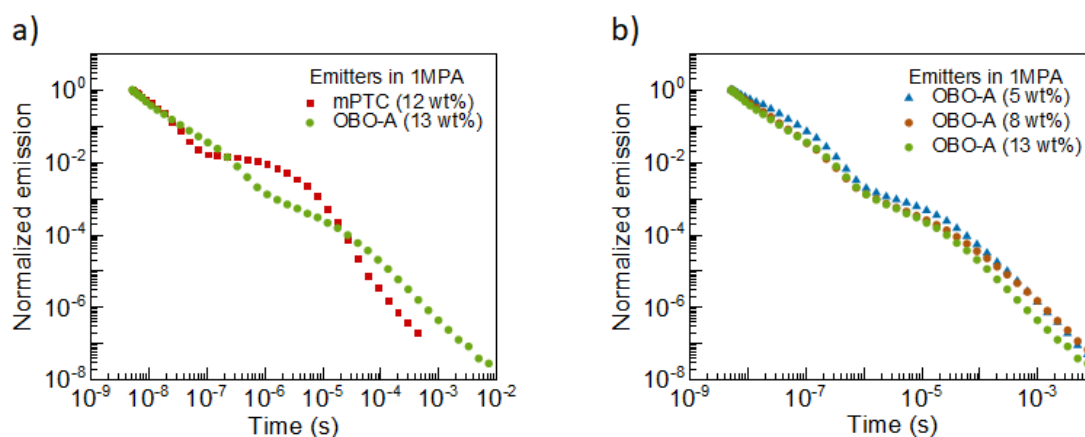
Figure S6: a) RT PL decay of **mPTC** (12 wt%) and **OBO-A** (13 wt%) doped films in **1MPA**. b) RT PL decay of **OBO-A** (5, 8 and 13 wt%) doped films in **1MPA**.

Table S1: Photolominescence quantum yield measurements of mPTC with different doping percentage in **1MPA** host.

| mPTC (wt%) in 1MPA | PLQY (%) |
|---|---|
| 3 | 19 |
| 5 | 23 |
| 10 | 34.5 |
| 20 | 33 |
| 30 | 21 |

| Emitter in 1MPA | Doping concentration | Average delayed lifetime |
|---|---|---|
| mPTC | 12 wt% | 6 µs |
| OBO-A | 5 wt% | 218 µs |
|  | 8 wt% | 343 µs |
|  | 13 wt% | 191 µs |

Table S2: A summary of average delayed fluorescence (DF) lifetimes $\left(\tau_{avg} = \frac{\int t.I_{DF}dt}{\int I_{DF}dt}\right)$ for the PL decays of doped emitter films in **1MPA**.

**Assignment of singlet and triplet states for 1MPA**

$S_2$ is an acridine based locally excited (LE) state (by comparison of steady state emission of 1MPA in **Figure S3e** with the steady state emission of acridine in **Figure S4**).

**Option A:** High energy 1MPA phosphorescence ($T_2$) is acridine based phosphorescence as it is observed only when acridine is excited, i.e. when $\lambda_{exc} < 330$ nm (**Figure S5a** and **Figure S1**). This also implies that the intersystem crossing (ISC) rate on acridine is faster and that the charge transfer (CT) from acridine to methylpyrimidine (MePy) to form a CT state is slower. The internal conversion from the high energy triplet state ($T_2$) to the low energy triplet state ($T_1$) is also slow because of the required CT.

**Option B:** High energy 1MPA phosphorescence ($T_2$) is from MePy based LE.

- **Argument in favor of it:** The MePy phosphorescence is close in energy to the observed $T_2$ emission (**Figure 5b**).

- **Arguments against it:** the absorption from MePy is very far away from the excitation energy ($\lambda_{exc} = 300$ nm, $E_{exc} = 4.13$ eV), i.e. MePy cannot be excited. Thus, the excitation would need to be transferred from acridine to MePy. However, the emission of acridine has negligible overlap with the MePy absorption (**Figure S5c**), implying poor energy transfer between these two units, since for excitations to be transferred efficiently via Förster/Dexter process some overlap is required.

**Low energy 1MPA phosphorescence ($T_1$):** It is assigned as an acridine based hybrid CT-LE state because emission at both 450 and 500 nm have strong contribution from acridine excitation ($\lambda_{exc} < 330$ nm) in the phosphorescence excitation spectrum (**Figure 5a**). The phosphorescence spectral shape (**Figure 3f**) has some signatures of acridine phosphorescence (**Figure S4**). Also, there is some weak absorption between 330-380 nm (**Figure S5a**) consistent with the expected position of CT absorption.
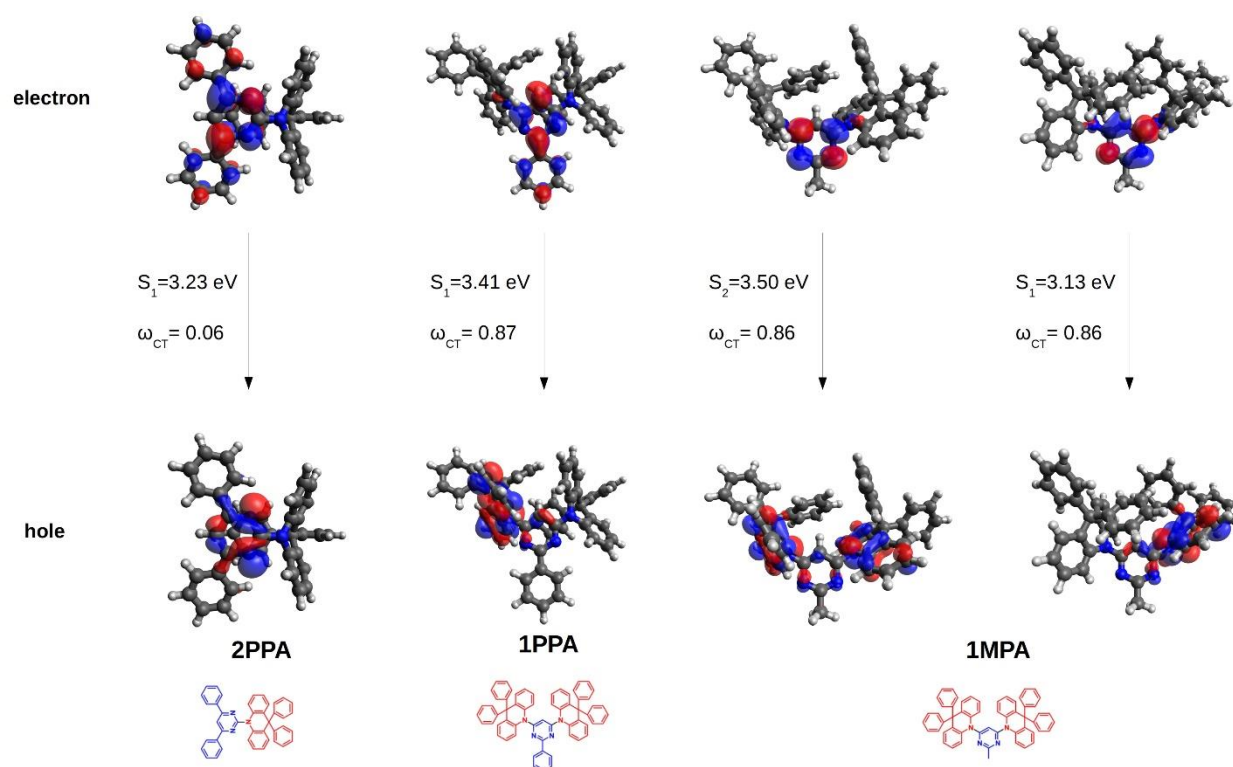
Figure S7: TDA-DFT computed natural transition orbitals, emission energies and charge transfer numbers for the lowest relaxed singlet states for **2PPA**, **1PPA** and **1MPA** at the M06-2X/6-31+G(d,p) level. For **1MPA** both the $S_2$ and $S_1$ state NTOs are shown. The relevant arrangement of the acridine and pyrimidine units is shown at the bottom.

| compound/state | $\omega_{CT}$ | $\Delta r$ (Å) |
|---|---|---|
| **1PPA/S$_1$** | 0.87 | 4.44 |
| **1PPA/T$_1$** | 0.27 | 3.09 |
| **1MPA/S$_2$** | 0.86 | 2.07 |
| **1MPA/S$_1$** | 0.86 | 3.26 |
| **1MPA/T$_1$** | 0.45 | 1.92 |

Table S3: Charge transfer numbers $\omega_{CT}$ and average electron-hole separation distance $\Delta r$ for the lowest relaxed singlet and triplet excited states of **1PPA** and **1MPA**.
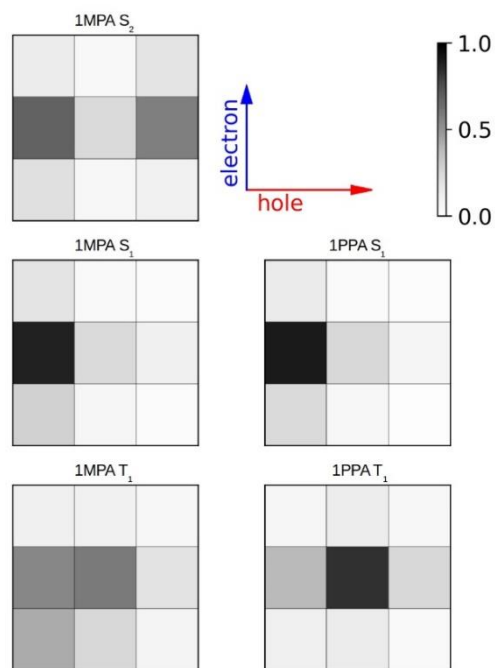
Figure S8: Electron-hole pair correlation plots of the Ω matrix with respect to the acridine-pyrimidine-acridine fragments for the lowest singlet and triplet state of **1PPA** and **1MPA.**
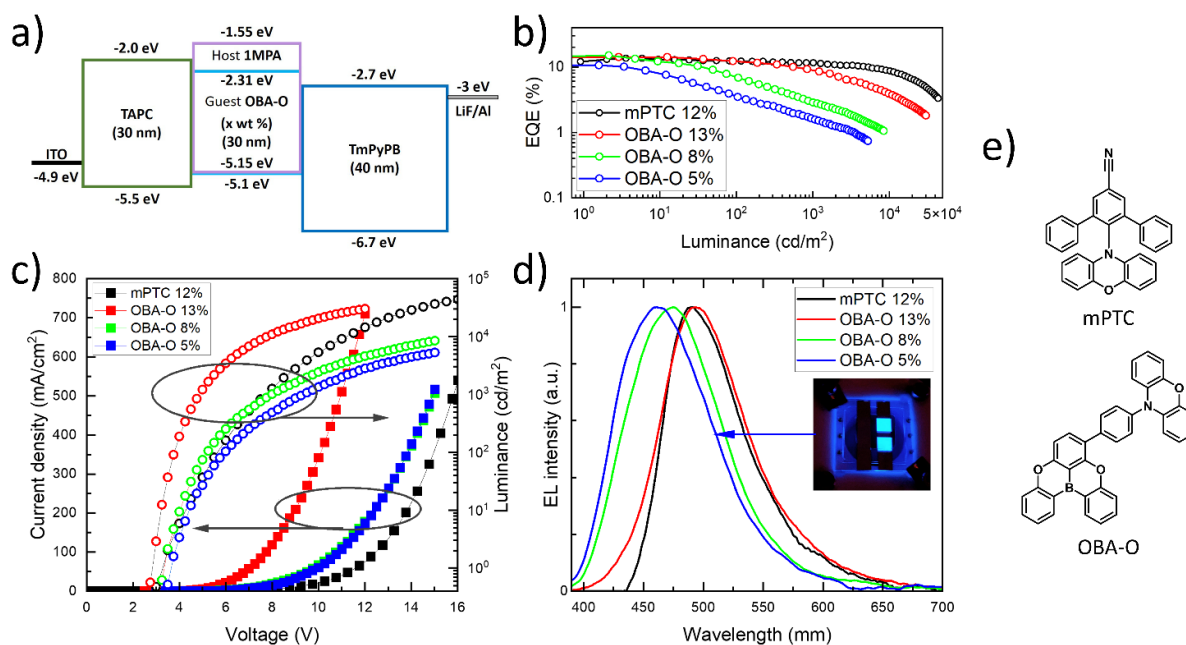


Figure S9: Main properties of the TADF OLED based on **1MPA** host doped with 5, 8 and 13 wt% of **OBA-O**. a) energy level diagram. b) EQE vs. luminance. c) current density and luminance vs. applied voltage. d) electroluminescence spectrum with working device picture shown in the inset. The properties of analogous device with **mPTC** (12 wt%) emitter is shown for reference. e) Molecular structure of the emitters.

## 4.3. Paper 3: Substitution Effects on a New Pyridylbenzimidazole Acceptor for Thermally Activated Delayed Fluorescence and Their Use in Organic Light-Emitting Diodes

**RESEARCH ARTICLE**

# Substitution Effects on a New Pyridylbenzimidazole Acceptor for Thermally Activated Delayed Fluorescence and Their Use in Organic Light-Emitting Diodes

*David Hall, Pachaiyappan Rajamalli, Eimantas Duda, Subeesh Madayanad Suresh, Francesco Rodella, Sergey Bagnich, Cameron L. Carpenter-Warren, David B. Cordes, Alexandra M. Z. Slawin, Peter Strohriegl, David Beljonne, Anna Köhler,\* Yoann Olivier,\* and Eli Zysman-Colman\**

In this work a new acceptor is used for use in thermally activated delayed fluorescence (**TADF**) emitters, pyridylbenzimidazole, which when coupled with phenoxazine allows efficient **TADF** to occur. *N*-functionalization of the benzimidazole using methyl, phenyl, and *tert*-butyl groups permits color tuning and suppression of aggregation-caused quenching (**ACQ**) with minimal impact on the **TADF** efficiency. The functionalized derivatives support a higher doping of 7 wt% before a fall-off in photoluminescence quantum yields is observed, in contrast with the parent compound, which undergoes ACQ at doping concentrations greater than 1 wt%. Complex conformational dynamics, reflected in the time-resolved decay profile, is found. The singlet–triplet energy gap, $\Delta E_{ST}$, is modulated by *N*-substituents of the benzimidazole and ranges of between 0.22 and 0.32 eV in doped films. Vacuum-deposited organic light-emitting diodes, prepared using three of the four analogs, show maximum external quantum efficiencies, $EQE_{max}$, of 23.9%, 22.2%, and 18.6% for BIm(Me)PyPXZ, BIm(Ph)PyPXZ, and BImPyPXZ, respectively, with a correlated and modest efficiency roll-off at 100 cd m$^{-2}$ of 19% 13%, and 24% of the $EQE_{max}$, respectively.

## 1. Introduction

The study and design of emitters showing thermally activated delayed fluorescence (TADF) have benefitted from a surge of interest in recent years,[1–3] with examples of organic light-emitting diodes (OLEDs) that rival their phosphorescent counterparts in terms of device efficiency. TADF involves triplet harvesting through a reverse intersystem crossing (RISC) mechanism, converting the normally nonemissive triplet states to emissive singlets.[4] In order to maximize triplet harvesting a small singlet-triplet excited state energy gap, $\Delta E_{ST}$, is required, which can be achieved by separating the hole and electron densities within the emitter by having poorly conjugated, covalently coupled donors (electron rich) and acceptors (electron deficient).[4] When $\Delta E_{ST}$ is sufficiently small, conversion of the lowest

D. Hall, P. Rajamalli, S. M. Suresh, C. L. Carpenter-Warren, D. B. Cordes,
A. M. Z. Slawin, E. Zysman-Colman
Organic Semiconductor Centre
EaStCHEM School of Chemistry
University of St Andrews
St Andrews KY16 9ST, UK
E-mail: eli.zysman-colman@st-andrews.ac.uk
D. Hall, D. Beljonne
Laboratory for Chemistry of Novel Materials
University of Mons
Mons 7000, Belgium

ⓘD The ORCID identification number(s) for the author(s) of this article
can be found under https://doi.org/10.1002/adom.202100846.

E. Duda, S. Bagnich, A. Köhler
Soft Matter Optoelectronics
BIMF and BPI
University of Bayreuth
Universitätsstraße 30, 95447 Bayreuth, Germany
E-mail: anna.koehler@uni-bayreuth.de
F. Rodella, P. Strohriegl
Macromolecular Chemistry I
BIMF and BPI
University of Bayreuth
95440 Bayreuth, Germany
Y. Olivier
Unité de Chimie Physique Théorique et Structurale and Laboratoire de
Physique du Solide
Namur Institute of Structured Matter
Université de Namur
Rue de Bruxelles, 61, Namur 5000, Belgium
E-mail: yoann.olivier@unamur.be

triplet excited state ($T_1$) to the lowest singlet excited state ($S_1$) becomes possible at room temperature.

Despite the many hundreds of examples of donor–acceptor TADF emitters, most designs involve the combination of a rather limited number of classes of electron-donating and accepting groups.[2] The most popular donors are carbazole, diphenylamine, dimethylacridine, phenoxazine (PXZ), phenothiazine, and derivatives thereof. Acceptors originate primarily from moieties containing cyano, pyridine, triazine, borane, sulfone, and ketone groups. Pyridylbenzimidazole (BImPy) has been reported previously in the literature as a fluorescent compound[5,6] or as a ligand that coordinates to metals.[7–12] While pyridine is an acceptor, the imidazole moiety has both electron rich and electron poor contributions[13] allowing it to act as either an acceptor or a donor, depending on what it is coupled to.[13,14] The use of BImPy as a component of a purely organic emitter in OLEDs has only been reported when the group is coordinated to boron, acting as a Lewis acid, producing blue fluorescent devices.[15] TADF was detected in one example where a BImPy D-A system with a PXZ donor was coordinated to Ag(I),[16] wherein the metal, again acting as a Lewis acid, contributes to a reduced $\Delta E_{ST}$ in the material, thereby turning on TADF. A similar observation was made for a pyridylpyrazol D-A ligand with 9,9-dimethyl-9,10-dihydroacridine as the donor, again coordinated to Ag(I).[17] In both of these examples the free ligand did not show any TADF.[16,17] To the best of our knowledge no organic TADF emitters have been reported utilizing the BImPy core alone or with a BImPy acceptor. Separately though, both pyridines and imidazoles have been investigated as acceptors in TADF emitter design. Representative examples are shown in **Figure 1**; several of the imidazole-containing compounds have been reported to emit by either triplet–triplet annihilation[18] or hot exciton mechanisms[13,19] in lieu of TADF. A summary of the structures of purely organic pyridine-containing TADF emitters and their properties can be found in Figure S1 and Table S1 in the Supporting Information while

those of imidazole-containing emitters are reported in Figure S2 and Table S2 in the Supporting Information.

Herein we report a series of structurally related functionalized BImPy TADF emitters containing a phenoxazine donor (PXZ). The parent emitter, **BImPyPXZ**, contains no *N*-substitution while methyl (**BIm(Me)PyPXZ**), phenyl (**BIm(Ph)PyPXZ**), and *tert*-butyl (**BIm(*t*Bu)PyPXZ**) derivatives present ever increasing torsions due to the increasing steric bulk of the *N*-substituent. The increased bulkiness of these groups was introduced as a strategy to aid in the suppression of aggregation-caused quenching (ACQ),[20] a common nonradiative pathway observed in films of emitters.[21] Each of the emitters displays TADF behavior in the solid state, with $\Delta E_{ST}$ of between 0.22 and 0.32 eV in doped mCP films. Green-emitting OLEDs were fabricated using **BImPyPXZ**, **BIm(Me)PyPXZ**, and **BIm(Ph)PyPXZ**, and show excellent maximum external quantum efficiencies, $EQE_{max}$, of 18.6%, 23.9%, and 22.2%, respectively.

## 2. Results and Discussion

### 1. Synthesis

Each of the emitters was obtained following a multistep synthesis as documented in **Figure 2**. 5-Bromopyridine-2-carbaldehyde was first protected as its acetal, **1**, in an excellent yield of 95%. Protection is essential for the subsequent crosscoupling step; direct crosscoupling was not possible, which we attributed to metal binding between the oxygen and nitrogen atoms of the substrate. A Buchwald–Hartwig crosscoupling reaction installed the phenoxazine donor onto the pyridine (**2**) in a good yield of 83%. Removal of the acetal under acidic conditions afforded a red-colored compound, **PXZPyCHO**, which itself was weakly emissive in solution and in the solid state (vide infra). Functionalized 2-nitroanilines were synthesized via $S_{NAr}$ reactions
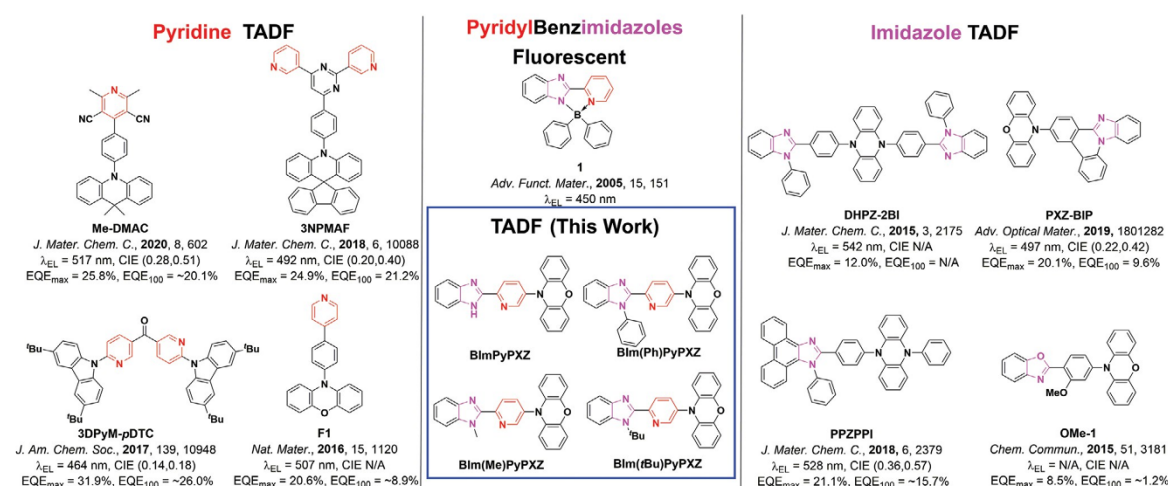


**Figure 1.** Structures of some of the previously reported pyridine- and imidazole-containing TADF emitters with the highest efficiencies along with the structure of the only purely organic example of pyridylbenzimidazoles being used in OLEDs as well as the structures of the emitters reported in this work. The use of the ~ indicates that the data were extracted from the figure in the literature report.
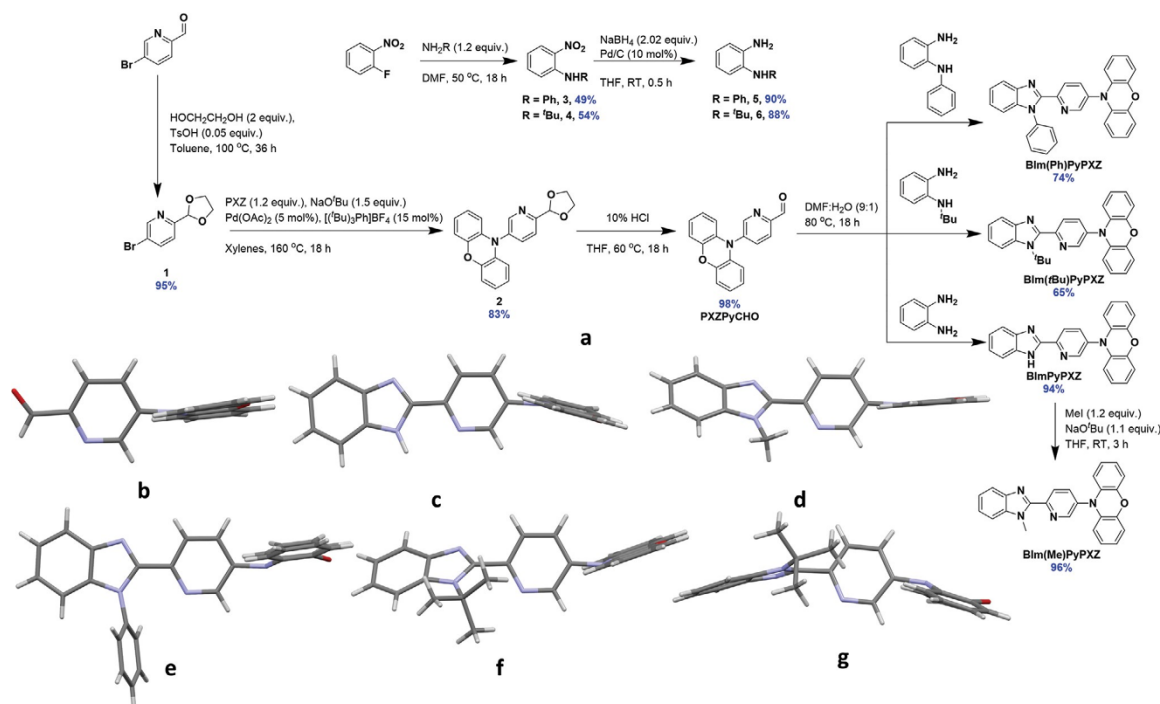
**Figure 2. a).** Synthesis of the four targets and crystal structures of b) **PXZPyCHO**, c) **BImPyPXZ**, d) **BIm(Me)PyPXZ**, e) **BIm(Ph)PyPXZ**, f) **BIm(tBu) PyPXZ** with planar PXZ, and g) **BIm(tBu)PyPXZ** with a puckered PXZ.

of 2-fluoronitrobenzene using *tert*-butylamine or aniline in reasonable yields (see the Supporting Information for details). Subsequent reduction afforded the relevant functionalized diaminobenzenes in good yield. Following the literature, condensation of these intermediates with **PXZPyCHO** produced **BImPyPXZ**, **BIm(Ph)PyPXZ**, and **BIm(tBu)PyPXZ** in yields of between 65% and 94%.[22] The last target compound, **BIm(Me) PyPXZ**, was synthesized via methylation of **BImPyPXZ** using MeI in 96% yield.

Purification by temperature-gradient vacuum sublimation afforded pure **BImPyPXZ**, **BIm(Me)PyPXZ**, and **BIm(Ph) PyPXZ**; however, cleavage of the *N-t*Bu bond in **BIm(tBu) PyPXZ** occurred under these conditions, thus preventing its use in vacuum-deposited OLEDs. Crystals suitable for single crystal X-ray diffraction were grown for **BImPyPXZ**, **BIm(Me) PyPXZ**, **BIm(Ph)PyPXZ**, **BIm(tBu)PyPXZ**, and **PXZPyCHO**. Both **BIm(Ph)PyPXZ** and **BImPyPXZ** were grown via slow vapor diffusion of hexane into a saturated solution of toluene. **BIm(Me)PyPXZ** was grown from a saturated solution of chloroform layered with ethanol. **BIm(tBu)PyPXZ** was grown from a saturated solution of dichloromethane layered with hexane. **PXZPyCHO** was grown via slow evaporation of a saturated solution of toluene. All the structures displayed similar PXZ-Py torsions, ranging from 60.0(15)° to 89.72(17)°. The large torsion is often observed in TADF emitters with PXZ donors owing to its large size, with some variation arising from the degree of pucker and how this interacts with the pyramidalization of the PXZ nitrogen.[23] **PXZPyCHO** and **BIm(Me)PyPXZ** both contain a planar PXZ, with $\pi$-stacking interactions occurring between cofacial PXZ groups (Figures S40 and S44, Supporting Information), resulting in $\pi$-stacked chains along the *a*-axes. The structure of **BImPyPXZ** shows PXZ donors with a range of slightly puckered conformations (angles between PXZ phenyl ring planes 5.4°–12.3°, Figure S45, Supporting Information). Given the closeness to planarity in this arrangement, it is somewhat surprising to see only one $\pi$-stacking interaction occurring between PXZ donor groups. The primary intermolecular interactions in this compound are hydrogen bonds between imidazole moieties, giving rise to chains along the *b*-axis. In contrast, the PXZ donor in **BIm(Ph)PyPXZ** has a decidedly puckered conformation (angle between PXZ phenyl ring planes 23.0°, Figure S43, Supporting Information), similar to that previously observed for phenothiazine donors.[24] In **BIm(tBu)PyPXZ**, two different PXZ conformers were observed in the same structure, one with a planar PXZ (Figure 2f) and the other adopting an intermediate puckered shape (angle between PXZ phenyl ring planes 16.5°, Figure 2g). No $\pi$–$\pi$ interactions are observed between planar PXZ moieties in this compound. There is no consistent trend to suggest that particular solid-state intermolecular interactions drive a tendency for planar versus puckered PXZ groups. The continuum seen between strictly planar, through various intermediate to more severely puckered forms of PXZ suggest a subtle source for this, possibly involving intermolecular $\pi\cdots\pi$ and CH$\cdots\pi$ interactions, and likely low energetic differences between different conformations. The next torsion of importance is $\alpha$, the torsion between the benzimidazole

**ADVANCED**
**SCIENCE NEWS**
www.advancedsciencenews.com

**ADVANCED**
**OPTICAL**
**MATERIALS**
www.advopticalmat.de

and the substituted pyridine (Figure S41, Supporting Information). This torsion will govern the conjugation length of the acceptor. The different compounds show three ranges of torsions, broadly corresponding to the steric bulk of the *N*-substituent within the plane of the benzimidazole. These result in near-planar arrangements of the two rings for **BImPyPXZ** (Figure S42, Supporting Information) and **BIm(Ph)PyPXZ** (Figure S43, Supporting Information) [torsions of $1.6(8)°$–$12.4(8)°$ and $4.59(19)°$, respectively], an intermediate arrangement for **BIm(Me)PyPXZ** (Figure S44, Supporting Information) [torsion of $23.9(2)°$], and the rings tending toward orthogonality for **BIm(*t*Bu)PyPXZ** (Figure S45, Supporting Information).

Thermogravimetric analysis (TGA) and differential scanning calorimetry (DSC) were performed to assess the thermal properties of the four emitters (Figures S46–S49 and Table S4, Supporting Information). **BImPyPXZ**, **BIm(Me)PyPXZ**, and **BIm(Ph)PyPXZ** showed similar TGA behavior with temperatures $T_d$ of 5% weight loss of 346, 341, and 355 °C, respectively, indicative of their high thermal stability. The fact that the weight drops to 0% shows that the three compounds do not in fact decompose but completely sublime already at atmospheric pressure during the TGA experiment. The $T_d$ of 276 °C is significantly lower for **BIm(*t*Bu)PyPXZ** indicating that the benzimidazole with the *tert*-butyl substituent is not thermally stable, which was also apparent during attempted vacuum sublimation.

**BImPyPXZ** shows a glass transition temperature ($T_g$) of 97 °C in the DSC experiment. The material recrystallizes at about 160 °C and finally melts at 260 °C. **BIm(Me)PyPXZ** exhibits a glass transition at 64 °C. Its melting behavior is rather complex and the occurrence of two melting temperatures in the first and second heating cycle in Figure S47b in the Supporting Information points to the formation of two polymorphs. This is further supported when the material is investigated using different cooling rates with slow and fast temperature ramps as shown in Figure S49 in the Supporting Information. Here, the melting points of both polymorph 1 at 225 °C and of polymorph 2 at 210 °C become visible. The $T_g$ of **BIm(Ph)PyPXZ** is 73 °C. In the first heating cycle, the material is observed to melt at 162 °C. Upon cooling, no recrystallization occurs and, in the 2nd, 3rd, and 4th heating only a $T_g$ is observed. Due to the thermal instability of **BIm(*t*Bu)PyPXZ** the DSC experiments have to be interpreted with great care. From Figure S48d in the Supporting Information only a $T_g$ of about 80 °C can be estimated.

## 2.2. Theoretical Modeling

Ground state geometry optimization using density functional theory (DFT) was performed on each of the emitters using the M062X functional in combination with the 6-31G(d,p) basis set (**Figure 3**). Vertical excitation calculations from the ground state geometry at the time-dependent DFT (TD-DFT) within the Tamm–Dancoff approximation (TDA-DFT) using the aforementioned functional and basis set were also carried out.[25,26] TDA-DFT calculations are preferentially employed with respect to TD-DFT because they address the triplet instability issue, which tends to overstabilize the triplet states bearing a strong

locally excited (LE) state character.[25] M062X was selected over the widely used PBE0 and B3LYP functionals since the latter two tend to overstabilize excited states containing a significant amount of charge transfer (CT) character due to their small content of Hatree–Fock exchange.[26]

In the ground state, changing the R group alters both the equilibrium torsion angle $\alpha$ and bond length $C_{\gamma'}$–$C_\gamma$ (Figure S50 and Table S5, Supporting Information). Both **BImPyPXZ** and **BIm(Me)PyPXZ** have a predicted ground state geometry that is planar ($\alpha = 0°$) likely stabilized due to a combination of increased conjugation and intramolecular hydrogen bonding.[27] The weakly inductive electron-donating ability of the methyl substituent increases the Lowest Unoccupied Molecular Orbital (LUMO) energy compared to the parent **BImPyPXZ**. A similar observation was reported previously for fluorescent imidazole-based emitters.[28] Owing to the larger size of the Ph and *t*Bu substituents compared to the parent and methylated structures, the torsion angle, $\alpha$, deviates from the usually favorable $\alpha = 0°$–$19.5°$ and $40.8°$, respectively, which in turn disrupts conjugation between the BIm and Py heterocycles, increasing the $C_{BIm}$–$C_{Py}$ bond length slightly (Table S5, Supporting Information). A consequence of this conformational change is a predicted increase in the LUMO energy. The destabilization is more pronounced in **BIm(*t*Bu)PyPXZ** as the inductively electron-withdrawing phenyl group in **BIm(Ph)PyPXZ** counteracts the decrease in conjugation due to this bulky substituent.[28] In each example there is very little change in the Highest Occupied Molecular Orbital (HOMO) level, which is localized on the PXZ. HOMO to LUMO transitions dominate vertical excitations to the $S_1$ while the $T_1$ state is a more complex picture involving several different transitions (Table S7, Supporting Information). The overall increase in the HOMO–LUMO energy gap for **BIm(Me)PyPXZ** compared to **BImPyPXZ** translates also in an increased $S_1$ energy level from 3.53 to 3.58 eV. Similarly, the $S_1$ energy increases from **BIm(Ph)PyPXZ** (3.59 eV) to **BIm(*t*Bu) PyPXZ** (3.69 eV). Calculated $\Delta E_{ST}$ values remain small at 0.05, 0.11, 0.09, and 0.15 eV for **BImPyPXZ**, **BIm(Me)PyPXZ**, **BIm(Ph)PyPXZ**, and **BIm(*t*Bu)PyPXZ**, respectively. The TADF efficiency is governed not only by the small $\Delta E_{ST}$ but also by the magnitude of the spin–orbit coupling (SOC) between the $S_1$ and $T_1$ states. Adherence to El Sayed's rules requires that the nature of $T_1$ and $S_1$ be different for state mixing to occur;[29] transitions between two purely CT or LE states are strictly forbidden.[30] Several groups[30–32] have highlighted that the presence of intermediate triplet states of a differing nature to those of $S_1$ can be recruited to bypass the unfavorable $T_1$–$S_1$ SOC-driven conversion. In this case, RISC occurs through a spin-vibronic mechanism, namely the $T_1$–$S_1$ conversion is a two-step mechanism involving reverse internal conversion between $T_1$ and a higher-lying triplet state $T_n$ followed by an SOC-driven spin RISC between $T_n$ and $S_1$.[32,33] We thus quantified the degree of charge-transfer character of the excited state by computing the $\varphi_S$ metric through postprocessing of the TDA-DFT calculations performed here.[34] The $\varphi_S$ metric is a measure of the overlap the electronic density of the frontier orbitals during the electronic transition. A $\varphi_S$ value of 1 represents an LE state while a value of 0 corresponds to a purely CT excited state, intermediate values are interpreted as mixed CT-LE excited states. The $S_1$ state of each emitter is predominantly CT in nature
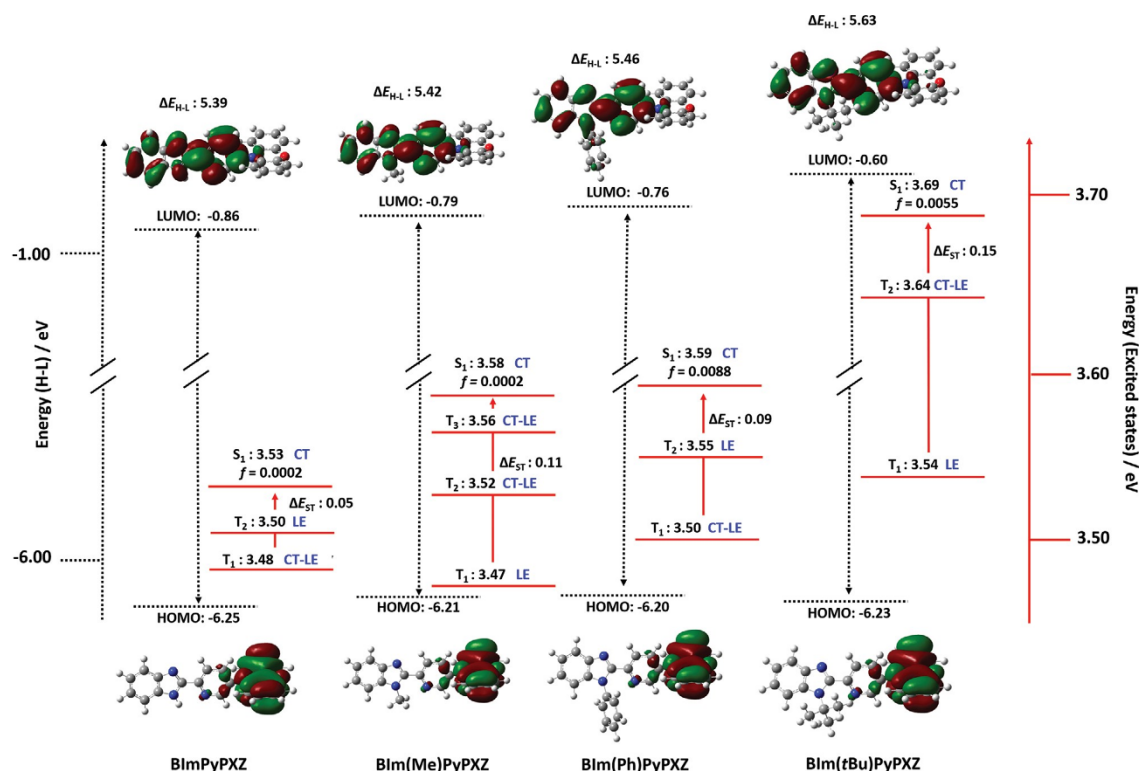
**Figure 3.** TDA-DFT calculated HOMO LUMO levels (dotted lines) and excited triplet and singlet state energies (solid lines), and electron density distribution plots of the HOMO and LUMO calculated using M062X//6-31G(d,p). The nature of singlet and triplet excited states is indicated in blue based on the $\varphi_S$ values of overlap where CT = 0, LE = 1 and CT − LE = 0.33–0.66 (isovalue = 0.02).

($\varphi_S$ < 0.33). This is a common occurrence for donor–acceptor TADF emitters and this assignment is supported by their positive solvatochromism (vide infra). The nature of $T_1$ varies, being mixed CT-LE for **BImPyPXZ** (0.48) and **BIm(Ph)PyPXZ** (0.65), and mostly LE for **BIm(Me)PyPXZ** (0.82) and **BIm(tBu)PyPXZ** (0.76). The intermediate states are of mixed CT-LE character for **BIm(Me)PyPXZ** (0.67 and 0.57) and **BIm(tBu)PyPXZ** (0.60) and LE for **BImPyPXZ** (0.82) and **BIm(Ph)PyPXZ** (0.81), which is the opposite trend to that observed for the nature of the $T_1$ state. These intermediate states of differing character to each other and to the $S_1$ state are expected to facilitate RISC due to spin-vibronic coupling.[30,35] A summary of the excited state energies and properties is found in Table S6 and Figure S51 in the Supporting Information. The intermediate, **PXZPyCHO**, was also investigated computationally and presents a very small $\Delta E_{ST}$ of 0.06 eV, suggestive that it too will show TADF. Its $S_1$ energy is lower than that of the **BImPyPXZ** series owing to the stronger electron-acceptor in this compound (Figure S54 and Tables S5 and S6, Supporting Information).

In the crystal structures, significantly different dihedral angles $\alpha$ between the pyridyl and benzimidazole units are observed for several of the compounds, caused by differences in local inter- and intramolecular interactions. In particular, for **BIm(tBu)PyPXZ**, we found two different conformers with

torsion angles of 47.16(19)° and 77.98(18)°. In order to probe the significance of torsion around $\alpha$ we computed the torsion potential about the $C_{BIm}$–$C_{Py}$ bond (**Figure 4**) for each emitter, varying the $\alpha$ dihedral angle in increments of 5°. Each conformer was reoptimized at M062X//6-31G(d,p) level in the ground state. Vertical excited state TDA-DFT calculations were then carried out for each ground-state conformer where we investigated the excited-state properties including $\Delta E_{ST}$, emission energy and the nature of the excited states. There are relatively few reports that systematically correlate the effects of conformation on the opto-electronic properties of TADF emitters.[33,34,36] Here we applied a Boltzmann population distribution analysis to assess the contribution at room temperature of the different conformers to the photophysical landscape (Figure 4). For **BImPyPXZ**, we observe a large increase in energy as conjugation is disrupted from the optimized conformation with $\alpha = 0°$, with a barrier to rotation occurring at 90° at ≈12 kcal mol$^{-1}$. There is a second, smaller rotational barrier of ≈10 kcal mol$^{-1}$ at 180° due to steric interaction between NH and CH hydrogen atoms on the adjacent heterocycles (Figure 4a). The rotational profile for **BIm(Me)PyPXZ** is similar with an energy minimum at $\alpha = 0°$, although the largest barrier of ≈11 kcal mol$^{-1}$ occurs at 180° due to steric hindrance between the proton and the methyl group on the Py and BIm units, respectively (Figure 4b). The lowest energy conformer for
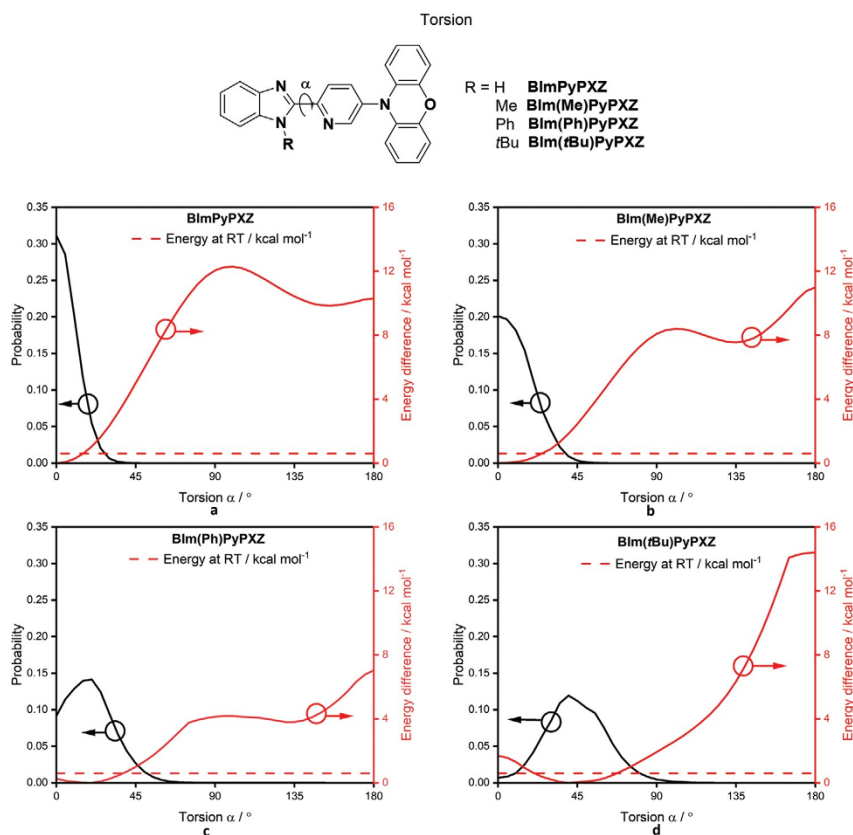
**Figure 4.** Boltzmann probability distribution and energy difference from lowest energy conformer calculated around torsion $\alpha$ for a) **BImPyPXZ**, b) **BIm(Me)PyPXZ**, c) **BIm(Ph)PyPXZ**, and d) **BIm(tBu)PyPXZ**. Calculated at M062X//6-31G(d,p) level of theory in the gas phase with dispersion effects included. The dashed horizontal line represents the energy at room temperature.

**BIm(Ph)PyPXZ** occurs at $\alpha = 20°$ and its rotational barrier is the lowest amongst the four compounds, peaking at $\approx 7$ kcal mol$^{-1}$ at 180° (Figure 4c). Finally, the steric interactions of the *tert*-butyl group in **BIm(tBu)PyPXZ** have more effect on both $\alpha$, which now is 40° for the lowest energy conformer, and the barrier to rotation, which is $\approx 14$ kcal mol$^{-1}$, centered at 180° (Figure 4d). In most of the examples in the present study the computed value of $\alpha$ in the lowest energy conformation and the value of $\alpha$ derived from the crystal structure deviate significantly ($\Delta \alpha > 15°$), likely due to the significant influence of both intra- and intermolecular interactions in the crystal exert on the conformational landscape. A summary of these data can be found in Table S9 in the Supporting Information, crystal packing forces are the primary causes for the discrepancy.

We computed vertical excitations energies for $S_1$ and $T_{1-3}$ excited states and their respective natures as well as the $\Delta E_{ST}$, varying the torsion angle, $\alpha$, within the ground state torsion energy potential calculated previously. For each compound, the hole density in the $S_1$ excited state is localized primarily on the PXZ unit with some overlap on the Py ring. A similar trend is observed for $T_1$ wherein it is located primarily on the PXZ except in cases where the conformation is coplanar (0° and

180° for **Imid(Me)PyPXZ**, and **Imid(tBu)PyPXZ**, and 180° for **Imid(Ph)PyPXZ**) where it is located across the whole BImPy unit. For each emitter the electron density is located across the BImPy component at 0° and 180°; however, with increasing torsion the conjugation is broken, with electron density now localized mostly on the Py ring, with only modest contribution from the PXZ (Figures S57–S60, Supporting Information). Interestingly, $\Delta E_{ST}$ is a maximum at 90°, which correlates with a maximum in $S_1$ and $T_1$ energies. This corresponds to a maximized hole and electron overlap near the PXZ unit and high $\varphi_S$ value for both $T_1$ and $S_1$. Overall, $T_1$ energy fluctuates much less than $S_1$. This is essentially due to higher LE character of $T_1$ in contrast to the high CT character of $S_1$. **Table 1** summarizes the conformational analysis of the Boltzmann-averaged excited state energies based on their population distribution, $\varphi_S$, $\Delta E_{ST}$, oscillator strength for each emitter. When comparing Table 1 and Table S6 in the Supporting Information it is clear that changing $\alpha$ actually has a very minimal impact on these parameters. The changes in the energies of $S_1$ and $T_2$ as a function of dihedral angle roughly mirror each other and so $\Delta E_{ST2}$ remains rather insensitive to changes in $\alpha$. The standard deviations of each of the excited state energies, $\varphi_S$ values and $\Delta E_{ST}$

**Table 1.** Boltzmann averaged vertical excitation energies and $\varphi_S$ values calculated in the gas phase within the TDA using M062X//6-31G(d,p) including dispersion correction over a range of conformations with $\alpha$ running from 0° to 180° at 5° intervals. The values in parentheses are the standard deviations on the different parameters computed.

| Compound | $T_1$ [eV] | $T_2$ [eV] | $T_3$ [eV] | $S_1$ [eV] | $\varphi_S\ T_1$ | $\varphi_S\ T_2$ | $\varphi_S\ T_3$ | $\varphi_S\ S_1$ | $\Delta E_{ST}$ [eV] |
|---|---|---|---|---|---|---|---|---|---|
| BImPyPXZ | 3.46 (0.02) | 3.52 (0.02) | 3.57 (0.02) | 3.54 (0.01) | 0.58 (0.07) | 0.80 (0.02) | 0.72 (0.02) | 0.26 (0.01) | 0.08 (0.02) |
| BIm(Me)PyPXZ | 3.48 (0.03) | 3.54 (0.03) | 3.59 (0.04) | 3.60 (0.02) | 0.75 (0.05) | 0.75 (0.06) | 0.64 (0.06) | 0.27 (0.01) | 0.11 (0.01) |
| BIm(Ph)PyPXZ | 3.48 (0.05) | 3.54 (0.03) | 3.63 (0.09) | 3.59 (0.03) | 0.65 (0.04) | 0.76 (0.07) | 0.76 (0.05) | 0.29 (0.03) | 0.11 (0.04) |
| BIm(tBu)PyPXZ | 3.53 (0.03) | 3.65 (0.08) | 3.81 (0.15) | 3.71 (0.07) | 0.75 (0.03) | 0.59 (0.14) | 0.77 (0.10) | 0.29 (0.01) | 0.19 (0.06) |

were also calculated across the range of torsion angles, which are indicated by the values in brackets in Table 1. We note that the standard deviations of the $T_1$, $T_2$, and $S_1$ excited state energies as well as their corresponding $\varphi_S$ are small for all compounds with the exception of **BIm(tBu)PyPXZ**. We stress that the excited state energies and their nature are rather insensitive with respect to the $\alpha$ torsion angle.

### 2.3. Optoelectronic Properties

The electrochemical behavior in acetonitrile of each emitter was investigated using cyclic voltammetry (CV) and differential pulse voltammetry (DPV) (**Figure 5**a and Table S11, Supporting Information). Each of the emitters displayed nearly identical reversible oxidation waves with values between 0.74 and 0.76 V vs SCE (Saturated Calomel Electrode), originating from oxidation of the PXZ donor. There is negligible impact on the oxidation potential from the presence or absence of $N$-substitution on the benzimidazole acceptor. Reduction waves involving the BImPy acceptor are irreversible, with the reduction potentials varying as a function of both the inductive effect of the $N$-substituent and the degree of conjugation present within the BImPy acceptor, ranging from −1.82 to −2.22 V when conjugation is greatest in **BImPyPXZ** and smallest for **BIm(tBu)PyPXZ**, respectively. The corresponding HOMO/LUMO levels are shown in **Table 2**. The changing $\Delta E_{H-L}$ values are in good agreement with DFT (Table S5, Supporting Information, and Figure 3), with an increase in the gap resulting mainly from

destabilization of the LUMOs while the HOMO values remain largely unchanged as these are situated predominantly on the PXZ (calculated to be −6.25 and −6.20 eV and measured between −5.18 and −5.16 eV). The electrochemical data of **PXZPyCHO** are shown in Figure S62 and Table S11 in the Supporting Information. The strongly electron-withdrawing nature of the aldehyde stabilizes the LUMO to −2.92 eV, reducing the HOMO–LUMO gap significantly to 2.28 eV in agreement with the calculated trend (Table S5, Supporting Information).

The UV–vis absorption spectra in toluene are shown in Figure 5b, which qualitatively agree with the simulated absorption spectra (Figure S52, Supporting Information). Each emitter shows a low energy band around 400 nm, with molar absorptivity values, $\varepsilon$, of 2000–3000 $m^{-1}\ cm^{-1}$ associated with a transition to a mixed $^1$CT-LE state with a predominant CT character; the hole density is situated on PXZ while the electron density is located on both PXZ and Py rings (Figure S53, Supporting Information). A second high-intensity ($\varepsilon$ of 19 000–35 000 $m^{-1}\ cm^{-1}$) band at between 300 and 333 nm is assigned to an LE transition with the hole and electron densities completely localized on the BImPy unit (Figure S53, Supporting Information). Both of these absorption bands in **BIm(tBu)PyPXZ** are blueshifted with respect to the other compounds because of its more twisted conformation resulting in a decrease of the conjugation length within the acceptor group. The decrease in the molar absorptivity is likewise explained by the increasing bulkiness of the peripherical substituents when comparing **BImPyPXZ** to **BIm(tBu)PyPXZ**, which is related to the more twisted conformation about the $C_{BIm}$–$C_{Py}$ bond
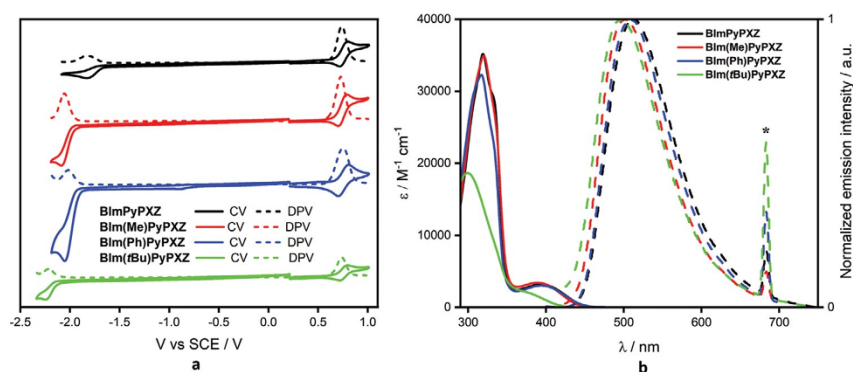


**Figure 5.** Solution optoelectronic spectra of the four emitters. a) CV and DPV in $N_2$-saturated MeCN with 0.1 m [$nBu_4N$]PF$_6$ as the supporting electrolyte and Fc/Fc$^+$ as the internal reference (0.38 V vs SCE)[11] and b) absorption (solid) and normalized emission (dashed) spectra in dilute toluene solution, where * indicates the transmission of the excitation pulse, $\lambda_{exc}$ = 340 nm, by the second order diffraction of the spectrometer's grating.

**Table 2.** Summary of the solution-state optoelectronic properties.

| Compound | $\lambda_{PL}$ [nm] [a] | $\Phi_{PL}$ [%] [b] | $S_1$ [eV] [c] | $T_1$ [eV] [d] | $\Delta E_{ST}$ [eV] [e] | HOMO [f] [eV] | LUMO [f] [eV] | $\Delta E_{H-L}$ [eV] [g] |
|---|---|---|---|---|---|---|---|---|
| **BImPyPXZ** | 513 | 31 | 2.74 | 2.62 | 0.12 | −5.16 | −2.60 | 2.56 |
| **BIm(Me)PyPXZ** | 501 | 36 | 2.93 | 2.64 | 0.29 | −5.16 | −2.37 | 2.79 |
| **BIm(Ph)PyPXZ** | 509 | 40 | 2.86 | 2.63 | 0.23 | −5.18 | −2.40 | 2.78 |
| **BIm(tBu)PyPXZ** | 497 | 25 | 3.11 | 2.78 | 0.33 | −5.16 | −2.20 | 2.96 |

[a]Concentration: $1 \times 10^{-5}$–$2 \times 10^{-5}$ m in toluene, $\lambda_{exc}$ = 340 nm; [b]Determined via the relative method compared to quinine sulfate as the reference ($\Phi_{PL}$ = 54.6% in 1 m $H_2SO_4$) under $N_2$, $\lambda_{exc}$ = 360 nm[37]; [c]Obtained from the onset of the fluorescence spectrum at 77 K, which was determined by subtraction of the phosphorescence spectrum at 77 K from the steady-state PL spectrum at 77 K; [d]Calculated from the onset of the phosphorescence spectra (delay: 2 ms, window: 10 ms integration); [e]$\Delta E_{ST} = E(S_1) - E(T_1)$; [f]The HOMO and LUMO energies were determined using the relation $E_{HOMO/LUMO} = -(E^{ox}_{onset}/E^{red}_{onset} + 4.8)$ eV,[38] where $E^{ox}$ and $E^{red}$ are the maxima of anodic and cathodic peak potentials, respectively calculated from DPV related to Fc/Fc⁻; [g]$E_{H-L} = |E_{HOMO} - E_{LUMO}|$.

that leads to greater CT character and hence a lower oscillator strength for the transition. A modest blueshift in absorption is observed upon increasing solvent polarity for each emitter (Tables S12–S15 and Figure S63, Supporting Information). In order to probe this, solvent state specific calculations using the integral equation formalism variant of the polarizable continuum model were performed considering two solvents of significantly different polarity: MeCN and cyclohexane in order to determine the solvated excited energies. In these calculations, the electronic density of the emitters and the solvent reaction field are relaxed together self-consistently. This requires calculations of the individual $S_{1-4}$ excited states. The observed hypsochromic shifts of these excited states is corroborated by these calculations, with both $S_3$ and $S_4$ showing an increase in energy moving from cyclohexane to MeCN (the $S_4$ state of **BIm(Me)PyPXZ** being the exception where there is a modest redshift predicted from 4.49 to 4.47 eV). Much like the experimental data, the predicted changes are modest (cf. Table S8, Supporting Information).

The photophysical properties in toluene are summarized in Table 2 and the photoluminescence spectra shown in Figure 5b. The emission for each compound is broad and unstructured, indicative of an excited state with a dominant CT character. In line with computations, and consistent with the ground state optoelectronic characterization, the bluest emission at a photoluminescence maximum, $\lambda_{PL}$ = 497 nm (2.49 eV) occurs for **BIm(tBu)PyPXZ**. **BImPyPXZ** shows the greenest emission at 513 nm (2.42 eV), followed by **BIm(Ph)PyPXZ** at 509 nm (2.44 eV) and **BIm(Me)PyPXZ** at 501 nm (2.49 eV). The trends in emission maxima match those calculated in the DFT study, when considering the Boltzmann-averaged population of conformations for each emitter (Table 1). Positive solvatochromism was observed, corroborating the CT assignment for the emissive excited state (Figure S64 and Tables S12–S15, Supporting Information). The photoluminescence quantum yields in toluene, $\Phi_{PL}$, range between 25% and 40%. We speculate that the lowest $\Phi_{PL}$ observed for **BIm(tBu)PyPXZ** is associated with a higher nonradiative decay rate toward the ground state, in line with the broader distribution of conformations accessible at room temperature (see Figure 4). The $\Delta E_{ST}$ values were determined from the difference in onset energies of the fluorescence and phosphorescence spectra recorded at 77 K (Figure S65, Supporting Information). $\Delta E_{ST}$ values are larger for **BIm(Me)PyPXZ**, **BIm(Ph)PyPXZ** and **BIm(tBu)PyPXZ**, with values of 0.29, 0.23, and 0.33 eV, respectively, while for **BImPyPXZ** $\Delta E_{ST}$

is much smaller at 0.12 eV (Figure S65, Supporting Information, and Table 2). Although the values recorded are larger than those predicted using TDA-DFT, the trends are manifestly the same (Table 2). A minimal delayed component was observed in toluene. We attribute the low intensity of the Delayed Fluorescence, DF, in solution to collisional quenching (Figure S66a, Supporting Information).

With a view to fabricating OLEDs, mCP was selected as a suitable host material owing to its high triplet energy (2.9 eV) and wide HOMO–LUMO gap (HOMO = −6.1 eV, LUMO = −2.4 eV).[39] For each emitter, a concentration screen was undertaken in order to determine the doping at which maximum $\Phi_{PL}$ occurs (Figure S67, Supporting Information). **BImPyPXZ** displayed severe ACQ (possibly arising from its ability to form strong hydrogen bonds, which were observed in the crystal, Figure S42, Supporting Information) with an exponential decrease in photoluminescence quantum yield with increased doping, and so 1 wt% was used in order to maintain a high $\Phi_{PL}$ (**Figure 6** and Table S17, Supporting Information). N-substitution mitigated somewhat ACQ and the highest values of $\Phi_{PL}$ were obtained at 7 wt% doping concentration for the other three emitters (Figure 6 and Tables S18–S20, Supporting Information). The addition of bulky substituents to suppress ACQ is a known strategy.[40] Photoluminescence quantum yields of 58%, 68%, and 49% were reported for 7 wt% films of **BIm(Me)PyPXZ**, **BIm(Ph)PyPXZ**, and **BIm(tBu)PyPXZ**, respectively, while the $\Phi_{PL}$ is 60% for the 1 wt% doped film of **BImPyPXZ**. The emission maximum shifted bathochromically from 1 to 100 wt% doping [1779 cm⁻¹ (0.221 eV) for **BImPyPXZ**, 1150 cm⁻¹ (0.143 eV) for **BIm(Me)PyPXZ**, 1009 cm⁻¹ (0.125 eV) for **BIm(Ph)PyPXZ** and 923 cm⁻¹ (0.114 eV) for **BIm(tBu)PyPX**, Figure S68 and Table S17–S20, Supporting Information]. The trend in emission maxima of the 7 wt% doped films in mCP is different to that observed in solution with **BIm(Ph)PyPXZ** exhibiting the most redshifted emission ($\lambda_{PL}$ = 517 nm), followed by **BImPyPXZ** ($\lambda_{PL}$ = 513 nm), **BIm(Me)PyPXZ** ($\lambda_{PL}$ = 508 nm), and **BIm(tBu)PyPXZ** ($\lambda_{PL}$ = 501 nm), following the trends in conjugation length observed in the crystal structures with **BIm(Ph)PyPXZ** and **BImPyPXZ** being the most conjugated due to the smallest $\alpha$, followed by **BIm(Me)PyPXZ** and **BIm(tBu)PyPXZ** (**Table 3** and Figure 6). The emission lifetime of each emitter was recorded using time-resolved PL. The PL decays are displayed in **Figure 7**. In addition to the prompt decay, a delayed decay is visible from about 100 ns, i.e., from 0.1 μs onward. The delayed decay is not monoexponential as
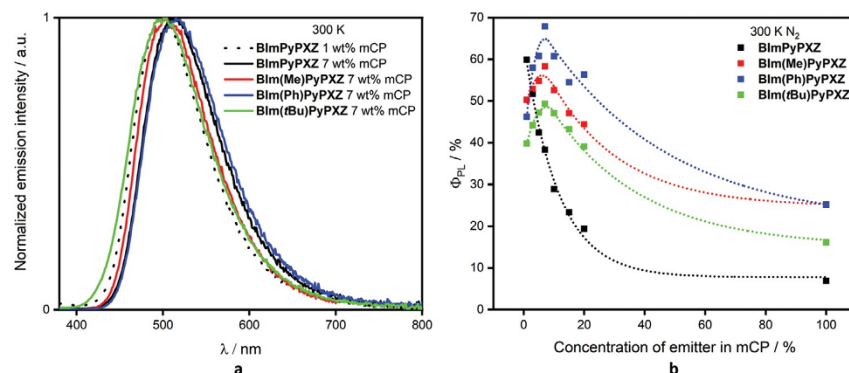
**Figure 6.** Solid-state photophysical data of the emitters. a) PL spectra of spin-coated doped mCP films. $\lambda_{exc}$ = 340 nm. b) $\Phi_{PL}$ at varying doping concentration of spin-coated mCP films under $N_2$. $\lambda_{exc}$ = 340 nm, where fittings were applied to guide the reader to trends in $\Phi_{PL}$.

we would expect from TADF behavior. Rather, its stretched-out nature indicates a superposition of a large number of decay times. We consider that this reflects the statistical distribution of torsion angles that prevails in a disordered thin film. There, molecules can be trapped in a kinetically frozen nonequilibrium geometry as opposed to a solution, where molecules can adopt their preferred equilibrium geometry. Correspondingly, the decay of the DF is not characterized by a single individual decay time, but rather by a mean value, calculated according to $\tau_{d,avg} = \int I(t) \cdot t \, dt / \int I(t) \, dt$ and listed in Table 3.[41] The introduction of the substituent leads to an average lifetime that is about two to three times that of the unsubstituted parent compound **BImPyPXZ**. A comparison of the shortest monoexponential decay contribution in this distribution of lifetimes for each compound shows that the main effect of the substitution is the addition of more longer-lived components. This is consistent with the larger range of available torsion angles observed in the theoretical calculations and illustrated in Figure 4. The conformers with the larger torsion angles will also be characterized by lower wavefunction overlap between the donor and acceptor part and lower oscillator strength, hence longer lifetime.

The shortest exponential decays in the distribution are indicated by a blue line in Figure 7 and their overall contribution to the DF intensity is listed in Table 3. The value of the longest-lived component would depend on how low intensities one wishes to consider. The decays with an initial intensity fraction of 0.02% have lifetimes around 1 ms and are indicated by a green line in Figure 7 for reference. This distribution of

lifetimes reflects a distribution of RISC rates. As detailed in the work by Gibson et al.,[33] the value of the RISC rate depends on the energy difference between $^3$CT and $^3$LE states (vibronic coupling between triplet states), and between $^1$CT and $^3$LE (spin–orbit coupling). In our compounds, a statistical distribution of torsion angles prevails, which implies a Gaussian distribution of the $^3$C–T$^3$LE and $^1$C–T$^3$LE energy differences. This results in a distribution of RISC rates, which manifests itself experimentally as a nonexponential decay of the delayed emission. If RISC rates are calculated on the basis of the measured lifetimes, then the average DF lifetimes imply average RISC rates in the range of $10^4$ s$^{-1}$ for all compounds. The highest RISC rates obtained from the shortest lifetime contributions are around $5 \times 10^5 \pm 1 \times 10^5$ s$^{-1}$ for all compounds (see the Supporting Information for details). The shortest decays are about 10–60 times shorter than the average decay times and similar for all compounds except **BIm(tBu)PyPXZ**, which is notably shorter at 6 µs. As this compound also has a lower $\Phi_{PL}$, we attribute this particular shorter lifetime mainly to an increased nonradiative decay due to its higher torsional degree of freedom (cf. Figure 4). Superimposed spectra at 10 µs and 1 ms were identical, which ruled out possible room temperature phosphorescence, which may have accounted for the long and variable lifetime at 300 K (Figure S71, Supporting Information).

The delayed emission is temperature dependent, showing the expected increase with rising temperature that is indicative of TADF (**Figure 8**). The $\Delta E_{ST}$ values range between 0.21 eV (for **BIm(Me)PyPXZ**) and 0.32 eV [for **BIm(tBu)PyPXZ**]. The

**Table 3.** Summary of the solid-state optoelectronic properties in spin-coated doped films in mCP.

| Compound | $\lambda_{PL}$ [nm] [a] | $\Phi_{PL}$ [%] [b] | $S_1$ [eV] [c] | $T_1$ [eV] [c] | $\Delta E_{ST}$ [eV] [d] | $\tau_P$ [ns] [e] | $\tau_{d,avg}$ [µs] [f] | $\tau_{short}$ [µs] [g] |
|---|---|---|---|---|---|---|---|---|
| **BImPyPXZ** [h] | 501 (513 [i]) | 59.3 | 2.77 | 2.56 | 0.21 | 10.1 | 260 | 27 (44%) |
| **BIm(Me)PyPXZ** [i] | 508 | 58.3 | 2.79 | 2.56 | 0.23 | 10.0 | 770 | 34 (25%) |
| **BIm(Ph)PyPXZ** [i] | 517 | 67.9 | 2.76 | 2.55 | 0.21 | 10.8 | 440 | 17 (30%) |
| **BIm(tBu)PyPXZ** [i] | 501 | 49.3 | 2.95 | 2.62 | 0.33 | 7.9 | 460 | 7.0 (21%) |

[a]$\lambda_{exc}$ = 340 nm; [b]Determined using an integrating sphere. $\lambda_{exc}$ = 340 nm; [c]$S_1$ and $T_1$ calculated from onset of the fluorescence spectrum at 77 K and the phosphorescence spectrum (delay: 2 ms; window: 10 ms integration) at 77 K, where the fluorescence was inferred by subtracting the phosphorescence spectrum from the steady-state PL spectrum; [d]$\Delta E_{ST} = E(S_1) - E(T_1)$; [e]Calculated from monoexponential fitting; [f]Calculated as the average lifetime, according to $\tau_{d,avg} = \int I(t) \cdot t \, dt / \int I(t) \, dt$; [g]Shortest monoexponential component of the lifetime distribution, along with its contribution to the overall DF signal in %; [h]1 wt% emitter in mCP; [i]7 wt% emitter in mCP.
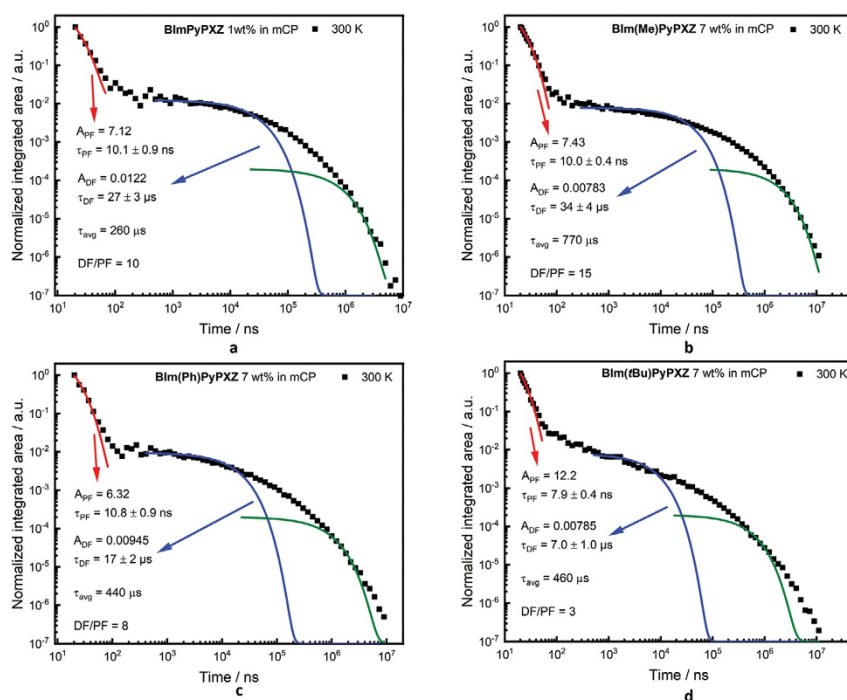
**Figure 7.** Room temperature PL decay of a) **BImPyPXZ**; b)**BIm(Me)PXZ**; c) **BIm(Ph)PXZ**; d) **BIm(tBu)PXZ** in mCP. Also shown are the prompt decay (red line), shortest monoexponential fit to the DF that is possible, $I(t) = A_{DF}\exp(-t/\tau_{DF})$, as a blue line along with the pertinent fit parameters. The longest possible monoexponential fits with $A_{DF} = 0.0002$ is also given as green line for reference.

differences in trends for $\Delta E_{ST}$ in mCP compared to both toluene and DFT calculations are likely due to different populations of conformers in each medium.

## 2.4. Device Performance

Owing to their promising photophysical behavior, vacuum-deposited OLEDs were fabricated for **BImPyPXZ**, **BIm(Me)PyPXZ**, and **BIm(Ph)PyPXZ**. Due to the instability of the emitter upon sublimation, devices containing **BIm(tBu)PyPXZ** were not prepared. The optimized device stack used was: indium tin oxide (ITO)/4,4′-cyclohexylidenebis[$N,N$-bis(4-methylphenyl)benzenamine] (TAPC) (40 nm)/tris(4-carbazoyl- 9-ylphenyl)amine (TCTA) (10 nm)/emitter: mCP (30 nm)/ bis[2-(diphenylphosphino)phenyl]ether oxide (DPEPO) (5 nm)/ TmPyPb (50 nm)/LiF (1 nm)/Al, where ITO is the anode, TAPC and TCTA act as hole-transporting layers, 1,3-bis($N$-carbazolyl) benzene (mCP) is the host, DPEPO acts as a hole-blocking layer, 1,3,5-tri($m$-pyridin-3-ylphenyl)benzene (TmPyPB) is the electron-transporting material, and LiF modifies the work function of the aluminum cathode (**Figure 9**). Four devices are presented where device **1a** contains 1 wt% **BImPyPXZ**, device **2a** contains 7 wt% **BIm(Me)PyPXZ**, device **3a** contains 7 wt% **BIm(Ph)PyPXZ** and device **4a** contains 1 wt% **BIm(Me)PyPXZ**, the latter of which was fabricated to assess the impact of doping concentration on the performance of the OLED. Another series of devices that used 40 nm TmPyPb were

prepared with lower efficiencies and are presented in the Supporting Information, designated as device series **b** (Table S22 and Figures S72 and S73, Supporting Information). The performance metrics of the OLEDs are summarized in **Table 4**.
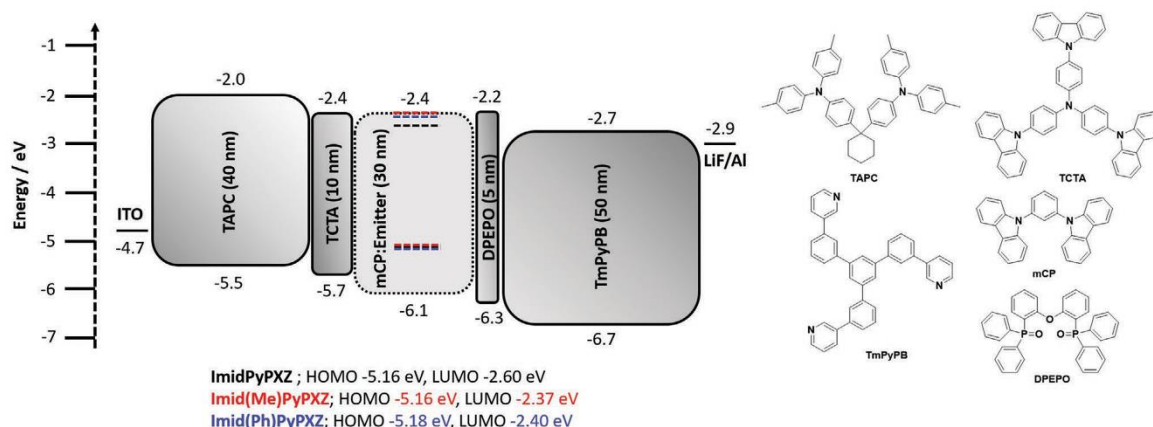
The electroluminescence spectra are shown in **Figure 10**a and the corresponding Commision International de l'Éclairage (CIE) coordinates plotted in Figure 10b. The electroluminescence maxima, $\lambda_{EL}$, match well with the corresponding $\lambda_{PL}$. Device **3a**, containing **BIm(Ph)PyPXZ**, shows the most red-shifted emission ($\lambda_{EL}$ 518 nm). Excellent EQE$_{max}$ were reported for the series of 18.6%, 23.9%, and 22.2%, respectively, for **BImPyPXZ** (1 wt% mCP), **BIm(Me)PyPXZ** (7 wt% mCP), and **BIm(Ph)PyPXZ** (7 wt% mCP) (Figure 10c). As the previous $\Phi_{PL}$s were recorded with spin-coated films, the $\Phi_{PL}$ of vacuum-evaporated films were also measured (1 wt% **BImPyPXZ** and 7 wt% **BIm(Me)PyPXZ** and **BIm(Ph)PyPXZ** in mCP), with values of 63%, 69%, and 62%, respectively. These values are similar to those obtained for spin-coated films (60%, 58%, and 68%, respectively); small differences are likely due to differences in packing in the films as a result of the two processes.[20] Considering these values and assuming 100% charge recombination and a maximum outcoupling efficiency of 30%, the theoretical maximum EQEs (EQE$_{max}$) for devices **1a**, **2a**, and **3a** are ≈19%, ≈21%, and ≈19% respectively, indicating 100% exciton utilization efficiency and confirming the operation of TADF in the device. Each of the devices shows moderate efficiency roll-off at 100 cd m$^{-2}$ of 24%, 19%, and 13% of the EQE$_{max}$ for devices **1a**, **2a**, and **3a**, respectively. There is a more severe efficiency roll-off at
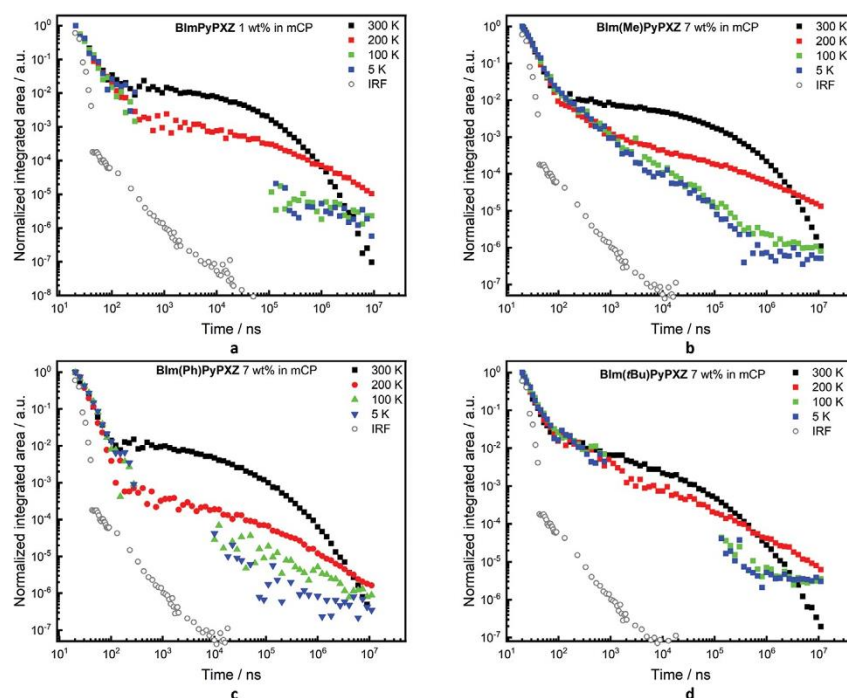
**Figure 8.** Temperature-dependent time-resolved PL in doped mCP films, $\lambda_{exc} = 355$ nm. a) 1 wt% **BImPyPXZ** in mCP. b) 7 wt% **BIm(Me)PyPXZ** in mCP. c) 7 wt% **BIm(Ph)PyPXZ** in mCP. d) 7 wt% **BIm(tBu)PyPXZ** in mCP. IRF is the instrument response function.

1000 cd m$^{-2}$, with EQE$_{1000}$ decreasing to 6.3%, 11.7%, and 9.6%, respectively. This is due to the increased number of charge carriers, increasing the likelihood of annihilation pathways, with the long lifetimes of the triplet state exacerbating this issue. We next compared the effect of doping concentration on the device performance (devices **2a** and **4a**) where the emitter, **BIm(Me)PyPXZ**, was doped into the mCP film at 7 and 1 wt%, respectively. There is a slight redshift apparent upon increased doping that is similar to the effect observed for increased doping on

the $\lambda_{PL}$ (Table 3), shifting from 501 to 511 nm when doping is increased from 1 to 7 wt%. The EQE$_{max}$ increased slightly from 21.4% to 23.9% upon increasing the doping, in line with the $\Phi_{PL}$ data (Table S7, Supporting Information). The improved exciton harvesting at higher brightness becomes apparent when considering the maximum luminance, which is doubled for devices with 7 wt% doping, nearing 18 000 cd m$^{-2}$, compared to the devices with the emitter at 1 wt% doping where it was ≈8000 cd m$^{-2}$. A similar value was achieved for the 1 wt%



ImidPyPXZ ; HOMO -5.16 eV, LUMO -2.60 eV
Imid(Me)PyPXZ; HOMO -5.16 eV, LUMO -2.37 eV
Imid(Ph)PyPXZ; HOMO -5.18 eV, LUMO -2.40 eV

**Figure 9.** Device architecture including energy levels for device series a and structures of materials used.

**Table 4.** Device properties of device series a of the various emitters in vacuum evaporated OLEDs.

| Compound (device/emitter concentration) | $V_{on}$ [V] | $\lambda_{EL}$ [nm] | $EQE_{max}$; $EQE_{100}$; $EQE_{1000}$ [%] | $Cd_{ma}$ × [A] | $lm_{max}$ [W] | $Lum_{max}$ [cd m$^{-2}$] | CIE (8 V) |
|---|---|---|---|---|---|---|---|
| **BImPyPXZ (1a/1 wt%)** | 3.5 | 508 | 18.6; 14.1; 6.3 | 50 | 42 | 8355 | 0.23, 0.47 |
| **BIm(Me)PyPXZ (2a/7 wt%)** | 3.3 | 511 | 23.9; 19.3; 9.6 | 68 | 62 | 17 711 | 0.25, 0.51 |
| **BIm(Ph)PyPXZ (3a/7 wt%)** | 3.3 | 518 | 22.2; 19.3; 11.7 | 67 | 60 | 21 227 | 0.28, 0.54 |
| **BIm(Me)PyPXZ (4a/1 wt%)** | 3.6 | 501 | 21.4; 15.7; 6.6 | 54 | 45 | 7697 | 0.21, 0.44 |
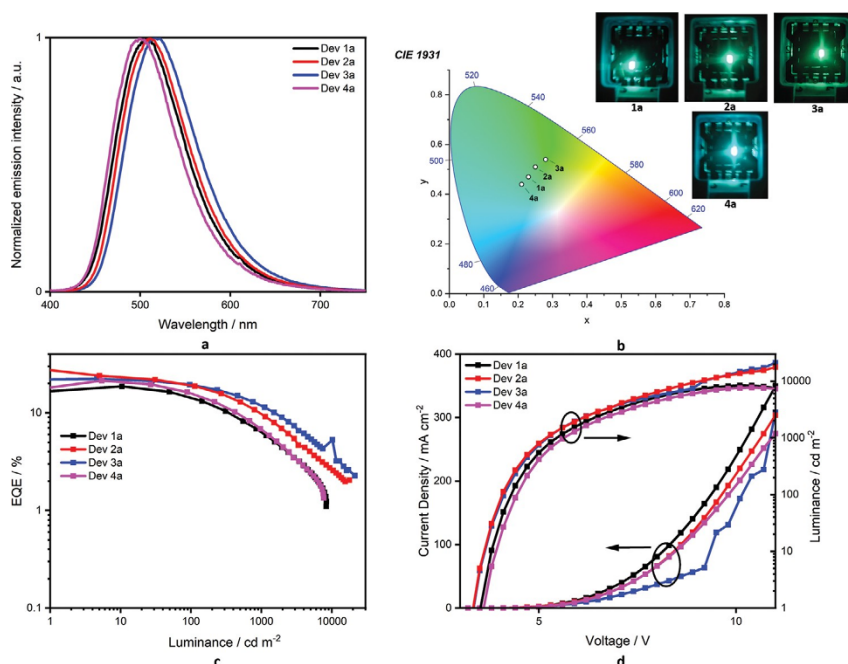


**Figure 10.** OLED device series a. a) Electroluminescence spectra. b) CIE coordinates. c) External quantum efficiency versus luminance. d) Current density/luminance versus voltage.

**BImPyPXZ** (device **1a**) at around 8000 cd m$^{-2}$. The device using **BIm(Ph)PyPXZ** showed the greatest lum$_{max}$, at more than 21 000 cd m$^{-2}$.

## 3. Conclusions

We have introduced a new acceptor unit, pyridylbenzimidazole into the donor–acceptor TADF lexicon, in which varying the $N$-substitution of the benzimidazole modulates both the emission energy and mitigates against ACQ. The bulkier the $N$-substituent, the larger the torsion between the pyridine and benzimidazole rings. This has a direct consequence on $\Delta E_{ST}$ and the emission color, with minimal impact on RISC efficiency, which is also facilitated by the presence of intermediate triplet states. Efficient OLEDs were fabricated, with $EQE_{max}$ surpassing 20% for **BIm(Me)PyPXZ** and **BIm(Ph)PyPXZ**. Functionalized derivatives allowed for high-performance OLEDs to be fabricated at increased doping, resulting in devices showing

much higher maximum luminance values. These results illustrate a family of high-performance TADF emitters.

## Supporting Information

Supporting Information is available from the Wiley Online Library or from the author.

## Conflict of Interest

The authors declare no conflict of interest.

## Data Availability Statement

The data that support the findings of this study are openly available in the University of St Andrews repository at https://doi.org/10.17630/19a1218e-1aea-4331-b65b-103b15b9699c.

## Keywords

DFT calculations, organic light-emitting diodes, photophysics, pyridylbenzimidazole, thermally activated delayed fluorescence

1  M. Y. Wong, E. Zysman-Colman, *Adv. Mater.* **2017**, *29*, 1605444.
2  Y. Liu, C. Li, Z. Ren, S. Yan, M. R. Bryce, *Nat. Rev. Mater.* **2018**, *3*, 18020.
3  Z. Yang, Z. Mao, Z. Xie, Y. Zhang, S. Liu, J. Zhao, J. Xu, Z. Chi, M. P. Aldred, *Chem. Soc. Rev.* **2017**, *46*, 915.
4  H. Uoyama, K. Goushi, K. Shizu, H. Nomura, C. Adachi, *Nature* **2012**, *492*, 234.
5  R. G. Brown, N. Entwistle, J. D. Hepworth, K. W. Hodgson, B. May, *J. Phys. Chem.* **1982**, *86*, 2418.
6  F. R. Prieto, M. Mosquera, M. Novo, *J. Phys. Chem.* **1990**, *94*, 8536.
7  G. S. Yellol, J. G. Yellol, V. B. Kenche, X. M. Liu, K. J. Barnham, A. Donaire, C. Janiak, J. Ruiz, *Inorg. Chem.* **2015**, *54*, 470.
8  Y. Qu, C. Wang, K. Zhao, Y. Wu, G. Huang, X. Han, H. Wu, *J. Coord. Chem.* **2019**, *72*, 3046.
9  T. Jella, M. Srikanth, R. Bolligarla, Y. Soujanya, S. P. Singh, L. Giribabu, *Dalton Trans.* **2015**, *44*, 14697.
10  A. M. Mansour, K. Radacki, *Dalton Trans.* **2020**, *49*, 4491.
11  V. V. Pavlishchuk, A. W. Addison, *Inorg. Chim. Acta* **2000**, *298*, 97.
12  K. C. Dash, H. Mohanta, *J. Inorg. Nucl. Chem.* **1978**, *40*, 499.
13  W.-C. Chen, Z.-L. Zhu, C.-S. Lee, *Adv. Opt. Mater.* **2018**, *6*, 1800258.
14  Z. Huang, S. Xiang, Q. Zhang, X. Lv, S. Ye, R. Guo, L. Wang, *J. Mater. Chem. C* **2018**, *6*, 2379.
15  Q. D. Liu, M. S. Mudadu, R. Thummel, Y. Tao, S. Wang, *Adv. Funct. Mater.* **2005**, *15*, 143.
16  T. Teng, K. Li, G. Cheng, Y. Wang, J. Wang, J. Li, C. Zhou, H. Liu, T. Zou, J. Xiong, C. Wu, H.-X. Zhang, C.-M. Che, C. Yang, *Inorg. Chem.* **2020**, *59*, 12122.
17  J.-H. Jia, D. Liang, R. Yu, X.-L. Chen, L. Meng, J.-F. Chang, J.-Z. Liao, M. Yang, X.-N. Li, C.-Z. Lu, *Chem. Mater.* **2020**, *32*, 620.
18  T. Shan, Z. Gao, X. Tang, X. He, Y. Gao, J. Li, X. Sun, Y. Liu, H. Liu, B. Yang, P. Lu, Y. Ma, *Dyes Pigm.* **2017**, *142*, 189.
19  Z. Huang, B. Wang, Q. Zhang, S. Xiang, X. Lv, L. Ma, B. Yang, Y. Gao, L. Wang, *Dyes Pigm.* **2017**, *140*, 328.
20  D. Hall, S. M. Suresh, P. L. dos Santos, E. Duda, S. Bagnich, A. Pershin, P. Rajamalli, D. B. Cordes, A. M. Z. Slawin, D. Beljonne, A. Köhler, I. D. W. Samuel, Y. Olivier, E. Zysman-Colman, *Adv. Opt. Mater.* **2020**, *8*, 1901627.
21  J. Mei, N. L. C. Leung, R. T. K. Kwok, J. W. Y. Lam, B. Z. Tang, *Chem. Rev.* **2015**, *115*, 11718.
22  Y.-S. Lee, Y.-H. Cho, S. Lee, J.-K. Bin, J. Yang, G. Chae, C.-H. Cheon, *Tetrahedron* **2015**, *71*, 532.
23  H. Tanaka, K. Shizu, H. Miyazaki, C. Adachi, *Chem. Commun.* **2012**, *48*, 11392.
24  M. K. Etherington, F. Franchello, J. Gibson, T. Northey, J. Santos, J. S. Ward, H. F. Higginbotham, P. Data, A. Kurowska, P. L. Dos Santos, D. R. Graves, A. S. Batsanov, F. B. Dias, M. R. Bryce, T. J. Penfold, A. P. Monkman, *Nat. Commun.* **2017**, *8*, 14987.
25  M. Moral, L. Muccioli, W. J. Son, Y. Olivier, J. C. Sancho-García, *J. Chem. Theory Comput.* **2015**, *11*, 168.
26  H. Sun, C. Zhong, J.-L. Brédas, *J. Chem. Theory Comput.* **2015**, *11*, 3851.
27  C. Li, D. Li, Y. Shi, Y. Liu, *Org. Electron.* **2018**, *54*, 177.
28  M. Tian, C. Wang, L. Wang, K. Luo, A. Zhao, C. Guo, *Luminescence* **2014**, *29*, 540.
29  M. A. El-Sayed, *Acc. Chem. Res.* **1968**, *1*, 8.
30  M. K. Etherington, J. Gibson, H. F. Higginbotham, T. J. Penfold, A. P. Monkman, *Nat. Commun.* **2016**, *7*, 13680.
31  T. Hosokai, H. Matsuzaki, H. Nakanotani, K. Tokumaru, T. Tsutsui, A. Furube, K. Nasu, H. Nomura, M. Yahiro, C. Adachi, *Sci. Adv.* **2017**, *3*, e1603282.
[32]  C. M. Marian, *J. Phys. Chem. C* **2016**, *120*, 3715.
33  J. Gibson, A. P. Monkman, T. J. Penfold, *ChemPhysChem* **2016**, *17*, 2956.
34  Y. Olivier, B. Yurash, L. Muccioli, G. D'Avino, O. Mikhnenko, J. C. Sancho-García, C. Adachi, T. Q. Nguyen, D. Beljonne, *Phys. Rev. Mater.* **2017**, *1*, 075602.
35  F. B. Dias, J. Santos, D. R. Graves, P. Data, R. S. Nobuyasu, M. A. Fox, A. S. Batsanov, T. Palmeira, M. N. Berberan-Santos, M. R. Bryce, A. P. Monkman, *Adv. Sci.* **2016**, *3*, 1600080.
36  Y. Olivier, M. Moral, L. Muccioli, J.-C. Sancho-García, *J. Mater. Chem. C* **2017**, *5*, 5718.
37  W. H. Melhuish, *J. Phys. Chem.* **1961**, *65*, 229.
38  C. M. Cardona, W. Li, A. E. Kaifer, D. Stockdale, G. C. Bazan, *Adv. Mater.* **2011**, *23*, 2367.
39  S. H. Kim, J. Jang, J. Y. Lee, *Appl. Phys. Lett.* **2007**, *90*, 223505.
40  K. Trofymchuk, A. Reisch, I. Shulov, Y. Mély, A. S. Klymchenko, *Nanoscale* **2014**, *6*, 12934.
41  J. R. Lakowicz, *Principles of Fluorescence Spectroscopy*, Springer, New York **2007**.

Supporting information available (DOI: 10.1002/adom.202100846):

https://onlinelibrary.wiley.com/action/downloadSupplement?doi=10.1002%2Fadom.202100846&file=adom202100846-sup-0001-SuppMat.pdf

#### 4.4. Paper 4: What Controls the Orientation of TADF Emitters?

# What Controls the Orientation of TADF Emitters?

Bilal A. Naqvi[1], Markus Schmid[1], Ettore Crovini[2], Prakhar Sahay[1], Tassilo Naujoks[1], Francesco Rodella[3], Zhen Zhang[4], Peter Strohriegl[3], Stefan Bräse[4,5], Eli Zysman-Colman[2] and Wolfgang Brütting[1]*

[1] Institute of Physics, University of Augsburg, Augsburg, Germany, [2] Organic Semiconductor Centre, EaStCHEM School of Chemistry, University of St Andrews, St Andrews, United Kingdom, [3] Macromolecular Chemistry, University of Bayreuth, Bayreuth, Germany, [4] Institute of Organic Chemistry, Karlsruhe Institute of Technology, Karlsruhe, Germany, [5] Institute of Biological and Chemical Systems – Functional Molecular Systems, Karlsruhe Institute of Technology, Eggenstein-Leopoldshafen, Germany

Thermally-activated delayed fluorescence (TADF) emitters—just like phosphorescent ones—can in principle allow for 100% internal quantum efficiency of organic light-emitting diodes (OLEDs), because the initially formed electron-hole pairs in the non-emissive triplet state can be efficiently converted into emissive singlets by reverse intersystem crossing. However, as compared to phosphorescent emitter complexes with their bulky—often close to spherical—molecular structures, TADF emitters offer the advantage to align them such that their optical transition dipole moments (TDMs) lie preferentially in the film plane. In this report, we address the question which factors control the orientation of TADF emitters. Specifically, we discuss how guest-host interactions may be used to influence this parameter and propose an interplay of different factors being responsible. We infer that emitter orientation is mainly governed by the molecular shape of the TADF molecule itself and by the physical properties of the host—foremost, its glass transition temperature $T_g$ and its tendency for alignment being expressed, e.g., as birefringence or the formation of a giant surface potential of the host. Electrostatic dipole-dipole interactions between host and emitter are not found to play an important role.

Keywords: OLEDs, TADF, emitter orientation, molecular orientation, emitter-host interaction

## INTRODUCTION

Organic light-emitting diodes (OLEDs) are thin-film structures where photons are produced from radiative recombination of electron-hole pairs through an excited state of a molecular emitter material that is commonly embedded in a suitable host matrix to avoid aggregation and, thus, luminescence quenching (Tang et al., 1989). While the primary steps of exciton formation and decay are quantum mechanical in nature and also involve selection rules related to the spin of the involved species, the propagation and extraction of the produced radiation can be treated in a semi-classical dipole model (Barnes, 1998; Penninck et al., 2011). The external quantum efficiency $\eta_{ext}$ of an OLED, i.e., the ratio between extracted photons from a device divided by the number of injected charges, is therefore split into an internal factor $\eta_{int}$ comprising charge balance $\gamma$, spin statistics $\eta_r$ and radiative exciton decay $q_{eff}$, and an outcoupling factor $\eta_{out}$ for the fraction of light that is actually emitted from the OLED and is visible to an observer (Tsutsui et al., 1997). Note that this separation is not strictly valid, because the radiative quantum efficiency is influenced by the device stack as well through the so-called Purcell effect, yielding an effective value $q_{eff}$ (Nowy et al., 2008; Brütting et al., 2013).

118

$$\eta_{ext} = \gamma \cdot \eta_r \cdot q_{eff} \cdot \eta_{out} \equiv \eta_{int} \cdot \eta_{out}$$

Thermally-activated delayed fluorescence (TADF) emitters—just like phosphorescent ones—can in principle harvest for 100% radiative excitons ($\eta_r = 1$) because the initially formed electron-hole pairs in the non-emissive triplet state can be efficiently converted into emissive singlets by reverse intersystem crossing (Uoyama et al., 2012). However, as compared to commercial iridium(III)-based phosphorescent complexes with their often close to spherical molecular structures, TADF emitters often possess similar shape to the host matrix molecules and offer the advantage to be aligned such that their optical transition dipole moments (TDMs) lie preferentially in the film plane (**Figure 1A**). Using the above mentioned semi-classical dipole model, it follows that the external quantum efficiency of a TADF OLED can be dramatically enhanced, if instead of an ensemble of randomly oriented emitter molecules, horizontally aligned TDMs prevail in the system (**Figure 1B**).

As described in detail in the **Supporting Material**, we use an order parameter $\Theta$ to quantify the degree of horizontal orientation of the emitting TDM (Schmidt et al., 2017), which is defined as the fraction of optical power emitted by vertical dipoles within the system. This parameter is equivalent to the second Legendre polynomial $P_2 (\vartheta) = < \cos^2 \vartheta >$, where $\vartheta$ is the angle between the substrate normal and the direction of the TDM vector (see **Figure 1A**). Ideally, the $\Theta$ values should be close to zero because the radiation from vertical dipoles remains trapped as wave-guided or surface plasmon modes and is not coupled out from an OLED.

This fact being known already for some time, the detailed mechanism driving non-isotropic orientation of molecular emitter materials in a guest-host system remained elusive. In an early work, Yokoyama has pointed out—at that time working with fluorescent-only materials—that the shape anisotropy of the molecules plays a decisive role (Yokoyama, 2011). The more rod-like (or disc-like) they are, the stronger their tendency to form optically anisotropic thin films, which he defined as the ratio of birefringence probed by ellipsometry. Alternatively, radiation pattern analysis under photoluminescence excitation (ADPL, "angular dependent photoluminescence"; see **Supporting Material** for details) was developed as a powerful method to study emitter orientation (Frischeisen et al., 2010). This technique enabled investigations on guest-host systems with only a small fraction of the light-emitting species embedded in a wider-gap host matrix. Surprisingly enough, non-isotropic radiation patterns indicating horizontal emitter orientation were observed even for systems where the host material alone does not show any anisotropy (Flämmich et al., 2011; Frischeisen et al., 2011).

An important step toward controlling emitter orientation came from the field of glass physics, where it was demonstrated that evaporated neat films of organic semiconductors can form anisotropic molecular glasses with their orientation being controlled by the temperature of the substrate $T_S$ (and the evaporation rate) in relation to the glass transition temperature $T_g$ of the organic material (Dalal et al., 2013). Specifically, it was shown that horizontal orientation of neat organic films leading to

birefringence can be obtained for $T_S/T_g \leq 0.8$. Instead of varying the substrate temperature $T_S$, Mayr showed that the same effect can be achieved in a guest-host system if hosts with different $T_g$'s are used (Mayr and Brütting, 2015). Subsequently, TADF emitters with completely horizontal orientation could be achieved by film growth on cooled substrates and their positive effect for OLED efficiency was clearly demonstrated (Komino et al., 2016).

The current understanding of orientation in OLEDs has progressed substantially, in particular as it pertains to fluorescent as well as phosphorescent emitters (Schmidt et al., 2017; Kim and Kim, 2018). Spherically octahedrally coordinated phosphorescent Iridium(III) complexes can show some degree of horizontal orientation (typically <80%), but other reports suggest that this effect is even more pronounced for TADF emitters with up to 100% of the emitters being horizontally aligned (Byeon et al., 2018). Since thermal evaporation is a non-equilibrium process, molecular orientation in such non-crystalline materials is determined at the surface of the growing film (Jurow et al., 2016; Friederich et al., 2017; Kim and Kim, 2018). Depending on substrate temperature, evaporation rate, molecular shape, and other—perhaps yet unknown—factors, the molecules at the surface may or may not have enough time to diffuse around, reorient and equilibrate with the underlying film, before they are covered by the next deposited layer such that their orientation becomes frozen (Ediger et al., 2019). Thus, film growth and morphology are kinetically controlled processes.

In this article, we address the question of which factors control the orientation of TADF emitters. Specifically, we discuss if it is an intrinsic property of the emitter and how guest-host interactions may be used to influence this parameter. Ultimately, we propose an interplay of different factors being responsible, as shown schematically in **Figure 2**.

## BASIC APPROACH

OLEDs based on TADF emitters can yield up to 100% internal quantum efficiency because all the generated triplet excitons under electrical operation are ideally converted to singlets through fast reverse intersystem crossing (Adachi, 2014). In order for this to happen the energy difference, $\Delta E_{ST}$, between singlet and triplet excited states must be sufficiently small (of the order of few $k_B T$ only) to be thermally enabled (Wong and Zysman-Colman, 2017). As $\Delta E_{ST}$ is governed by the exchange integral of the frontier orbitals responsible for the transition to these excited states, which is usually defined as the wavefunction overlap of HOMO and LUMO, i.e., the respective highest occupied and lowest unoccupied molecular orbitals (Penfold, 2015; Yersin, 2018)

$$\Delta E_{ST} \propto <\Psi_{HOMO}| \frac{1}{r_{12}} |\Psi_{LUMO} >$$

the key is to separate them spatially, which is typically done by using a twisted donor-acceptor molecular architecture that strongly electronically decouples these two moieties. However,

FIGURE 1 | (A) The process of light emission in an OLED can be described as an oscillating dipole inside a micro-cavity formed by the two electrodes, which emits perpendicularly to its axis where $\vartheta$ is the angle between TDM vector and substrate normal (Schmidt et al., 2017). Light emitted from horizontally oriented dipoles (left) will be coupled out directly or goes to substrate modes, while vertical dipoles (right) couple mainly to surface plasmons and waveguide modes. Thus, to maximize the light outcoupling to air horizontally oriented TDMs are crucial. (B) Optical simulation that shows the dependency of $\eta_{ext}$ on the orientation factor $\Theta$ ($\Theta = 0$ for horizontally aligned TDMs and 1 for completely vertically aligned TDMs). The stack used for this simulation with DMAC-TRZ as the emitter is shown in the Supporting Material. The $\Theta$ value of DMAC-TRZ varies between 0.21 in an mCBP-CN matrix, which corresponds to 79% of the TDMs being horizontally aligned, and 0.52 in mCP, i.e., <50% horizontal TDMs in this case. The corresponding $\eta_{ext}$ of the device is around 22% for the former case (gray point) and goes down to below 14% in the latter case (white point).



FIGURE 2 | Proposed model for the dominant factors affecting TADF emitter orientation. (See text for further details).

because the HOMO-LUMO overlap also is proportional to the oscillator strength for the radiative decay to the ground state, it should not become too small lest efficient luminescence will no longer be possible (Weissenseel et al., 2019).

Accordingly, the optical transition dipole moment, which is given by a similar expression,

$$\overrightarrow{p}_{TDM} \propto\; <\Psi_{HOMO}|\, \overrightarrow{r}_{12}\, |\Psi_{LUMO}>$$

also depends on the distribution of these orbitals on the molecule. TADF compounds thus typically possess emissive charge-transfer (CT) states and the direction of their TDM often coincides with (or is very close to) the long molecular axis between donor

and acceptor units. Note that there are some exceptions like the well-known 4CzIPN, which is an almost spherical molecule (Hasegawa et al., 2018). Nevertheless, the inline alignment of TDM and long molecular axis of TADF emitters holds great potential for manipulating their TDM orientation, and thus the light outcoupling from the OLED, by controlling molecular orientation upon thermal evaporation of films.

## MATERIALS AND METHODS

**Figure 3** shows the two emitter materials, DMAC-TRZ and ICzTRZ, used in this study together with their photoluminescence spectra. Both molecules are TADF emitters and emit sky-blue light. Its constituents, DMAC as donor and
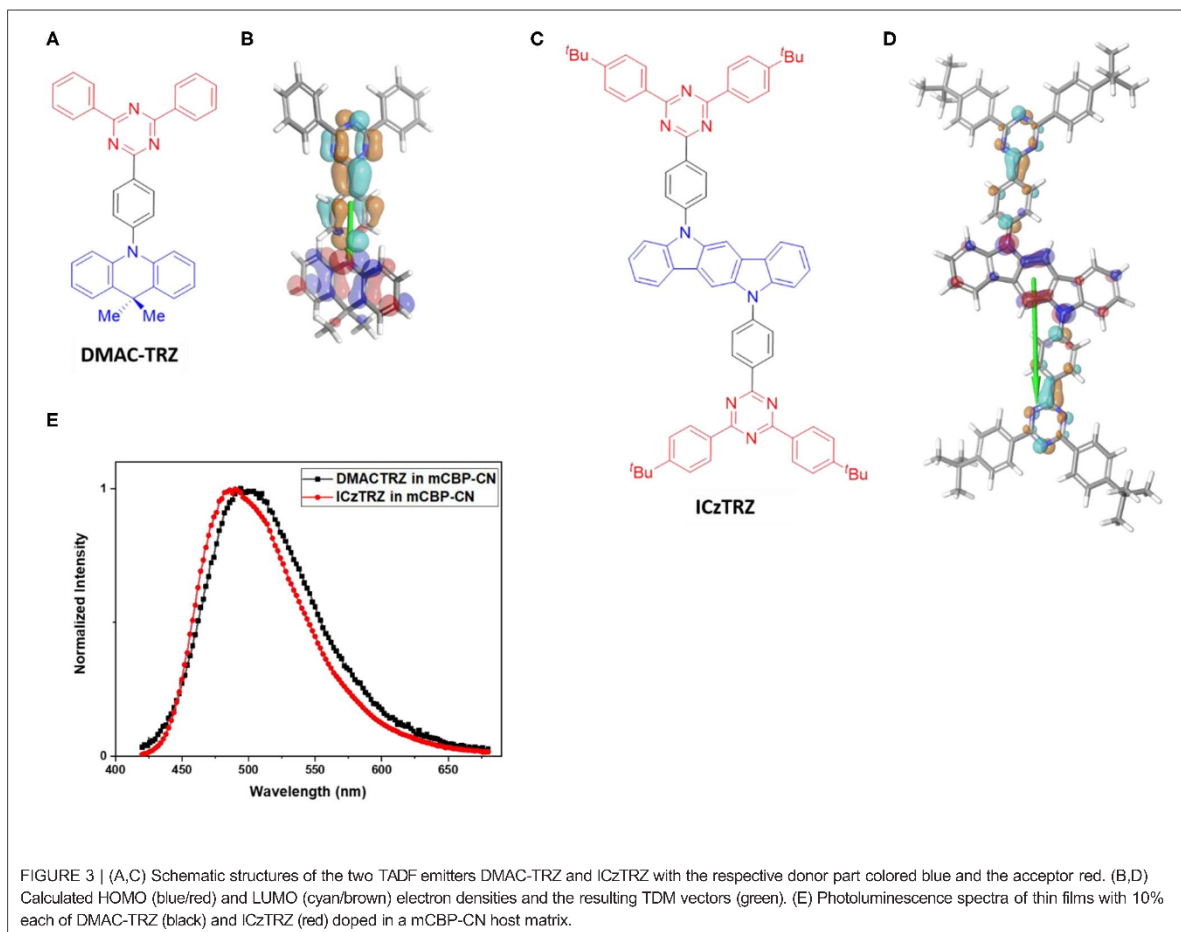
FIGURE 3 | (A,C) Schematic structures of the two TADF emitters DMAC-TRZ and ICzTRZ with the respective donor part colored blue and the acceptor red. (B,D) Calculated HOMO (blue/red) and LUMO (cyan/brown) electron densities and the resulting TDM vectors (green). (E) Photoluminescence spectra of thin films with 10% each of DMAC-TRZ (black) and ICzTRZ (red) doped in a mCBP-CN host matrix.

TRZ as acceptor, are frequently used in other TADF emitters as well and can, thus, be considered as prototypical building blocks (Wong and Zysman-Colman, 2017). ICzTRZ is a newly synthesized TADF emitter (Zhang et al., 2020), having the said TRZ as one compartment, which has almost identical emission spectrum to DMAC-TRZ (see **Figure 3E**) and, thus, similar energetics. Also shown in that figure are the calculated electron density distributions of the HOMO and LUMO (details in the **Supporting Material**). It is evident that HOMO and LUMO are spatially separated in both emitters. In DMAC-TRZ, the HOMO is located at the acridine donor and the LUMO at the triazine acceptor, while in ICzTRZ the HOMO resides at the indocarbazole donor whereas the LUMO is extended on the two triazine acceptors on both sides of the central core. Remarkably, they are largely different in both size and permanent dipole moment (PDM): DMAC-TRZ consists of a single DA building block, while ICzTRZ follows a symmetric ADA design and is therefore roughly twice as long. Moreover, because of their different designs, the DA-type system DMAC-TRZ is a polar molecule (2.01 D) while the ADA-type molecule ICzTRZ is not (0.33 D). Likewise, the longer and heavier ICzTRZ possesses a

higher glass transition temperature $T_g$ of 253°C, whereas the shorter and lighter DMAC-TRZ has a comparatively lower $T_g$ of 93°C. The calculated HOMO and LUMO distributions shown in **Figure 3** support this notion and, particularly, indicate that the TDM is parallel to the long molecular axis.

These two TADF emitters were co-evaporated with up to nine different host materials (**Figure 4**). In general, a suitable host material should have a larger optical gap to allow for energy transfer to and emission from the guest molecules; however, not all of these hosts are actually suitable hosts for efficient OLEDs because of additional requirements with respect to their triplet levels and their charge transport properties. Nevertheless, these host materials were chosen because they cover a wide range of glass transition temperatures $T_g$ (see **Table 1**), which is expected to have an effect on orientation as discussed above. Moreover, since a CT excitation results in a polar state, TADF emitters are known to be strongly affected by the polarity of the surrounding host material (Dos Santos et al., 2016). Thus, almost all of the chosen hosts also have non-negligible permanent electric dipole moment as specified in **Table 1**. This also allows investigating the potential influence of electrostatic dipole-dipole interactions

FIGURE 4 | Schematic structures of hosts used in this study.
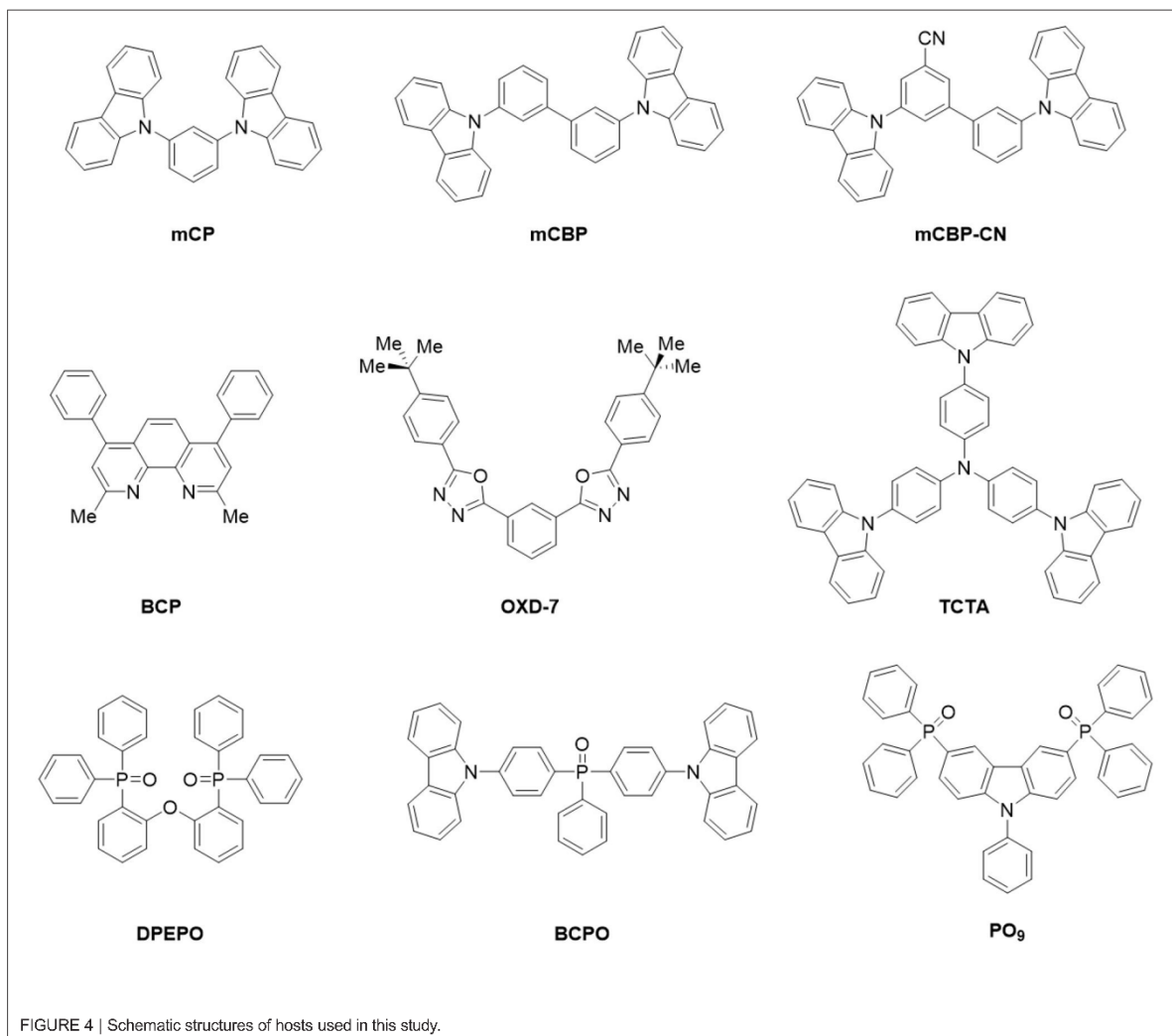
between host and emitter on the orientation process of the latter. Furthermore, these host matrices do not just consist of randomly oriented polar species but, upon thermal evaporation, some of them form films with a macroscopic dielectric polarization, which can be equivalently expressed as a non-vanishing surface charge and is often termed the giant surface potential (GSP). These values can be measured by Kelvin probe or impedance spectroscopy, as discussed in the **Supporting Material**, and are also given in **Table 1**. Finally, the A parameter quantifies alignment of the host PDMs as will be discussed later in detail.

## RESULTS AND DISCUSSION

DMAC-TRZ and ICzTRZ were co-evaporated with the different hosts as thin films on glass substrates. These films were then subjected to ADPL measurements and numerical simulation (details can be found in the **Supporting Material**). To avoid

artifacts caused by crystallization of the host matrix (especially, for low-$T_g$ materials), samples were measured as soon as possible after film deposition, but in any case, on the same day of their fabrication. **Figure 5** shows exemplary results for the two emitters together with fits to determine the emitter orientation as well as simulations indicating the expected shape of the curves for the limiting cases of $\Theta = 0.0$ (completely horizontal) and $\Theta = 0.33$ (isotropic). The determined orientation parameters of the TDMs of both emitters in the different hosts are summarized in **Table 2**.

It was observed that ICzTRZ is stronger horizontally oriented in five of these hosts as compared to DMAC-TRZ. The orientation factor for DMAC-TRZ ranges from $\Theta = 0.52$ in mCP to $\Theta = 0.21$ in an mCBP-CN matrix, while for ICzTRZ the values are not as divergent. ICzTRZ has the highest orientation factor of $\Theta = 0.12$ in mCP and the lowest is $\Theta = 0.06$ in DPEPO, which is among the best values reported for TADF emitters (Mayr et al., 2014; Byeon et al., 2018;

Tanaka et al., 2020). It is apparent from this analysis that the TDM orientation in DMAC-TRZ is affected much more strongly by the nature and polarity of the host material than in ICzTRZ.

As mentioned in the introduction, Yokoyama et al. found a correlation between anisotropic molecular shape and the tendency for horizontal molecular orientation for a series of rod-like fluorescent dyes (Yokoyama, 2011). This effect is also seen in the case of these two TADF emitter molecules, where the TDM is almost parallel to the long molecular axis. Therefore, the long ICzTRZ molecule has a much stronger horizontal TDM orientation as compared to the short DMAC-TRZ molecule. Moreover, the anisotropy factor of ICzTRZ is less effected by different hosts because alignment

is predominantly induced by the extended molecular shape of the emitter.

We recall that the different TDM orientations have important consequences for light-outcoupling in OLEDs. As already shown in **Figure 1B**, the simulated EQE of DMAC-TRZ in an OLED stack is expected to vary from <14% in mCP as the host to about 22% if the orientation obtained in mCBP-CN is taken (see the **Supporting Material** for actual device data of DMAC-TRZ). OLEDs with ICzTRZ have been the subject of a separate study (Zhang et al., 2020) where an $EQE_{max}$ of 22.1% has been achieved in mCBP as the host.

We now turn to the question of how the large variation of orientation in DMAC-TRZ can be further understood. Apparently, the molecule is not long enough to be intrinsically oriented horizontally. Thus, guest-host interactions become the dominant factor. Following the surface equilibration model

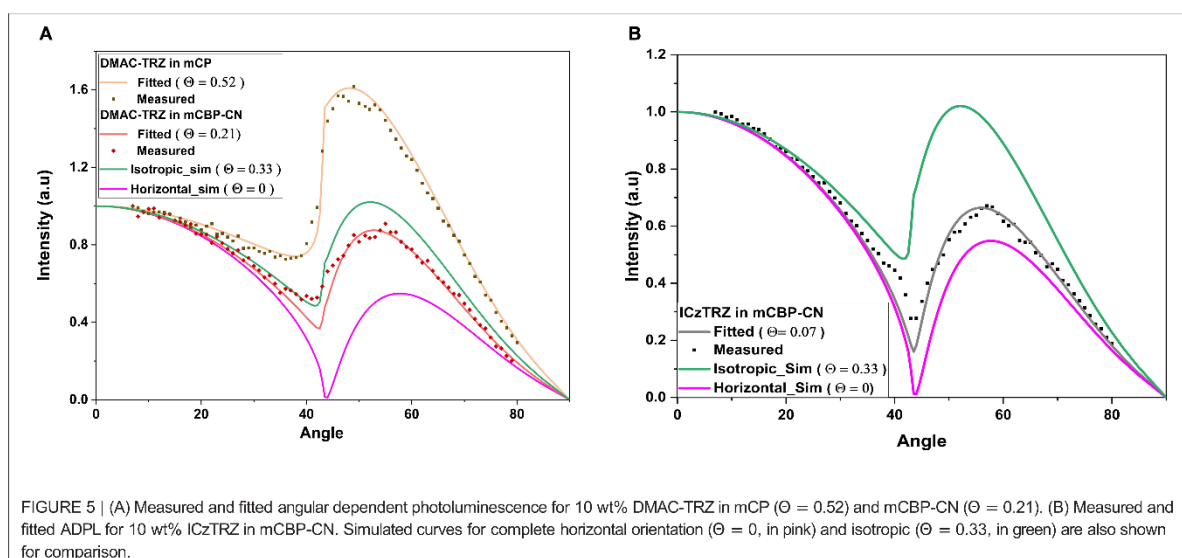TABLE 1 | Physical properties of host materials used in this study.

| Host | $T_g$ (°C) | PDM (D) | GSP (mV/nm) | Degree of PDM alignment A |
|---|---|---|---|---|
| BCP | 62[a] | 2.8 | 33 | 0.050 |
| mCP | 65[c] | 1.35 | −3.9 | 0.015 |
| OXD-7 | 77[a] | 5.5 | 68 | 0.069 |
| mCBP | 92[c] | 1.57 | 0 | 0 |
| DPEPO | 93[c] | 5.5 | 61.7 | 0.071 |
| mCBP-CN | 113[c] | 3.7 | 62.5 | 0.11 |
| BCPO | 137[b] | 3.5 | 45.6 | 0.088 |
| PO₉ | 122[b] | 6.7 | 163 | 0.18 |
| TCTA | 151[a] | 0 | 0 | 0 |

PDMs were calculated using Schrodinger Maestro Software Package. GSP was measured using impedance spectroscopy and from the measured GSP a A parameter was calculated quantifying the degree of the hosts' PDM alignment as discussed in detail in the Supporting Material. The hosts' glass transition temperatures $T_g$ were either taken from literature, as indicated, or measured by differential scanning calorimetry in this study, as described in the Supporting Material. [a] Mayr and Brütting (2015), [b] Chou and Cheng (2010), and [c] Measured values using DSC—details in Supporting Material.

TABLE 2 | Determined orientation factors (Θ) for 10 wt% doping ratio of DMAC-TRZ and ICzTRZ in different hosts.

| Host | TDM orientation factor Θ for DMAC-TRZ | TDM orientation factor Θ for ICzTRZ |
|---|---|---|
| mCP | 0.52 ± 0.01 | 0.12 ± 0.01 |
| mCBP | 0.48 ± 0.01 | 0.09 ± 0.02 |
| BCP | 0.42 ± 0.03 | - |
| DPEPO | 0.36 ± 0.02 | 0.06 ± 0.02 |
| OXD-7 | 0.33 ± 0.01 | - |
| PO₉ | 0.27 ± 0.01 | - |
| BCPO | 0.24 ± 0.01 | - |
| TCTA | 0.24 ± 0.02 | 0.07 ± 0.03 |
| mCBP-CN | 0.21 ± 0.02 | 0.07 ± 0.02 |

See Supporting Material for a complete set of the measured and fitted ADPL data.



FIGURE 5 | (A) Measured and fitted angular dependent photoluminescence for 10 wt% DMAC-TRZ in mCP (Θ = 0.52) and mCBP-CN (Θ = 0.21). (B) Measured and fitted ADPL for 10 wt% ICzTRZ in mCBP-CN. Simulated curves for complete horizontal orientation (Θ = 0, in pink) and isotropic (Θ = 0.33, in green) are also shown for comparison.

discussed in the introduction, we therefore plot the extracted $\Theta$ values vs. the $T_g$'s of the host in **Figure 6A**. As predicted by this model, the orientation depends strongly on the host: the larger its $T_g$, the lower are the $\Theta$ values. Since the substrate temperature is always kept at or slightly above room temperature ($T_S \sim$ 300K), we arrive at a ratio of $T_S/T_g \sim$ 0.9 for low-$T_g$ hosts like mCP or BCP, while the highest $T_g$ hosts yield a ratio of about 0.7. According to the work of Ediger et al. these values are above and below the critical value ($T_S/T_g \sim$ 0.85), respectively, to change molecular orientation from more vertical in the former case, to more horizontal in the latter (Ediger et al., 2019).
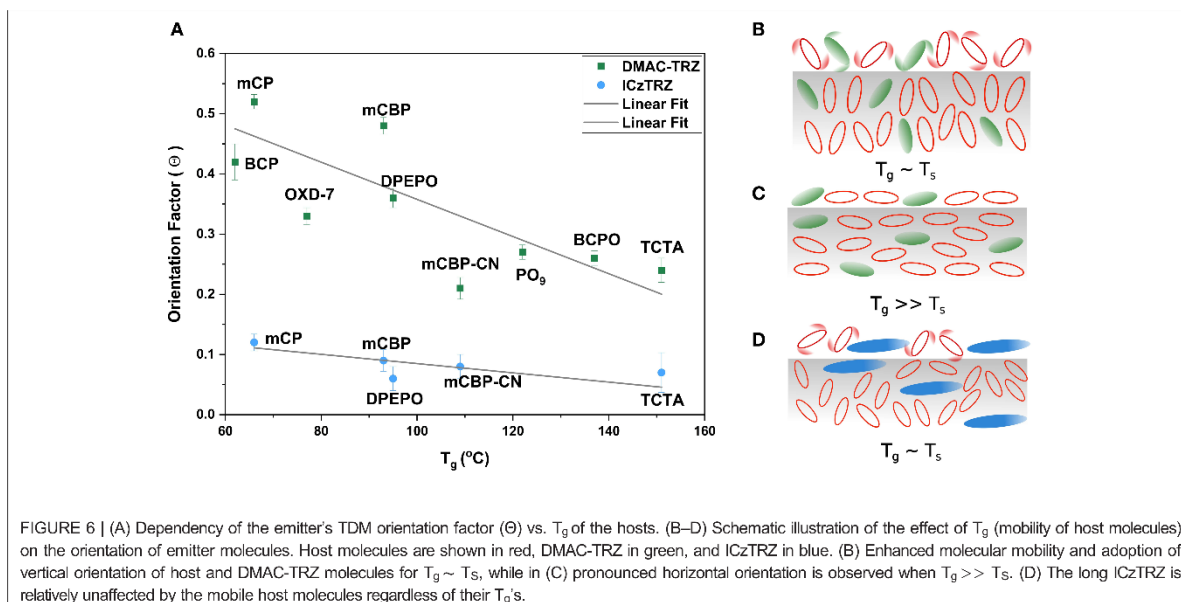
Thus, we propose a possible model for this behavior based upon these trends and previous studies (Mayr and Brütting, 2015; Ediger et al., 2019). If the substrate temperature is close to the $T_g$ of the host material, molecules landing on the surface will have high mobility and, consequently, enough time to adapt to the surface equilibrium structure, which consists of predominantly vertically aligned molecules (**Figure 6B**). However, if $T_g \gg T_S$, the molecules will not have enough time to diffuse and reorient on the surface before being immobilized by the next layer of molecules and will thus not be able to equilibrate (**Figure 6C**). Thus, the initial horizontal orientation at the surface will be effectively frozen because mobilities in the bulk are orders of magnitude lower than at the surface of the film (Ediger et al., 2019). If the substrate temperature is fixed and we co-deposit an emitter with hosts having different $T_g$, a similar effect will therefore be observed. This effect is seen when DMAC-TRZ is co-deposited with hosts with a range of different $T_g$. It is highly vertical ($\Theta = 0.52$) in mCP, which has $T_g$ of 62°C, while this factor becomes less than half as large ($\Theta = 0.24$) in a host with high $T_g$ like BCPO and TCTA.

This trend was also followed for ICzTRZ but, overall, it shows horizontal orientation in all the different hosts. The highest value of the orientation factor ($\Theta = 0.12$) for ICzTRZ is much lower than the lowest in DMAC-TRZ ($\Theta = 0.21$). Thus, we believe that ICzTRZ is not much affected by the mobility of host molecules owing to its long molecular shape and its high $T_g$ as neat material (**Figure 6D**). This is confirmed by the fact that the strongest horizontal orientation is already observed in DPEPO as host, which has a moderate $T_g$, and does not further improve even for the highest $T_g$ host TCTA.

However, there are also some outliers for DMAC-TRZ in **Figure 6A**. This means that for some hosts we see a stronger horizontal alignment than expected from the $T_g$ alone; see e.g., BCP in comparison to mCP, DPEPO compared to mCBP, or OXD-7 and mCBP-CN. All of them are relatively polar materials. Thus, we have to extend the above presented model to include polarity of the host, but more importantly, the possibility of orientational order of the host itself.

To this end, the concept of spontaneous orientation polarization is very useful. It is known that many polar organic semiconductors exhibit a giant surface potential in thin films grown by vacuum deposition. In this case, the orientation of their permanent electrical dipole moments has a preferential alignment perpendicular to the film plane, i.e., in the vertical direction (Noguchi et al., 2019). This can even occur if the molecules have almost spherical structure, like $Alq_3$, and do not exhibit any optical anisotropy. The GSP of the host materials has been determined by Kelvin probe and impedance spectroscopy as discussed in the **Supporting Material**. The obtained values are listed in **Table 1**.

**Figure 7A** shows the TDM orientation parameter $\Theta$ of DMAC-TRZ plotted vs. the GSP of the host materials.



FIGURE 6 | (A) Dependency of the emitter's TDM orientation factor ($\Theta$) vs. $T_g$ of the hosts. (B–D) Schematic illustration of the effect of $T_g$ (mobility of host molecules) on the orientation of emitter molecules. Host molecules are shown in red, DMAC-TRZ in green, and ICzTRZ in blue. (B) Enhanced molecular mobility and adoption of vertical orientation of host and DMAC-TRZ molecules for $T_g \sim T_S$, while in (C) pronounced horizontal orientation is observed when $T_g \gg T_S$. (D) The long ICzTRZ is relatively unaffected by the mobile host molecules regardless of their $T_g$'s.
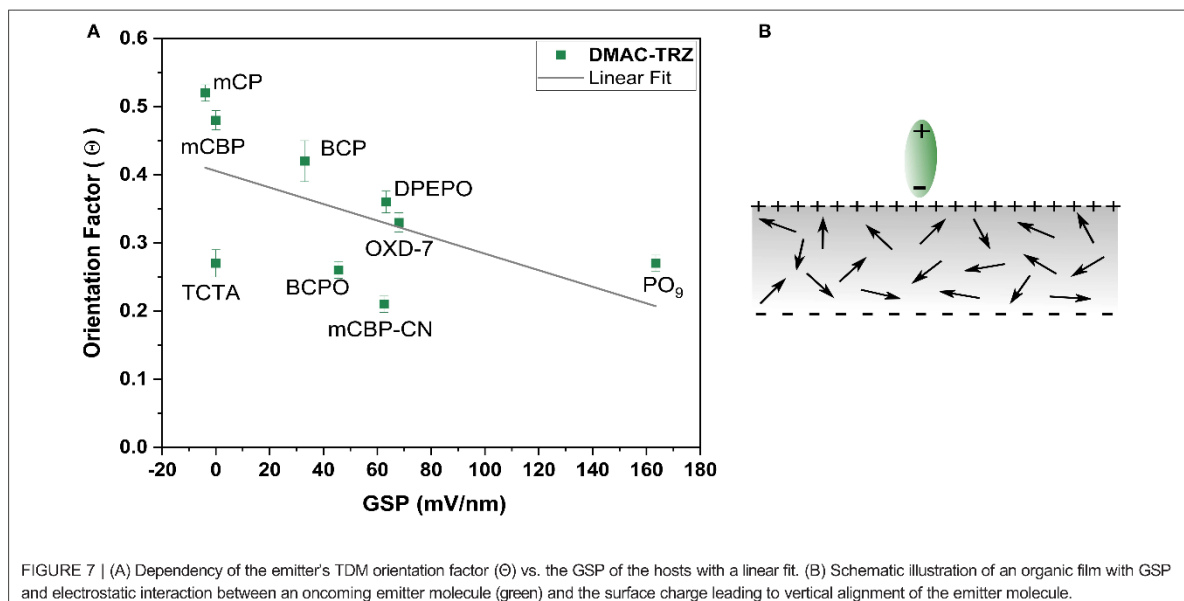
124

FIGURE 7 | (A) Dependency of the emitter's TDM orientation factor ($\Theta$) vs. the GSP of the hosts with a linear fit. (B) Schematic illustration of an organic film with GSP and electrostatic interaction between an oncoming emitter molecule (green) and the surface charge leading to vertical alignment of the emitter molecule.
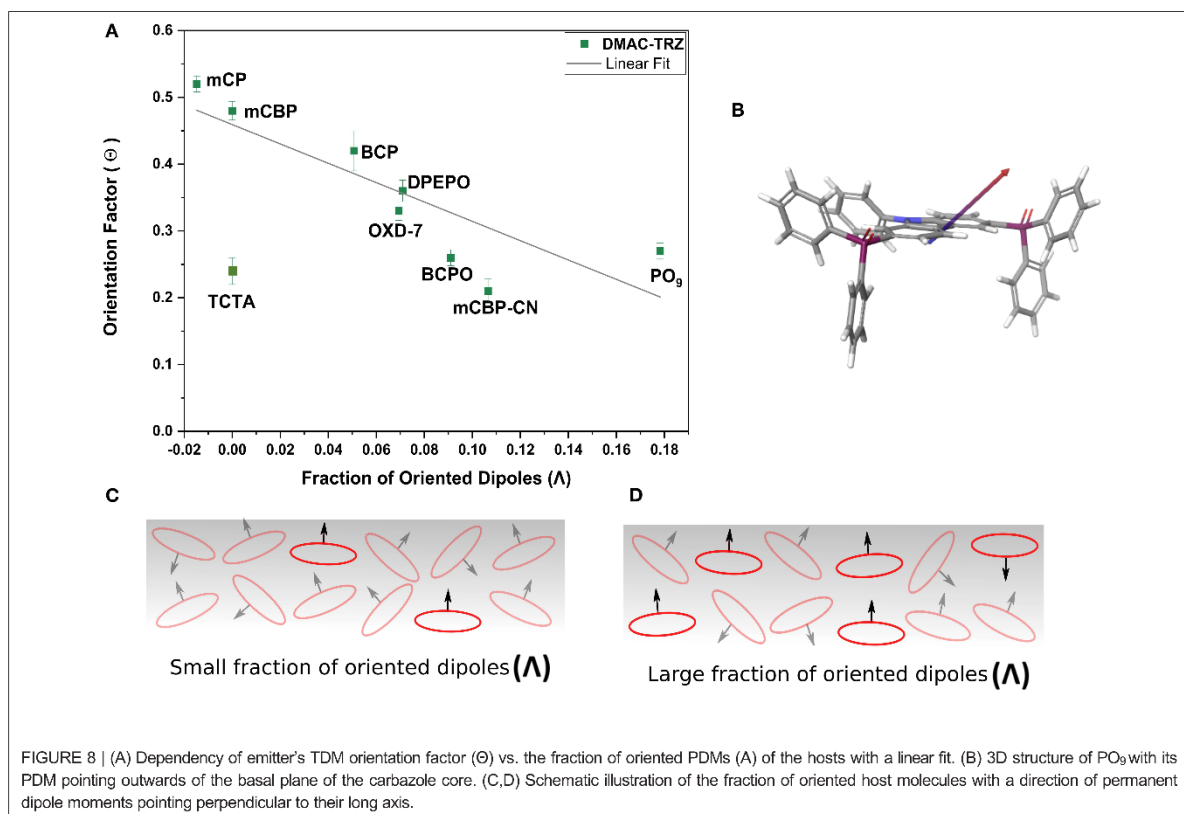


FIGURE 8 | (A) Dependency of emitter's TDM orientation factor ($\Theta$) vs. the fraction of oriented PDMs ($\Lambda$) of the hosts with a linear fit. (B) 3D structure of PO$_9$ with its PDM pointing outwards of the basal plane of the carbazole core. (C,D) Schematic illustration of the fraction of oriented host molecules with a direction of permanent dipole moments pointing perpendicular to their long axis.

# 4. Publications

Apparently, there seems to be a trend of more horizontal TDM orientation with increasing surface potential; but still some data points clearly deviate from the fitted linear trendline. First and most obviously, this is TCTA, which does not have a GSP, because it is a non-polar molecule. Secondly, also BCPO and mCBP-CN show stronger orientation as compared to host materials with similar GSP. This raises the question, if the GSP, i.e., the density of polarization charges sitting at the surface of the film is a suitable parameter to explain TADF emitter orientation. In a simple electrostatic interaction model (see **Figure 7B**) the electric field originating from the positive surface charge would rather align the arriving polar TADF emitter molecules in the vertical direction. The larger the GSP, the more vertical alignment would be expected. This is obviously not observed, because for DMAC-TRZ the PDM is roughly parallel to the TDM, and the latter is more and more horizontal the larger the GSP of the host becomes. Thus, the argument using the macroscopic orientation polarization of the host materials has to be revised.

In general, the degree of alignment in such host materials is rather low. If an order parameter $A$ is defined as the ratio between the measured GSP and the theoretically possible value for perfect vertical alignment of its PDMs (see **Supporting Material** for details), one typically finds numbers in the range 5–10% (Jäger et al., 2016). This means that either most of their PDMs are randomly oriented with just a small net alignment in vertical direction or that most of the PDMs align pairwise antiparallel so that their net dipole moment vanishes.

In order to investigate the potential influence of host alignment on TDM orientation we have analyzed the order parameter $A$ for all the host materials (values were given already in **Table 1**). **Figure 8A** shows the TDM orientation $\Theta$ of the emitter DMAC-TRZ plotted vs. the PDM orientation parameter $A$ of the host. In this case, the correlation is significantly improved compared to that in **Figure 7A**, which indicates that the horizontal alignment of the emitter molecules is not driven by an electrostatic interaction according to the GSP at the film surface, but rather by the higher degree of ordering of the host molecules.

At first glance this may appear somewhat counterintuitive, but one must be aware that many of the studied host molecules have a PDM pointing perpendicular to the long molecular axis (**Figure 8B** and **Supporting Material**) This is true specifically for phosphine oxides like DPEPO, BCPO, and PO9, but also to some extent for mCBP-CN and OXD-7. Thus, a higher degree of vertical alignment of their PDMs actually means that these host molecules preferentially lie flat on the film surface (see **Figures 8C,D**). We note that this consideration is true even for the remaining outlier in **Figure 8A**: TCTA. It does not have a PDM; therefore, $A = 0$. However, TCTA is known to be birefringent with the ordinary component of the refractive index being about 0.15 larger than the extraordinary one (see the optical constants in the **Supporting Material**), indicating that it adopts a preferential horizontal orientation. This is not surprising in view of its high $T_g$ if the above discussed surface equilibration model is being considered not only for the emitter molecules but for the host as well.

Finally, we also want to note that chemical interactions between host and emitter molecules may cause specific combinations of them to orient better than predicted by the general $T_g$ trend. It has been reported recently, that specific molecular units may allow π-π stacking or weak hydrogen bonds between host and emitter and, thus, promote horizontal orientation (Watanabe et al., 2019; Sasabe et al., 2020). Probably, this could contribute to the observation that DMAC-TRZ is relatively more horizontally aligned in mCBP-CN as compared to other hosts with similar physical properties.

## CONCLUSIONS

The answer to the question: "What controls the orientation of TADF emitters?" has—at least—three components. In the first place, it is an intrinsic property of the emitter molecule itself. The longer and more rod-like it is, the stronger will be its tendency to lie down when evaporated on a surface. In addition, due to their relatively high molecular mass, such emitter molecules will be affected only little by the arrangement of surrounding host molecules. In this respect, the ADA (or, equivalently, DAD) design principle of many TADF emitters can be regarded as highly beneficial for horizontal alignment.

In the second place, if the TADF emitter is shorter (containing only one DA building block), the host matrix takes over the dominant role for determining emitter orientation and, in particular, the glass transition temperature of the host is of paramount importance. A high $T_g$ reduces the surface diffusivity of molecules such that they do not have enough time to equilibrate and, thus, often adopt the favored lying flat orientation. As a third factor, we could identify alignment of the host material itself as an additional parameter to promote TADF emitter orientation.

Although one can already find several examples in the literature, where researchers have used these guidelines on purpose (or perhaps even without knowing), we anticipate that designing TADF emitters in a way to promote their horizontal alignment could further boost this third generation of OLEDs to outcompete phosphorescent ones, specifically in the blue spectral region.

## DATA AVAILABILITY STATEMENT

All datasets generated for this study are included in the article/**Supplementary Material**.

## AUTHOR CONTRIBUTIONS

BN, MS, EC, EZ-C, and WB conceived the project. BN prepared samples and performed angular dependent PL measurements and their analysis to obtain TDM orientation. MS and EC performed TD-DFT on the emitter molecules. MS further calculated PDMs of host materials and analyzed their alignment by impedance spectroscopy. OLEDs were prepared and analyzed

126

in experiment and simulation by PSa and TN. FR measured glass transition temperatures of the emitters and some of the hosts. ZZ synthesized the emitter ICzTRZ. PSt, SB, EZ-C, and WB supervised the project. All authors discussed the results and commented on the manuscript.

## FUNDING

## SUPPLEMENTARY MATERIAL

The Supplementary Material for this article can be found online at: https://www.frontiersin.org/articles/10.3389/fchem.2020.00750/full#supplementary-material

## REFERENCES

Adachi, C. (2014). Third-generation organic electroluminescence materials. *Jpn. J. Appl. Phys.* 53:060101. doi: 10.7567/JJAP.53.060101

Barnes, W. L. (1998). Fluorescence near interfaces: the role of photonic mode density. *J. Mod. Opt.* 45, 661–699. doi: 10.1080/09500349808230614

Brütting, W., Frischeisen, J., Schmidt, T. D., Scholz, B. J., and Mayr, C. (2013). Device efficiency of organic light-emitting diodes: progress by improved light outcoupling. *Phys. Status Solidi Appl. Mater. Sci.* 210, 44–65. doi: 10.1002/pssa.201228320

Byeon, S. Y., Kim, J., Lee, D. R., Han, S. H., Forrest, S. R., and Lee, J. Y. (2018). Nearly 100% horizontal dipole orientation and upconversion efficiency in blue thermally activated delayed fluorescent emitters. *Adv. Opt. Mater.* 6, 1–6. doi: 10.1002/adom.201701340

Chou, H. H., and Cheng, C. H. (2010). A highly efficient universal bipolar host for blue, green, and red phosphorescent OLEDs. *Adv. Mater.* 22, 2468–2471. doi: 10.1002/adma.201000061

Dalal, S. S., Fakhraai, Z., and Ediger, M. D. (2013). High-throughput ellipsometric characterization of vapor-deposited indomethacin glasses. *J. Phys. Chem. B* 117, 15415–15425. doi: 10.1021/jp405005n

Dos Santos, P. L., Ward, J. S., Bryce, M. R., and Monkman, A. P. (2016). Using guest-host interactions to optimize the efficiency of TADF OLEDs. *J. Phys. Chem. Lett.* 7, 3341–3346. doi: 10.1021/acs.jpclett.6b01542

Ediger, M. D., De Pablo, J., and Yu, L. (2019). Anisotropic vapor-deposited glasses: hybrid organic solids. *Acc. Chem. Res.* 52, 407–414. doi: 10.1021/acs.accounts.8b00513

Flämmich, M., Frischeisen, J., Setz, D. S., Michaelis, D., Krummacher, B. C., Schmidt, T. D., et al. (2011). Oriented phosphorescent emitters boost OLED efficiency. *Org. Electron.* 12, 1663–1668. doi: 10.1016/j.orgel.2011.06.011

Friederich, P., Cochoorn, R., and Wenzel, W. (2017). Molecular origin of the anisotropic dye orientation in emissive layers of organic light emitting diodes. *Chem. Mater.* 29, 9528–9535. doi: 10.1021/acs.chemmater.7b03742

Frischeisen, J., Yokoyama, D., Adachi, C., and Brütting, W. (2010). Determination of molecular dipole orientation in doped fluorescent organic thin films by photoluminescence measurements. *Appl. Phys. Lett.* 96, 1–4. doi: 10.1063/1.3309705

Frischeisen, J., Yokoyama, D., Endo, A., Adachi, C., and Brütting, W. (2011). Increased light outcoupling efficiency in dye-doped small molecule light-emitting diodes with horizontally oriented emitters. *Org. Electron.* 12, 809–817. doi: 10.1016/j.orgel.2011.02.005

Hasegawa, Y., Yamada, Y., Sasaki, M., Hosokai, T., Nakanotani, H., and Adachi, C. (2018). Well-ordered 4CzIPN ((4s,6s)-2,4,5,6-tetra(9-H-carbazol-9-yl)isophthalonitrile) layers: molecular orientation, electronic structure, and angular distribution of photoluminescence. *J. Phys. Chem. Lett.* 9, 863–867. doi: 10.1021/acs.jpclett.7b03232

Jäger, L., Schmidt, T. D., and Brütting, W. (2016). Manipulation and control of the interfacial polarization in organic light-emitting diodes by dipolar doping. *AIP Adv.* 6, 1–7. doi: 10.1063/1.4963796

Jurow, M. J., Mayr, C., Schmidt, T. D., Lampe, T., Djurovich, P. I., Brütting, W., et al. (2016). Understanding and predicting the orientation of heteroleptic phosphors in organic light-emitting materials. *Nat. Mater.* 15, 85–91. doi: 10.1038/nmat4428

Kim, K. H., and Kim, J. J. (2018). Origin and control of orientation of phosphorescent and TADF dyes for high-efficiency OLEDs. *Adv. Mater.* 30, 1–19. doi: 10.1002/adma.201705600

Komino, T., Sagara, Y., Tanaka, H., Oki, Y., Nakamura, N., Fujimoto, H., et al. (2016). Electroluminescence from completely horizontally oriented dye molecules. *Appl. Phys. Lett.* 108:241106. doi: 10.1063/1.4954163

Mayr, C., and Brütting, W. (2015). Control of molecular dye orientation in organic luminescent films by the glass transition temperature of the host material. *Chem. Mater.* 27, 2759–2762. doi: 10.1021/acs.chemmater.5b00062

Mayr, C., Lee, S. Y., Schmidt, T. D., Yasuda, T., Adachi, C., and Brütting, W. (2014). Efficiency enhancement of organic light-emitting diodes incorporating a highly oriented thermally activated delayed fluorescence emitter. *Adv. Funct. Mater.* 24, 5232–5239. doi: 10.1002/adfm.201400495

Noguchi, Y., Brütting, W., and Ishii, H. (2019). Spontaneous orientation polarization in organic light-emitting diodes. *Jpn. J. Appl. Phys.* 58:SF0801. doi: 10.7567/1347-4065/ab0de8

Nowy, S., Krummacher, B. C., Frischeisen, J., Reinke, N. A., and Brütting, W. (2008). Light extraction and optical loss mechanisms in organic light-emitting diodes: influence of the emitter quantum efficiency. *J. Appl. Phys.* 104:123109. doi: 10.1063/1.3043800

Penfold, T. J. (2015). On predicting the excited-state properties of thermally activated delayed fluorescence emitters. *J. Phys. Chem. C* 119, 13535–13544. doi: 10.1021/acs.jpcc.5b03530

Penninck, L., De Visschere, P., Beeckman, J., and Neyts, K. (2011). Dipole radiation within one-dimensional anisotropic microcavities: a simulation method. *Opt. Express* 19:18558. doi: 10.1364/OE.19.018558

Sasabe, H., Chikayasu, Y., Ohisa, S., Arai, H., Ohsawa, T., Komatsu, R., et al. (2020). Molecular orientations of delayed fluorescent emitters in a series of carbazole-based host materials. *Front. Chem.* 8:427. doi: 10.3389/fchem.2020.00427

Schmidt, T. D., Lampe, T., Daniel Sylvinson, M. R., Djurovich, P. I., Thompson, M. E., and Brütting, W. (2017). Emitter orientation as a key parameter in organic light-emitting diodes. *Phys. Rev. Appl.* 8, 1–28. doi: 10.1103/PhysRevApplied.8.037001

Tanaka, M., Noda, H., Nakanotani, H., and Adachi, C. (2020). Molecular orientation of disk-shaped small molecules exhibiting thermally activated delayed fluorescence in host-guest films. *Appl. Phys. Lett.* 116:023302. doi: 10.1063/1.5140210

Tang, C. W., Vanslyke, S. A., and Chen, C. H. (1989). Electroluminescence of doped organic thin films. *J. Appl. Phys.* 65, 3610–3616. doi: 10.1063/1.343409

Tsutsui, T., Aminaka, E., Lin, C. P., and Kim, D. U. (1997). Extended molecular design concept of molecular materials for electroluminescence: sublimed-dye films, molecularly doped polymers and polymers with chromophores. *Philos. Trans. R. Soc. A Math. Phys. Eng. Sci.* 355, 801–814. doi: 10.1098/rsta.1997.0045

Uoyama, H., Goushi, K., Shizu, K., Nomura, H., and Adachi, C. (2012). Highly efficient organic light-emitting diodes from delayed fluorescence. *Nature* 492, 234–238. doi: 10.1038/nature11687

Watanabe, Y., Yokoyama, D., Koganezawa, T., Katagiri, H., Ito, T., Ohisa, S., et al. (2019). Control of molecular orientation in organic semiconductor films using weak hydrogen bonds. *Adv. Mater.* 31, 1–8. doi: 10.1002/adma.201808300

Weissenseel, S., Drigo, N. A., Kudriashova, L. G., Schmid, M., Morgenstern, T., Lin, K. H., et al. (2019). Getting the right twist: influence of donor-acceptor dihedral angle on exciton kinetics and singlet-triplet gap in deep blue thermally

127

activated delayed fluorescence emitter. *J. Phys. Chem. C* 123, 27778–27784. doi: 10.1021/acs.jpcc.9b08269

Wong, M. Y., and Zysman-Colman, E. (2017). Purely organic thermally activated delayed fluorescence materials for organic light-emitting diodes. *Adv. Mater.* 29:1605444. doi: 10.1002/adma.201605444

Yersin, H. (2018). *Materials Based on Thermally Activated Delayed Fluorescencele, 1st Edn.* Weinheim: Wiley-VCH.

Yokoyama, D. (2011). Molecular orientation in small-molecule organic light-emitting diodes. *J. Mater. Chem.* 21, 19187–19202. doi: 10.1039/c1jm13417e

Zhang, Z., Crovini, E., Santos, P. L. D., Naqvi, B., Sahay, P., Cordes, D., et al. (2020). Efficient sky-blue organic light-emitting diodes using a highly horizontally oriented thermally activated delayed fluorescence emitter. (Submitted).

Supporting information available (DOI: 10.3389/fchem.2020.00750):
https://www.frontiersin.org/articles/10.3389/fchem.2020.00750/full#supplementary-material

128

## 4.5 List of publications

**Paper 1**

Rodella, F.; Bagnich, S.; Duda, E.; Meier, T.; Kahle, J.; Athanasopoulos, S.; Köhler, A.; Strohriegl, P. High Triplet Energy Host Materials for Blue TADF OLEDs-A Tool Box Approach. *Frontiers in chemistry [Online]* **2020,** *8*, 657.

https://www.frontiersin.org/articles/10.3389/fchem.2020.00657/full

**Paper 2**

Rodella, F.; Saxena, R.; Bagnich, S.; Banevičius, D.; Kreiza, G.; Athanasopoulos, S.; Juršėnas, S.; Kazlauskas, K.; Köhler, A. and Strohriegl, P. Low efficiency roll-off blue TADF OLEDs employing a novel acridine-pyrimidine based high triplet energy host.

Submitted to Journal of Materials Chemistry C.

During the reviewing process of the thesis, the manuscript has been published in Journal of Materials Chemistry C (*J. Mater. Chem. C*, 2021, **9**, 17471-17482. DOI: 10.1039/D1TC03598C) https://pubs.rsc.org/en/content/articlelanding/2021/tc/d1tc03598c

**Paper 3**

Hall, D.; Rajamalli, P.; Duda, E.; Suresh, S. M.; Rodella, F.; Bagnich, S.; Carpenter-Warren, C. L.; Cordes, D. B.; Slawin, A. M. Z.; Strohriegl, P.; Beljonne, D.; Köhler, A.; Olivier, Y.; Zysman-Colman, E. Substitution Effects on a New Pyridylbenzimidazole Acceptor for Thermally Activated Delayed Fluorescence and Their Use in Organic Light-Emitting Diodes. *Adv. Optical Mater. [Online]* **2021**, 2100846.

https://onlinelibrary.wiley.com/doi/10.1002/adom.202100846

**Paper 4**

Naqvi, B. A.; Schmid, M.; Crovini, E.; Sahay, P.; Naujoks, T.; Rodella, F.; Zhang, Z.; Strohriegl, P.; Bräse, S.; Zysman-Colman, E.; Brütting, W. What Controls the Orientation of TADF Emitters? *Frontiers in chemistry [Online]* **2020,** *8*, 750.

https://www.frontiersin.org/articles/10.3389/fchem.2020.00750/full

**Acknowledgments**

First of all, I want to thank my supervisor Prof. Peter Strohriegl for welcoming me into the lab and helping me settle down in Germany. He gave me full support, trust, and the best working conditions I could get, allowing me to grow and improve during my stay. I also want to thank the group of Prof. Anna Köhler for the fruitful collaboration and the whole EU Marie Skłodowska-Curie ITN TADFlife group for the high-level research and the great experiences spent together. Thanks also to all the people who contributed to the manuscript and publications that are objects of the thesis.

Aside from the research, many other people at the Uni Bayreuth have to be acknowledged. All of these people have contributed, in different ways, to make these three years special. Identifying them as "Colleagues" would be downgrading. They have become friends. The party-mate, the super Crossfit group, the bike-tour group, and the pasta evenings group. No need to mention, you already got it. A big thank goes to my labmates and the whole MCI family for the great environment, lunches, coffee breaks, Kicker, parties, hiking, and adventures. So many to count.

Finally, a lovely thank goes to Michelle, whose dazzling light makes everything brighter. It would not have been the same without you. Thanks also to the great Upper Franconian second family for the warm welcome and help.

To conclude, I want to thank my longtime friends and brothers Nicola, Riccardo, Niccolò, Mattia and Filippo, as well as those found in Parma: Matteo and Saverio. Thank you for your support over the years and in times of need. I know you are there and you will always be.

The whole journey so far would not have been possible without my special family. You have always believed in me, more than anyone else, giving me the strength to face everything. I have no words to describe how grateful I am. Thanks to Silvana, Eleonora, Lucia and Sandro (and also Achille). This is dedicated to you.

**Ringraziamenti (Acknowledgments)**

Prima di tutto, voglio ringraziare il mio supervisore Prof. Peter Strohriegl per avermi accolto nel laboratorio e avermi aiutato a stabilirmi in Germania. Mi ha dato pieno supporto, fiducia e le migliori condizioni di lavoro che potessi ottenere, permettendomi di crescere e migliorare durante il mio soggiorno. Voglio anche ringraziare il gruppo della Prof.ssa Anna Köhler per la proficua collaborazione e tutto il gruppo EU Marie Skłodowska-Curie ITN TADFlife per la ricerca di alto livello e le grandi esperienze trascorse insieme. Grazie anche a tutte le persone che hanno contribuito alla realizzazione del manoscritto e delle pubblicazioni oggetto della tesi.

A parte la ricerca, molte altre persone all'Uni Bayreuth devono essere riconosciute. Tutte queste persone hanno contribuito, in modi diversi, a rendere speciali questi tre anni. Identificarli come "Colleghi" sarebbe un declassamento. Li considero amici. Il compagno di feste, il super gruppo di Crossfit, il gruppo bike-tour e il gruppo delle serate a base di pasta. Non c'è bisogno di nominarti, ti sei già riconosciuto. Un grande ringraziamento va ai miei compagni di laboratorio e a tutta la famiglia MCI per l'ottimo ambiente, pranzi, pause caffè, bigliardino, feste, escursioni e avventure. Così tanti da contare.

Infine, un bel ringraziamento va a Michelle, la cui luce abbagliante rende tutto più luminoso. Non sarebbe stato lo stesso senza di te. Grazie anche alla grande seconda famiglia dell'alta Franconia per la calorosa accoglienza e l'aiuto.

Per concludere, voglio ringraziare gli amici e fratelli di sempre Nicola, Riccardo, Niccolò, Mattia e Filippo, così come quelli trovati a Parma: Matteo e Saverio. Grazie per il vostro supporto negli anni e nei momenti di bisogno. So che ci siete e ci sarete sempre.

Tutto il percorso fatto sino ad ora non sarebbe stato possibile senza la mia famiglia speciale. Avete sempre creduto in me, più di chiunque altro, dandomi la forza per affrontare ogni cosa. Non ho parole per descrivere quanto sia grato. Grazie a Silvana, Eleonora, Lucia e Sandro (e anche Achille). Questo è dedicato a voi.

**Erklärung**

(Eidesstattliche) Versicherungen und Erklärungen

(§ 9 Satz 2 Nr. 3 PromO BayNAT)

Hiermit versichere ich eidesstattlich, dass ich die Arbeit selbstständig verfasst und keine anderen als die von mir angegebenen Quellen und Hilfsmittel benutzt habe (vgl. Art. 64 Abs. 1 Satz 6 BayHSchG).

(§ 9 Satz 2 Nr. 3 PromO BayNAT)

Hiermit erkläre ich, dass ich die Dissertation nicht bereits zur Erlangung eines akademischen Grades eingereicht habe und dass ich nicht bereits diese oder eine gleichartige Doktorprüfung endgültig nicht bestanden habe.

(§ 9 Satz 2 Nr. 4 PromO BayNAT)

Hiermit erkläre ich, dass ich Hilfe von gewerblichen Promotionsberatern bzw. -vermittlern oder ähnlichen Dienstleistern weder bisher in Anspruch genommen habe noch künftig in Anspruch nehmen werde.

(§ 9 Satz 2 Nr. 7 PromO BayNAT)

Hiermit erkläre ich mein Einverständnis, dass die elektronische Fassung meiner Dissertation unter Wahrung meiner Urheberrechte und des Datenschutzes einer gesonderten Überprüfung unterzogen werden kann.

(§ 9 Satz 2 Nr. 8 PromO BayNAT)

Hiermit erkläre ich mein Einverständnis, dass bei Verdacht wissenschaftlichen Fehlverhaltens Ermittlungen durch universitätsinterne Organe der wissenschaftlichen Selbstkontrolle stattfinden können.

Bayreuth, den 14.10.2021

Francesco Rodella